Distributed Fiber Optic Strain Sensing in Hydraulic Concrete and Earth Structures

Measuring Theory and Field Investigations on Dams and Landslides

von

Roland Hoepffner

Dr.-Ing. Roland Hoepffner, Lehrstuhl und Versuchsanstalt für Wasserbau und Wasserwirtschaft der Technischen Universität München

Technische Universität München

Lehrstuhl für Wasserbau und Wasserwirtschaft

80290 München, Arcisstraße 21
Germany

Tel.: 089 / 289 23161
Fax: 089 / 289 23172
E-Mail: wabau@bv.tum.de

Versuchsanstalt für Wasserbau und Wasserwirtschaft (Oskar von Miller - Institut)

82432 Obernach, Walchensee
Germany

Tel.: 08858 / 9203 0
Fax: 08858 / 9203 33
E-Mail: obernach@bv.tum.de

ISSN 1437-3513

ISBN 978-3-940476-13-5

Berichte des Lehrstuhls und der Versuchsanstalt für
Wasserbau und Wasserwirtschaft

Herausgegeben von Prof. Peter Rutschmann
Ordinarius für Wasserbau und Wasserwirtschaft, TU München

Druck und Einband: Meissner Druck GmbH, Oberaudorf

Preface and Acknowledgements

The research presented in this thesis has been carried out during my time as a research associate at the Institute of Hydraulic and Water Resources Engineering of the Technische Universität München. The idea for this work evolved during a research project with the Brazilian research institute LACTEC in Curitiba.

First of all I would like to express my sincere gratitude to Prof. (em.) Dr.-Ing. Theodor Strobl. His way of encouraging, guiding and supporting me both professionally and personally was exemplary. I thank him in every possible way for the valuable discussions and the support, which allowed me to bring this work to a good end.

I greatly thank my doctoral advisor Prof. Dr.-Ing. habil. Markus Aufleger, now head of the chair of Hydraulic Engineering at the University of Innsbruck, for his continuous support, his profound advisory input, the necessary trust and his open ears and mind. Thanks to his commitment I was able to receive all personal and material support necessary to realize all required tests. At this point I would also like to thank the University of Innsbruck and its staff for providing me their laboratory facilities for several tests.

I would also like to express my thanks to Prof. Dr. rer. nat. Kurosch Thuro, head of the chair of Engineering Geology, for his support and valuable discussions in the final stages of this work. I am also deeply grateful to Dipl.-Geol. John Singer for the exceptional cooperation at the Aggenalm Landslide.

I thank Prof. Dr.-Ing. Peter Rutschmann for giving me the opportunity to finish this work at the Institute of Hydraulic Engineering in Munich and for chairing the dissertation procedures.

The whole work would not have been possible without the never ceasing enthusiasm of MSc Douglas E. Moser. At the time of the tests in Brazil he was responsible for the excellent team of workers at the construction site. Eng. Amauri Garcia deserves special thanks for his kind, patient and creative support. I also thank Sensornet Ltd, especially Dan Watley, for providing us cables, sensing equipment and excellent technical support.

During my field tests I could always count on the helping hands of Valerie Neisch and Bernhard Simon. I also wish to thank Marco Conrad, Markus Fischer, Christian Stelzl, Lutz Keydel, my dad Lutz and my sister Dorothee for valuable discussions and the final review of this work.

Last but not least I am very grateful to all friends and colleagues in Munich and Obernach that contributed to an unforgettable time both in and outside the office.

Munich, December 2008 Roland Hoepffner

Zusammenfassung

Glasfaserkabel zur verteilten faseroptischen Dehnungsmessung werden seit einigen Jahren zur Überwachung von Ingenieurbauwerken eingesetzt. Ziel ist es, ganzheitliche Informationen zu Deformationen innerhalb einer Struktur zu bekommen um somit auf ihren Zustand und ihr Verhalten schließen zu können.

Die vorliegende Arbeit befasst sich mit der Anwendbarkeit von verteilten faseroptischen Dehnungsmessungen in unterschiedlichen Wasserbauwerken und Bodenstrukturen. Neben Grundlagenversuchen zu den Dehnungskabeln wurden Versuche zur Rissortung und Rissbreitenbestimmung an einer Betonsäule, einem Betonbalken und an einem Block aus Walzbeton durchgeführt. Darüber hinaus wurden Feldversuche an einer Staumauer aus Walzbeton und an einer Hangbewegung zur Bestimmung der Gleitzone und oberflächlicher Relativbewegungen durchgeführt. Vorversuche zur Dehnungsmessung in Schüttdämmen wurden im Labor gemacht. Die Anwendbarkeit der verteilten faseroptischen Dehnungsmessung im Beton wurde nachgewiesen. Dies gilt sowohl für die Installation als auch die Genauigkeit der Dehnungsmessung und Rissbreitenbestimmung.

Summary

Fiber optic cables for distributed fiber optic strain sensing are being used for monitoring of civil engineering structures for several years. The aim is to receive integral information on deformations inside a structure to evaluate its state and behavior.

The present work deals with the applicability of distributed fiber optic strain sensing in different hydraulic engineering and soil structures. Besides basic tests on strain sensing cables, tests for crack detection and crack width evaluation in different concrete structures were conducted: A concrete column, a concrete beam and a roller compacted concrete (RCC) block. Field tests were carried out at an RCC dam and at a slope movement to evaluate the sliding zone and relative surface movements. Preliminary tests concerning strain measurements in embankment dams were carried out in the laboratory. The applicability of distributed fiber optic strain sensing in concrete was confirmed. This applies for the installation as well as for the accuracy for strain detection and crack width evaluation.

Distributed Fiber Optic Strain Sensing in
Hydraulic Concrete and Earth Structures
Measuring Theory and Field Investigations on Dams and Landslides

- Contents -

1 Introduction

Since the beginning of the last century, hydraulic structures for energy production, irrigation, drinking water supply and flood protection quickly gained in interest. With the advances in construction technology, those structures could be built larger with rising volumes of concrete and filling material. This development however also lead to rising problems as it was not possible for a long time to get information about the state of a structure from its inside. In concrete dams, the appearance of cracks could only be estimated from distributed or single point temperature measurements, single point strain sensors and the evaluation of seepage water. With the recent developments in fiber optic strain sensing and its progress to full scale field applications, this work will show that it is now possible to localize even small cracks inside of large concrete structures along several kilometers of optical strain sensing cable. The potential of distributed strain sensing is not limited to concrete structures but can also find application in earthen structures such as dams and dikes as well as in landslides.

Distributed fiber optic measurements are defined as measurements in an optical fiber, where information on temperature and/or strain can be gathered principally at every single point along the fiber. The spatial resolution hereby describes the distance between two measuring points and depends on the sensing method and physical limitations. With the development and commercialization of the first distributed strain sensing devices, this technique gained in interest also for hydraulic engineering applications. The technology of distributed fiber optic strain sensing is still being further developed in terms of spatial resolution and measurement accuracy. Already today it can be emphasized that this technology is suitable to close the gap between conventional monitoring systems and integral monitoring in many different hydraulic engineering applications.

This thesis focuses on the appliance of distributed fiber optic strain sensing in three different structures and materials. Tests for strain and crack detection in reinforced and roller compacted concrete structures have been carried out in the laboratories of the Technische Universität München in Obernach and on an RCC dam in Brazil. On a landslide in the German Alps, fiber optic strain sensing cables have been installed vertically and close to the surface for the monitoring of crack developments, surface movements and the detection of large shear zones. Apart from basic tests on the measuring accuracy using different strain sensing cables, fundamental tests on the installation and deformation sensing in embankment dams have been carried out in the laboratories of the University of Innsbruck. The first part of this work discusses the needs and opportunities of fiber optic strain sensing especially in the three above mentioned disciplines. The second part gives an insight into the technique of fiber optic strain sensing, followed by analyses and discussions of the field and laboratory tests in concrete structures, landslides and embankment dams. The last part of this work will give an outlook to future opportunities for distributed fiber optic strain sensing in hydraulic engineering.

2 Needs for distributed fiber optic strain sensing in hydraulic engineering

2.1 Introduction

Distributed fiber optic strain sensing is especially useful to monitor the inside of large structures where single point, visual or geodetic observations are not able to deliver the location or the appearance of excessive strain, deformations, movements or cracks. This applies even more in regions that are difficult to access. Especially in hydropower plants, the loads on the concrete due to vibrations could be very high. While electrical strain sensing methods are sensitive to electromagnetic interferences from lightning strokes or overvoltage, fiber optic measurements are not affected. Landslides that might need to be monitored in the vicinity of reservoirs and dams are sometimes difficult to access. Conventional methods, mostly based on remote sensing are not able to collect data in case of bad sight. Also locating large shear zones is not possible with conventional methods. Just as the monitoring of cracks in concrete, the settlements in embankment dams are only possible to be measured at specific points, where extensometers or inclinometers are installed.

2.2 Strain and cracks in concrete structures

2.2.1 Basic considerations

Cracks in concrete appear when its tensile strength is exceeded. The formation of cracks in concrete therefore depends on the structure itself and the affecting stresses at first place. It has to be distinguished between unreinforced concrete (e.g. mass concrete) and reinforced concrete. Mass concrete describes the concrete for structures or structural parts whose cross section is large enough so the hydration heat from the cement has to be taken into consideration in order to avoid the development of cracks due to thermal stresses. Incorporating a low cement factor with a high proportion of large coarse aggregate, the low cement content keeps the hydration heat in the young concrete down. The restrained decrease of the cooling concrete volume leads to cracks in concrete when the tensile strength of the mass concrete is exceeded. Depending on the orientation of cracks, the safety of gravity dams will often not be affected by thermal cracks but they might well reduce the serviceability of a structure. Problems for the safety however might arise in arch dams, where the stability of the structure can be affected due to changes in the load transfer into the foundation.

When external forces are applied on a stationary object, the appearance of stress and strain is the result. Stress is defined as the object's internal resisting force, and strain is defined as the displacement and deformation that occurs. For a uniform distribution of internal resisting forces, stress σ can be calculated by dividing the force F applied on the unit area A:

$$\sigma = \frac{F}{A}$$ *Eq. 2-1*

σ	stress [N/mm²] or [MPa]
F	force [N]
A	unit area [mm²]

Strain ε is defined as the amount of deformation per unit length of an object when an external load is applied. It is calculated by dividing the elongation by the initial length:

$$\varepsilon = \frac{\Delta L}{L_0}$$ *Eq. 2-2*

ε	strain [-] or [m/m]
ΔL	elongation [m]
L_0	initial unit length [m]

Typical values for strain in concrete are considerably less than 0.01 m/m and are consequently expressed in micro-strain units (1 μ-strain = 1 με = $1 \cdot 10^{-6}$ m/m). Negative strain is equal to the strain that is a consequence of compressive stresses while strain in the common sense is equal to tensile strain thus the deformation due to tensile stresses. The tensile strength of concrete is very depending on the aggregate bond (interface between aggregate and binder matrix) in connection with the maximum aggregate size. The compressive strength mainly depends on the composition and the properties of the hardening matrix of the cementitious material and in some extent on the aggregate quality and its gradation. As the direct tensile strength of concrete is more difficult to test, the splitting tensile strength may be used to characterize its ability to withstand tensile forces. Equation 2-3 is one of many approaches to predict the splitting tensile strength from the compressive strength (USACE 2000).

$$f_{sts} = 0.7055 \cdot \sqrt{f_c} \qquad \textit{Eq. 2-3}$$

f_{sts} splitting tensile strength [MPa]
f_c compressive strength [MPa]

Stress is the response of concrete to strain. The relation between strain and stress is generally represented by stress-strain-curves. A typical stress-strain-curve for concrete is shown in Fig. 2-1.

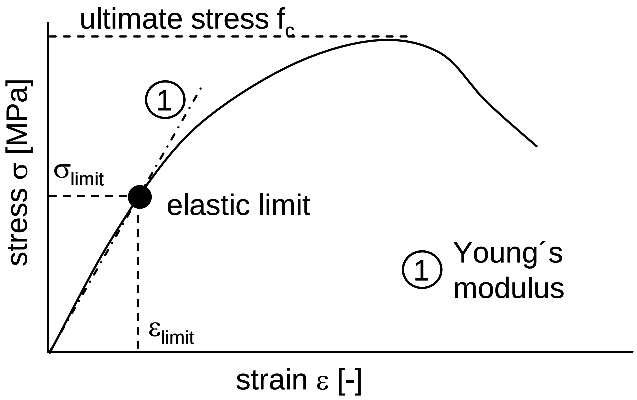

Fig. 2-1: Typical stress-strain curve for concrete based on Conrad (2006)

The modulus of elasticity that is important for further calculations is the Young's modulus. It correlates stress and strain in the linear portion of the stress-strain-curve up to the elastic limit σ_{limit} at 40 % of the ultimate stress f_c (Eq. 2-4).

$$E = \frac{\sigma}{\varepsilon} \qquad \textit{Eq. 2-4}$$

E Young's modulus (elastic modulus) [MPa]

The modulus of elasticity can be calculated directly from the ultimate stress and the compressive strain at the elastic limit ε_{limit}. The elastic behavior of RCC lasts at least up to 40 % of the ultimate compressive strength (Schrader 1995; Dunstan and Ibánez-de-Aldecoa 2003).

The volume change of mass concrete due to the development of hydration heat is a major concern. Hydration heat develops during the hardening of the concrete. The reaction of water with the cement is an exothermic process, which generates a considerable amount of heat over an extended period of time. The amount of hydration heat Q in kJ/kg depends on the fraction and type of cement. To keep the temperatures low, mass concrete has lower cement contents where a part of the cement may be substituted by puzzolan or fly ash. The adiabatic fractional change in length or volume of a material for a unit change in temperature at constant pressure is expressed by the thermal expansion coefficient α_T. The fractional change in length can be expressed as:

$$\frac{\Delta L}{L_0} = \Delta T \cdot \alpha_T \qquad \textit{Eq. 2-5}$$

ΔL	deformation [m]
L_0	initial unit length [m]
ΔT	temperature difference [K]
α_T	coefficient of linear thermal expansion [K^{-1}].

The adiabatic volumetric change of a matrix can be expressed in the same way by exchanging the change in length with volume and applying the coefficient of volumetric thermal expansion. Taking Equation 2-2 into account, the strain can be expressed in terms of temperature change and α_T, which is depending on the material and can be evaluated experimentally from concrete specimens:

$$\varepsilon_T = \Delta T \cdot \alpha_T \qquad \textit{Eq. 2-6}$$

In mass concrete, the contraction of the concrete due to cooling is barely sufficiently possible as it is restrained from the surrounding concrete (internal restraint). When the tensile strength of the concrete is exceeded, cracks are the consequence. This is counteracted by joints in massive concrete structures, sometimes supported by other options like e.g. temperature control (Moser, Hoepffner et al. 2006).

2.2.2 Conventional- and roller compacted concrete (RCC)

Mass concrete and roller compacted concrete basically differ in their placing method and their mix design. RCC can be much drier, has considerably lower cement and water contents than conventional mass concrete and essentially has no slump, which makes it support heavy earth moving machinery for its compaction. RCC is usually compacted in layers of around 30 cm. Two basic concepts in concrete mix design can be distinguished: low cementitious RCC with a cement content of 99 kg/m³ or less (Schrader, López et al. 2003) and high cementitious RCC with 150 kg/m³ cement or more with a high volume replacement by puzzolan

(Dunstan 2004). Watertightness through horizontal joints (in between layers) in low cementitious RCC is achieved by using PVC membranes and grout enriched vibratable RCC on the upstream side of the dam. According to the current state-of-the-art, conventional vibratable mass concrete (CVC) is only seldom used for sealing purposes on the upstream side. CVC and RCC basically show similar characteristics with regard to crack formation.

The process of the formation of cracks in mass concrete can be ascribed to thermal reactions, influences by alkaline aggregate reaction, settlements in the foundation, dead weight and static and dynamic loading. Cracks can appear on the dam surface as surface cracks or on the inside as mass cracks. Surface cracking because of temperature occurs due to the constraint of the warm interior of the mass concrete to the faster cooling outside. The disproportionate contraction of the cooling concrete on the outside leads to the formation of surface cracks (Fig. 2-2).

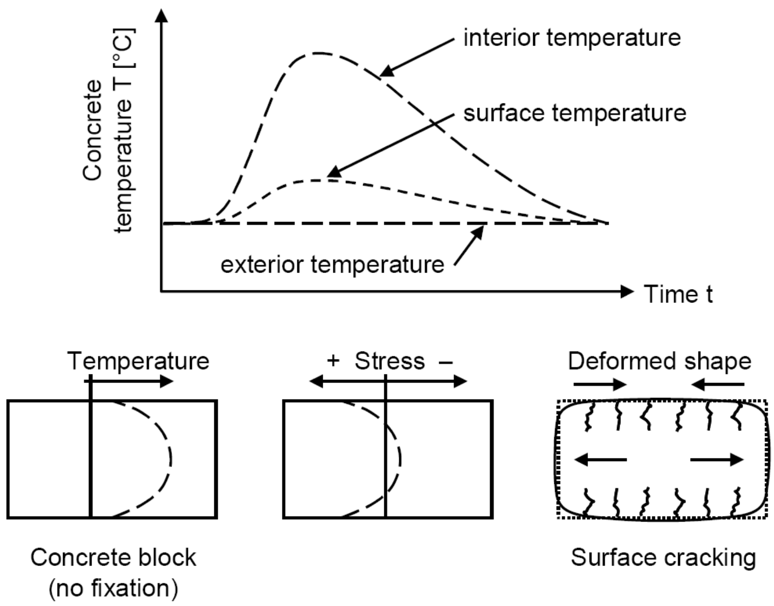

Fig. 2-2: Internal restraint and surface cracking (Conrad 2006)

Mass cracking on the other hand may appear when the concrete cools down and thus contracts but is hindered by the foundation or adjacent structures (Fig. 2-3). Deformations from non-thermal effects in concrete dams can be considered minor (Andriolo 1998).

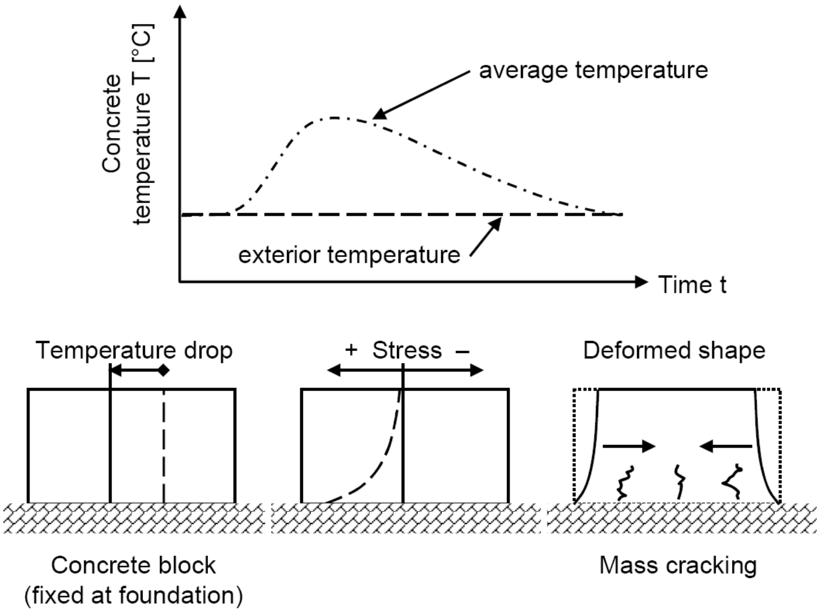

Fig. 2-3: External restraint and mass cracking (Conrad 2006)

Mass cracking in a concrete dam can occur in both, transversal and longitudinal direction. The investigation of longitudinal cracks however is not completed yet and the detection of transversal cracks is still not unfailing (Conrad, Hoepffner et al. 2007). As depicted in Fig. 2-4, cracks in both directions can develop when the concrete body contracts while cooling and is hindered by the foundation. While transversal cracks are visible at the surface or sometimes in the gallery, longitudinal cracks remain hidden in the dam structure.

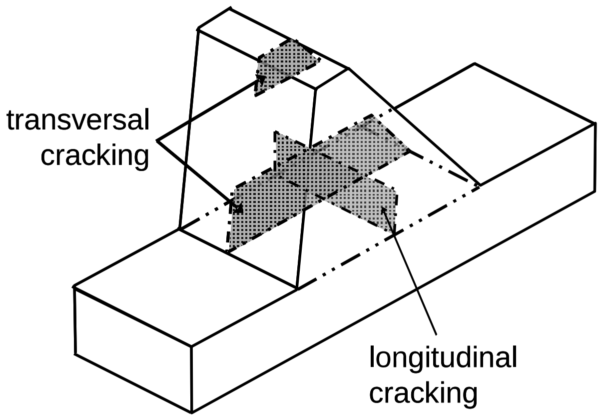

Fig. 2-4: Cracking in concrete dams (Conrad, Hoepffner et al. 2007)

Therefore, one focus in mass concrete technology research is the development of thermal stresses in the dam body. After placement of the concrete, the temporal growth of stiffness and the initial release of hydration heat in conjunction with present restraint (internal and external) results in moderate compressive temperature stresses, also due to high relaxation of stresses and creep effects in the early age (Conrad, Aufleger et al. 2003). When the hydration process nearly finalizes and the rate of heat release retards, the temperature of the concrete begins to drop. In this phase, the concrete has gained a much higher stiffness, so only a small drop of temperature may compensate the initially built up compressive stresses. Further cooling of the concrete leads to tensile stresses, which may exceed the tensile strength of the concrete, which in turn leads to thermal cracking. The development of stresses in young concrete under restrained deformation is shown in Fig. 2-5.

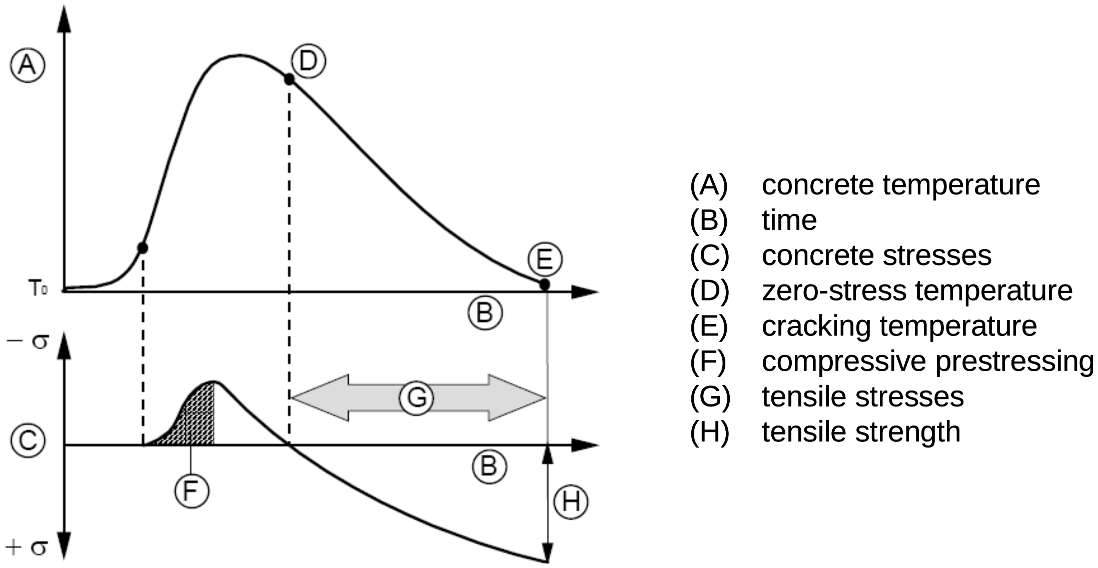

Fig. 2-5: Stresses in young concrete under restrained deformation (Aufleger, Conrad et al. 2003)

Thermal cracking is usually evaluated from temperature distributions in the concrete. Intensive research has therefore been conducted regarding the development of temperature and modulus of elasticity in young mass concrete (Padevet 2002; Conrad, Aufleger et al. 2003; Siew, Puapansawat et al. 2003). Great advances have also been made in terms of simulating the unsteady temperature development and the resulting state of stress in RCC using finite element (FE) models (Conrad 2006; Zhu, Semprich et al. 2007). Regarding monitoring it is hardly possible to receive information on local temperature gradients in mass concrete from conventional single point thermocouples. They can be obtained with high accuracy by distributed fiber optic temperature measurements (around ± 0.1 °C). From analyses in two RCC dams and numerical parametrical studies, Conrad (2006) found out that problematic temperature gradients for surface cracking in the facing are 2.5 to 3 K/m and temperature differentials of 15 K or more between the dam core and the dam exterior.

However the problem of crack detection remains, temperatures can only give information on the cracking potential but cannot localize cracks. It was also stated before that temperature criteria alone are not sufficiently accurate for cracking prediction and stress-strain criteria are more reliable (Bosnjak 2000). They additionally consider the crucial factors of autogenous deformation, mechanical properties and restraint conditions. Crack detection was carried out in the past by single point stress meters that give localized information on changes in stress, to gather information if cracks occurred in the vicinity of the measuring instrument (Wiegrink 2002). A direct in-situ detection especially of longitudinal cracks was not possible yet. The aim of this thesis is to contribute to the genuine crack detection in mass concrete by means of distributed fiber optic strain sensing. The tests on an RCC block and in an RCC dam in Brazil show that the technique and the sensing cables are at a state of development today that allows very accurate detection of small cracks (> 0.1 mm) within a concrete body.

2.2.3 Reinforced concrete

The crack width in a reinforced concrete structure has to be kept in its limits as it might reduce its serviceability. DIN standard 1045-1 (2001) regulates the maximum crack width for reinforced concrete to 0.3 mm. The alkaline environment of the concrete acts as corrosion protection of the reinforcing steel bars inside the structural part. If cracks are not detected and the steel is exposed to the acid environment, it can corrode and jeopardize the structure's serviceability and safety (Adler, Stützel et al. 2006). The second problem concerns the tensile strength of the reinforced concrete. When cracks occur, the tensile strength of the concrete is zero and can no longer be taken into account. The coefficients of thermal expansion of steel and concrete are almost the same with $\alpha \approx 1 \cdot 10^{-5}\ K^{-1}$, which eliminates temperature induced eigenstresses in the composite. A typical stress-strain curve for steel, loaded under tensile stress is shown in Fig. 2-6. The development of hydration heat in reinforced concrete structures is also of concern as the amount of cement is much higher than in mass concrete. As a consequence cracks can also occur in the absence of mechanical load (Siew, Puapansawat et al. 2003).

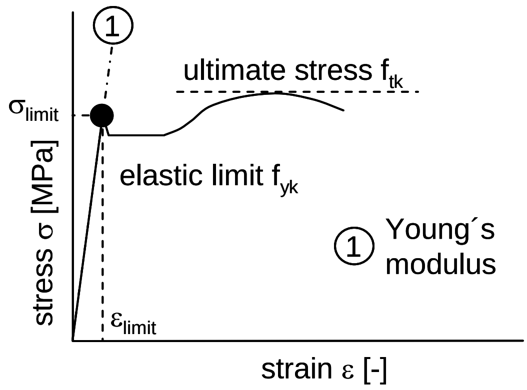

Fig. 2-6: Typical stress-strain curve for steel

Cracks in reinforced concrete structures can usually be identified by visual inspection using crack indicators and loupes or by electronic measuring systems like strain gauges (Lange and Benning 2006). The inspection of civil structures in remote areas or in inaccessible places can be made by single point sensors or so called quasi-distributed sensors that can evaluate the strain between two distinct points (see section 3.1.3). As the sensors for distributed fiber optic measurements are the optical fibers itself, they can due to their small size be incorporated into a concrete part during construction or attached to the outside without weakening the reinforced concrete part. This allows the distributed monitoring of a whole structure, collecting information on strain, cracks and crack widths. In the laboratory tests that will be presented in chapter 7, a reinforced concrete column and a reinforced concrete beam are investigated.

2.2.4 Previous fiber optic strain and crack detection installations

The research in the beginning of fiber optic strain sensing was mostly based on laboratory applications (Bongolfi and Pascale 2003; Kurokawa, Shimano et al. 2004) and for structural health monitoring (SHM) issues, especially concrete bridges and buildings (Inaudi, Vurpillot et al. 1996; Thévenaz, Niklès et al. 1998; Lienhart and Brunner 2003; Bastianini, Rizzo et al. 2005; Kluth and Watley 2006). Installations of fiber optic sensors for crack detection in concrete dams are rare. The installation of crack sensors into the gravity dam Gottleuba in Germany in 1988 was the first application of fiber optic sensors for crack detection in dam engineering (Holst, Habel et al. 1992). Those sensors were installed into the joints of the dam where the crack width was evaluated by an extrinsic microbending sensor (section 3.1). Further research on crack detection followed by mostly using interferometric fiber optic sensors that are capable of monitoring the change of distance between two distinct points inside optical fibers embedded into the concrete (Nanni, Yang et al. 1991). An installation of a distributed fiber optic strain sensing cable into the inspection gallery of Pļaviņu HES dam on the Daugava River in Latvia for monitoring of the joints was published by Inaudi and Glisic (2005). Today, new methods for distributed fiber optic strain sensing are being developed in order to increase the opportunities especially for crack detection (Hotate 2004).

2.2.5 Prospects for distributed strain sensing

Little in-situ research has been made on the longitudinal cracking inside the body of concrete dams since no distributed instrumentation has been available and its detection by single point strain measurements is not targeting. With the great experience of the installation of temperature sensing cables and the distributed measurements, a cross sectional strain distribution including the location of cracks will be possible. When a crack is located, the information on the crack width and its development is of great interest. Chapters 7 and 8 show some laboratory tests on crack detection in concrete specimens and the first installation of strain sensing cables into an RCC dam.

2.3 Reservoir landslides

2.3.1 Types and movement of landslides

The evaluation and monitoring of landslides is essential especially in the scope of planning dams and reservoirs to ensure their safety during impoundment and operation over the entire service life. The focus of this section is on reservoir landslides, which usually do not directly affect the foundation of the hydraulic structure but rather the slopes of the reservoir (Schuster 2006). Since the Vajont catastrophe in 1963, when a 3 km long slope with a volume of around 270 million cubic meters slid into the reservoir, triggering a flood wave, which killed almost 2,000 people (Semenza 2005), the focus became sharp on the topic of reservoir landslides.

A landslide can be defined as “the movement of a mass of rock, debris or soil down a slope” (Cruden and Varnes 1996). It is very common to find evidence of past landsliding activity at dam and reservoir sites that are located across a river valley. The disturbance of an old or active landslide can cause reactivation or increased rates of movement (Fell, MacGregor et al. 2005). The term landslide describes basically five different types of mass movement: falls, topples, slides, spreads and flows (Cruden and Varnes 1996). A combination of different types of landslides is commonly referred to as complex landslide. Rock falls could be one single stone falling down a slope up to rock avalanches with huge volumes. A topple describes the forward rotation out of the slope of a mass of soil or rock beyond the center of gravity of the displaced mass. Flows are usually shallow landslides with high water content, mostly initiated after heavy rainfall, also known as mudflow or debris flow.

Slides are masses of rock, debris or soil that come into motion when the shear strength in a rather distinct sliding surface is too low to withstand the gravity of the mass. This process does not happen randomly but needs a trigger, which usually is heavy rainfall that is infiltrating into the soil, changing the pore pressure. Fine grained soil layers that come into contact with water may gradually lose cohesion and friction and become sliding planes. At reservoirs, the materials that are most likely to generate mass movements appear to comprise loess, clay, especially swelling clays, silt and soluble materials such as halite, gypsum and sand (Riemer 1992; Fell, MacGregor et al. 2005). Referring to Fig. 2-7, slides comprise an upper region, which is called zone of depletion with a significant scarp at the crown. The lower part is called the zone of accumulation. Rotational slides usually carry out complex movements and basically rotate around a slope-parallel axis downwards. This leads to large internal deformations with additional scarps, transverse elevations and radial cracks. Rotational slides mostly occur in homogeneous materials. A translational slide by definition moves linearly without rotation. Translational slides are often shallower than rotational ones and experience only little internal deformation, which then becomes visible on the surface as transverse and radial cracks.

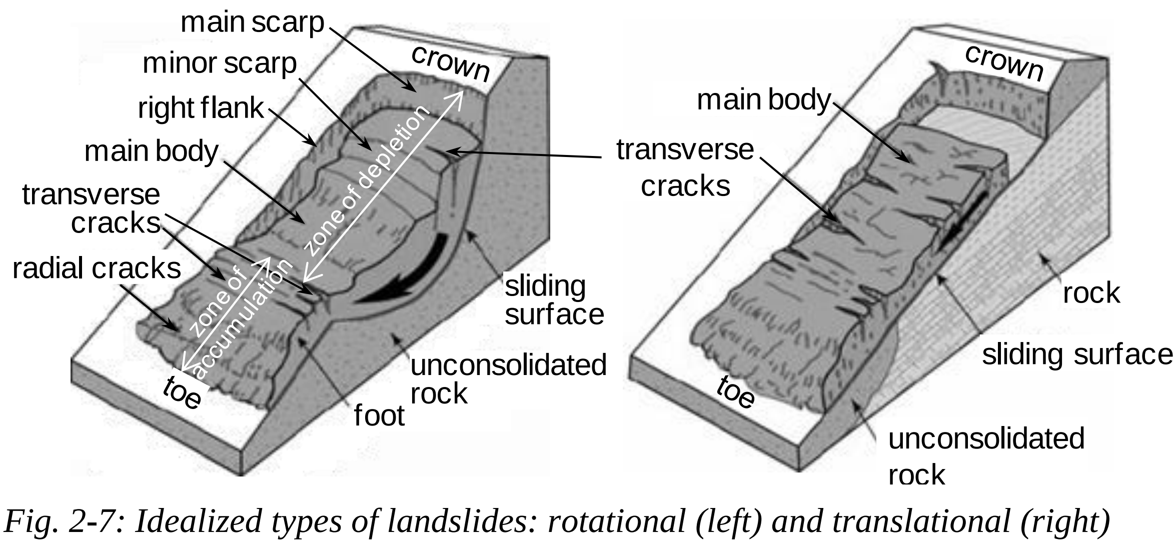

Fig. 2-7: Idealized types of landslides: rotational (left) and translational (right) slides, based on ClimChAlp (2008)

The term spread had been introduced to describe the subsidence of a fractured mass of cohesive material into softer underlying material, which may also translate, rotate, disintegrate or liquefy and flow (Cruden and Varnes 1996). Many slow moving landslides that would commonly be referred to as slides should be classified into the very complex group of spreads.

2.3.2 Interaction of reservoir and landslide

Water is the main factor for the initiation or the change of behavior of landslides. The operation of reservoirs always affects the groundwater regime up- and downstream of the barrage. Imagining the amount of mass and energy stored just above or within the slopes of a reservoir illustrates the hazard potential for the reservoir, the hydraulic structures and the whole region. Landslides can either be active, inactive or just not existing, yet. The construction of a reservoir disturbs the hydraulic regime in the valley slopes. An old, inactive landslide can be reactivated or an active landslide might increase its rate of movement (Fell, MacGregor et al. 2005). Depending on the geology and the impact of the new constructions and the reservoir on the valley slopes, also new landslides can develop. Those slides are very difficult to predict. In the ICOLD Bulletin 124 (2002), “Reservoir Landslides: Investigation and Management”, reservoirs with slope stability problems worldwide were gathered and analyzed. According to this, 75 % of all landslides that are affecting reservoirs were pre-existing. 85 % of the slide events that were reported happened during construction, first impoundment and within the first two years of operation. In 2002, 156 reservoirs were reportedly affected by mass movements (ICOLD 2002).

Most critical with regard to the interaction between reservoir and landslides is the reservoir’s first impoundment and significant reservoir level fluctuations during operation. The rising water table penetrates into the slopes where it can turn initially dry soil layers into saturated sliding surfaces. The hydrostatic uplift additionally lowers the shear strength in the sliding surface. In translational slides, the sliding plane that is affected by water is growing linearly with rising water level. This is different for rotational slides, where the effect of static uplift is a non-linear function of the elevation of the reservoir level as the slip surface is curved. The effect of changes in the reservoir level on the groundwater and thus the potential landslide is depicted in Fig. 2-8. In the initial state, the landslide is not affected by water. When filling the reservoir, the pore water pressure in the potential landslide rises as a function of the reservoir water level $p = f(h_w)$. If the pore water pressure cannot dissipate from the mass that is susceptible to sliding during rapid drawdown, the shear stresses in the sliding surface will rise due to the rising water load (Wieczorek 1996). This is the most critical state. When the reservoir is operated at a lower water level for a while, the water will dissipate. The time that is needed for the water to drain out of the slopes, depends on the permeability, the stratification and the porosity of the soil and rock mass. Additional factors that can influence the stability of a slope are external erosion, especially by waves, internal erosion in fine grained soils, the collapse of karst terrain due to water level fluctuations and thermal influences of the reservoir, especially in permafrost regions. Chemical effects are comparatively rare. Depending on the geology, changes in the groundwater regime might also lead to the built up or pressure changes in confined aquifers that are being fed from the reservoir. This might lead to the built up of pore pressure in a slope even in neighboring valleys (Cornforth 2007). The barrage can also cause changes in the hydrogeology of the downstream slopes. Scours from the spillway jet or the bottom outlet, spillway spray, downstream degradation due to the interception of sediments and the new runoff regime can affect the stability of the slopes downstream of the reservoir (Riemer 1992).

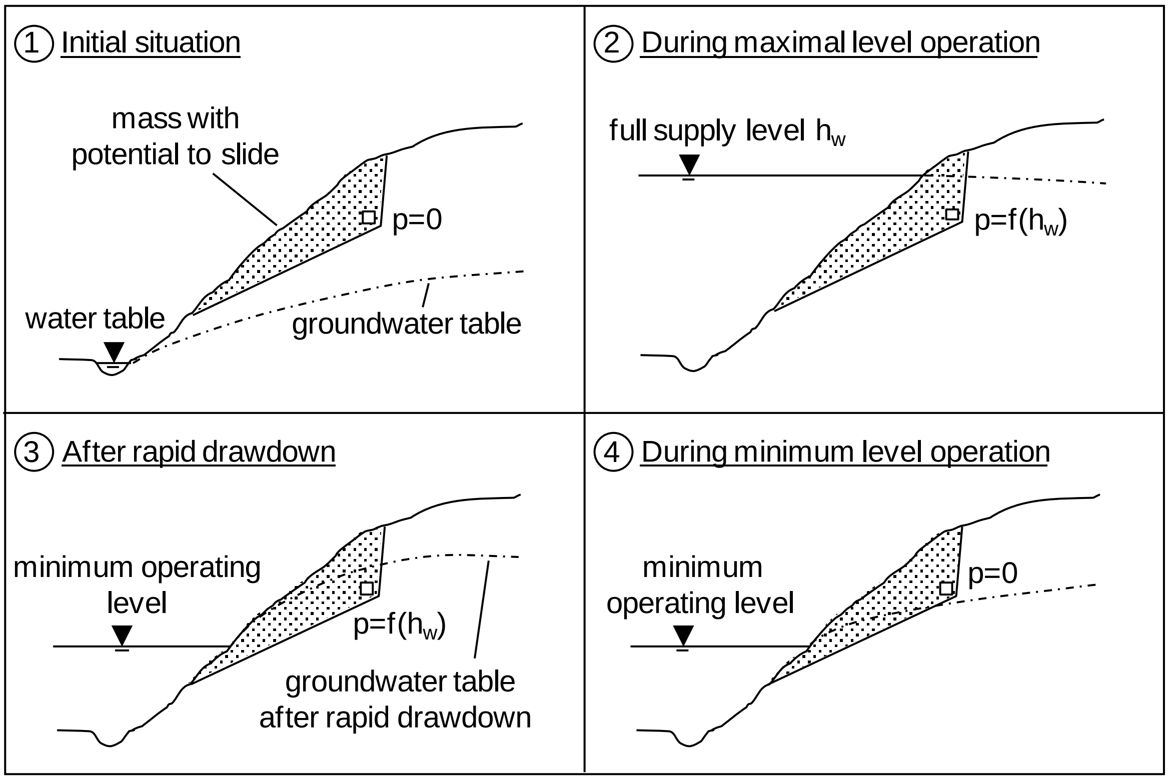

Fig. 2-8: Impact of varying water levels for landslide (re-) activation, referring to Lambe and Whitman (1969)

Depending on their actual state and type, landslides can move in different velocities, which lead to different impacts on the reservoir. Fast moving landslides may cause impulse waves that can damage hydraulic structures, infrastructure around the reservoir or may even overtop the dam, causing additional damage downstream of the dam (Heller 2008). However most of the more obvious landslides associated with reservoirs are likely to be slow moving (Fell, MacGregor et al. 2005). The mass of rock and soil that is entering the reservoir or also subaquatic landslides can block the bottom outlets, the power intakes, the spillways, desanding and flushing facilities, jeopardizing the safety and serviceability of the dam if slope stability is not sufficiently accounted for in the dam design. The infrastructure like roads, railway tracks, telecommunication and power supply lines are affected by landslides of no matter which velocity. This also accounts for landuse along the shoreline, buildings and tourism. Especially in case a reservoir is used for the storage of drinking water, landslides can change the turbidity in the water, degrading the water quality. Additional economic losses might occur due to reduced storage volume and possible operational restrictions regarding drawdown rates (ICOLD 2002).

In some cases, the reservoir can however have positive influences on the stability of the slopes. Landslides might stop moving or at least decrease the rate of movement when erosion by the river of the slope toe stops. In slopes of very low permeability like clay, the stability might increase when the water is pushing against it.

2.3.3 Conventional methods for landslide monitoring

Detailed information on the distribution, orientation and the amount of deformation on the surface and in the depth alongside boreholes with high temporal resolution for the hazard assessment of a landslide is essential. Additionally the effect of triggering mechanisms (as e.g. precipitation) on the movement and their temporal relation are of great importance. Landslides are monitored with measuring devices and methods that can be divided into four different main groups: geodetic, geotechnical, geophysical and remote sensing. The monitoring instruments are summarized in ClimChAlp (2008), a state of the art report for monitoring methods as of 2008.

Geodetic sensing

Within the field of geodesy, geodetic sensing involves the description of geometrical changes of a site’s surface by measuring a multitude of geometric elements like angles, distances and differences in height. To gather information of velocity, distance and direction of a movement, usually a network of measurement points is set up, including immovable benchmarks. Commonly used systems are tacheometry, terrestrial laser scanning, precise leveling and global positioning (GPS) either static/relative (RGPS) or differential (DGPS).

Geotechnical sensing

Geotechnical methods are used to gather information on the deformation of a landslide. The development and displacement of surface cracks can be some of the first indicators of landslide deformation as they reflect the behavior of the landslide at depth, especially in the upper half to two thirds of a landslide. Measurements are usually limited to the relative monitoring of cracks by installing fixed reference points on either side and measuring the development of the distance. Methods for the monitoring of crack displacement can be simple pins that are brought into the ground, measuring their distance, tension wires and mechanical and electrical strain meters. Electrical strain meters as vibrating wire instruments or strain gauges are primarily placed on sites with poor access where the continuous record of strain is required. Vertical or horizontal tiltmeters are installed in landslides that are susceptive to toppling; extensometers are used in areas of extensive surface cracking where they span a distance of up to several tens of meters between anchor and head of the instrument. To receive information on internal deformations and the shear zone(s), other instruments are installed vertically into boreholes. Extensometers measure vertical deformations along the borehole where inclinometers can measure the perpendicular deformation, which might indicate a sliding plane or a larger shear zone. A comparative method is time domain reflectometry (TDR), where the deformation of a coaxial cable can be measured, giving information on distinct shear planes (see also section 10.6). For the monitoring of groundwater conditions, piezometers are installed into landslides to measure the water pressure under ground, which is essential especially after rapid reservoir drawdown and extreme rain events.

Geophysical sensing

Geophysics is the study of the earth by quantitative physical methods. For landslide monitoring, direct current geoelectric gives information on electric resistivity in the soil, which mainly depends on the porosity, saturation, pore fluid conductivity and clay content. Changes in those parameters are mainly caused by changes in the subsoil water content. The structure of different soil and rock layers under ground can be evaluated by geoseismology.

Remote sensing

Remote sensing involves the small or large scale acquisition of information of an object by the use of sensing devices that are not in physical contact with the object such as by way of aircraft, spacecraft or satellite. The methods that are used for landslide monitoring are photogrammetry, airborne laserscanning, satellite-borne radar interferometry and ground-based radar interferometry. Monitoring methods that are used for small surface extensions of smaller than 1 km² are listed in appendix A1 and for medium surface extensions of landslides that have a surface between 1 and 25 km² in appendix A2.

2.3.4 Previous fiber optic monitoring installations

Fiber optic strain sensing methods can give valuable information in addition to conventional sensing methods. Briancon, Nancey et al. (2005) developed “smart geosynthetics”, which comprise of regular geotextiles with optical fibers woven into them. The fibers are grated with fiber Bragg gratings (FBG) in uniform distances to measure the local strain in the fiber and thus in the geotextile. Fiber Bragg gratings are described in more detail in section 3.5. Nöther, Wosniok et al. (2006) wove optical fibers into geogrids, measuring strain in the fibers with a distributed strain sensor based on stimulated Brillouin scattering. Sensors based on stimulated Brillouin scattering will be described in more detail in section 3.4.3. The combination of geosynthetics and optical fibers for strain sensing comprises a mitigation measure that gives a soil structure additional stability and a surveillance system by monitoring the effectiveness of the measures at the same time. Extensometers that are based on interferometry in optical fibers were installed into a landslide by Brunner, Macheiner et al. (2007). Extrinsic sensors based on optical time domain reflectometry (OTDR) were designed and installed into a landslide by Higuchi, Fujisawa et al. (2007). The outline of that installation where only relative movements within one sensor can be monitored is shown in Fig. 2-9, left. Several authors already showed possible layouts for real distributed landslide monitoring with Brillouin sensors (Hiroyuki 2001; Komatsu, Fujihashi et al. 2002). Field tests with fiber optic strain sensing cables for deformation measurements in soil were carried out by Kluth, Farhadiroushan et al. (undated). The cables were clamped to the ground at a depth of 50 cm. By pushing a part of the slope with a pushing tool, the deformation along the cable could be measured (Fig. 2-9), right.

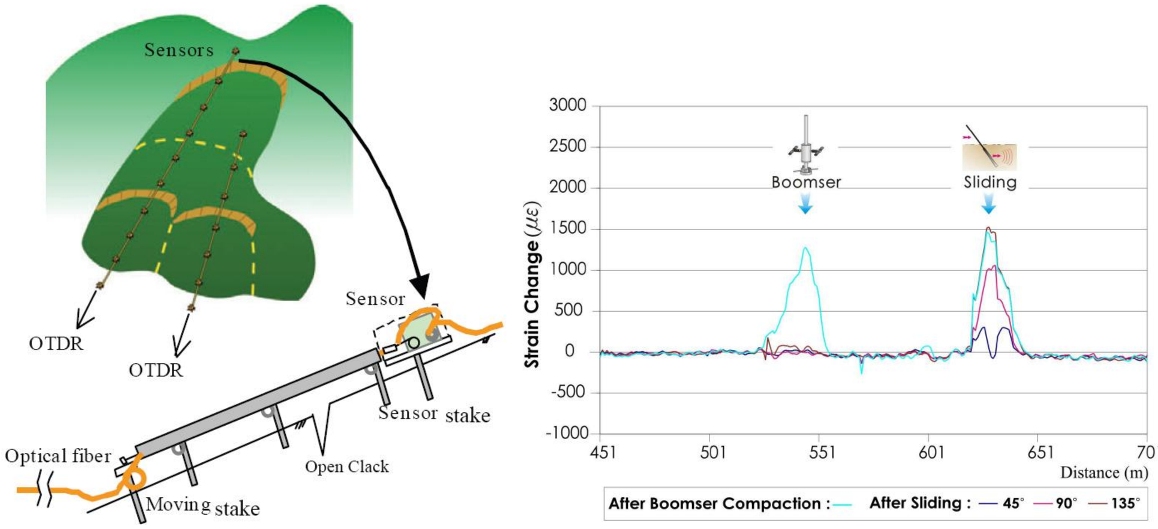

Fig. 2-9: Landslide monitoring with an extrinsic fiber optic loss-sensor on the left (Higuchi, Fujisawa et al. 2007) and results from a distributed soil deformation test (Kluth, Farhadiroushan et al., undated)

2.3.5 Prospects for distributed strain sensing

Distributed fiber optic strain sensing in landslides so far can only be limited to landslides with small rates of movement as well on the surface and in the subsoil. The big advantages of optical fibers come into account in regions that are difficult to access. Cables can be dug underground without being affected by the moist environment, which might affect electrical instruments like strain gauges. Strain sensing cables could also be installed into subaquatic slopes before filling the reservoir to be alarmed in case of increasing movement. Optical fibers could make up a valuable tool in cooperation with other sensors (e.g. with TDR for shear zone and distinct sliding plane detection). For the tests that are presented in chapter 10, optical strain sensing cables were installed into a slow moving landslide (~ 2 cm/a) close to the surface across surface cracks and vertically into a borehole next to a TDR cable and an inclinometer for the detection of shear zones.

2.4 Deformations and cracks in embankment dams

2.4.1 Deformation mechanisms

Embankment dams include earthfill dams of various types and rockfill dams with earth cores, upstream concrete or asphaltic concrete facings and internal sealing elements. Deformations in embankment dams appear due to settlings of the core, the transition layers, the embankment material, the foundation, the influence of earthquakes and the load of water during and after impoundment.

In comparison to concrete dams, embankment dams have the advantage that settlements in the foundation can be compensated by movements of the dam material. Additionally the dam material itself is subject to settling due to consolidation, which is the decrease of the materials bulk volume when the soil particles are packed closer together while reducing the pore volume. Even though a dam is compacted in layers between 0.2 to 1 m thickness, the dam itself will experience further consolidation in the time after construction (Bureau of Reclamation 1987). The compactibility and stiffness of the material in variable dam zones is different, which leads to differential settlements within the dam body. The transition and filter zones are supposed to compensate the differential settlements in order to avoid distinct shear zones (Dunnicliff 1993). When the shear stress cannot be completely compensated, the stiffer material tends to take a part of the less stiff materials weight. This effect is depicted in Fig. 2-10, where the filling material is "hanging" on the stiffer core and consequently influencing the stress in the dam cross section and the foundation.

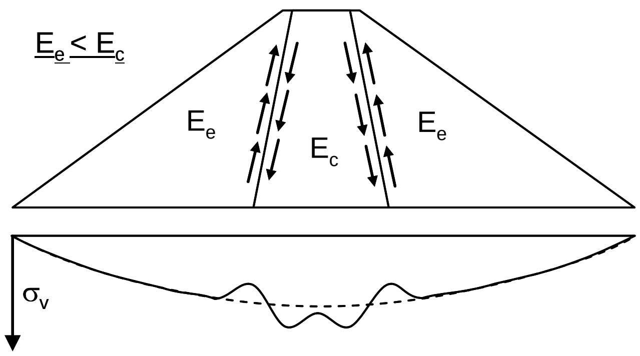

Fig. 2-10: The filling material is "hanging" on the stiffer core, based on Aufleger (1996)

If the water pressure in the core material exceeds the earth pressure, it could break (Park 2003), increasing the risk of piping and internal erosion. The risk of reduced earth pressure is especially critical in dams with slender natural sealings and stiff cores. Information on stress-deformation curves from different dam materials help to control the differential settlements.

In dams that are constructed in valleys with gently inclining valley slopes, each dam material can settle quasi uniformly by approximately the same amount. If the abutments are steep, the settlements in the center of the valley are significantly larger, which may put the crest of the dam in tension, possibly causing cracks transverse to the axis of the dam (Fig. 2-11). The movements inside the dam tend to follow gravity, thus the valley slopes towards the center of the valley floor. Consequently, the core might also slip down along the abutment when it settles. Due to differential settlements, the accumulation of stresses towards the center of the valley floor may lead to an “arching effect” where the compact dam material is transferring the load into the valley slopes, while the effective stresses underneath might even decrease. Hydraulic fracturing might be the result.

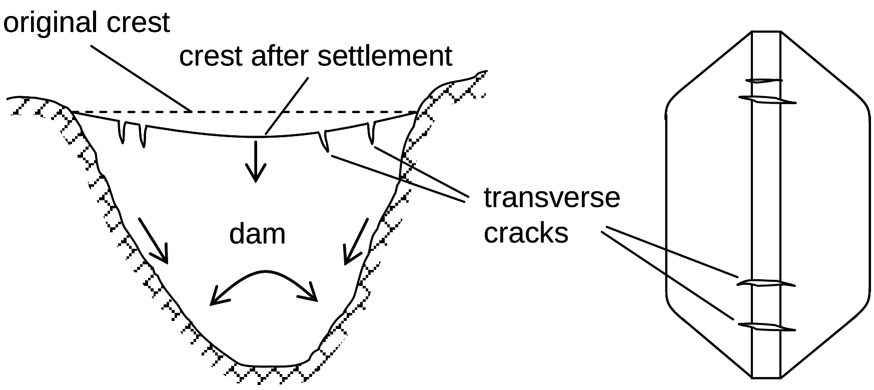

Fig. 2-11: Longitudinal cut through an embankment dam and top view

The geology of the foundation is of special concern in case a dam is not founded on stable rock. While the dam itself is constructed by following a very high standard of compaction, the subsoil can settle up to several meters due to additional load of the dam (Kutzner 1996).

The dam in Fig. 2-12 is founded on alluvial deposit, which is overlying bearable rock in irregular elevations throughout the longitudinal section of the dam. Differential settlements might result in transversal cracks in the crest of the dam. Deformation in a dam appears not only vertical but a considerable amount is also taking place in horizontal direction. Horizontal movements could affect narrow and stiff sealing systems especially after impoundment when the water pressure adds to the horizontal stresses (Schmid 1992). The influence of water after impoundment also leads to deformations within the dam body in terms of uplift, saturation settling and additional load on abutments of low permeability.

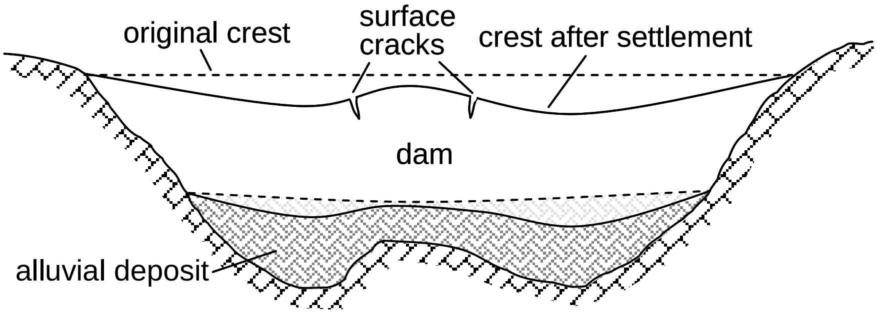

Fig. 2-12: Longitudinal cut through an embankment dam

An extensive study on the deformations within a rockfill dam with an asphaltic concrete core has been carried out by Schwab and Pircher on the Finstertal Dam in Austria (Pircher and Schwab 1982; Schwab 1984; Schwab and Pircher 1985). Data from almost 800 measuring points was collected and evaluated during the first seven years of operation. Figure 2-13 shows the isolines of vertical strain measurements in the main cross section of the dam after the end of construction in 1980 and four years later after the first drawdown. Positive strain numbers hereby refer to compaction. The maximum vertical deformation of up to 20 ‰ compression after 1st drawdown is located as expected in the low center of the dam.

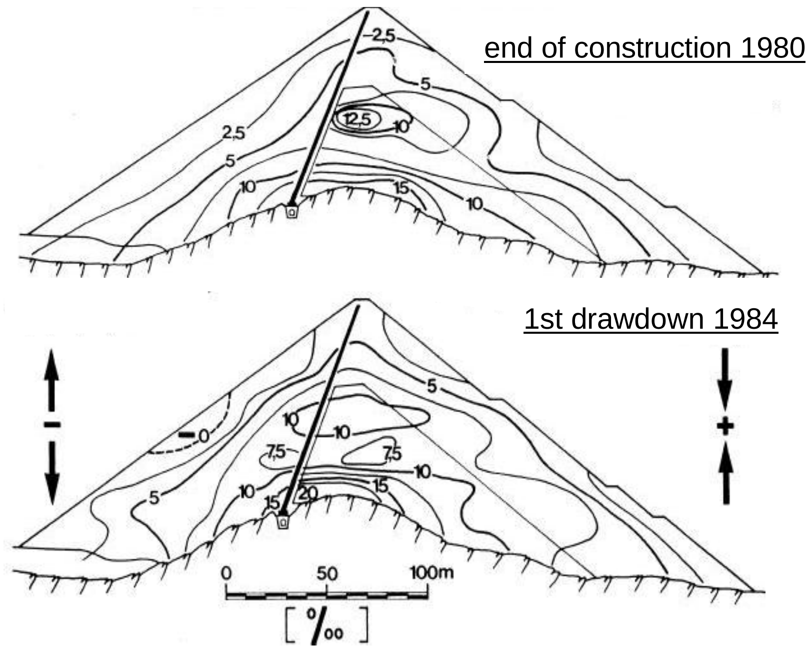

Fig. 2-13: Vertical strain measurements in the main cross section of Finstertal Dam (Schwab and Pircher 1985)

Large vertical stresses at the end of construction lead to tensile strain in horizontal direction in the main cross section of the dam as depicted in Fig. 2-14. The maximum horizontal deformation at the end of construction of up to 3 ‰ (3,000 με) on the downstream side can be found just underneath the maximum of vertical deformation.

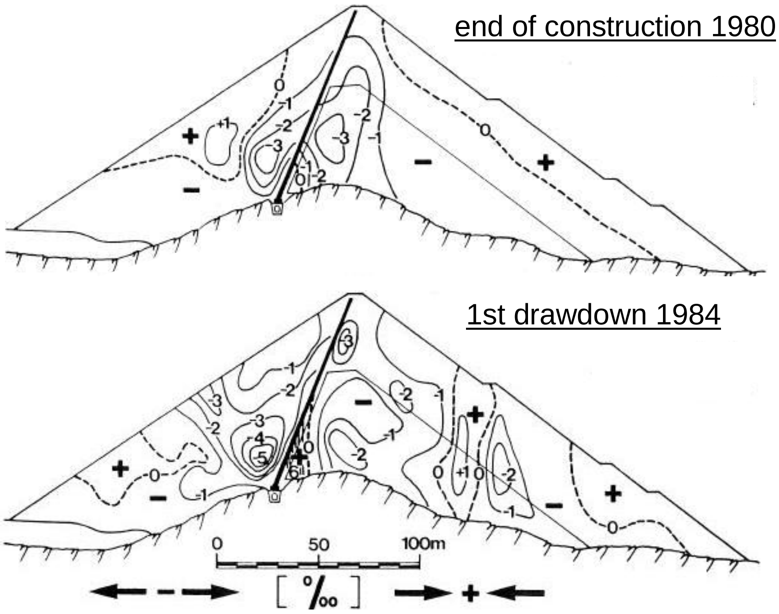

Fig. 2-14: Horizontal strain measurements in the main cross section of Finstertal Dam (Schwab and Pircher 1985)

Horizontal deformations in the longitudinal section of Finstertal Dam confirm the tendency of the material to relocate towards the center of the valley (Fig. 2-15). The "arching effect" can to some extent be present in any dam.

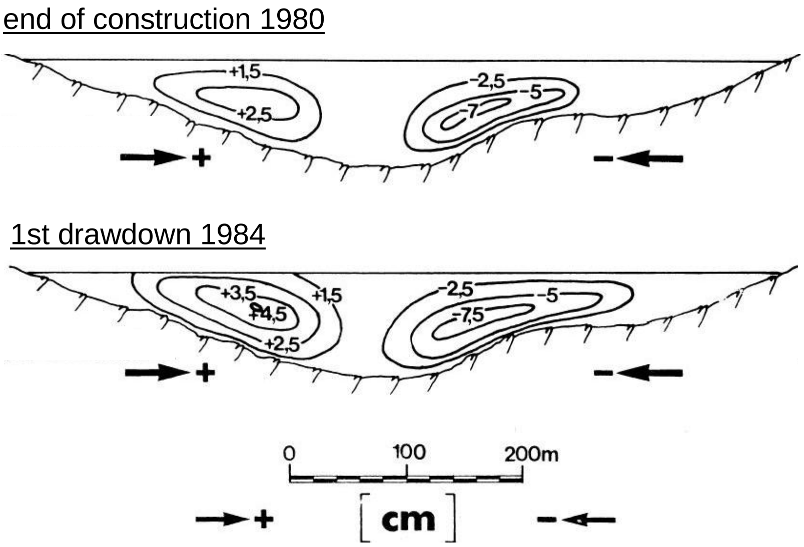

Fig. 2-15: Horizontal deformations in the main longitudinal section of Finstertal Dam (Schwab and Pircher 1985)

In Fig. 2-16, the movements of the crest (a) and the dam surface (b) between the 2nd and 8th year after initial impoundment are depicted on the example of Gepatsch Dam (rockfill with earth core).

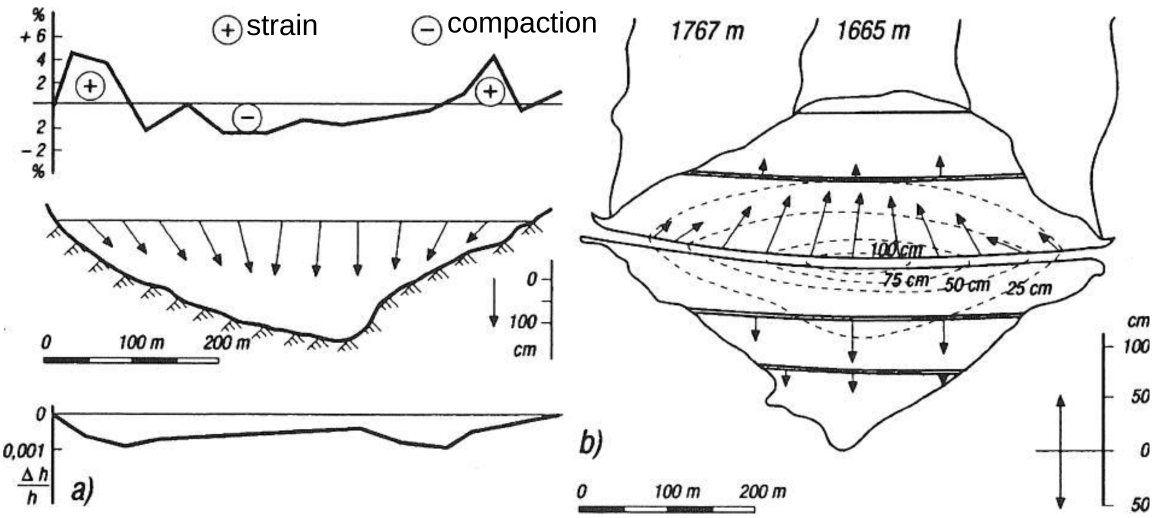

Fig. 2-16: Strain measurements in the crest and deformations of the surface of Gepatsch Dam, 2nd to 8th year (Striegler 1998)

The movement of the rockfill is again going from the valley slopes towards the center of the valley, resulting in measured compaction of the crown in the middle part and considerable strain values of more than 5 % (50,000 με) in both end sections.

2.4.2 Conventional methods for deformation monitoring

Embankment dams are usually equipped with instruments for internal and external deformation measurements, hydraulic measurements and diverse optional project-specific installations e.g. for stress measurements (Muckenthaler 1989). Besides dam safety control, those measurements can also be used to compare the predicted behavior with reality and to calibrate numerical models (Osuji and Anyata 2007; Holzmann 2008). The amount of instrumentation highly depends on the size, the location and the foundation of the dam.

External deformation measurements are made with geodetic instruments as described in section 2.3.3. Internal deformations appear in all directions. They are evaluated by geotechnical methods like barometric level gauges, extensometers, inclinometers and horizontal and vertical settlement gauges. Stresses in the dam are measured using earth pressure gauges. Hydraulic measurements can be made with piezometers and water level gauges. The amount of seepage is evaluated by different volume, flow or weight evaluation methods. Temperature measurements inside a dam can give additional information on leakage such as analyses of the seepage water. Accelerometers are mainly installed in regions with high risk of earthquakes (FEMA 2005). The installation of monitoring instruments should be made in at least two cross sections of the dam with one of them in the maximum dam height. Dunnicliff (1993) recommends the horizontal installation of instruments and cables into a dam as the upward installation usually causes interference with the structure due to insufficient compaction. Vertical installations should as far as possible be limited to the inside of the filters.

2.4.3 Previous installations using fiber optic technology

First research on distributed fiber optic strain sensing in embankment dams was conducted by Johansson, Dahlin et al. (2000), when the Swedish Sädva embankment dam was equipped with fiber optic strain sensing cables. Unfortunately, those tests could not be brought to an end as the cables got severely damaged during installation. The same research team installed strain sensing cables in Ajaure dam, also an embankment dam in Sweden (Johansson, Parker et al. 2004; Johansson and Watley 2005). The cables were installed in a loop configuration into the crest of the dam in the scope of its rise of 1 m (Watley and Johansson 2004; Johansson and Watley 2005; Kluth and Watley 2006). The cable broke at one point in the dam but the measurements could still be taken from two sides. The measurements showed small changes in strain. More installations of strain sensing cables were carried out in three more dams in Sweden: Seitevare, Suorva and Hällby Dam (Johansson and Watley 2004). Here, additional tests with different kinds of cables were carried out for the evaluation of the direction of the movement. The dam cable they used is similar to one cable that was used in the tests that have been carried out in dam material and on the landslide as described in later chapters.

Deformation tests on an experimental banking were carried out by Hiroyuki (2001). A moving plate was placed underneath the banking, which was roughly 1 m wide, 40 cm high and around 10 m long. The 2 m wide plate was moved in transverse direction of the banking in steps of 20 mm, deforming the banking. Figure 2-17 shows the results of the distributed strain measurements where the deformation could be measured from the first 20 mm deformation-step on. The rise in strain left and right of the deformation reflects the slipping of the fiber in the cable and the cable within the gravel and the sand.

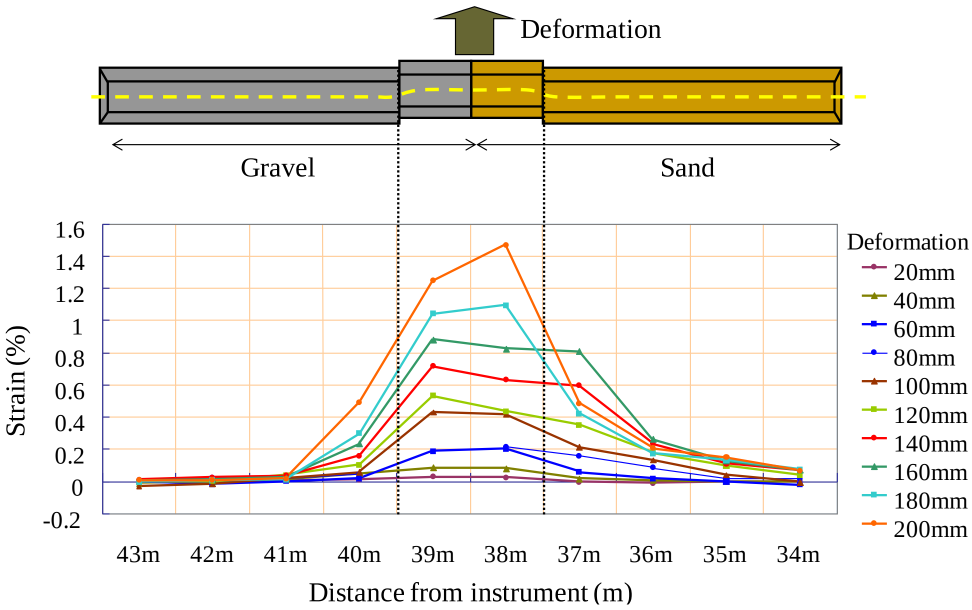

Fig. 2-17: Deformation tests in a model embankment using distributed fiber optic measurements (Hiroyuki 2001)

Other recent research, which deals with fiber optic cables that are embedded into geotextiles (smart geotextiles) has been mentioned in the previous section on landslide monitoring with fiber optic technology and could also be applicable for the monitoring of embankment dams where geotextiles might be of interest (section 2.3.4).

2.4.4 Prospects for distributed strain sensing

The big advantage of strain sensing cables is their small diameter, which reduces interferences with the structure to a minimum. At the same time, the data density can be huge, depending on the method. Correctly installed into the right places, strain sensing cables could give valuable information on the strain behavior within the structure. The installation within the core could also be an option in order to locate zones of high strain that might be susceptible to cracks. The tests in chapter 9 deal with the possibility of strain sensing in soil material.

3 Distributed fiber optic strain sensing technology

3.1 Fiber optic strain sensors

The foundation of every distributed fiber optic strain sensing system is a sensor, a coherent, monochromatic light source and a processing unit including a photo detector. The sensor is an optical fiber, which is embedded into a specially designed cable. Fiber lengths of up to 40 km can be monitored. The design and the layout of the cable in the structure or in the soil are depending on the required data and the surrounding material properties. The installation and the right cable design make up the most important part in distributed strain sensing as detection devices can be replaced and further developed but the fibers are usually built into the structure without the opportunity of replacing or repairing them after the installation is finished.

The starting point for distributed fiber optic strain measurements was laid by Horiguchi, Kurashima et al. (1989) when they discovered the tensile strain dependence of the Brillouin frequency shift in silica optical fibers. Shortly after that, they also discovered the thermal effects on the Brillouin frequency shift in optical silica fibers (Kurashima, Horiguchi et al. 1990), which interferes with the shift due to strain and therefore challenges scientists and users until the present day. Initially this technique seemed to be vital for the telecommunication industry in order to find strain peaks in existing glass fiber telecommunication lines. After it was proved that strain in communication lines is not a major problem (Tateda, Horiguchi et al. 1990), scientists and engineers began their search for new applications for the technology of fiber optic strain sensing. Till today, this technique is constantly being improved in terms of strain resolution, spatial resolution and temperature compensation. With the improvements of the instruments and sensors, the field of applications grows constantly bigger.

In the past, hydraulic structures were built according to state-of-the-art technology but it was very difficult and costly to monitor an entire structure with a multitude of single point sensors. In the 1990’s, with the new developments in fiber optic technology, the expression of structural health monitoring SHM was born. Bragg grating sensors and interferometers were the first reliable strain sensors using fiber optic technology (Brunner 2004). Fiber optic sensors can be divided into different groups. The most important distinction has to be made between extrinsic and intrinsic sensors.

3.1.1 Intrinsic sensors

In intrinsic sensors, the interaction between the light and the environmentally perturbed fiber, in which the light is propagated, is used to receive the desired information. The relevant parameter can usually be measured in any place along the fiber. The distributed methods, which extract their data from the backscattering light in the Raman frequency shift for temperature and the Brillouin frequency shift for temperature and strain, are consequently intrinsic methods. Other widely used intrinsic sensors are fiber Bragg gratings (FBG), which are grit patterns carved into a fiber by UV irradiation (section 3.5) as well as microbending sensors. Those sensors take advantage of the backscatter signal in the Rayleigh frequency that gives information on the amount of attenuation in the fiber. Microbending sensors transfer strain changes or movements of a structure mechanically into local losses in the fiber and give a rise to the local attenuation by deforming the fiber core. Macrobending sensors take advantage of excessive bending of the whole fiber, also resulting in local attenuation losses. Macro- and microbending sensors belong to the group of intensiometric sensors as the measurand is determined from the change of intensity of the light power transmitted through an optical fiber. The local losses in the fiber due to bending can be used to determine strain, pressure and vibration in the structure, depending on the setup (Measures 2001; Jasenek 2007). Other large and important subclasses of intrinsic sensors are interferometric sensors, which are able to give averaged information on temperature, strain and pressure along their total length. Figure 3-1 schematically shows the installation of intrinsic sensors into a random material.

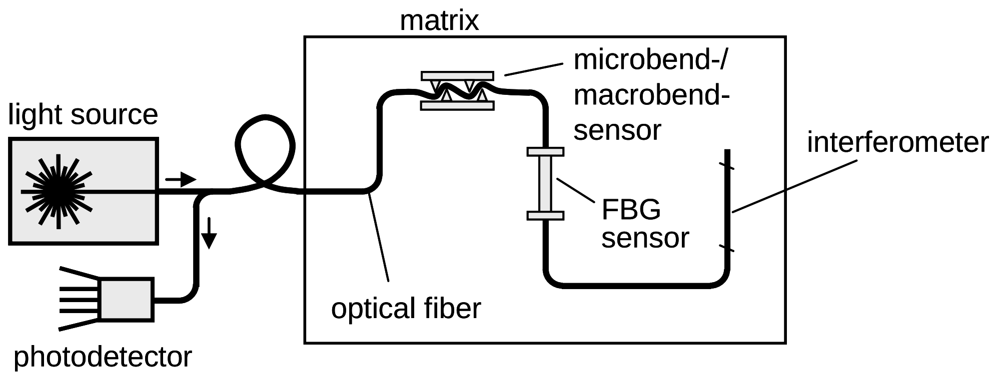

Fig. 3-1: Single ended setup for intrinsic fiber optic sensors

3.1.2 Extrinsic sensors

In extrinsic sensors, the modulation of the signal, which could be intensity or frequency shift, occurs outside of the fiber (Merzbacher, Kersey et al. 1996; Measures 2001) while the fiber only transports the information. As sketched in Fig. 3-2, the glass fiber serves as a transmission medium for the light, which propagates to the sensing element or device and either the same or another optical fiber is used to convey the processed signal back to the receiver.

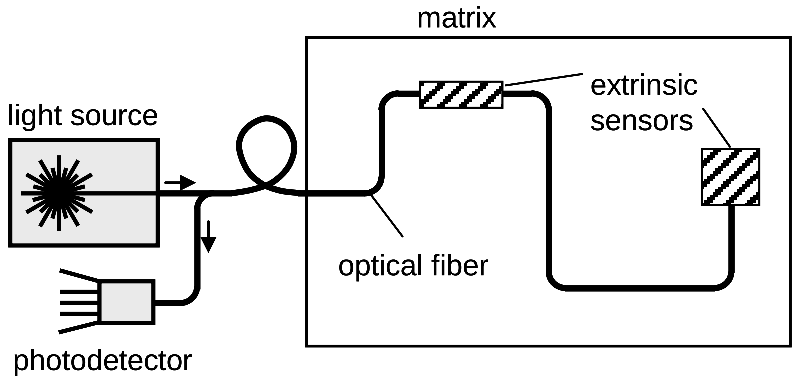

Fig. 3-2: Single ended setup for extrinsic fiber optic sensors

Hybrid fiber optic sensors belong to the same family. They can be thought of as a "black box" where the light is carried to the box and either directly conveyed back in the optical fiber or the light is used to power an electric sensor before the data is returned.

3.1.3 Single point - versus distributed strain measurements

Real distributed optical strain sensing methods are essentially intrinsic. Measurement results are obtained from the physical property changes in the glass core of the optical fiber itself. The changes on the fiber are induced by mechanical impacts from the fiber optic cable, which is directly affected by its surrounding or temperature. The distributed method can clearly be distinguished from the non-distributed ones as the locations of the sensors are not fixed since the whole optical fiber is the sensor. Referring to Fig. 3-3, the spacing z_j is constant over the length of the optical fiber to be measured and depends on physical restrictions, the length (duration) of the laser pulse that is sent into the fiber, the measurement method (e.g. stimulated or spontaneous Brillouin scattering) and the length of the fiber to be measured. The spatial resolution can vary between few centimeters (Hotate and Tanaka 2002) and many meters, whereas the smallest resolution for spontaneous backscattering is about 1 m due to the lifetime of optical phonons.

Most conventional strain sensing methods fall into the field of single point measurements. Each sensor has to be connected individually to a cable in order to provide the sensor with power and to transmit the data. Strain or other measurands can consequently be detected in the vicinity of the sensor only. To receive complex information on a structure, the expected locations of interest have to be identified in detail before installing the sensors to keep the amount of cables and connections to an acceptable limit. Examples for fiber optic point measurement devices are Bragg grating- and all extrinsic sensors.

Some fiber optic single point sensors can be multiplexed in order to have multiple single point sensors in or connected to one fiber (Jones and McBride 1998). The sensors are placed in intervals along the fiber wherein each sensor can be isolated by wavelength, time or frequency discrimination, allowing profiling parameters throughout the structure. An often used method is fiber Bragg grating where different grated regions inside the optical fiber can be distinguished by the flight time of light or special interferometer configurations. Even though the number of Bragg sensors could theoretically be several hundred (Zhang 2003), their number is usually limited to a maximum of 10 to 50 sensors in one fiber (wavelength division multiplexing). Figure 3-3 shows a schematic comparison of the different sensing methods. The continuous line represents the real strain distribution along the z-axis.

3.2 Optical glass fibers for distributed strain sensing

3.2.1 Transmission of light in optical fibers

The principle of data collection is always the same; a short impulse of monochromatic light is coupled into an optical fiber in which the beam of light propagates along. Due to different optical characteristics of the fiber core and the enclosing material, the beam of light is reflected on the inside and thus stays in the fiber core under certain circumstances. The information on temperature and strain is contained in the backscattered signal that is recorded and processed in the strain sensing unit.

Light exhibits properties of both, waves and particles (wave-particle-duality). In optical fibers, a mode (or beam) of light, which travels along the core of the fiber due to total internal reflection, can contain several wavelengths. Monochromatic laser light, which is used for distributed fiber optic strain sensing, only contains light of one wavelength.

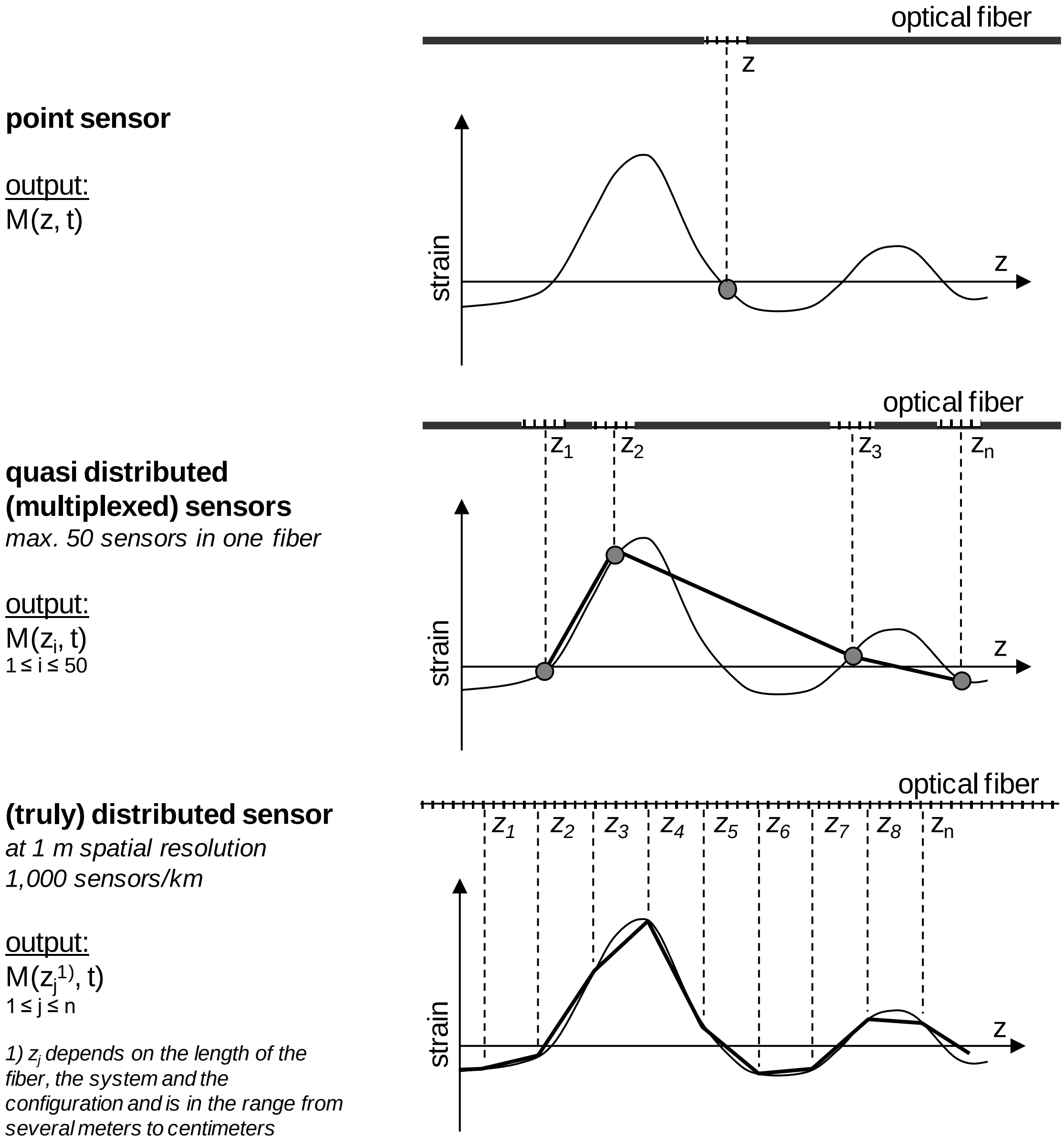

Fig. 3-3: Schematic comparison of point, quasi distributed and distributed sensors

Electromagnetic radiation (light) that is visible for the human eye has a wavelength λ between around 380 and 780 nm, spanning the spectrum colors violet, blue, green, yellow, orange and red. The light used in fiber optics is located in the near infrared spectrum (NIR) of electromagnetic radiation between around 850 and 1600 nm (Mahlke and Gössing 2001). On its way through the fiber, the light is subject to attenuations which depend on intrinsic physical properties, the purity of the glass, the wavelength and extrinsic factors.

The major merit of optical fibers is their ability to conduct light along multiple kilometers of an optical fiber while the attenuation of the light can be in an area of considerably less than 1 dB/km today, depending on the wavelength (Fig. 3-7). In addition, the wavelength of the light that is propagated through and backscattered in the fiber contains information that can be used to obtain distributed information on temperature and strain in the fiber. The propagation is possible as the beam of light is being deflected in the transition zone of two media with different refractive indexes. The refractive index n is a dimensionless parameter, which describes the optical properties of a homogeneous medium:

$$n = \frac{c_0}{v} \qquad \textit{Eq. 3-1}$$

n	refractive index [-]
c_0	speed of light in vacuum (299.792.458 m/s)
v	speed of light in a specific medium [m/s] (see Tab. 3-1)

The refractive index of a material is not a constant value but is depending on the wavelength of the transmitted light. Figure 3-4 shows the dependence of the refractive index from the wavelength.

Tab. 3-1: Refractive indexes and propagation times at λ = 589 nm (Goff 2002)

medium	speed of light [m/s]	propagation time [ns/m]	refractive index [-]
vacuum	299,792,458	3.336	1.0000
air	299,711,534	3.337	1.0003
water	$2.249 \cdot 10^8$	4.446	1.333
fused silica (SiO_2)	$2.056 \cdot 10^8$	4.863	1.4584
germanium dioxide (GeO_2)	$0.750 \cdot 10^8$	13.343	4.000

To compare the optical properties of materials, the refractive index of optical materials at a wavelength of 589 nm is usually used (Goff 2002). Fused silica, which is the main component in optical fibers, has a refractive index of 1.458 at 589 nm. Amorphous germanium dioxide (GeO_2), which is similar to fused silica, has a refractive index of 4.0 and is consequently the main dopant in optical fibers, used to raise the refractive index of the fiber core n_1 above the surrounding cladding n_2: $n_1 > n_2$.

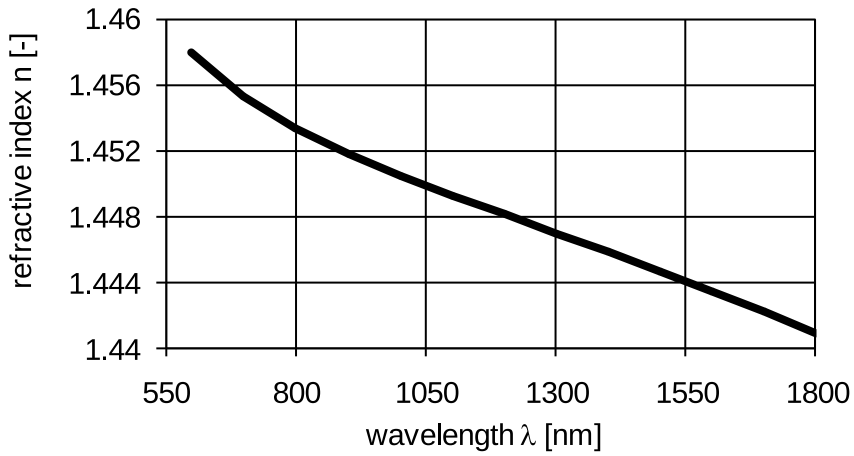

Fig. 3-4: Dependence of the refractive index from the wavelength in pure silica (Hecht 2001)

The relative difference of two refractive indexes n_r is vital for the angle of the beam of light being reflected at the border between core with n_1 and cladding with n_2, the core cladding interface (CCI) and is calculated according to Equation 3-2.

$$n_r = \frac{n_2}{n_1}, \qquad n_1 > n_2 \qquad \textit{Eq. 3-2}$$

n_r	relative refractive index [-]
n_1	refractive index of the fiber core [-]
n_2	refractive index of the cladding [-]

The larger the difference in the reflective index, the smaller is the critical angle for total reflection of the light beam in the fiber core. In fiber optic technology, this angle should be as large as possible to allow the light to stay in the fiber core, minimizing losses into the cladding. For that reason, the refractive index of the fiber core n_1 is always slightly larger than of the surrounding cladding.

3.2.2 Attenuation

The distance for distributed fiber optic strain measurements is today limited to close to 40 km. That limitation is founded in the attenuation losses that occur in the optical fiber and the limited amount of light (power) that can be coupled into the fiber core. Especially in long range applications, the losses in the connecting splices and the connectors have to be kept at a low level of usually less than 0.1 dB per connection in order to assure a strong and distinguished signal for good measurement results. The sources for attenuation along the fiber, which could also be pictured simply as signal loss, are summarized in Tab. 3-2.

Tab. 3-2: Sources of attenuation

intrinsic attenuation	extrinsic attenuation
scattering *(interaction of light with fiber core medium)* depending on variations in the structure and wavelength. material absorption impurities (necessary) impurities (unavoidable) wavelength dependent path length dependent	microbending *(deformation of the CCI)* macrobending *(deformation of the optical fiber)* CCI imperfections

While losses due to micro- or macrobending are volitional in sensing techniques based on local attenuation in the fiber, they have to be avoided in distributed fiber optic sensing. Microbending is caused from excessive bending of an optical fiber when the reflection angle of light on the CCI inside the fiber falls below a critical angle Θ_c. As a result, light that is traveling in the core can refract out and loss occurs (Aufleger 2000). A rule of thumb for bending radii of single mode fibers is 15 times the cable diameter, which should not be exceeded. Microbending in contrary is a very local small-scale distortion of the CCI, generally an indication of lateral pressure on the fiber. Figure 3-5 illustrates the difference between micro- and macrobending.

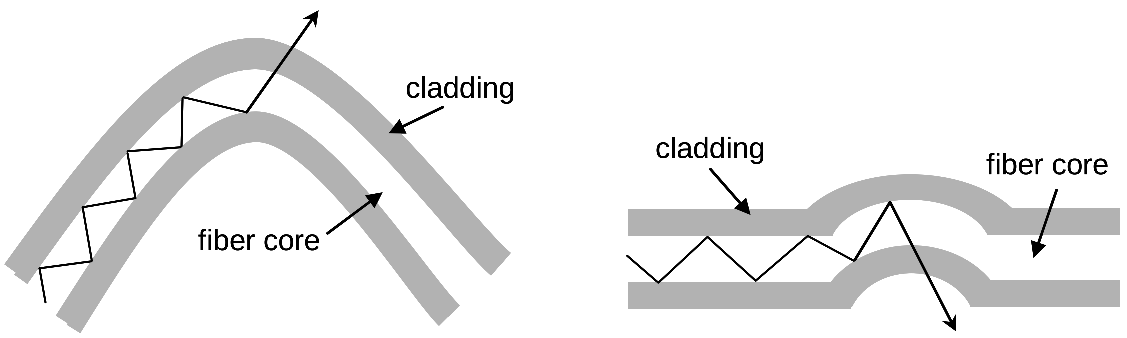

Fig. 3-5: Losses due to macrobending (left) and microbending (right)

Reductions of attenuation in modern fibers have been accomplished by developing optical fiber fabrication techniques that eliminate impurities. In the near infrared wavelengths, the lowest achievable values are almost reached. They are limited by fundamental physical phenomena in the glass that are not determined by impurities. It has to be emphasized that the reason for the attenuation of the light is not found in the number of reflections on the CCI but in the distance, the light covers in the core. The scattering of light in optical fibers happens in every place of the fiber. As drafted in Fig. 3-6, some of the incident beam of light is being scattered at angles that enter the adjacent material and are lost.

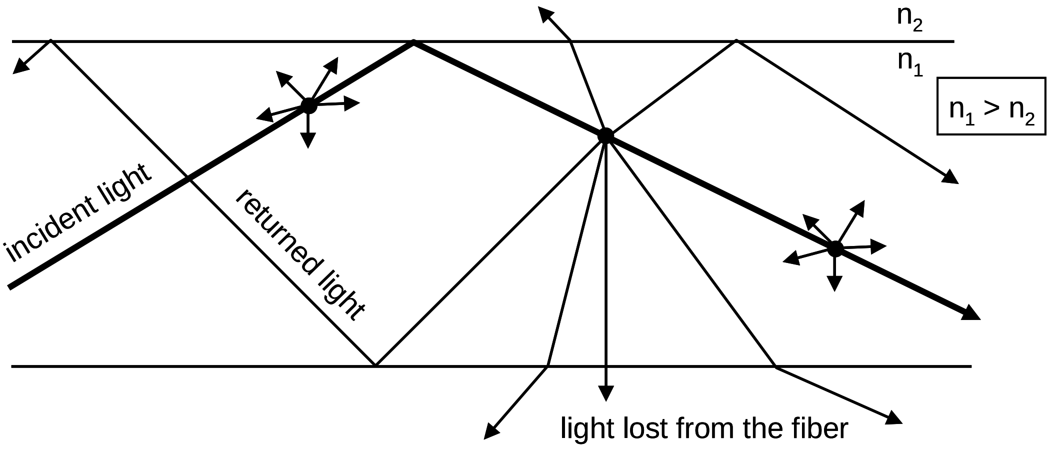

Fig. 3-6: Scattering of light inside a waveguide

The rest of the light is either scattered into the direction of the incident light or backscattered, carrying information on temperature and/or strain at every point in the fiber due to shifts in the reflected wavelengths.

Even though losses in the fiber should be kept at a very minimum, distributed fiber optic strain measurements would not be possible without the losses due to scattering in the fiber as the relevant light for sensing applications is the backscatter. The four types of scattering that occur in the fiber core are:

Rayleigh scattering (elastic)
Mie scattering (elastic)
Brillouin scattering (inelastic)
Raman scattering (inelastic)

In the production process of optical fibers, the glass freezes back into an amorphous solid after leaving the melting oven. The high level of thermal agitation at the transition temperature (melting point) of glass and the thermodynamic disorder leads to compositional and density fluctuations. These random variances are frozen into the glass and serve as the source for Rayleigh and Mie scattering. *Rayleigh scattering*, which is elastic, thus has the same wavelength as the incident light, occurs due to the impact of the incident light with particles much smaller than the wavelength. *Mie scattering*, also an elastic effect, is caused by particles in the fiber which are only a little smaller, equal or larger compared to the wavelength of the propagating light. *Brillouin scattering* occurs when the light interacts with density variations in the fiber (changes of the refractive index) that are a result of acoustic waves (acoustic phonons) traveling through the fiber. The effect is inelastic, so the backscattered light is frequency shifted, carrying information on temperature and strain at a specific point in the fiber. *Raman scattering* occurs due to the interaction of incident photons with optical phonons. This highly inelastic process causes a very significant frequency shift, carrying information only on temperature of a specific part of the fiber and is independent from strain. The attenuation losses from Rayleigh scattering are 20-100 times higher than from any of the other three scattering phenomena and consequently the reflected signal is by far the strongest. The predominant Rayleigh scattering and the measured total attenuation losses in glass fibers referring to the wavelength are depicted in Fig. 3-7. The wavelength for distributed strain measurements is usually in the second or third frequency window, around 1310 or 1550 nm. Depending on the fiber length and the setup of the equipment, the wavelength is sometimes tuned by a few µm into either direction in order to optimize data acquisition.

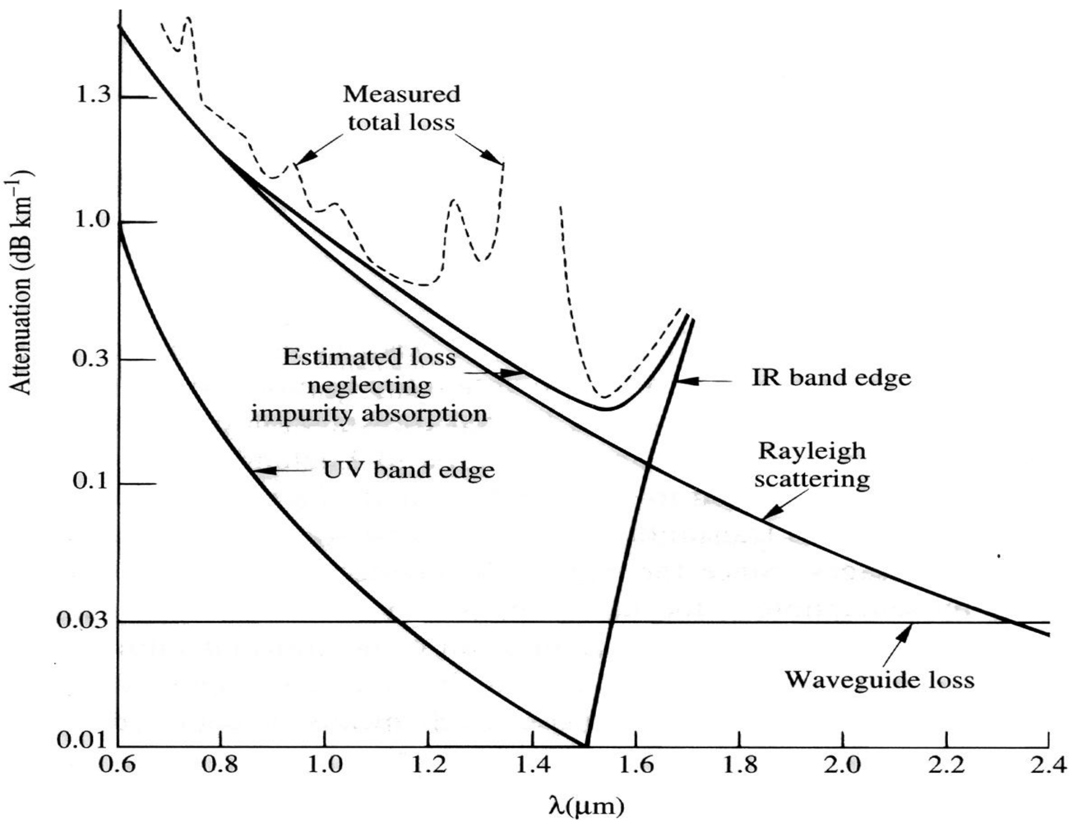

Fig. 3-7: Variation of attenuation with wavelength in a typical modern fiber (Davis, undated)

3.2.3 Single mode optical fibers

In fiber optic communication technology, single mode (SM) and multi mode (MM) fibers are the mostly used fiber designs which are basically the same, only differing in the core diameter. In single mode (or mono mode) fibers, outlined in Fig. 3-8, the diameter of the silica fiber core is usually between 8 and 10 µm. The cladding is also made of silica with a slightly lower refractive index than the fiber core to allow the reflection of the light that propagates through the core on the interface between core and cladding.

A buffer jacket or primary coating protects the fiber from the intrusion of water and chemicals that could be harmful to the optical core. When many fibers are used to form a cable, each coating can be in a different color, which allows distinguishing one from another. The coating is made from plastic material, which is applied on the fiber directly after manufacturing with a common diameter of 250 µm. The refractive index of the primary coating is considerably larger than of the cladding to prevent light that leaves the fiber core into the cladding to be reflected back into the fiber core, causing dispersion.

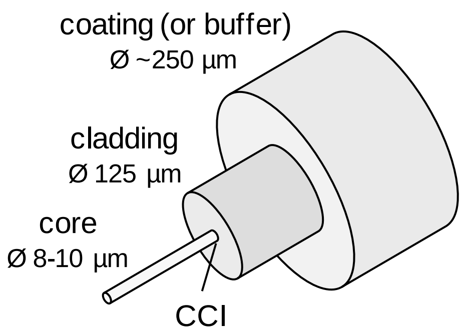

Fig. 3-8: Basic design of a single mode optical fiber

The core of SM fibers is small enough so only one single mode of light can be propagated through it. This solves the problems of modal dispersion, which has to be faced in fibers with larger core diameters, where multiple modes of light are propagated at the same time (multi mode fibers). One mode of light can contain a variety of different wavelengths, which is eliminated in distributed fiber optic strain sensing by the laser, which emits monochromatic light of only one wavelength. As outlined in Fig. 3-9, the beam of light travels nearly parallel to the axis of the fiber. Typical electromagnetic wavelengths of the light used in SM fibers are 1310 or 1550 nm (Murata 1996). Due to the small diameter of the fiber core and the single mode that is transmitted, a stepped refractive index, which means that the refractive index of the core is the same throughout the core diameter, is usually sufficient.

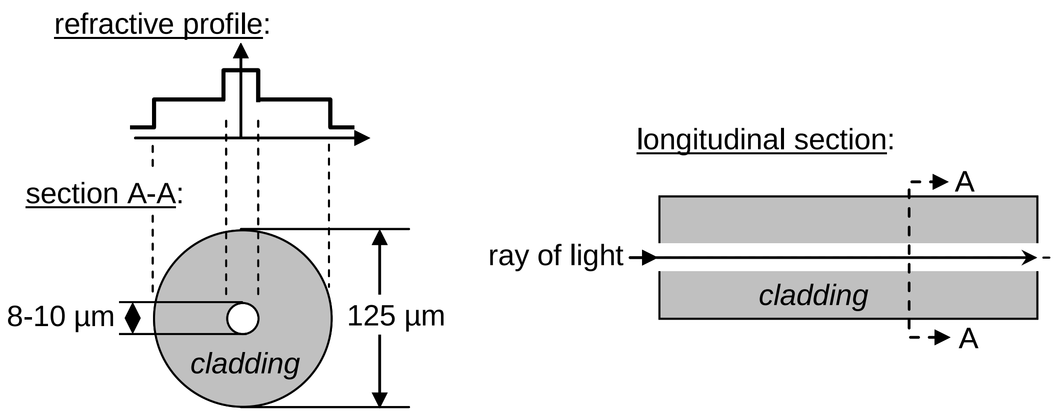

Fig. 3-9: Sketch of standard single mode fiber

More modern SM fibers have evolved into more complex designs such as matched claddings or depressed claddings, where different cladding layers of different refractive indices are surrounding the core of the fiber. Due to the almost linear propagation of light through the fiber and the consequently shorter distance the light covers in the fiber core, the attenuation of SM fibers is considerably lower than for fibers with larger cores. One problem of sensing with fibers of small core diameters however is the smaller amount of light that can be coupled into it due to the small cross sectional area of the core and the low numerical aperture (N.A). Even though that limitation is eliminated in multi mode fibers that have core diameters of 50 µm (European standard) or 62.5 µm (US standard), those fibers are unsuitable for distributed strain sensing in standard configurations (Lenke and Nöther 2007). The problem is the modal dispersion due to the propagation of multiple modes of light in one core at the same time. As much more light can be coupled into the large core, the power of the input pulse as well as the reflections are of much higher intensity. For temperature only measurements that exclusively depend on the shift of the Raman peaks in the reflected light, which is situated far away from all other reflected peaks (Brillouin and Rayleigh), the dispersion of multiple modes only has a minor influence. Therefore MM fibers are mostly used for distributed temperature sensing based on Raman scattering. Further research is being made on the use of multi mode fibers, polarization maintaining fibers (PMF) and photonic crystal fibers (PCF) for strain sensing applications.

3.2.4 Physical properties of optical fibers

The diameter of a human black hair is up to 100 µm, only slightly smaller than an optical fiber without primary coating. The size leads to one common misconception about optical fibers, that they must be extremely fragile because they are tiny in diameter and made out of glass. In fact, research, theoretical analysis and practical experience prove that the opposite is true. As all glasses, fused silica has an amorphous[1] atom structure, which means that the atoms have no order but form an irregular pattern (Fellay 2003). The precondition for the amorphous state of fused silica is that the atoms of the melted glass are not able to rearrange regularly during cooling. The result is a disordered atomic configuration, which is frozen into solid state. Even though correctly considered a solid, glass is in the physical sense also referred to as a frozen, supercooled liquid, having a viscosity η of several orders of magnitude higher than 10^{13} poise (10^{12} Pa·s), which is the viscosity at the glass transition temperature or generally spoken the limit for a liquid to flow (Doremus 2002).

While traditional bulk glass is still very fragile, the ultra pure glass of optical fibers exhibits both high tensile strength and extreme durability. In Tab. 3-3, the properties of fused silica are compared to the metals copper, aluminum and steel. The extremely low coefficient of thermal expansion of 0.5 µm/m/K accounts for the remarkable ability of optical fibers to undergo large and rapid temperature changes without cracking. As mentioned above, the glass transition temperature or solidifying temperature of glass marks the temperature, above which silica gradually becomes more viscous and changes from being solid to liquid state.

---

[1] From the Greek „without form“

Tab. 3-3: Physical properties of fused silica glass compared to other materials, based on Murata (1996)

property	fused silica	copper	aluminum	steel
chemical sign	SiO_2	Cu	Al	Fe
density [kg/m³]	2,200	8,900	2,700	7,900
tensile strength [MPa]	5,000	250	100	1.200
Young’s modulus [MPa]	72,000	120,000	63,000	210,000
breaking elongation [%]	2-8	20-30	7-20	5-15
coefficient of thermal expansion [µm/m/K]	0.5	17	23	10
bulk modulus [MPa]	36,900	140,000	76,000	160,000
glass transition temperature	~ 1400 °C	-	-	-

Without the protective primary coating, the fiber is very susceptible to external damage. Consequently, the fiber receives a primary coating during the production process. Possessing this protection, fibers are usually embedded into cables or applied directly on a structural part, which is basically limited to laboratory applications.

3.3 Brillouin scattering for distributed strain measurements

3.3.1 Spontaneous Brillouin scattering

The basic principle of distributed strain measurements is based on the evaluation of frequency changes between the incident light and the light that is backscattered in every point of the fiber. A distributed strain sensing system consists of at least three major parts, an optical fiber, a monochromatic laser source and an evaluation unit. When the dependence of the Brillouin shift in optical fibers on strain and temperature was published for the first time, the determination of temperature from Raman shift was already well known (Horiguchi, Kurashima et al. 1989; Kurashima, Horiguchi et al. 1990). Since that time major research is being made in order to receive reliable distributed values for strain from the Brillouin backscatter in optical fibers.

In principle, Brillouin scattering is caused from the interaction of light with sound. Acoustic waves can simplified be described as variations of material quantities in the crystal lattice of an optical medium that could also be expressed in terms of values like pressure, density or entropy (Mills 1998). When those variations travel along the medium at sound velocity, they periodically change its refractive index

(Banerjee 2004). The effect on an optical fiber however only takes place in a molecular layer and is not affecting the fiber from a macro point of view. The velocity of acoustic waves in air at ambient temperature is usually specified with 343 m/s, which is much smaller than in amorphous silica. The longitudinal acoustic velocity can be expressed as:

$$V_a = \sqrt{\frac{E}{\rho}} \qquad \text{Eq. 3-3}$$

V_a	velocity of an acoustic wave [m/s]
E	Young's modulus [Pa]
ρ	medium density [kg/m³]

Calculating the value for the velocity of sound in an optical fiber at ambient temperature and atmospheric pressure with $\rho = 2.2\ 10^3$ kg/m^3 and E = 72.0 GPa, it comes to V_a = 5,721 m/s.

The acoustic velocity is depending on the material density of the medium, which again is depending on the temperature and the strain applied. Consequently, the Brillouin frequency shift ν_B expressed in Hertz (1/s) is directly depending on the acoustic velocity and the wavelength of the incident light (Eq. 3-4): $\nu_B \sim V_a \sim T, \varepsilon$.

$$\nu_B = \frac{2nV_a}{\lambda_0} \qquad \text{Eq. 3-4}$$

ν_B	Brillouin frequency shift [Hz] or [1/s]
λ_0	vacuum wavelength of incident light [m]

By using the longitudinal sound velocity in silica calculated from Eq. 3-3 (V_a = 5,721 m/s) and a refractive index of 1.444 at 1550 nm wavelength, the Brillouin shift can be calculated to 10.7 GHz.

According to the physical conceptualization of the wave-particle duality, light can either be described in terms of “particles” or “waves”. The “parts of the light” are the photons, which can also appear as “light waves” that interfere with each other. This can cause changes in the interacting waves, which range from overlapping to the cancellation of each other. As a particle, light can only interact with matter by transferring an amount of energy.

Brillouin scattering is an effect caused by the nonlinearity of a medium. As long as the optical power within an optical fiber is low, it can be treated as a linear medium, which means that its loss and the refractive index are independent of the optical power. This changes when using highly intense light sources such as lasers. In case the optical power reaches a certain threshold, nonlinear effects in the optical fiber occur that are the source of Brillouin scattering. Above the threshold, incident light waves interact with acoustic waves in the optical medium and change their path. In case of single mode optical fibers, the only possible change of path is forward ($\Theta = 0°$) or backward ($\Theta = 180°$), which is commonly referred to as "backscattering".

In fiber optic sensing, the required information is contained in the frequency shift of the backscattered light waves. Due to the fact that the periodic shift in the refractive index of the medium is moving at sound velocity with the acoustic wave, the diffracted light undergoes a Doppler frequency shift (Sutherland 2003). The interaction between light waves and moving acoustic waves can also be seen like a moving Bragg diffraction. Figure 3-10 shows a sketch of the formation of Brillouin scattering, where the incident light with wavelength ν_0 is interfering with an acoustic wave (or grating) that is moving at sound velocity. This interaction leads to an up- or downshift of the incident light wave's frequency, which could either turn out to $\nu_0+\nu_a$ (up) or $\nu_0-\nu_a$ (down). The up-shifted part of the backscattered spectrum is called anti-Stokes scattering, the down-shifted part Stokes scattering. In Brillouin scattering, the shift is equal to the frequency (energy) of the acoustic phonons in the fiber, which is in the 10 GHz region. Consequently ν_a is equal to the Brillouin shift ν_B.

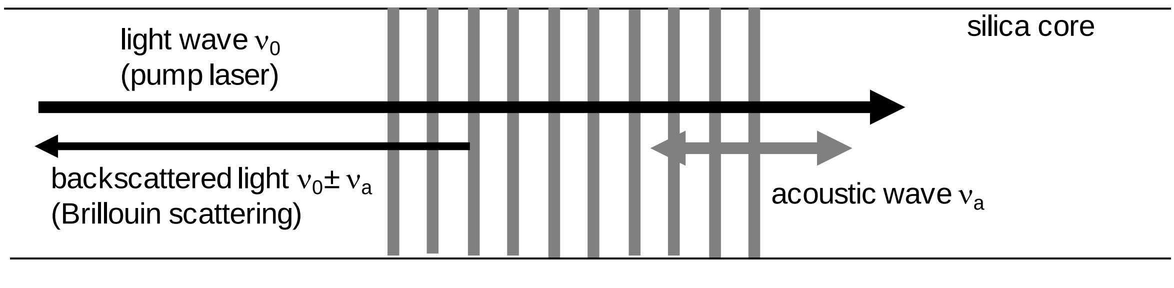

Fig. 3-10: The effect of spontaneous Brillouin scattering

The inelastic process of Brillouin scattering can also be seen from a molecular point where the photons on their way through the fiber gain or lose energy when interacting with the phonons in the silica. Phonons can be categorized as quasi-particles and be described as quantized lattice vibration. Consequently the backscattered photons experience an energy shift from their incident energy state. The efficiency of spontaneous Brillouin scattering depends on the number of acoustic phonons that are generated by thermal excitation and thus do not have a preferred propagation direction. Due to the fact that every phonon carries a quantum of vibrational energy, the internal energy of the object also rises with temperature. Figure 3-11 shows the spectral components in the backscattered light.

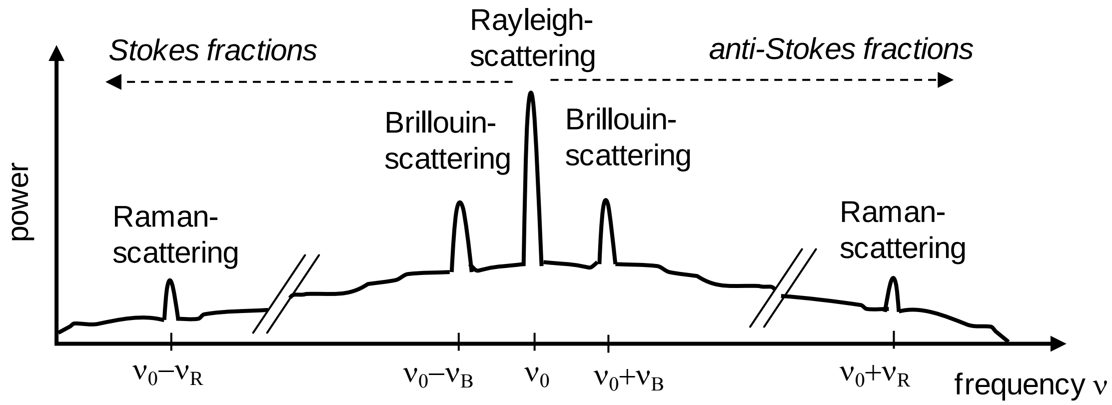

Fig. 3-11: Typical spectral components in the backscattered light

The limit for spatial resolution in distributed strain sensing is founded in the bandwidth of the Brillouin scattering. The so called Brillouin linewidth $\Delta\nu_B$ at full width at half maximum, depicted in Fig. 3-12, is depending on the acoustic damping time T_B of the phonons (Agrawal 2001).

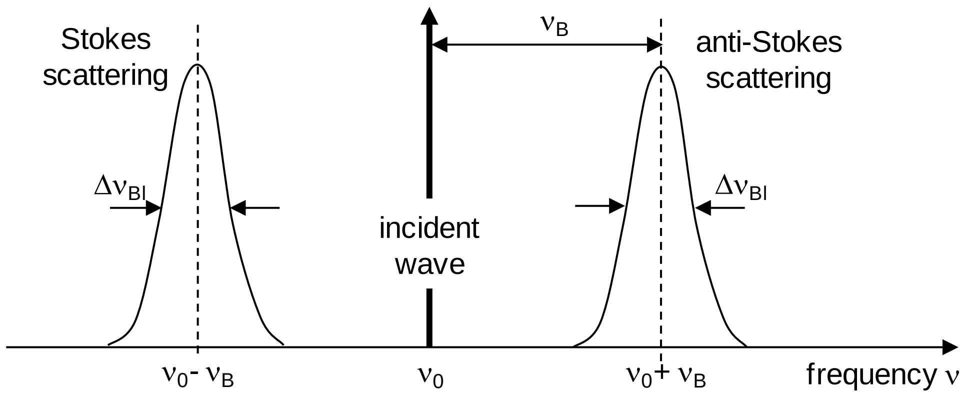

Fig. 3-12: Typical spectrum for Brillouin scattering

The damping time is depending on the acoustic damping coefficient Γ_B, following the relation $T_B = 1/\Gamma_B$, which is used in Eq. 3-5. The damping time is sometimes also expressed as phonon lifetime T_p where the relation $T_B = 2T_p$ is valid (Geinitz 1998).

$$\Delta\nu_{Bl} = \frac{1}{\pi \cdot T_B} = \frac{\Gamma_B}{\pi} \qquad \textit{Eq. 3-5}$$

$\Delta\nu_{Bl}$	Brillouin linewidth [Hz]
Γ_B	acoustic damping coefficient [Hz]

A typical and often used value for the acoustic phonon lifetime T_p for bulk silica is 10 ns (Kalosha, Ponomarev et al. 2006), which is strongly depending on the wavelength of the incident light.

3.3.2 Sensitivity to dopant concentration and pressure

The Brillouin shift in optical fibers is depending on several intrinsic and extrinsic parameters such as the dopant concentration, strain, temperature and pressure. Dopants in variable fractions are used to increase the refractive index of the fiber core in order to assure total reflections in the core cladding interface. The dopant concentration is usually constant over the length of a fiber. As the acoustic velocity in pure GeO_2, which is mostly used as dopant, is considerably lower than in pure silica (~3,780 m/s), the Brillouin frequency shift is linearly decreasing with rising dopant concentrations. As the dopant concentration is usually equal over the whole length of the fiber or at least the measuring section, the Brillouin shift due to the dopant concentration can be seen as the fingerprint of a fiber.

The effect of high pressure on the Brillouin shift can be described by the influence of the density of the fiber material. If applying high pressure, the fiber gets compressed in transversal direction and thus its density is increasing. The linear relationship between hydrostatic pressure on the fiber and Brillouin shift was experimentally evaluated by Le Floch (2001) to C_p = -0.091 MHz/bar. The negative algebraic sign suggests that the Brillouin shift decreases with high hydrostatic pressure values. The influence of hydrostatic pressure on optical fibers, especially when they are embedded into a cable, can usually be considered to be very small in hydraulic engineering purposes. As an example, 100 bar or 10 MPa transversal pressure directly on the fiber would result in a decrease of Brillouin shift of 9.1 MHz, which is equal to a decrease of strain or temperature of roughly 200 με or 10 K, referring to Tab. 3-4.

3.3.3 Sensitivity to strain

Due to the elastic properties of silica, the appliance of longitudinal strain or compression leads to a volume change of the fiber. This changes the material density and has an influence on the sound velocity. As the comparison with other materials in Tab. 3-3 shows, the elongation of fused silica in optical fibers is quite limited. This in return confines the measuring range for distributed fiber optic strain sensing in bare fibers. The largest value for strain that was measured in an optical fiber is 2.83 % (Li, Parker et al. 2004).

The normalized strain coefficient C_{ε}' (sometimes also referred to as normalized slope coefficient) gives normalized information on the amount of strain ε that corresponds to the shift of the Brillouin peak ν_B in Hertz. To clarify the influence of the velocity of sound again, ν_B is substituted in the following equation with Eq. 3-4:

$$C_{\varepsilon}' = \frac{1}{\nu_B}\frac{\partial \nu_B}{\partial \varepsilon} = \frac{1}{n}\frac{\partial n}{\partial \varepsilon} + \frac{1}{V_A}\frac{\partial V_A}{\partial \varepsilon} \qquad \textit{Eq. 3-6}$$

C_{ε}'	normalized strain coefficient [1/µε]
V_a	velocity of an acoustic wave [m/s]
ν_B	Brillouin frequency shift [Hz]

Strain in relation to the Brillouin shift is usually expressed in the absolute strain coefficient C_{ε} and is roughly located in the area around 50 kHz/µε[2] at 1550 nm wavelength, which is among other factors depending on the dopant concentration in the fiber:

$$C_{\varepsilon} = \frac{\partial \nu_B}{\partial \varepsilon} \qquad \textit{Eq. 3-7}$$

C_{ε}	absolute strain coefficient [Hz/µε]

Experiments showed that the dependency of elongation and Brillouin frequency shift behaves linearly until the breaking point of the fiber (Thévenaz, Niklès et al. 1998).

---

[2] The unit µε ("micro strain") indicates the elongation of 1 µm (0.000001 m) per 1 m length (0.0001 %), thus would correctly be µm/m strain.

3.3.4 Temperature cross-sensitivity

One of the major challenges in distributed fiber optic strain sensing is the dependence of the Brillouin shift and the Brillouin power on both, temperature and strain. For isothermal conditions this problem becomes irrelevant and it is possible to determine the strain of a fiber by simply measuring the frequency shift. The relation between strain and temperature is given by Eq. 3-8 (Parker, Farhadiroushan et al. 1997).

$$\Delta\nu_B = C_\varepsilon \cdot \Delta\varepsilon + C_T \cdot \Delta T \qquad \textit{Eq. 3-8}$$

C_T absolute temperature coefficient [Hz/K]

The factor C_T is determined analogous to the absolute strain coefficient C_ε:

$$C_T = \frac{\partial\nu_B}{\partial T} \qquad \textit{Eq. 3-9}$$

Due to those relations it is not possible to distinguish between temperature and strain just from the measurement of the Brillouin frequency shift ν_B. Fellay (2003) reported that a linear temperature dependence is valid for values around ambient temperature (~ -30 ÷ 90 °C), but becomes different at extreme temperatures. Figure 3-13 shows the influence of two different temperatures (top) and two different strains (bottom) on the backscatter signal for a spontaneous Brillouin scattering setup. The small peaks on the Rayleigh wing in the lower case are insignificant contributions from an unstrained lead fiber that was used in the test setup for those measurements (Parker, Farhadiroushan et al. 1997).

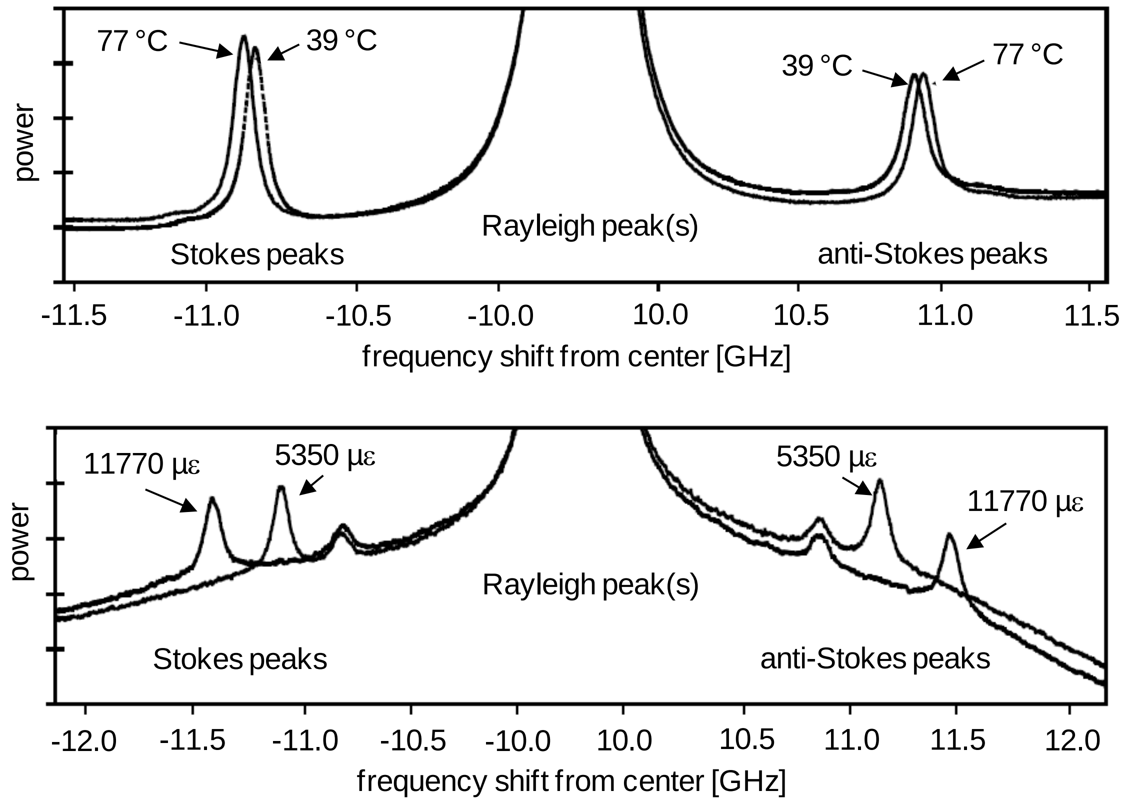

Fig. 3-13: Effect of changing temperatures (top) and strain (bottom) on the Brillouin spectra based on Johansson, Dahlin et al. (2000)

The increase of temperature in the upper graph of Fig. 3-13 clearly indicates a rise of Brillouin power and an increasing shift of the peaks from the center frequency. For rising strain, an increase of the Brillouin shift can be seen clearly. In a stimulated Brillouin scattering test arrangement (section 3.4.3), the anti-Stokes peaks are depleted by a counter propagating Stokes wave.

As the effect especially of temperature on the power of the backscattered Brillouin signal is obvious, efforts are being put into overcoming the effect of the undistinguishable temperature-strain relationship regarding the Brillouin frequency shift by using the signal power. The Brillouin power can be expressed as follows:

$$\frac{\Delta P_B}{P_B(\varepsilon, T)} = C_{P\varepsilon} \cdot \Delta\varepsilon + C_{PT} \cdot \Delta T \qquad \textit{Eq. 3-10}$$

P_B	Brillouin power [W]
$C_{P\varepsilon}$	coefficient for strain induced change of Brillouin power [W/με]
C_{PT}	coefficient for temperature induced change of Brillouin power [W/K].

The two coefficients for strain and temperature $C_{P\varepsilon}$ and C_{PT} can either be evaluated theoretically or by experiments (see Tab. 3-4). However additional problems turn out to be the fluctuations in the input pump power (power of the pulsed incident light) and the depletion of the signal along the fiber which affects the growth of the Brillouin scatter highly nonlinear. By mathematically combining the values of the Stokes and anti-Stokes powers, Parker, Farhadiroushan et al. (1998) define a power P_B^{lin} that behaves linear with pump power and equals the Stokes and anti-Stokes power in the linear regime. The authors also introduce the normalized Brillouin power P_B^{norm}, which describes the normalization of P_B^{lin} against the Rayleigh backscattered power. It is supposed to be independent of pump power, only depending on temperature and strain, while the Rayleigh backscattered power only has a negligible temperature and strain dependence and is proportional to the local power along the fiber. By calculating the temperatures, the Brillouin shift can be compensated for temperature in one and the same measured frequency and power spectrum. Using the absolute strain coefficient C_T, the temperature compensated strain can be calculated. This method can be used in sensing devices based on spontaneous Brillouin scattering BOTDR (section 3.4.2).

As mentioned above, the constants for the dependence of Brillouin power and shift can be calculated if all parameters are known. If the fibers are embedded in a cable, only experimental values for C should be used. In Tab. 3-4, some experimentally determined values for strain and temperature coefficients at 1320 and 1550 nm wavelength are listed. They are consistent with other tests and calculations (Parker, Farhadiroushan et al. 1997). The “exemplary ratio” shows the difference of the relationship between temperature and strain in terms of Brillouin shift and Brillouin power. Comparing the ratios of Brillouin power and shift, a great difference can clearly be seen as the effect of temperature is around 20 times higher in the power- than in the shift relationship compared to strain. As the dependence between power and temperature is linear (Kurashima, Horiguchi et al. 1998), some authors state that the effect of strain on the change of Brillouin power can be neglected (Kurashima, Usu et al. 1997; Kurashima, Horiguchi et al. 1998; Johansson, Dahlin et al. 2000).

Tab. 3-4: Cross-sensitivity of strain and temperature in the Brillouin backscatter

Brillouin shift:	strain	$\partial\nu_B/\partial\varepsilon$	0.0581 MHz/με at 1320 nm (Kurashima, Horiguchi et al. 1993) 0.0483 ± 0.004 MHz/με at 1550 nm (Parker, Farhadiroushan et al. 1997)
	temperature	$\partial\nu_B/\partial T$	1.18 MHz/K at 1320 nm (Kurashima, Horiguchi et al. 1993) 1.10 ± 0.02 MHz/K at 1550 nm (Parker, Farhadiroushan et al. 1997)
	exemplary ratio	$\boldsymbol{\partial\varepsilon/\partial T}$	1:20 at 1320 nm **1:23 at 1550 nm**
Brillouin power:	strain	$\partial P_B/\partial\varepsilon$	-(0.00077 ± 1.4) %/με at 1550 nm (Parker, Farhadiroushan et al. 1997)
	temperature	$\partial P_B/\partial T$	0.36 ± 0.006 %/K at 1550 nm (Parker, Farhadiroushan et al. 1997)
	exemplary ratio	$\boldsymbol{\partial\varepsilon/\partial T}$	**1:467 at 1550 nm**

3.4 Instrumentation for distributed fiber optic strain sensing

3.4.1 Introduction

Distributed fiber optic strain sensing systems are all based on optical time domain reflectometry (OTDR), where an optical pulse is launched into a fiber and the backscattered signal is detected as a function of time (time-of-flight-method). OTDR systems are used to evaluate the optical loss (attenuation) in a fiber, in connectors, in splices or from extrinsic mechanical impacts, by measuring the power of the reflected Rayleigh scattering at any point in the fiber. The research group around Kurashima, Horiguchi, Tateda et al. that were the first to report on the strain and temperature dependence of the Brillouin scattering, named the two fundamental systems BOTDR and BOTDA, Brillouin optical time domain reflectometer and Brillouin optical time domain analysis respectively. Sometimes the abbreviation DTSS for distributed temperature and strain sensor is also used for the BOTDR setup. A basic difference between the two methods lies in their access to the sensor, the optical fiber. While the BOTDR is based on spontaneous Brillouin scattering and thus needs access to only one end of the optical fiber, thus allowing measurements also in damaged fibers, the BOTDA system is based on stimulated Brillouin scattering and thus needs access to both ends of the fiber. Using a mirror at one end of the fiber can enable single end measurements even with the BOTDA setup; however the cable has to be continuous.

New strain sensing systems have recently been developed which allow spatial resolutions in the cm-range like the Brillouin optical correlation domain analysis – BOCDA (Hotate and Tanaka 2002). Other research groups aim at low-price distributed fiber optic strain sensing alternatives like Brillouin optical frequency domain analysis (BOFDA) that is tested for dike monitoring with a spatial resolution of 3 m at a maximum sensor length of 2 km (Nöther, Wosniok et al. 2008).

The distance of the specific strained fiber section from the measured end is determined by using the OTDR technique, where the time of flight can be measured using the following relationship (Horikawa, Komiyama et al. 2004):

$$L_i = \frac{c_0 \cdot T_i}{2n} \qquad \textit{Eq. 3-11}$$

L_i	distance from incident edge [m]
c_0	speed of light in vacuum [m/s]
T_i	elapsed time after pulse has been launched [s]
n	refractive index [-].

Today, distributed strain sensors based on BOTDR and BOTDA are commercially available. In A3, the systems that are on the marked up to this date are listed and compared. All details are taken from the official specifications of the instruments that are published by the companies. The spatial resolution of the sensing systems and their physical limitations lead to the effect that only an average value within the spatial resolution can be evaluated. Consequently the sharp change of strain within the spatial resolution could lead to problems in data interpretation (Bernini, Fraldi et al. 2006).

3.4.2 Brillouin Optical Time Domain Reflectometry – BOTDR

The method of BOTDR is based on the evaluation of the non amplified (spontaneous) backscattered light in the Brillouin spectrum, as well in the Stokes as in the anti-Stokes fraction. As the backscattered signal is not amplified, it has a weak signal power, which has to be countervailed with signal amplifiers in the detection unit. The big advantage of this technology is the possibility to measure the strain along a single mode fiber by accessing it only from one end as depicted in Fig. 3-14. Especially in field applications in rugged environments like installations in concrete or soil, this is a vital point. As the sensing cables are usually installed during heavy construction, the risk of damage of the cable and thus the fiber is always present. If the cable is installed in a loop configuration anyway, the measurements can still be carried out from both sides of the fiber until a potential break.

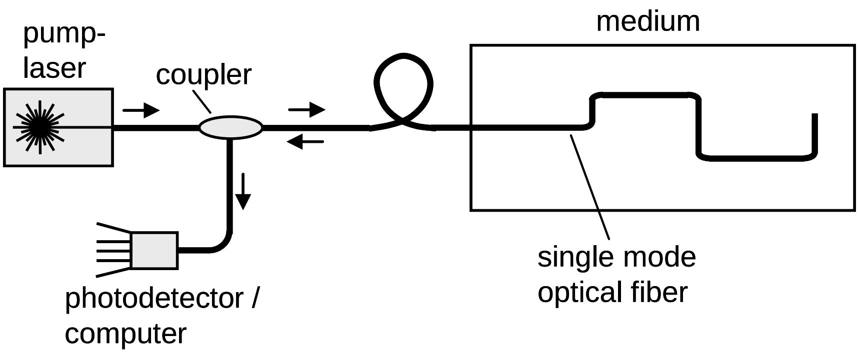

Fig. 3-14: Simplified BOTDR setup

Several setups for BOTDRs have been presented by different research groups. Apart from optical devices, the basic difference lies in the handling of the cross-sensitivity between temperature and strain as discussed in the previous section. At isothermal conditions, strain can easily be evaluated from the change in Brillouin shift only. However in most field applications the temperature is not consistent, especially not along the entire fiber. Some authors work with devices without the possibility of temperature compensation when temperature changes are not an issue (Kurashima, Horiguchi et al. 1993; Kurashima, Usu et al. 1997) or where excessive strain is the clearly predominant part in the process (Komatsu, Fujihashi et al. 2002) or the measurement time is short without significant changes in temperature (Bastianini, Matta et al. 2006). Isothermal conditions can be found in most laboratory applications. Horikawa, Komiyama et al. (2004) propose a setup of two devices, a BOTDR without temperature compensation and an as they call it

ROTDR – for Raman optical time domain reflectometer, more commonly known as distributed temperature sensor (DTS), to measure the distributed temperature from the Raman backscatter, which is independent from strain, simultaneously. This can therefore happen in the same cable or fiber. Another possibility is the use of special cables by installing loose tubed and tight cables next to each other in order to have a non-strained temperature-only measurement for reference (Thévenaz, Niklès et al. 1998). By filtering the temperature induced Brillouin shift from the total shift, the strain in the fiber can be calculated. For this purpose, special cables with loose and tight fibers lying next to each other have been developed and will be discussed in more detail in chapter 4.

A physical limitation for distributed strain measurements is the spatial resolution, which is limited to close to 1 m. This is a consequence of the before mentioned phonon lifetime of around 10 ns in optical fibers. The spatial resolution depends on the duration (or length) of the light pulse that is being sent out from the laser source. Pump durations of less than the phonon lifetime lead to excessive broadening of the Brillouin linewidth $\Delta\nu_{Bl}$, making the exact evaluation of the Brillouin shift impossible. For a pulse length of 10 ns, the highest spatial resolution can be calculated by Eq. 3-11, which turns out to be 1.039 m in case of a refractive index n = 1.444 at 1550 nm wavelength. As a rule of thumb it can therefore be stated that a pulse length of 10 ns equals a spatial resolution of 1 m, 20 ns of 2 m and so on. The limit in resolution leads to problems in case of sharply changing temperature and/or strain within the length of the spatial resolution (Parker, Farhadiroushan et al. 1997).

The only BOTDR device where the temperature compensation is completely being made from the Brillouin spectrum without additional temperature sensing devices or reference fibers was presented by Parker, Farhadiroushan et al. (1997). The strain evaluation in their patented distributed temperature and strain sensor (DTSS) system is based on the combination of temperature and strain induced changes not only of the Brillouin shift but also of the power. As described in the previous section on temperature compensation, the Brillouin power only has a very small dependence on strain. In their setup, the influence of strain on the Brillouin power is neglected and thus the temperature is evaluated from the power and the strain is calculated from the Brillouin shift (Farhadiroushan and Parker 1998). The above described normalization factor P_B^{norm}, which is normalized against Rayleigh scattering also has to be taken into account. A basic sketch of the proposed setup is shown in Fig. 3-15.

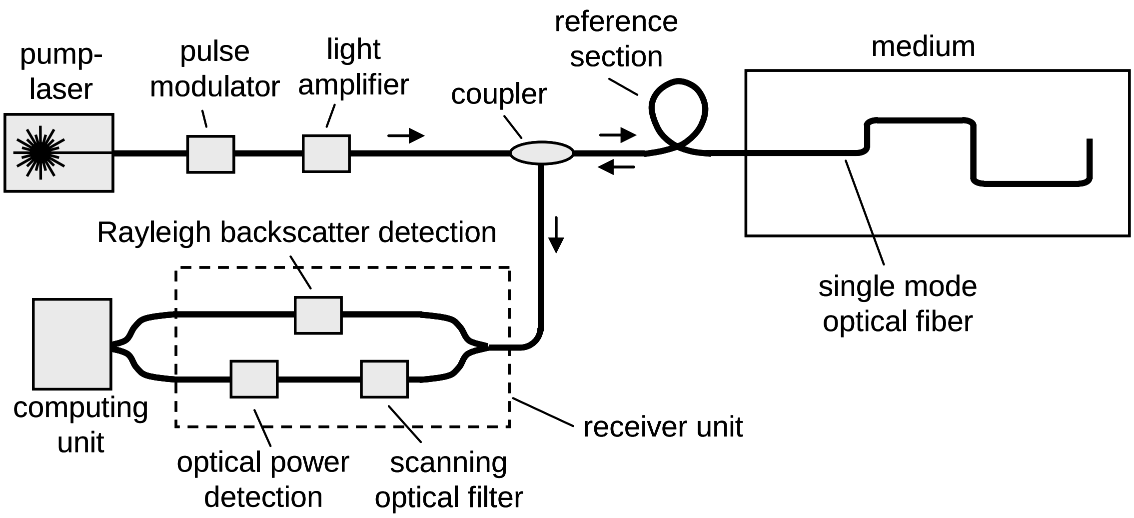

Fig. 3-15: Basic elements of the Sensornet DTSS referring to Farhadiroushan and Parker (1998)

Optical amplifiers are used to amplify the backscatter signal and additionally multiple signals are superimposed in multiple time intervals for an improved signal to noise ratio (SNR). Specific software is used to carry out the needed calculations and average determinations in order to present the optical signals that are being converted into electrical signals in a receiver unit. Today the DTSS system is still under further development in a pre-production state (Kluth and Watley 2006). The tests that were carried out with that device in the scope of this thesis showed that the power is reacting very sensitive to local losses and thus the internal temperature compensation considerably worsens the evaluated strain values (section 8.5).

3.4.3 Brillouin Optical Time Domain Analysis – BOTDA

BOTDA is based on stimulated Brillouin scattering (Chiao, Townes et al. 1964). A constant light wave (CW) called the Stokes wave, is coupled into an optical fiber from one end. It is amplifying the Stokes shifted Brillouin waves that were backscattered due to the interaction of a short wave called the pump wave, that was coupled into the other end of the fiber, with acoustic phonons. The basic layout of a BOTDA concept is depicted in Fig. 3-16. The constant Stokes wave with the same frequency as the Brillouin reflection in an unaffected fiber is coupled into the fiber (here from the right side). A pump wave of several ns duration, depending on the desired spatial resolution, is coupled into the fiber from the other side, interfering with the CW in every point of the fiber.

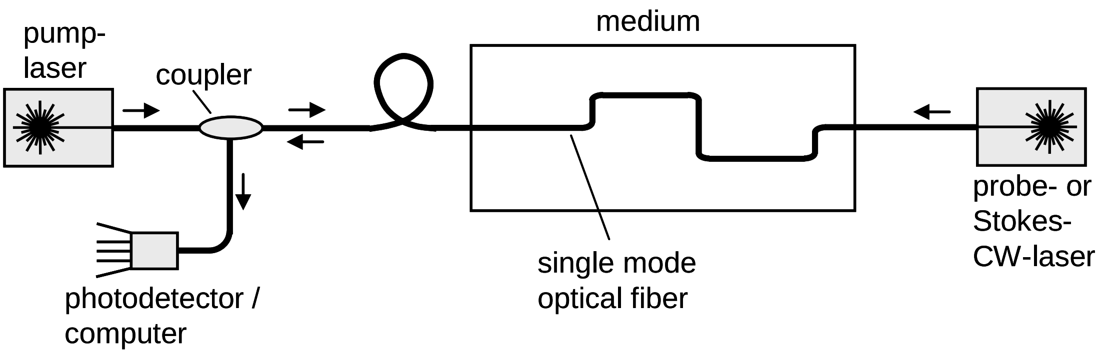

Fig. 3-16: Simplified BOTDA setup

The interaction between the constant wave signal and the pump signal is illustrated in Fig. 3-17. On the left side, the frequency of the probe signal is equal to the Stokes shifted Brillouin scatter in an unstrained part of the fiber, $\Delta\nu = \nu_{B0}$. Strain or temperature is applied to the highlighted section of the fiber. As the pump pulse is moving along the fiber, some of its light is backscattered while undergoing a Brillouin shift. In the unstrained part of the fiber this is equal to the CW light, which is consequently stimulating the backscattered Stokes light (a). The affected fiber section has an effect on the Brillouin shift, which is not equal to the frequency of the CW signal. The probe signal does not interact with the backscattered Stokes shifted light in that region and thus is not stimulated. In order to receive information on the magnitude of Brillouin shift in the affected section, the frequency of the CW probe signal is modulated. At a probe frequency equal to the Brillouin shifted light in the affected section, the Brillouin backscatter from the pump pulse does not experience stimulation in the unaffected fiber as $\Delta\nu \neq \nu_{B0}$ (right side). When passing the affected section, the Brillouin shifted backscatter from the pump light matches the frequency of the probe light and thus the CW is being stimulated (increased).

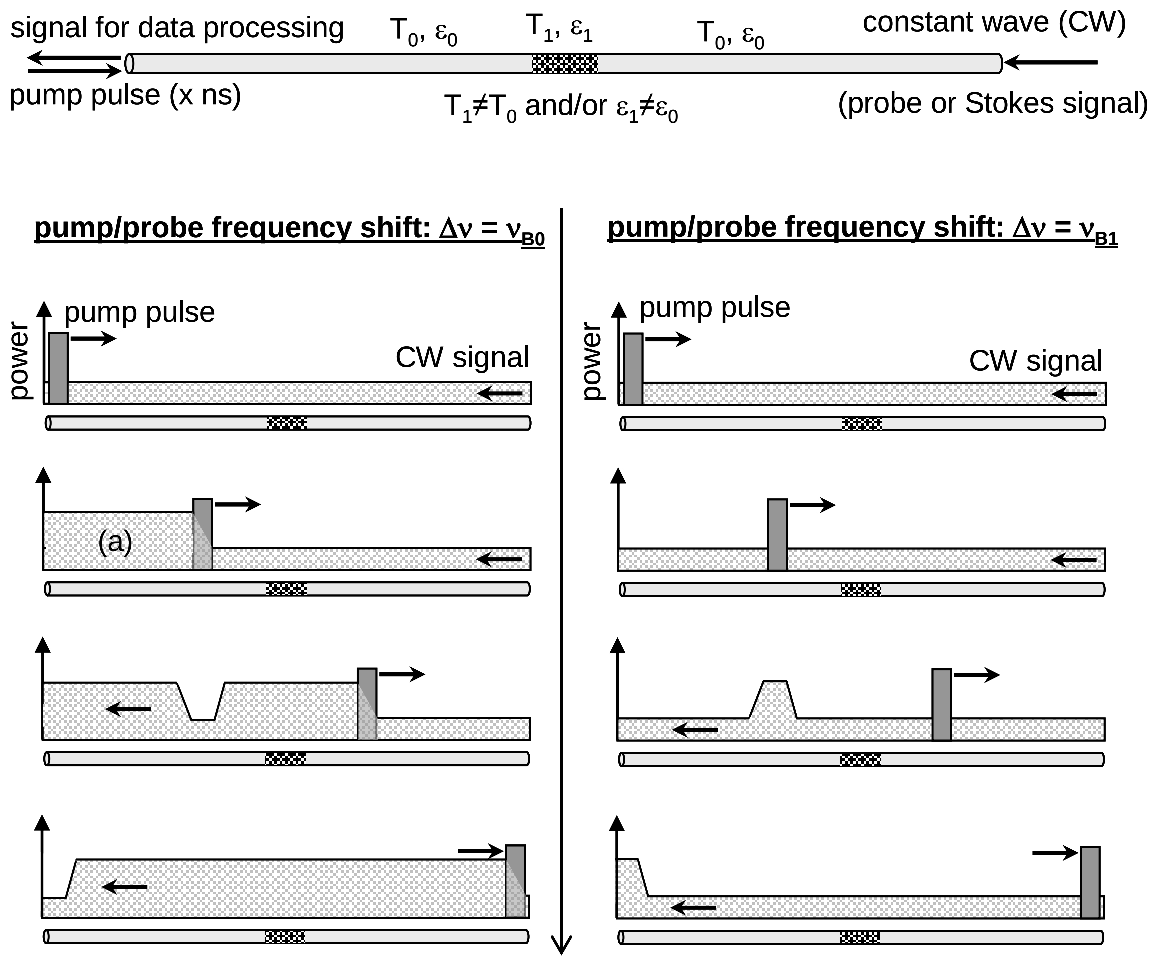

Fig. 3-17: Principle of the pump-probe method

As the Stokes backscattered light is amplified thus is gaining power, this method is called the “gain method”. The inverse method, where the CW signal acts as pump light and undergoes a local decrease in power is called the “loss method”. The process of data acquisition and the processed output is exemplarily given in Fig. 3-18. Graph a) shows the Brillouin gain along the fiber at a probe frequency of 10.80 GHz with high Brillouin peaks (gain factors) in the rear part of the fiber. Graph b) shows the Brillouin gain spectrum at a specific point in the fiber (here: 500 m) with a maximum Brillouin gain at little less than 10.80 GHz. By evaluating the Brillouin frequency and the maximum gain at every point in the fiber and putting those data together, the 3D picture in c) can be plotted. The result is the Brillouin frequency shift at maximum gain factors in relation to the position along the fiber as shown in graph d). Assuming isothermal conditions, the strain distribution along the fiber can directly be calculated from d).

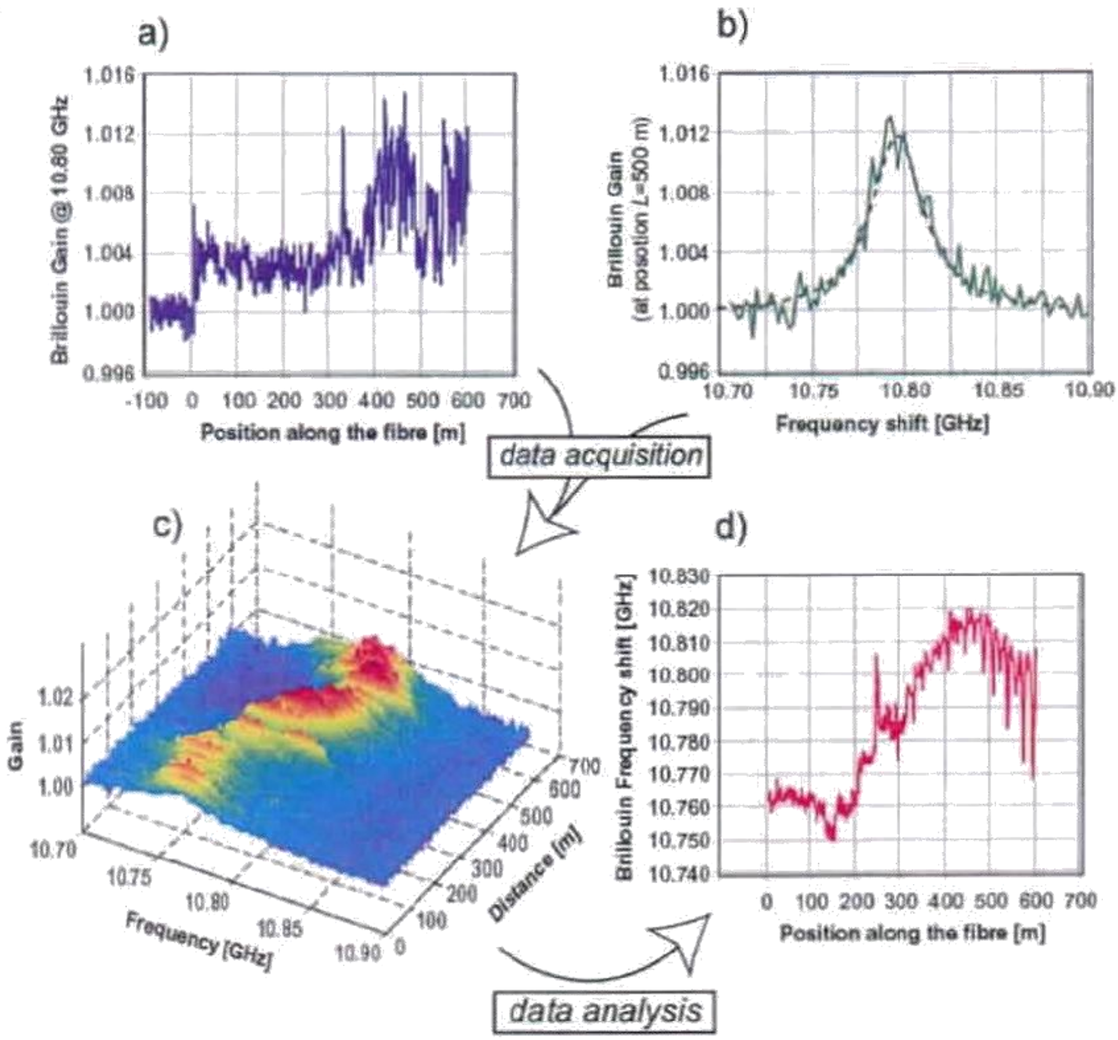

Fig. 3-18: Brillouin gain- and frequency spectrum (Facchini 2001)

The big advantage of BOTDA over BOTDR setups is the considerably stronger Stokes signal due to the amplification process and hence a better resolution (Thévenaz 2006). The cable has to be accessible from two ends or from one end with an all fiber mirror on the other end. Also a distinct Fresnel reflection at the end of the fiber could be enough to allow the measurements (Facchini 2001). However those limitations prohibit reliable measurements in case of a damaged fiber. Additionally, two lasers, one to generate the pump, the other to generate the probe wave have to be in operation. A method to overcome that limitation was presented by Thévenaz, Facchini et al. (2001) whose BOTDA setup only requires one laser source. This is achieved by an electro-optic modulator (EOM), which is being used on the one hand for pulsing the CW light, forming the pump signal and on the other hand for the generation and frequency tuning of the probe signal through modulation of the laser light.

While the spatial resolution in BOTDR applications is limited to 1 m due to linewidth broadening when the pump light has a shorter duration than the phonon lifetime of 10 ns, BOTDR setups can handle this problem under certain circumstances, attaining considerably better spatial resolutions. The spatial resolution for stimulated Brillouin scattering is depending on the group velocity ν_g ($2.05 \cdot 10^8$ m/s in silica fibers at λ = 1550 nm), which accounts for the two interacting waves (Facchini 2001). As the two waves are propagating against each other at same speed, the pulse time has to be divided by two:

$$L = \frac{1}{2} \cdot T_P \cdot \nu_g \qquad \textit{Eq. 3-12}$$

L	pump pulse spatial length [m]
T_P	pump pulse duration [s]
ν_g	group velocity [m/s]

Filling in numbers, the spatial resolution again turns out to have the same relationship as for spontaneous backscattering where a 10 ns pulse leads to a spatial resolution of 1 m and so on. While spectral broadening limits the spatial resolution in BOTDR applications, this can be overcome in the stimulated regime. By reducing the SNR, Brown, DeMerchant et al. (1999) attained a spatial resolution of 15 cm. In the scope of expanding the applications for distributed fiber optic strain sensing, other research teams are working on long range sensors by counter propagating or in-line Raman amplification (Alahbabi, Cho et al. 2006; Gong 2006).

3.5 Quasi-distributed fiber optic strain sensing with fiber Bragg grating (FBG) sensors

Some of the outstanding properties of fiber Bragg grating (FBG) sensors are the option of multiplexing several sensors and the measurement accuracy. The sensed information is directly encoded into wavelength, which is an absolute parameter and does not directly depend on the total light levels, system setups or losses in the fibers and connectors (Merzbacher, Kersey et al. 1996). A Bragg grating sensor is fabricated by grating the core region of a single mode optical fiber. A grating is a periodic change of the refractive index as depicted in Fig. 3-19. The simplest structures are uniform FBGs where the gratings are positioned in equal distances in the fiber core. The gratings are produced by using a UV light beam with a silica phase mask between the light and the fiber, which diffracts the incident light, creating an interference pattern (phase mask method). As the fiber is doped with Germanium, it turns sensitive to UV light. The refractive index of the optical fiber core changes where the intensity is brightest and thus produces a periodic refractive index n. The changes in the index of refraction within the fiber caused by the gratings lead to reflections whose wavelengths are sensitive to the period of the gratings Λ, the Bragg wavelength:

$$\lambda_B = 2n_{eff}\Lambda \qquad \textit{Eq. 3-13}$$

λ_B	Bragg wavelength [m]
n_{eff}	effective mean refractive index [-]
Λ	period of the grating [m]

Other wavelengths that do not fulfill the condition of the Bragg wavelength will pass through the gratings that have an effective mean reflective index n_{eff}, undisturbed (Habel and Hofmann 2007). The length of the gratings is usually in a range from 0.1 mm to several centimeters (Botsis, Humbert et al. 2005).

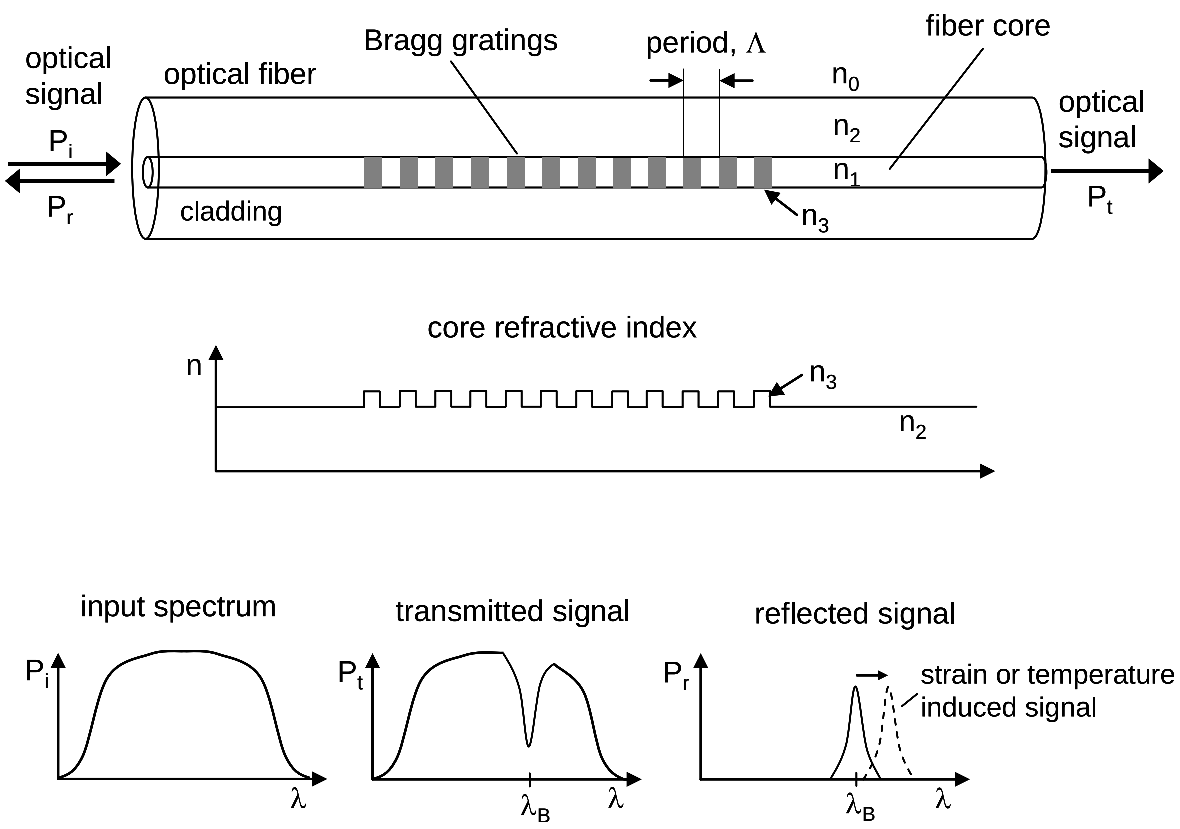

Fig. 3-19: Principle of an FBG sensor

The period of the gratings changes with expansion or contraction of the optical fiber that result from axial strain and/or temperature changes in the grated fiber region. As a consequence, the Bragg wavelength moves to higher or lower frequencies (Döring 2006). The shift of the Bragg wavelength contains the information on axial strain and temperature according to:

$$\frac{\Delta\lambda_B}{\lambda_B} = G_\varepsilon \cdot \Delta\varepsilon + S_T \cdot \Delta T \qquad \textit{Eq. 3-14}$$

$\Delta\lambda_B$	shift of Bragg wavelength [Hz]
λ_B	Bragg wavelength [m]
G_ε	strain gauge factor (approximated to ≈ 0.78)
$\Delta\varepsilon$	change of strain in the Bragg region [-]
S_T	temperature sensitivity (approximated to ~ $6 \cdot 10^{-6}$ K^{-1})
ΔT	change of temperature in the Bragg region [K]

In Eq. 3-14, $\Delta\varepsilon$ and ΔT represent the change in strain and temperature from the initially measured reference values (Measures 2001). G_ε and S_T represent the strain-gauge factor and the temperature sensitivity respectively, which depend on the input wavelength and can be approximated to $G_\varepsilon \approx 0.78$ and $S_T \approx 6 \cdot 10^{-6}$ K^{-1}.

According to Inaudi (2005), resolutions in the order of 1 με and 0.1°C can be achieved with the best modulators. For strain sensing, the temperature cross-sensitivity from Eq. 3-14 is a major problem for long term observation. Also here, one solution could be to have a loose grated section that is not affected by strain next to a grated section for strain sensing to cancel out the temperature-only changes (Inaudi 2005). Different sensor designs have been developed in order to optimize the transmission of strain and temperature into the grated region of the fiber (Zhou and Ou 2004). An example of two FBG strain sensors that were installed into the RCC block for the tests in chapter 7 is shown in Fig. 3-20.

Multiplexing of FBG sensors is accomplished by producing a fiber with a sequence of spatially separated gratings, each with different grating pitches. The reflected spectrum will then contain a series of peaks, each associated with different Bragg wavelengths.

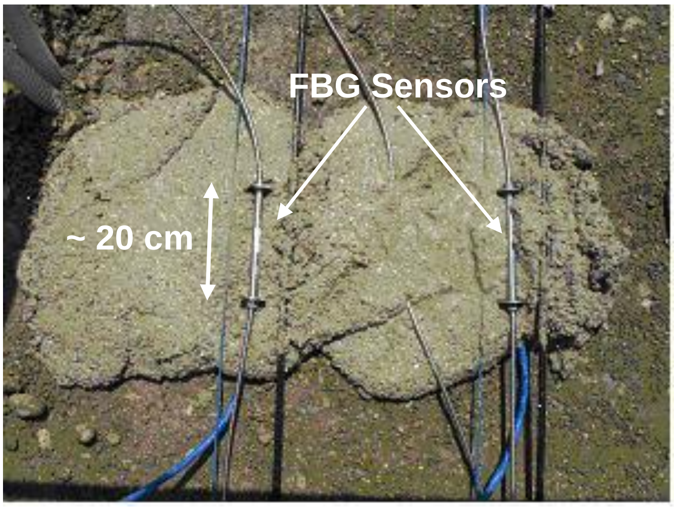

Fig. 3-20: Two FBG sensors for strain sensing in concrete

Information on temperature and/or strain at multiple points along a single mode optical fiber is obtained by assigning the peaks to the sensing points (Moser, Aufleger et al. 2007). As mentioned before, the number of Bragg sensors could theoretically be several hundred (Zhang 2003), their number is usually limited to a maximum of 10 to 50 sensors in one fiber using wavelength division multiplexing.

4 Cables for distributed fiber optic strain sensing

4.1 Introduction

Cables in common sense are one or more wires and/or optical fibers bound together and surrounded by a protective jacket (also referred to as mantle or sheath). As the propagation of light and thus the measurements take place only in the fiber, all other layers fulfill protective functions and to allow the fibers to slip by a certain amount, as will be discussed in chapter 6. Different layers of plastic, embedded glass rovings or aramid fibers are combined according to the specific needs that depend on the anticipated mechanical load, the required resistance against chemicals (i.e. alkaline environment in concrete) and water, deformations to be measured and the available sensing system. For strain sensing, the bond between fibers, the subsequent protective layers and the surrounding material has to be adequately good. On the other hand the transmission of strain from the outside of the cable to the fiber should still allow slip to some extent in order to avoid early breaking of the fiber. This could happen in case of excessive strain or especially of a local crack, which would rapidly exceed the breaking elongation of the fiber. Figure 4-1 shows the layout of a basic fiber optic strain sensing cable. The design of special strain sensing cables however cannot be reduced to one specific layout as it depends on the temperature compensation method and specific protective and installation requirements.

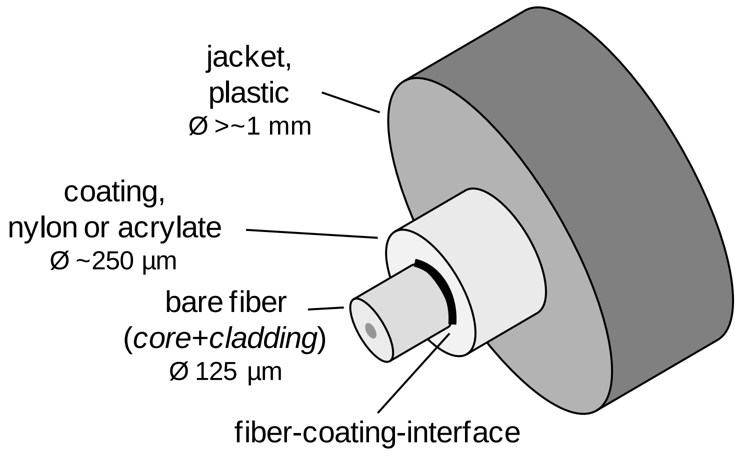

Fig. 4-1: Optical fiber cable for strain sensing with according diameters

4.2 Influence of fiber coating on strain measurements

For strain sensing purposes, the coating and the jacket around the fiber have to be in good connection to each other in order to allow the transfer of longitudinal forces from the surrounding material to be transferred into the cable and into the fiber. Referring to Fig. 4-1, the coating material is applied on the fiber during the drawing process of the fiber, to make it more rigid and workable for further processing. The coating material is usually made of resin based polymeric, silicone or acrylic materials, basically to protect the fiber from humidity and weak physical impacts. The subsequent layers in the cable strongly depend on the desired specifications.

4.2.1 Temperature influences

The effects of temperature on the Brillouin power and shift have been discussed in previous sections. Temperature however can also have a physical effect on the strain measurement from thermal stress due to the differences of the thermal expansion coefficients in the bare fiber and its coating and jacket material. Kurashima, Horiguchi et al. (1990) examined the influence of different coating materials (nylon and acrylate) on the bare fiber. The temperature dependence of the Brillouin frequency in coated single mode fibers is given by:

$$\frac{\partial \nu_B}{\partial T} = \left(\frac{\partial \nu_B}{\partial T}\right)_{\text{fiber}} + \left(\frac{\partial \nu_B}{\partial T}\right)_{\text{jacket}} \qquad \textit{Eq. 4-1}$$

ν_B Brillouin frequency shift [Hz].

The first term on the right hand side is the temperature dependence of the Brillouin frequency shift for the bare fiber. The second term specifies the Brillouin frequency shift change caused by the thermal strain in the coated fiber and is given by:

$$\left(\frac{\partial \nu_B}{\partial T}\right)_{\text{jacket}} = \left(\frac{\partial \nu_B}{\partial \varepsilon}\right)_{\text{fiber}} + \left(\frac{\partial \varepsilon}{\partial T}\right)_{\text{jacket}} = C_\varepsilon + \left(\frac{\partial \varepsilon}{\partial T}\right)_{\text{jacket}} \qquad \textit{Eq. 4-2}$$

C_ε absolute strain coefficient [Hz/με].

Thermal strain is caused by the difference in the thermal expansion coefficients of the fiber and the different coating materials α_i, assuming that no sliding is present at their interface:

$$\frac{\partial \varepsilon}{\partial T} = \frac{\sum A_i E_i \alpha_i}{\sum A_i E_i} \qquad \textit{Eq. 4-3}$$

E	modulus of elasticity [MPa]
A	cross section [mm²]
i	index for each coating layer
α	thermal expansion coefficient [1/K]

Kurashima, Horiguchi et al. (1990) found out that regarding the values in Tab. 4-1, the influence of the acrylate coating on the Brillouin shift can be neglected, whereas nylon at temperatures of less than 30 °C has an effect of roughly 2 MHz/°C on the frequency shift. At temperatures above 30 °C this is roughly 1.5 MHz/°C, as nylon undergoes a phase transition and starts softening (Facchini 2001).

Tab. 4-1: Young's moduli and thermal expansion coefficients of silica and coating materials

material	E [MPa]	α [1/K]
silica	72,000	$5 \cdot 10^{-7}$
nylon	1,000	$1 \cdot 10^{-4}$
acrylate	400	$1 \cdot 10^{-4}$

A transfer of temperature induced strain from other cable layers highly depend on the design and the material of the layers of the cable. The temperature induced strain is mostly directly associated to the load transmission between the different layers.

4.2.2 Load transmission

The ability to measure strain in a fiber is depending on the quality of load transmission between the different interfaces from the matrix material to the optical fiber. The stresses that occur in an optical cable when axial stress is applied are depicted in Fig. 4-2. As the coating is applied on the fiber during its production process, the bond, described by $\tau_{c,f}$, can usually be considered as perfect. This might be different for the other interfaces that highly depend on the cable design and its production procedure. Details on the bond between coating and jackets regarding the different designs will be discussed in the next section, which is dealing with different cable designs.

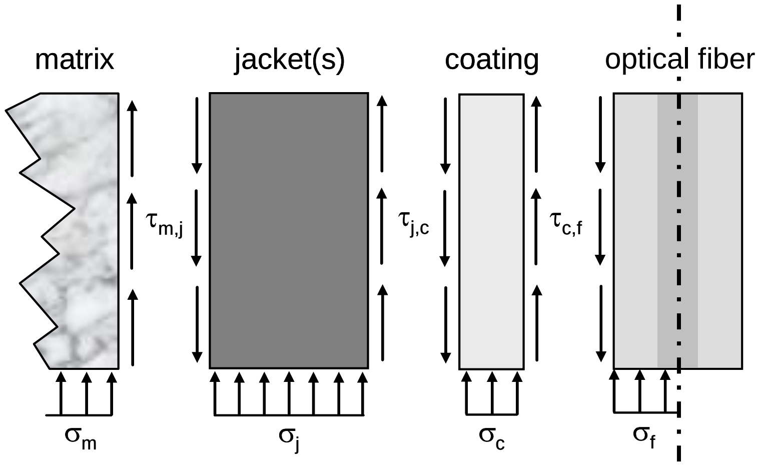

Fig. 4-2: Normal stresses and shear stresses inside an optical cable

Apart from the bonding between different layers, the transmission is also depending on the mechanical properties of the optical fiber, the protective coating, the jackets and the length of the optical fiber (Ansari and Libo 1998). A portion of the strain in the matrix material is always absorbed in the coating and the jackets as their Young's moduli are in almost all cases considerably lower than of the fiber. The relation between the axial deformation δ of the different cable layers can be described as:

$$\delta_m(x) = \delta_f(x) + \delta_c(x) + \delta_{j_i}(x) \qquad \textit{Eq. 4-4}$$

$\delta_m(x)$	axial deformation of matrix material [m]
$\delta_f(x)$	axial deformation of the optical fiber [m]
$\delta_c(x)$	shear deformation of the protective coating [m]
$\delta_{ji}(x)$	shear deformation of i protective jackets [m].

Theoretical and physical tests showed that in assumption of perfect bond, strain decaying effects occur especially in the end regions in the transition from loose cable to attached (or installed) cable (Bernini, Fraldi et al. 2006). The same can be observed in regions of quick changes of strain (Nanni, Yang et al. 1991). The best results for load transmission could be achieved when the bare fiber was directly glued onto the test specimen. This however appears not to be applicable for field applications due to the extreme fragility of bare fibers and their limited extensibility. All above mentioned research teams however stated that the effect of strain decay due to load transmission strongly depends on the overall length of the fiber. It has an effect especially in the last few mm or cm of the fiber, which is for most measuring setups beyond the spatial resolution. The tests in chapter 6 will show that slip inside the cable is actually needed in case the strained cable section is smaller than the spatial resolution of the strain sensing system.

4.3 Cable designs

Cable designs strongly depend on the boundary conditions and their specific needs, thus a basic cable design, which fits all requirements, cannot be presented. Therefore different cable designs for different monitoring requirements have been developed to fit the needs for best possible data quality. Strain sensing cables are subject to completely different requirements than standard telecommunication cables that have extensively been studied and can be used for distributed temperature sensing. The main concerns for the cable design are the protection needs, the bonding between the different layers of the cable, temperature cross-sensitivity measures and specific project-requirements. Cable designs can basically be separated into three different groups: Cables for external installation thus cables that are attached onto the structure to be measured, cables for the installation inside of concrete and cables for the installation into natural soils. Some cable designs are possible to install into multiple surrounding materials thus cannot strictly be categorized in one group.

4.3.1 Cables for external installation

Cables for external installation can be attached onto the outside of structures by simply gluing them onto the cleaned and pretreated surface. They can also be attached punctually or could be placed on a support layer, which can be attached to the host material (e.g. concrete). This last method was used by Inaudi and Glisic (2005) when a strain sensing cable was installed into the gallery of Pļaviņu HES dam in Latvia. Figure 4-3 shows the cable, which can be described as a regular adhesive tape (0.2 x 13 mm) with an embedded polyimide coated fiber (typical losses at 1550 nm = 5 dB/km). It is commercially available as SMARTape. The jacket material was chosen to be glass fiber reinforced thermoplastic with polyphenylene sulfide (PPS) matrix, which has excellent mechanical and chemical resistance properties. Due to its extremely small dimensions, this cable is very fragile but as the thermoplastic is melted directly around the fiber, the strain transmission from the outside to the fiber is supposedly very good.

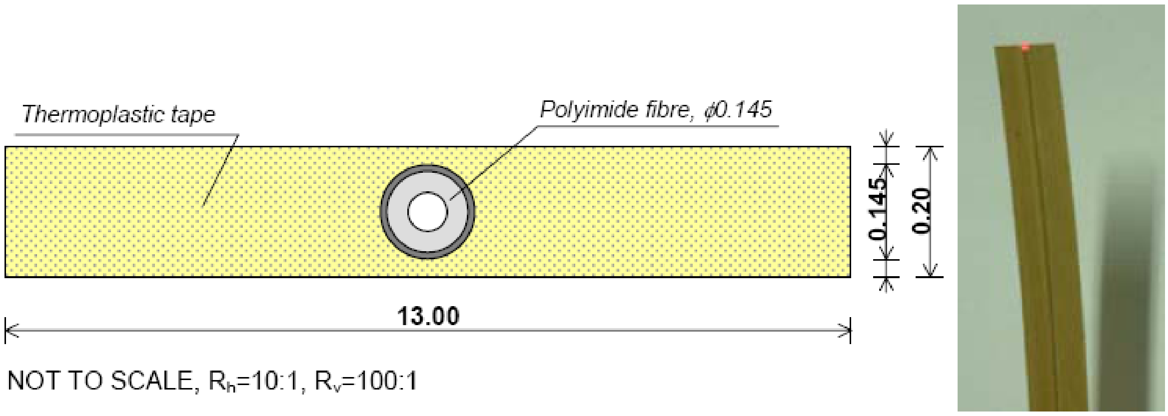

Fig. 4-3: Superelevated cross-section and photo of the SMARTape strain sensing cable. Dimensions in mm (Inaudi and Glisic 2005)

The same research team presented another cable design as depicted in Fig. 4-4, which is commercially available as SMARTprofile. In order to have redundancy and the option for separate temperature measurements for temperature compensation, multiple bonded and free single mode fibers can be embedded into the polyethylene thermoplastic profile. Depending on the individual requirements, the number of fibers can be chosen individually. The cable should not be bent in a diameter of less than 40 cm and has a loss of 2 dB/km in the strain sensing fibers. Usually it is glued or clamped onto a structure where no permanent UV radiation and high chemical impact is present.

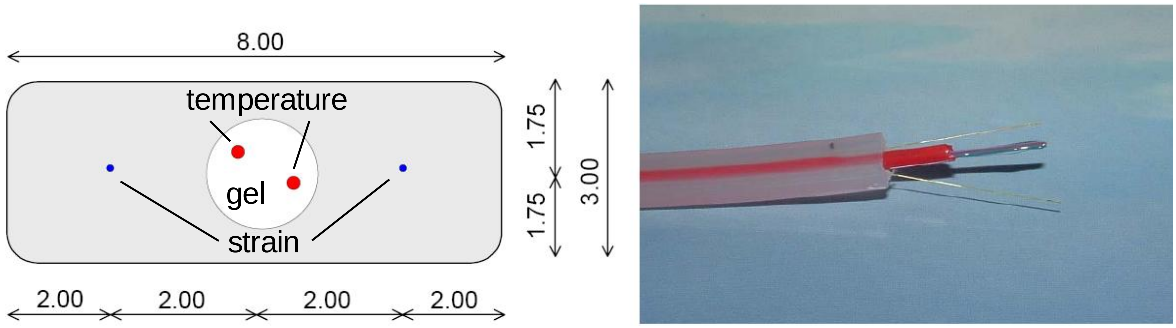

Fig. 4-4: Cross-section of the SMARTprofile strain sensing cable with temperature sensing fibers in the center. Dimensions in mm (Inaudi and Glisic 2005)

Another cable design for external installation is called smart FRP (fiber reinforced polymer). Those cables can be arbitrarily customized and manufactured according to the specific monitoring needs. Bastianini, Matta et al. (2005) presented a smart FRP with two tight and two loose single mode optical fibers embedded for redundant strain sensing and distributed thermal compensation by Brillouin sensing, which is depicted in Fig. 4-5.

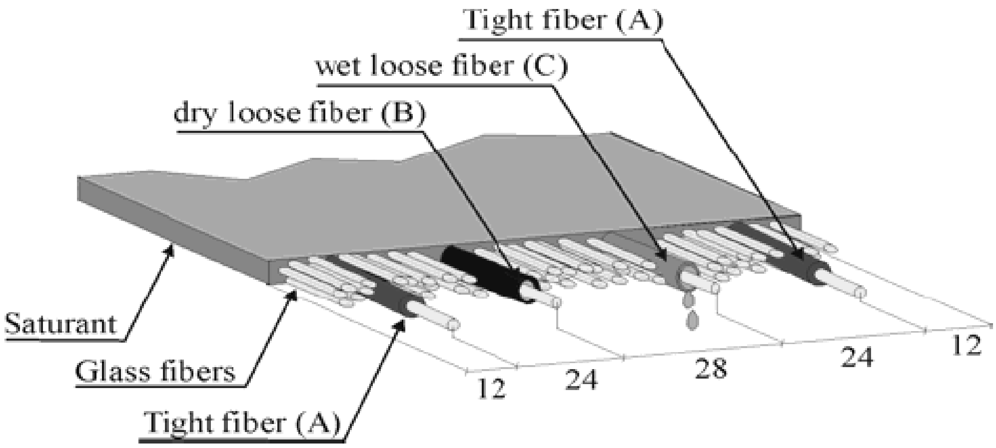

Fig. 4-5: Example of a customized smart FRP tape. Dimensions in mm (Bastianini, Matta et al. 2005)

This tape like smart FRP cable was glued onto a steel bridge with epoxy resin for strain sensing but could as well be embedded into a structure. Tests were also conducted by Bastianini, Rizzo et al. (2005) to find out the effectiveness of smart FRP tapes for crack detection when glued onto the surface of a reinforced concrete structure in comparison to coated fibers installed into few cm deep grooves that were cut into the concrete and later filled with epoxy resin. Their tests showed that the installation time and the performance were better for the surface mounted smart FRP tape. In the tests that are presented in chapter 6, the excellent bond between plastic sheathed cables and epoxy resin could be confirmed.

The advantage of cables that are specially designed for external installation lies in the easy installation on existing structures. The surfaces have to be prepared very well in order to secure a lasting bond. In case of UV exposure, special measures have to be taken concerning the cable material. It also has to be assured to protect the surface mounted cables from external mechanical forces.

4.3.2 Cables inside of concrete

In 1993, Mendez, Morse et al. reported on tests with optical fiber cables that were installed into concrete specimens. The results showed that the bond between the cable and the cement matrix as well as the bond between the different cable layers is not appropriate for the transmission of loads from the cement into the fiber. They stated that optical cables should rather be used for the communication with embedded extrinsic sensors as they are not suitable for strain sensing. Today, more than 10 years later, strain sensing cables are specially designed cables with good bonding between the optical fibers and the concrete matrix.

Especially for crack detection in concrete, the slip between fiber, cable and surrounding material is vital for the integrity of the fiber. There must be a de-bonding with strain redistribution on the fiber to both sides of the crack as the fiber would not survive a localized strain peak in case of perfect bonding (Wu, Xu et al. 2006). Cables for the installation directly into concrete have to withstand the forces from the installation and compaction processes but at the same time, the strain applied on the outside has to be transferred to the inside of the cable. In order to insure a perfect bond between cable jacket and concrete, cables with helical or slotted threads on the external surface have been developed (Bastianini, Rizzo et al. 2005). A sketch of such a fiber with an FRP layer for protection and a helical resin coating for perfect adhesion is displayed in Fig. 4-6.

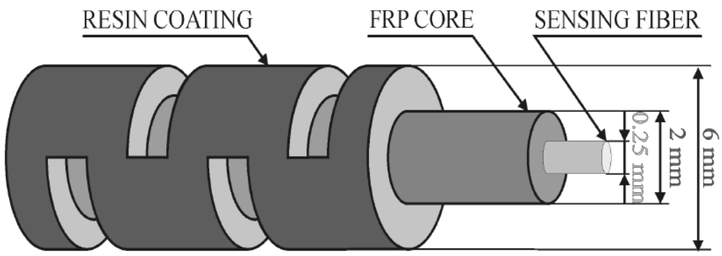

Fig. 4-6: Concrete embeddable cable (Bastianini, Rizzo et al. 2005)

The cables that were used in the field test of the present thesis have a more conventional design. They can be customized in terms of fibers that are supposed to be in the cable. As already mentioned in the previous section, the assembly of two fibers for strain sensing and two for temperature compensation has proved to be the most effective setup in terms of temperature compensation and redundancy. The cable cross section in Fig. 4-7 has all four fibers in tight contact with their surrounding. As the Raman shift of the backscattered light is not depending on strain, this design either needs a separate distributed temperature sensor for the evaluation of the Raman shift or a compensation method where separate temperature measurements are not required (Parker, Farhadiroushan et al. 1998). In that case, the assembly of two single mode fibers for strain sensing and two multi mode fibers for temperature sensing is most appropriate for standard distributed strain sensing purposes (DTS plus DTSS). Temperature sensing with a Raman based DTS is also possible in SM fibers but more robust in MM fibers.

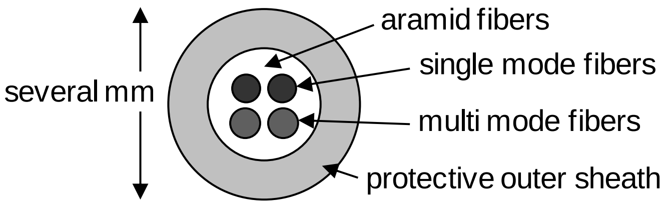

Fig. 4-7: Example of a customized strain sensing cable

For extra strength, the fibers are surrounded by aramid fibers and polyurethane to protect against the intrusion of water. The protective layers are applied under vacuum conditions for good mechanical friction bonding with the fibers (Kluth and Watley 2006), still allowing a certain amount of slip. As investigated in section 6.4, the bond between concrete and cables with a smooth plastic surface is sufficiently good and appropriate for strain sensing and crack detection inside concrete structures.

In reinforced concrete, the reinforcing steel allows attaching the cables right onto the structure with epoxy or by clamping them to the steel bars. In terms of installation this presents a mixture of the external and the internal installation method.

4.3.3 Cables in soil

Load transmission from the outside material to the fiber and the extreme mechanical forces that work on the cable in soil are the main issues for the installation of strain sensing cables in soil. Early research concerning the installation of strain sensing cables into embankment dams was undertaken by Johansson, Dahlin et al. (2000). At Sädva dam in Sweden, a temperature and a strain sensing cable next to each other were installed directly into the dam material, which was compacted afterwards. Unfortunately the sensitive strain sensing cable was damaged right at the entrance to the dam (Johansson, Parker et al. 2004). Later installations in other dams in Sweden with further developed cables comprising the basic design as depicted in Fig. 4-7, were successful. In other installations, the same research team investigated the applicability of a SMARTprofile cable (Fig. 4-4) for the evaluation of the deformation direction as the strain sensing fibers are off the longitudinal axis of the cable. The cable worked for general deformation detection with relatively high attenuation but not for the evaluation of the deformation direction (Johansson and Watley 2004). Two types of the further developed strain sensing cable were used in some of the tests that are described in the upcoming chapters.

Other research groups are currently developing geotextiles with integrated fiber optic sensors, so called “intelligent geotextiles” (Briancon, Nancey et al. 2005; Nöther, Wosniok et al. 2006; Nöther, Wosniok et al. 2007; Nöther, Wosniok et al. 2008). The goal is to have a multifunctional geotextile, which is improving earthen structures like dams and dikes and that is concurrently equipped with strain sensors to measure soil displacements (Habel 2006). Using a warp-knitting technique, the fibers are fixed to the geotextiles (Fig. 4-8). The fibers are attached in a straight line, which enables automatically manufacturing of the fiber equipped geosynthetics. As the cables, in which the fibers are embedded, have a diameter of only a few mm, they are very fragile. Consequently the cables broke during a field test installation in a dike due to the high load of the heavy construction equipment (Nöther, Wosniok et al. 2006). Research on the use of optical fibers in conjunction with geotextiles is still proceeding.

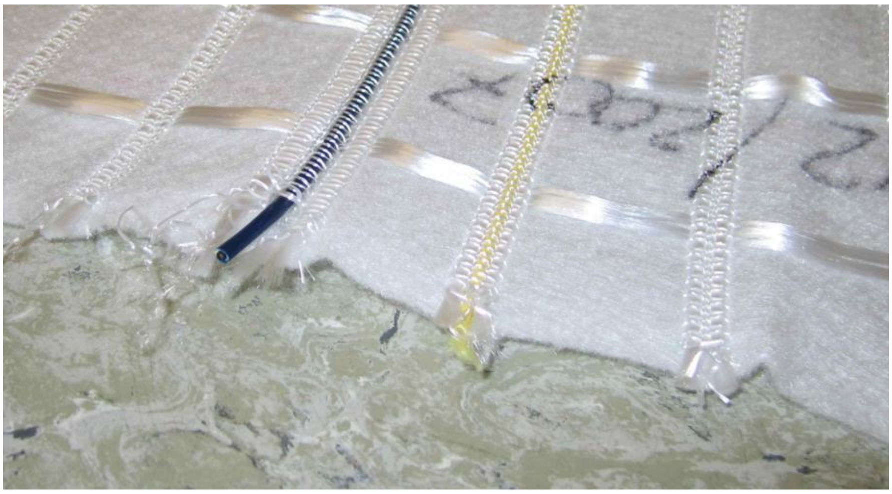

Fig. 4-8: Optical strain sensing cables (left cable by Fiberware GmbH) embedded into a non-woven geosynthetics (STFI, Technische Universität Chemnitz)

Great importance is ascribed to the installation and protection of the cables in soil. The transmission of loads into the cable is depending on the mantle friction between cable and soil. A solution to improve the transmission in case the mantle friction is too small to achieve the desired strain relief could be the fixation of the cable at multiple points along the measuring section. More on that issue will follow in chapters 9 and 10.

5 Fiber optic instrumentation for the laboratory and field tests

5.1 Temperature and strain sensing devices

The most important instrument of the tests was the Sensornet distributed temperature and strain sensor (DTSS), which was provided by Sensornet Ltd from Great Britain for the whole duration of testing. The strain sensing cables were also provided by Sensornet. The DTSS is characterized by having the opportunity of integrated temperature compensation by separately evaluating the temperature from Brillouin power (section 3.3.4). Strain sensing is carried out by evaluating spontaneous Brillouin scattering, which only requires access to one end of the fiber (single-end measurement). In case of a break, the whole fiber can still be measured from two ends if both are accessible. The spatial resolution of the DTSS is 1.021 m. A strain value that is measured is assumed to be the average strain within the spatial resolution. For post processing, the DTSS system internally carries out several calculations for more convenient data evaluation. Data files include among others the system configuration, including strain and temperature coefficients, raw measures of attenuation (OTDR), raw Brillouin frequency shift along the fiber, uncompensated strain, and temperature compensated strain data, which is the standard output value. Referring to appendix A3, the rated resolution for strain is 20 $\mu\varepsilon$ and 1 K for temperature. Some of the following tests show that the temperature evaluation from Brillouin power to compensate the Brillouin shift for temperature is not adequate for the evaluation of small amounts of strain or small cracks as the quality of strain data is significantly decreased.

When starting a measuring cycle, an OTDR measurement is followed by tuning the modulators and the laser. An important factor for the data quality is the measuring period that can be varied in the DTSS system. One measuring period describes the time that is needed to evaluate one strain distribution along the fiber. Every measuring period starts with an OTDR measurement followed by a number of sweeps over the Brillouin spectrum, which indicates the number of measurement samples or averages. The number of sweeps during one measurement period depends on the length of fiber to be measured. The influence of the measurement period on the repeatability for strain sensing at steady conditions can be seen in Fig. 5-1, where the strain in three points of an unstrained fiber section is displayed. The fiber length was hereby set to 500 m, which resulted in a maximum number of sweeps of 8, 13, 18, 24, 49 and 95 for the 6 measurement periods from Fig. 5-1.

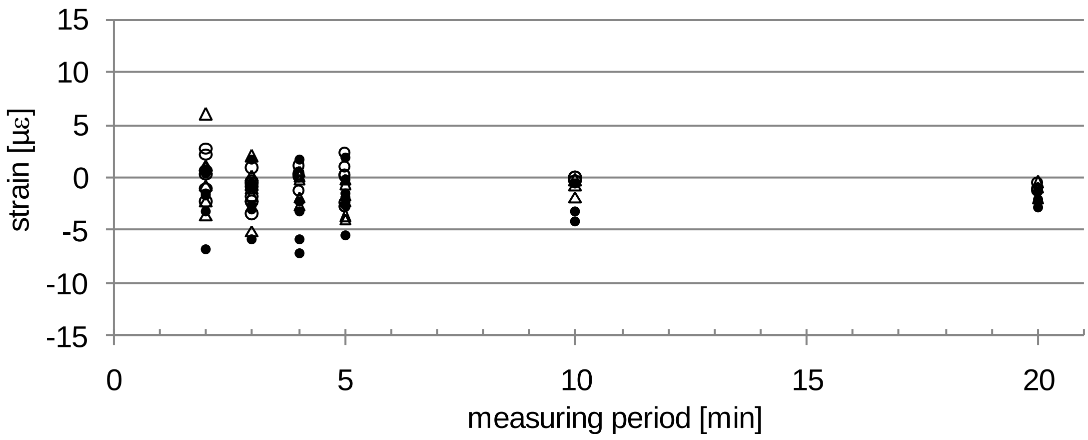

Fig. 5-1: Influence of the measuring period

In most of the following tests, the fiber section that was measured was very short so a measuring period of 2 to 4 minutes could be chosen, giving adequate data quality. In longer fibers like in the RCC dam in Brazil, the measurement period was chosen to be longer in order to have enough sweeps for adequate data quality.

A Raman based distributed temperature sensing device (DTS) can measure the temperature in an optical single mode or preferably multi mode fiber and is not influenced by strain. Connecting a DTS sensor to the same cable that is used for strain sensing allows better temperature compensation than with the internal method, which is evaluating the power of the backscattered Brillouin signal. A Sensa DTS 800 system was available to measure temperature for compensation. Its temperature accuracy is given with ± 0.1 °C.

5.2 Temperature and strain sensing cables

Three different types of strain sensing cable were used in different tests. Referring to Tab. 5-1, the most rugged cable with an outer diameter of 6 mm and a rugged, quite hard polyurethane (PU) sheath has 2 single mode (SM) and 4 multi mode (MM) fibers inside, which are surrounded by aramid fibers and an opening cord (red). The cable was assembled by applying vacuum, which leads to a good load transfer from the outside to the fibers. If pulling on the fibers manually, they can be moved by a few millimeters inside the cable. This cable was used in the borehole at the landslide and was tested inside of soil material. The setup of the second cable is similar to the first one with two SM and two MM fibers inside and an outer diameter of 5 mm. The polyurethane of the outer sheath is considerably softer, making it very easy to bend. This cable was installed into the RCC dam in Fundão, close to the surface of the landslide and was tested inside of soil material in the laboratory.

Tab. 5-1: Cables from the field and lab tests

cable	design	ultimate tensile strength	tests
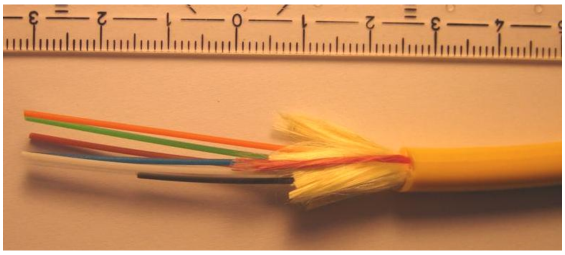	Ø 6 mm dam cable 2 SM 4 MM rugged, hard PU mantle	4.2 kN	-slip tests -soil -landslide vertical
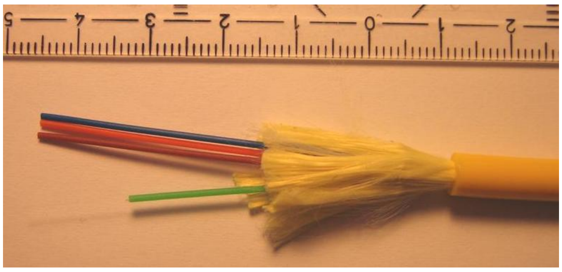	Ø 5 mm dam cable 2 SM 2 MM soft PU mantle	3.0 kN	-slip tests -RCC dam Brazil -soil -landslide surface
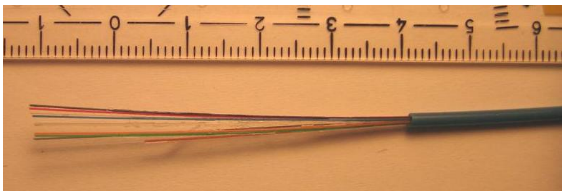	Ø 2 mm 2 SM 2 MM	0.13 kN	-lab tests in concrete
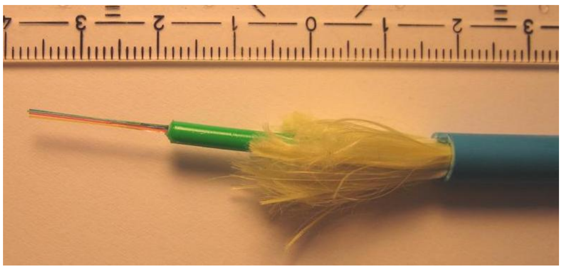	Ø 6 mm 2 SM 2 MM not suitable for strain sensing	-	-landslide extension

The third cable was installed into all concrete specimens in the laboratory of the Technische Universität München in Obernach, a beam, a column and a roller compacted concrete (RCC) block. With only 2 mm in diameter it is considerably smaller and weaker than the other strain sensing cables. It has two SM and two MM fibers inside, which are surrounded by silicone instead of aramid fibers. The load transfer from the sheath to the fibers is very good as the fibers are not significantly moving when manually pulling on them. The last cable in Tab. 5-1 cannot be used for strain sensing. Two SM and two MM fibers are embedded into an inner tube which is filled with gel to eliminate the transfer of strain into the fibers. This cable was connected to the strain sensing cable that was installed close to the surface into the landslide. A standard cable with SM fibers inside is a low priced alternative to extend the sensing cable into remote areas. The ultimate tensile strength of the cables was estimated by clamping them into a strain rig and pulling until failure (section 6.1).

Before measuring a cable, a connector should be spliced to the end of the measured fiber to reduce additional Fresnel reflections at its end. Alternatively tying multiple knots into the fiber at the end also eliminates Fresnel reflections at the interface to the air.

5.3 Calibration

The strain and temperature dependence of Brillouin shift at ambient temperature has a linear relationship. Every cable has its own optical characteristics regarding dopant concentration, core size and cable structure. For that reason, the exact boundary conditions for temperature and strain to affect a particular fiber need to be calibrated. The strain coefficient C_ε is experimentally evaluated by using the linear relationship from Eq. 3-7 and Eq. 3-9 for temperature.

$$C_\varepsilon = \frac{\partial \nu_B}{\partial \varepsilon} \qquad \textit{Eq. 3-7}$$

To evaluate the strain coefficient, a 10 m piece of strain sensing cable is clamped into a strain rig and strained by moving the fixation points apart (Johansson and Watley 2004). The cables that were used in the experiments were pre-calibrated at the strain rig and in the temperature chamber of Sensornet. The coefficients for the two dam cables are the same. Their calibration curve for strain is depicted in Fig. 5-2. It shows the linear relationship between the applied strain and the according Brillouin shift.

The temperature coefficient C_T is evaluated by using the same linear relationship. Around 30 m of cable is therefore placed into an environmental test chamber where the temperature is then varied from -10 to 40 °C in steps of 5 °C.

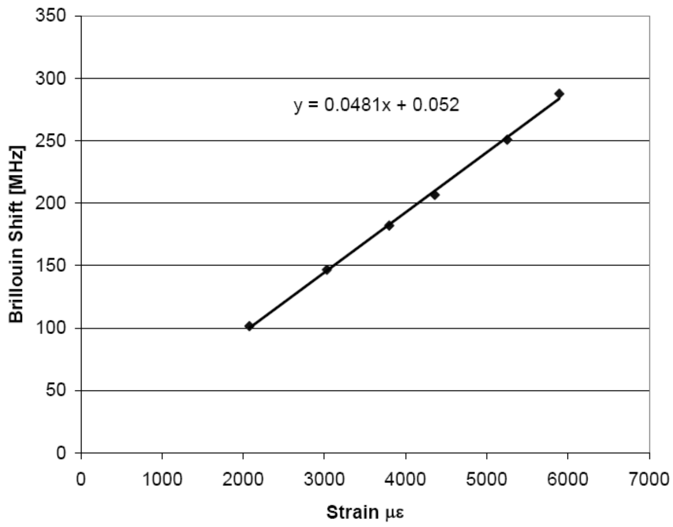

Fig. 5-2: Calibration of the Sensornet dam cables for strain (Johansson and Watley 2004)

The calibration coefficients for temperature and strain and the dependence of power versus strain and temperature, which are needed for the automatic temperature compensation of the DTSS, are listed in Tab. 5-2. The four coefficients can be assumed to be constant along the fiber and are fed into the DTSS configuration file prior to measuring. That way the strain and temperature can automatically be calculated.

Tab. 5-2: Calibration coefficients for the Sensornet dam cables

coefficient	description	measured value
$C_{\nu\varepsilon}$	change in Brillouin frequency versus strain	0.0481 MHz/με
$C_{\nu T}$	change in Brillouin frequency versus temperature	2.488 MHz/°C
$C_{P\varepsilon}$	change in Brillouin power versus strain	$-14.0 \cdot 10^{-4}$ %/με
C_{PT}	change in Brillouin power versus temperature	0.417 %/K

The calibration coefficients for the 2 mm cable that was used in the laboratory tests on the concrete specimens are listed in Tab. 5-3. It shows a significant lower dependence on temperature referring to Brillouin frequency.

Tab. 5-3: Calibration coefficients for the 2 mm strain sensing cable that was used in the tests on the concrete specimens

coefficient	description	measured value
$C_{\nu\varepsilon}$	change in Brillouin frequency versus strain	0.043 MHz/µε
$C_{\nu T}$	change in Brillouin frequency versus temperature	1.063 MHz/°C
$C_{P\varepsilon}$	change in Brillouin power versus strain	$-0.8 \cdot 10^{-4}$ %/µε
C_{PT}	change in Brillouin power versus temperature	0.295 %/K

The strain and temperature coefficients are used for the evaluation of temperature and strain changes from the Brillouin shift but are not suitable to calibrate for zero-strain. This is mostly depending on the coating (buffer) of the fiber. Therefore, the DTSS is equipped with three internal reference coils with different types of fiber. As shown in Fig. 5-3, a piece of 950 m loose fiber is followed by 50 m of bare (250 µm) and 50 m of buffered fiber (900 µm) that are both inside of an internal reference oven. A PT100 platinum resistor for temperature sensing is located inside the oven to be able to calibrate the measurements for zero-strain. Depending on the cable type, either the buffered or the bare fiber section can be chosen for calibration.

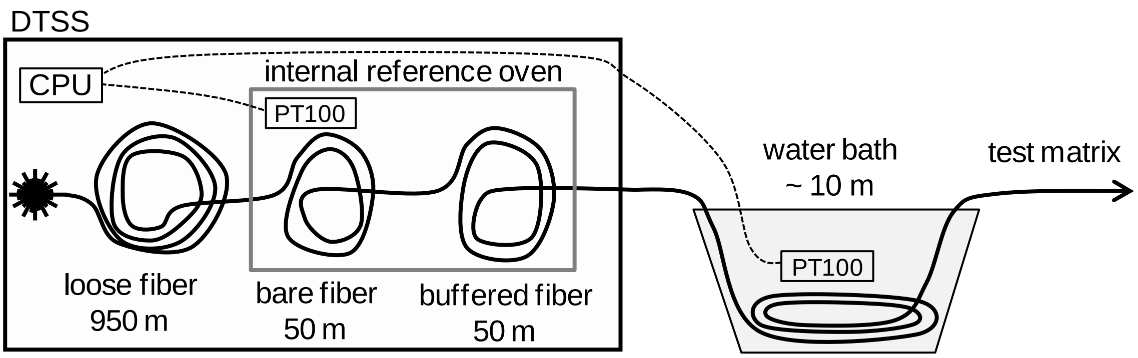

Fig. 5-3: Setup for internal or external zero-strain calibration

For a more accurate calibration of the specific fiber, some meters of the strain sensing cable should be placed into a water bath. An external PT100 measures the temperature of the water. In that case, the cable part that is inside of the water bath has to be chosen as reference section. To assure good calibration quality, the cable inside of the water bath should be at least 10 m long. The external reference section could either be in the first part of the cable as depicted in Fig. 5-3 or in any other section along the fiber, where the temperature is both constant and known or can be measured with the external PT100.

5.4 Fiber Bragg grating sensors

For the purpose of comparability, fiber Bragg grating (FBG) strain sensors were installed next to the strain sensing cables in all three structures at crucial points. They were provided by FiberSensing, Portugal. FBG sensors can be designed for single point temperature or strain sensing. The functionality of FBG sensors is outlined in section 3.5. Figure 3-20 shows two FBG strain sensors that are about to be installed into concrete. The 20 cm long bar between the two discs on each end of the sensor represents the measurable distance. Even though the strain can only be evaluated locally, the accuracy of fiber Bragg sensors is up to 1 με.

6 Laboratory tests on crack width evaluation, system accuracy and slip between fibers, cable and concrete

6.1 Test setup

The tests that are presented in this chapter are needed to validate the accuracy of distributed strain measurements for crack width evaluation. The goal is also to receive information on the influence of the length of the strained fiber section on strain resolution. As sketched in Fig. 6-1, this will reveal if a local crack is detectable, even if the fiber is only strained very locally which would happen around a local crack in case of tight bond between fiber and cable mantle. The tests have been carried out on two different dam cables that were introduced in section 5.2. The strained fiber section inside a cable includes the slip between the surrounding material and the cable, the slip within the cable and the influence of mantle deformation. The slip between fibers and cable is very depending on the cable design and setup. To evaluate the influence of slip inside the cable and the mantle material in a second test, one end of each strained cable is embedded into epoxy resin, which guarantees perfect bond to the cable mantle. Exemplarily, the two dam cables are compared. Some previous tests on crack detection using buffered fibers without cable protection were published by Wu, Xu et al. (2006).

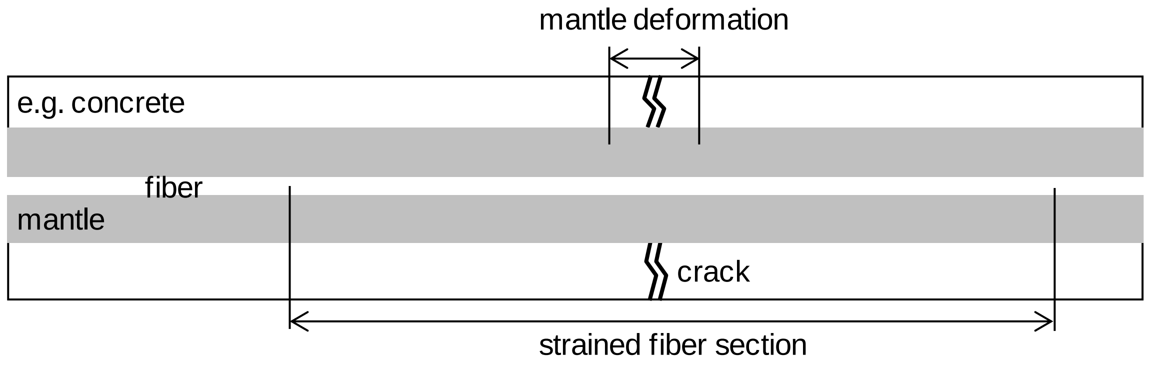

Fig. 6-1: Basic thoughts

The strain rig that is depicted in Fig. 6-2 is used to evaluate the accuracy and limits of the DTSS system. The base of the strain rig is a 4 m long aluminum beam with guiding tracks on its side. As the fixed clamp in the end of the rig can be detached and fixed at another distance along the construction, the strained fiber section can be adjusted between 50 and 345 cm.

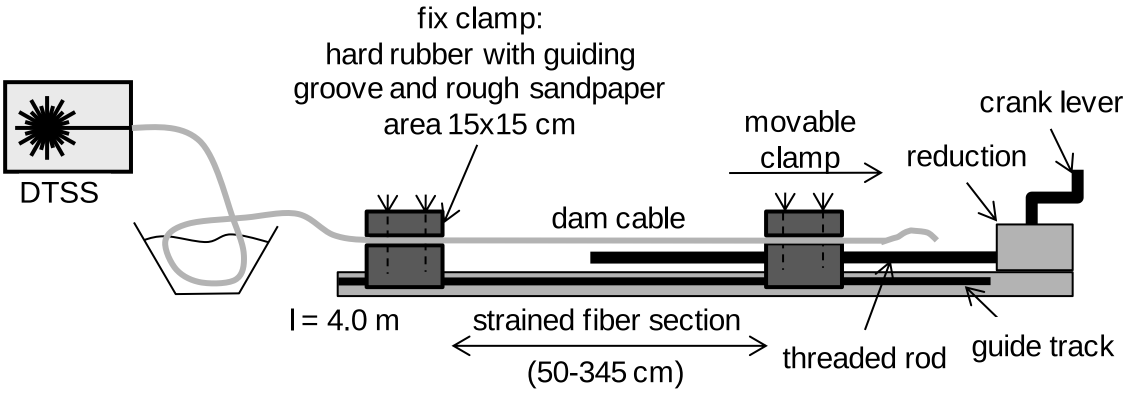

Fig. 6-2: Setup for fundamental deformation and slip tests

The deformation can be adjusted by turning a crank lever which is connected to a reduction gear that reduces the movement of the movable clamp by 10:1. A distance laser, which has a resolution of ± 0.01 mm is used to control the movement of the movable clamp (Fig. 6-3). One end of the cable is connected to the DTSS. Roughly 10 m of the cable are placed into a water bath for zero-strain calibration. At least 5 meters of the cable are left loose after the straining rig to avoid reflections from the end of the fiber to the measuring section. To reduce additional Fresnel reflections in the end of the fiber at the interface to the air, multiple knots were tied into the fiber.

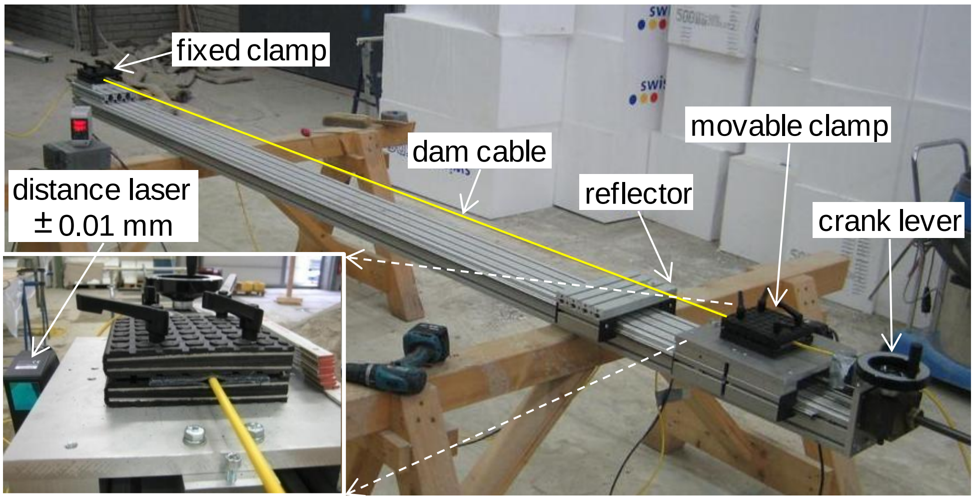

Fig. 6-3: Photo of the strain rig

Figure 6-4 illustrates the difference between the two above mentioned tests. The first test does not allow slip within the cable. The second test on deformation evaluation in respect to the slip between the cable and the mantle material allows slip inside the cable at one side of the strained cable section. The movable clamp is therefore replaced by a metal tube where the cable is guided through.

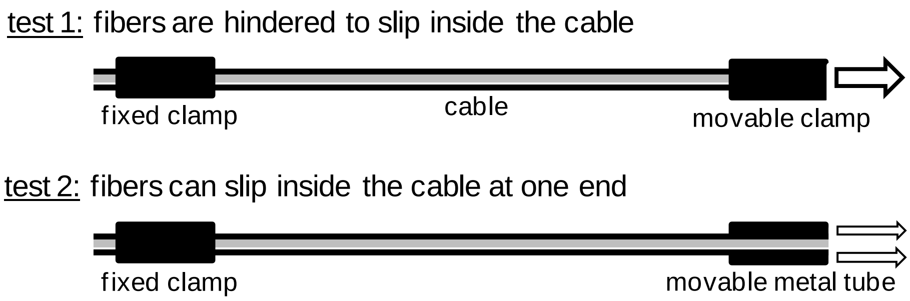

Fig. 6-4: Difference between test 1 (section 6.2) and test 2 (section 6.3)

The tube is filled with epoxy resin to simulate perfect bond to the surrounding material (Fig. 6-5). By cutting through the tube after testing the cable, it could be noted that only 3 cm of the cable on the strain side was detached from the epoxy resin. Perfect bond within the 18 cm long tube could consequently be confirmed. No pressure is applied on the cable during testing which allows the fibers to slip inside the cables.

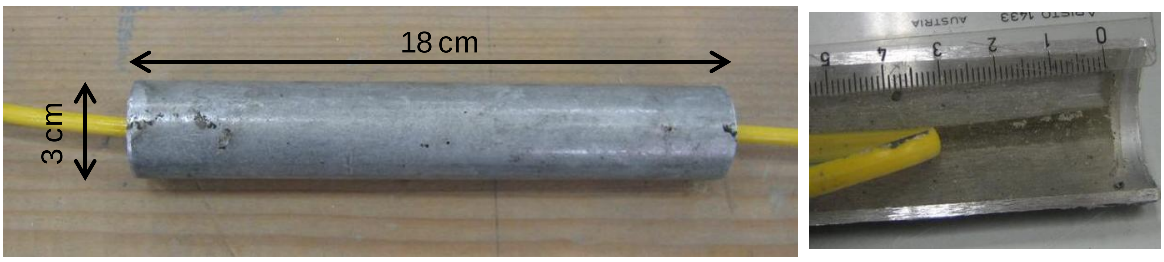

Fig. 6-5: Cable ingrained in epoxy resin in metal tube and longitudinal cross section after testing

The measuring time of the DTSS was set to 2 minutes for all measurements. Strain data is not temperature compensated for the sake of resolution as temperature changes in the laboratory were negligible.

6.2 Influence of the strained fiber length on the evaluation of deformation

As the strained fiber length is only marginally depending on the cable type, only the 6 mm dam cable was tested in the strain rig. The strained fiber length thus the spacing between the two clamps was varied in three steps (spacings): 345, 200, 100 and 50 cm. The cable was slightly pre-strained, which represents the reference measurement for the following tests. By doing so, the minimal detectable strain for each of the four spacings can be evaluated. Figure 6-6 shows the strain in the clamped cable part at a spacing of 2 m before (start) and after (end) testing.

The dashed lines represent the strain in the cable that is clamped into the straining rig without applying strain. Residual strain in the cable leads to the non-zero strain distribution. Solid lines represent the pre-strained state of the cable. While the reference strain, thus no dislocation between the two clamps before and after testing is identical, the strain in the loose cable is up to more than 100 µε higher. This is a result of plastic deformation of the cable. To minimize the influence of plastic deformation, the tests started at the largest spacing of 3.45 m. The movable clamp was displaced in increasing steps between 0.1 and 0.5 mm from 0 to a maximum of 3.0 mm for each spacing. As a consequence, the strain at e.g. 2 mm displacement is four times larger for 0.5 m spacing than for 2 m. The pre-tension for all tests was around 3,000 µε.

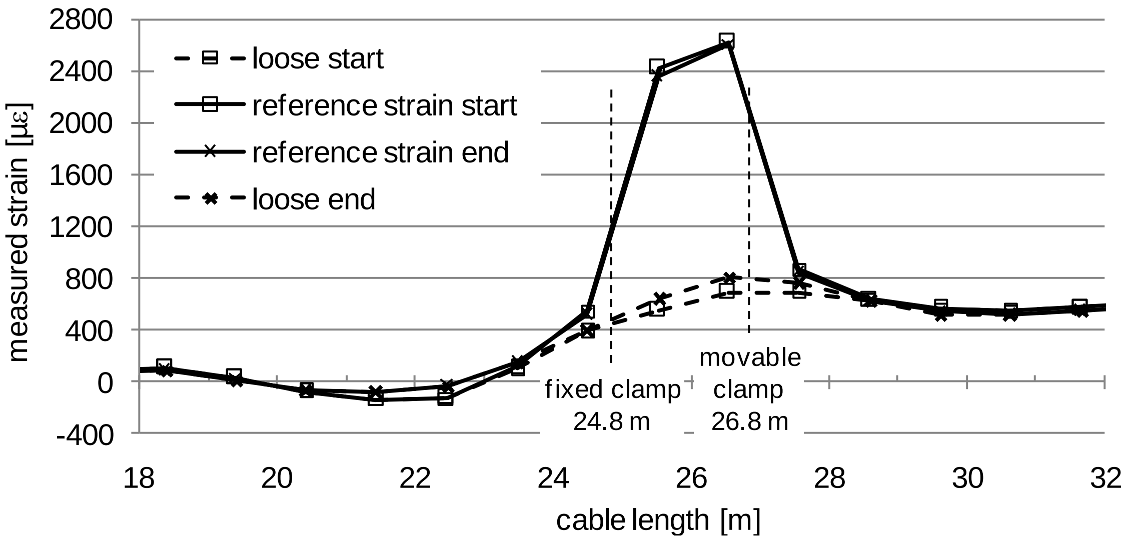

Fig. 6-6: Strain measurements before and after clamping and testing at 2 m spacing

Strain measurements at a deformation of 0.8 mm for each spacing are shown in Fig. 6-7. The fixed clamp is located at 24.8 m from the DTSS thus between the DTSS measuring point at 24.5 and 25.5 m. The movable clamp is located the according distance further along the cable. The reference measurement is already subtracted from the data, leading to zero strain in the un-strained fiber part. From a first sight it is remarkable that the strain at 1.0 m spacing involves 2 peaks that both overtop the other values by far. At 0.5 m spacing, which is below the spatial resolution of the DTSS of 1.02 m, the strain even shows negative values.

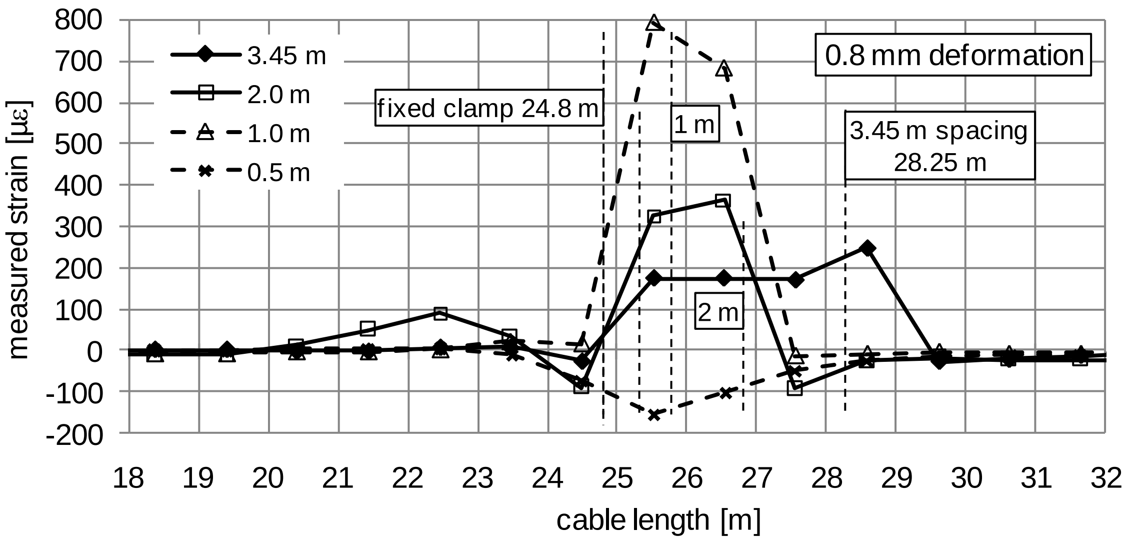

Fig. 6-7: Measurements at 0.8mm deformation at different spacings

At least three DTSS strain measurements of 2 minutes each were taken at every strain step. Figure 6-8 shows the strain that was mechanically applied by moving the movable clamp, controlled by the distance laser versus the strain that was measured by the DTSS at 3.45 m spacing between the clamps. The spacing affects 4 measuring points (25.5 to 28.6 m) at all amounts of applied strain. As also visible in the strain distribution in Fig. 6-8, the measurement at 28.6 m is higher throughout all strain steps.

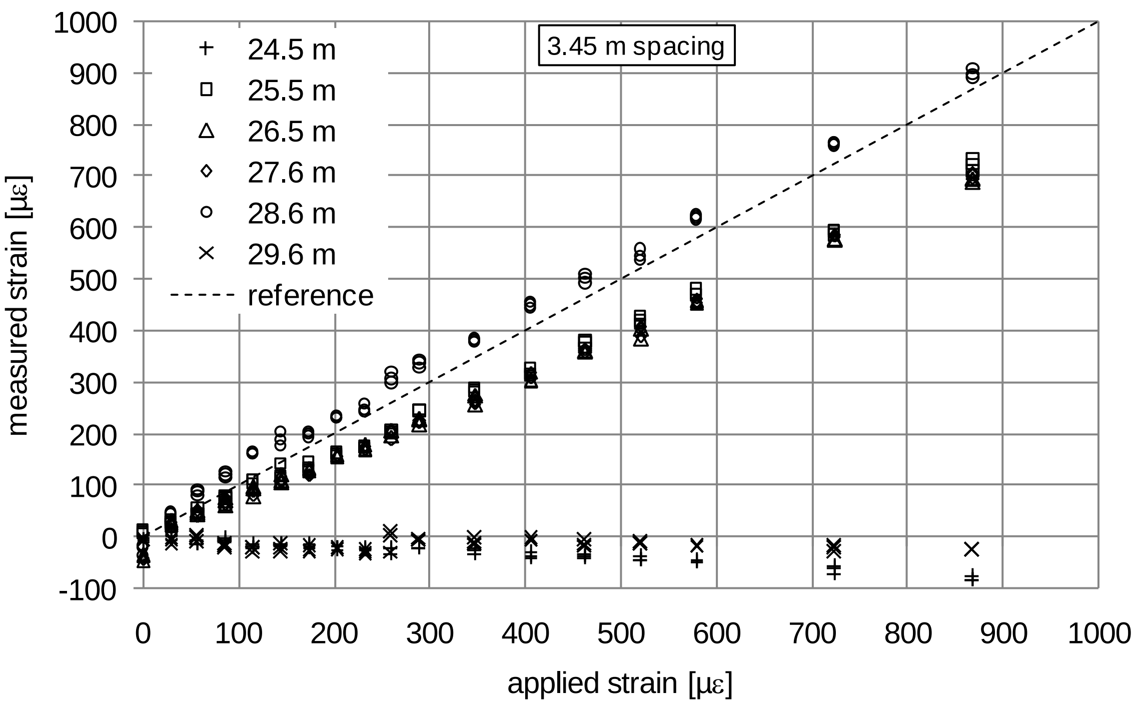

Fig. 6-8: Strain in the pulled section of the cable at 3.45 m spacing

Taking the average strain value of the affected DTSS measuring points at each spacing (except 0.5 m as no strain could be detected) without considering the distance, and graph them against the mechanically applied strain, the relationship from Fig. 6-9 appears. It is obvious for all spacings that the measured strain becomes underestimated with rising strain. At 2.0 m spacing, the pre-strain was some 100 με below the reference strain of 1 and 3.45 m spacing, which leads to the slight up-shift of the 2.0 m values compared to the rest. To receive further information on the amount of strain, at which the measured values start to deviate from the applied amounts of strain, additional measurements that start at reference values close to zero would be necessary. Additional tests showed that the reason for the underestimation of strain cannot be found in the measuring device or in the evaluation of the strain coefficient but rather in the small amount of creep at the clamps that could be observed.

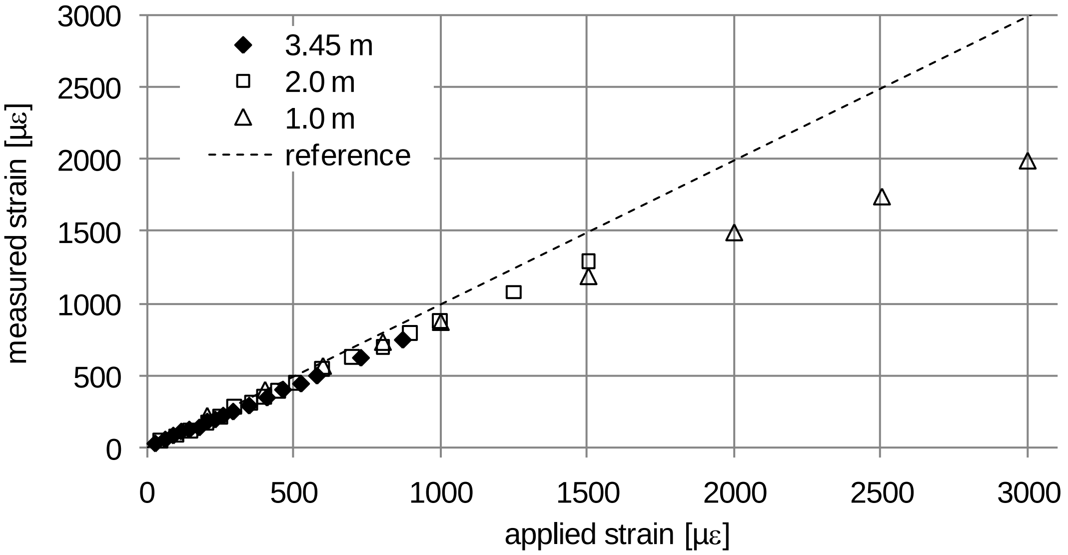

Fig. 6-9: Measured average strain versus mechanically applied strain for all spacings

A method to estimate the amount of deformation of the fiber, which is equal to the crack width in later tests, is introduced in Fig. 6-10 at the example of 0.8 mm deformation at 3.45 m spacing. It is assumed that the strain that is measured represents the average strain within the spatial resolution of the DTSS of 1.02 m. The deformation is then equal to the integral of the strain over the cable length in the affected fiber section (every affected ε-value x 1.02 m). It is important to emphasize at this point, that the distance between each measuring point is depending on the spatial resolution of the strain sensing system (1.02 m in case of the DTSS) and is not automatically equal to 1.00 m. This difference always has to be taken into consideration.

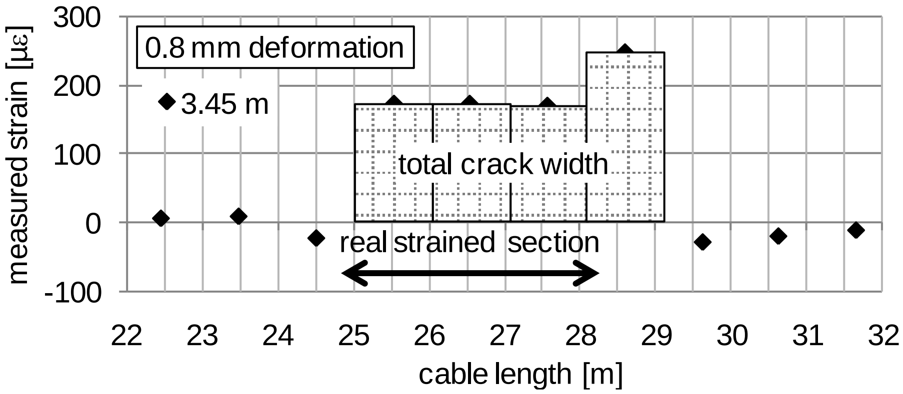

Fig. 6-10: Evaluation of deformation

The applicability of this method for affected fiber lengths that exceed the spatial resolution of the system setup is displayed in Figures 6-11 and 6-12. The applied deformation by moving the movable clamp is in very good accordance with the measured (and integrated) deformation. At the largest spacing that accordance does not deviate from the real value by more than 0.08 mm at a deformation of 3 mm. The deformation at 2.0 m spacing is underestimated with increasing strain to up to 0.4 mm at 3 mm deformation (equal to 1,500 με). At 1.0 m spacing, which is equal to the spatial resolution of the DTSS, the strain values and consequently the deformation is vastly overestimated.

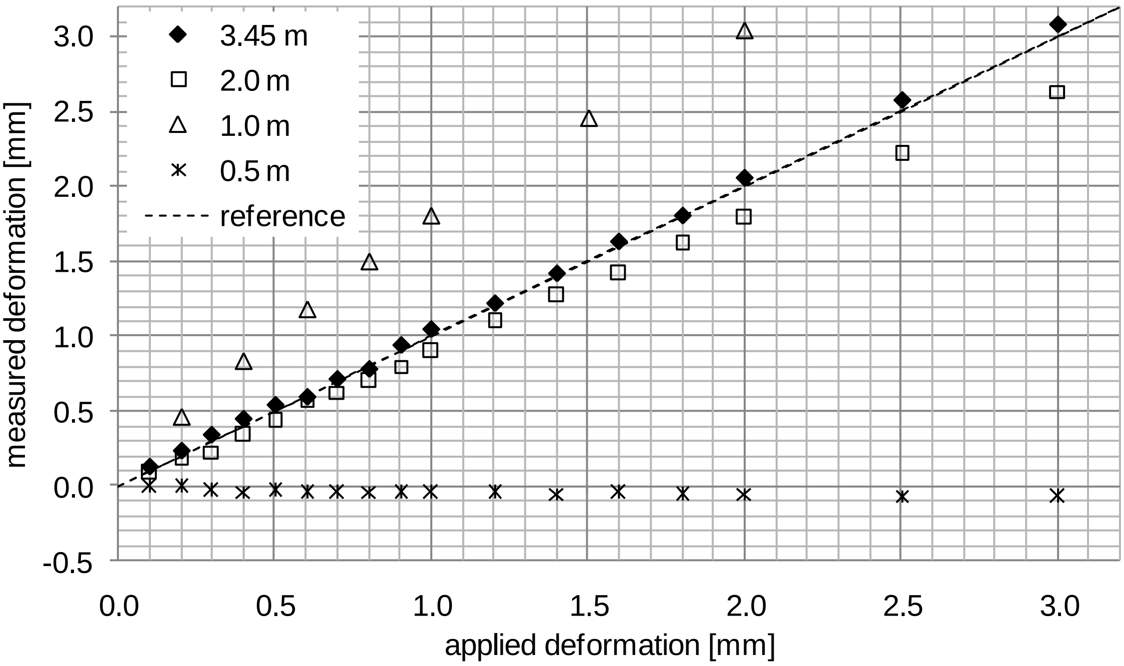

Fig. 6-11: Integrated from strain measurements versus conventionally measured deformation

As noted before, no strain could be measured at 0.5 m spacing. As this was observed in all tests, it can be noted, that strain that is locally applied onto an optical fiber in the DTSS setup is only detectable if the affected fiber length increases a certain length.

The magnification of the same relationship in the region of up to 1.0 mm is shown in Fig. 6-12. Again both, the strain measurements at the maximum spacing and at 2.0 m spacing show very good agreement with the applied deformation. Here the maximum deviation of the measured values at 3.45 m spacing is 0.03 mm thus only 3 % of the actually applied deformation. For future tests, the clamping mechanism should be improved to avoid slip and creep at increasing strain levels.

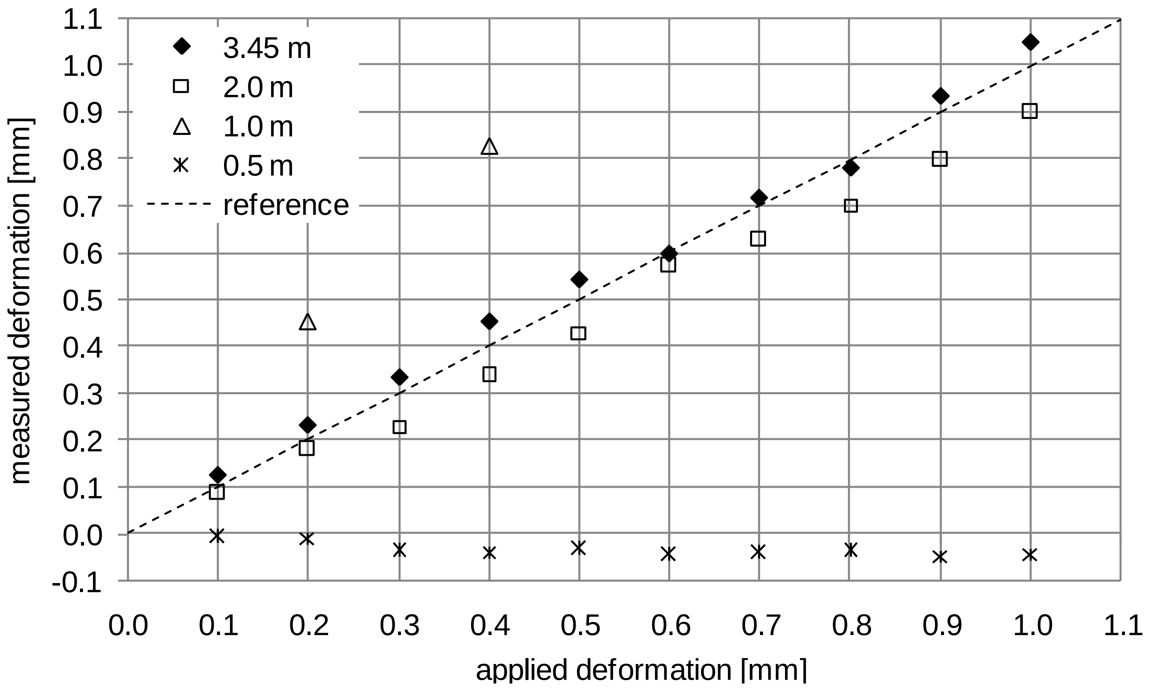

Fig. 6-12: Measured deformation versus conventionally measured deformation below 1.1 mm

As the above mentioned method for the evaluation of the amount of deformation (or crack width) showed to be very accurate for spacings that are larger than the spatial resolution of the strain sensing system, this method will also be used for the evaluation of crack widths in later tests on concrete specimens.

6.3 Influence of slip inside the cable on the evaluation of deformation

To evaluate the influence of slip inside the cable, both dam cables that were introduced in section 5.2 were installed into a tube filled with epoxy resin and were then fixed onto the strain rig, replacing the movable clamp. One side of the cable was again tightly fixed with a clamp, allowing the fiber inside the cable only to slip at the glued end where no pressure was applied on the cable. The strain distribution in the rugged dam cable in shown in Fig. 6-13, in the soft dam cable in Fig. 6-14.

In the rugged cable, the strain at 0.5 and 1 m spacing shows negative values even though strain was applied. For 0.5 m spacing this confirms the findings from the fixed cable and additionally shows that strain, which is applied on a fiber at a length smaller or close to the spatial resolution of the strain sensor seems not to be suitable for reliable distributed strain sensing with the BOTDR based DTSS. The reason for the strain behind the straining rig at 3.45 m spacing in Fig. 6-13 could not assigned but is neither an effect of the straining nor affecting the measurements.

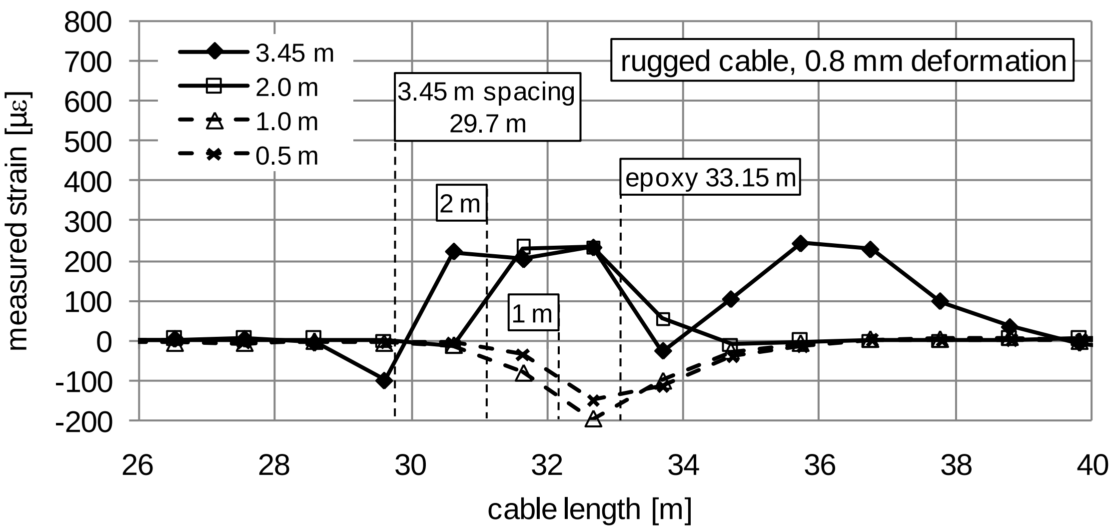

Fig. 6-13: Strain development in the affected cable part of the rugged dam cable

In Fig. 6-14, the strain in the soft cable at 0.5 m spacing stays at zero. For 1 m spacing it shows negative values. Comparing the strain distribution for both cables, the different shapes of the strain curves at equal spacings and deformations can be seen. While for example four DTSS measuring points at 3.45 m spacing in the soft cable show values around 300 µε, the same measurement in the rugged cable shows only three affected points at strain values around 200 µε.

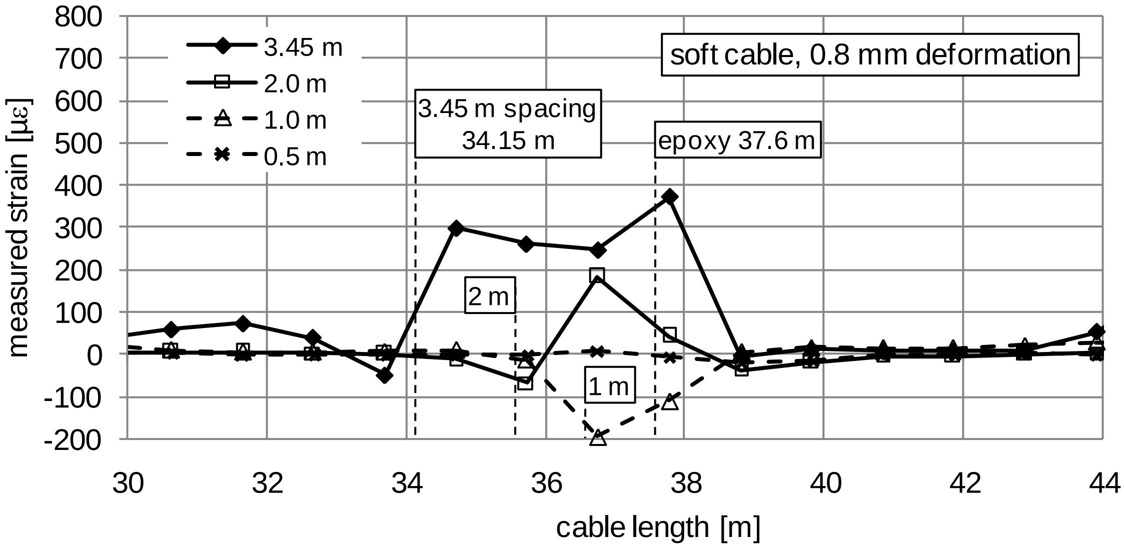

Fig. 6-14: Strain development in the affected cable part of the soft dam cable

This effect becomes visible when graphing the deformation of the rugged, the soft and the fixed cable from the previous test into one graph (Fig. 6-15). As expected, the measured deformation in the soft cable is overestimating the applied values. The rugged cable shows quite accurate measurements at low strain, deviating from the applied strain with increasing deformation while underestimating the deformation, which happens due to creep in the cable. Compressive strain outside of the straining rig could not be measured in any of the tests.

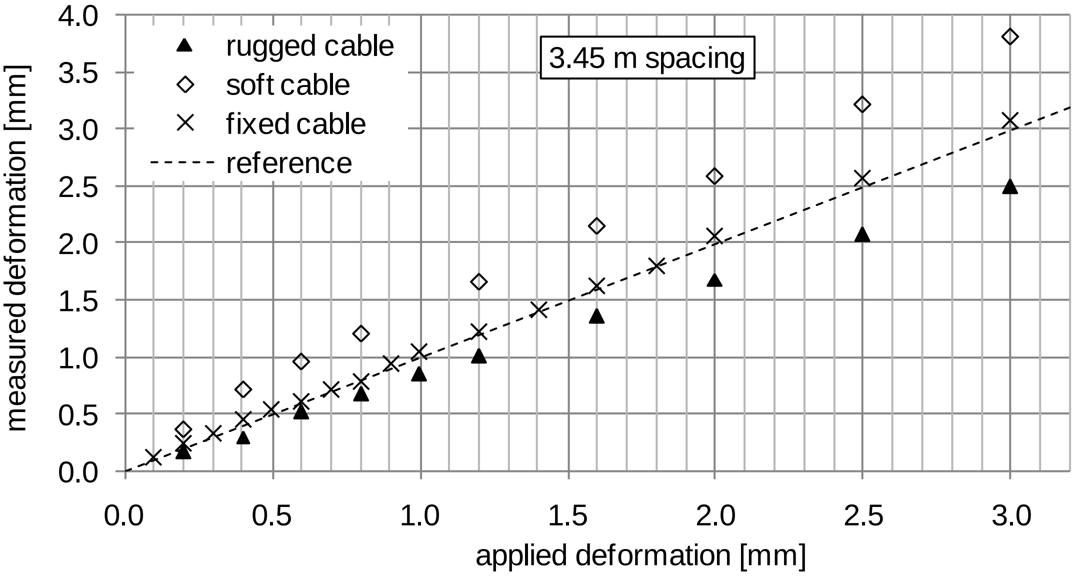

Fig. 6-15: Comparison of deformation measurements of different cables

The principal applicability of this test to evaluate the influence of slip within the cable can be seen in the evaluation of the deformation of the rugged cable (Fig. 6-16). At a spacing of 1 m, no meaningful deformation can be measured until an applied deformation of 2.0 mm. After that point, the load from the cable mantle to the fiber was redistributed along the fiber, affecting more than 1 m of the fiber. As a consequence, it is showing very accurate values for the deformation.

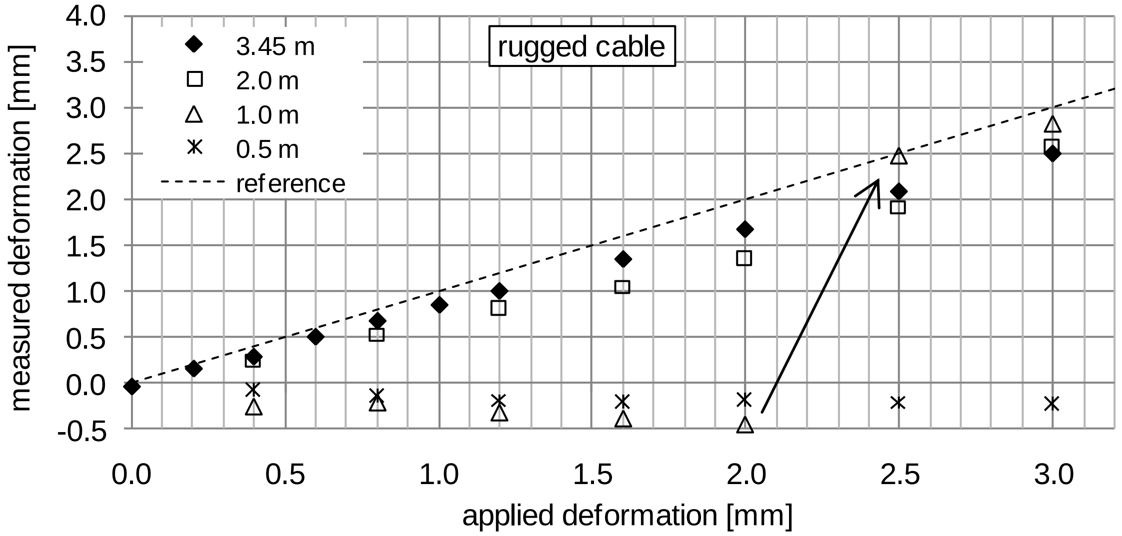

Fig. 6-16: Deformation in the rugged cable at variable spacings

Exactly the same process can be seen in Fig. 6-17, where the deformations of the soft cable are graphed. Here the load transfer starts at a deformation of 2.0 mm. And again the data goes from meaningless while close to the spatial resolution to quite accurate values after the load transfer in the cable. The strongly underestimated measurements of the cable at 2.0 m are a result of plastic deformations in the cable from previous measurements. As the 2 m section was supposed to be loaded up to the braking limit, that measurement was carried out last. Residual and ongoing compressive deformations in the soft cable from the previous tests at different spacings are therefore affecting the measurements.

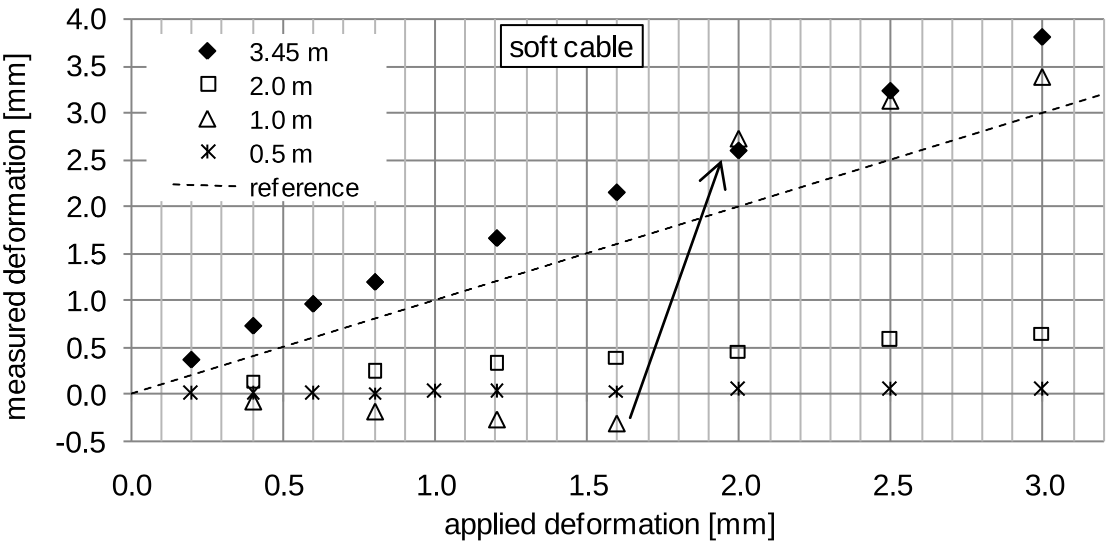

Fig. 6-17: Deformation in the soft cable at variable spacings

The influence of the cable setup on strain sensing becomes very obvious when excessively straining the cables. The lack of response of the fiber to deformation when exceeding 0.5 % (10 mm) deformation in case of the rugged cable can be seen in Fig. 6-18. The measured data follows the reference line up to 10 mm deformation. When increasing the deformation, the cable mantle compensates almost the entire deformation increase as the cable is starting to intensively deform (elastic and plastic - Fig. 6-20).

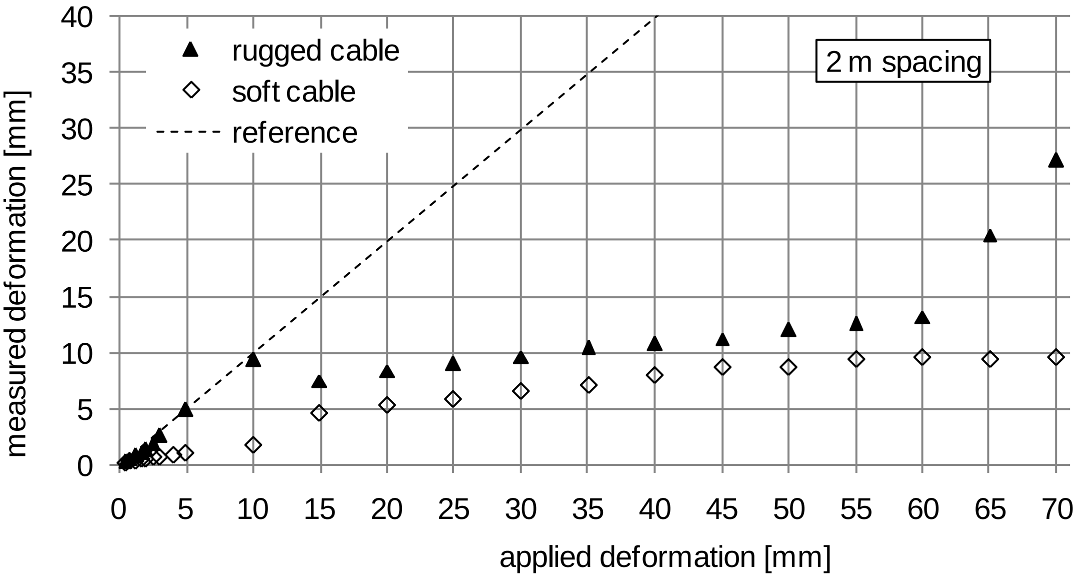

Fig. 6-18: Excessive deformation at 2 m spacing

The restarted increase in the rugged cable can again be explained when taking the strain values of the respective DTSS measuring points in Fig. 6-19 into account. As noted above, the restraint forces within the cable are exceeded in a section outside the strained part, leading to strain transfer along the cable. At an applied strain of 32,500 µε – which is equal to 65 mm deformation at 2 m spacing – the first sensing point outside the strained section at 32.7 m is showing strain. Only one load step later slipping continues so that the strained fiber part increases by another DTSS sensing point. As expected, the overall strain values of the stiffer, rugged cable are higher than for the soft one as the stronger mantle can bear a larger amount of shear stress before being plastically deformed.

Towards the end of the tests, the fibers in the cables were extensively bent within the cable (Fig. 6-20). This deformation went along with a strong increase of attenuation in the fiber. At 70 mm deformation, the fiber in the rugged cable was short before braking due to excessive bending. The mantle of the soft cable was literally stripped off the fibers at the end of the attached cable so that the losses were large but still not close to breaking. When taking the rugged cable out of the pulling rig, the fiber broke when the elastic part of the mantle deformation suddenly relaxed.

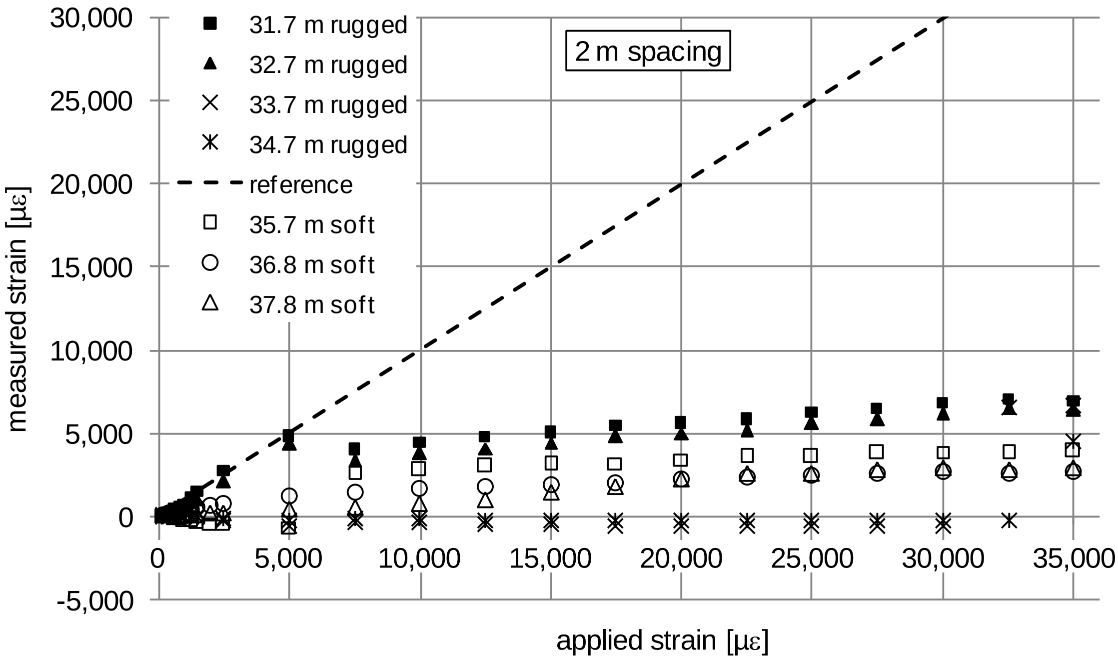

Fig. 6-19: Strain values at 2 m spacing in the soft and the rugged cable

Those tests confirm the importance and the great influence of the cable design for distributed strain measurements as slip inside a cable is mandatory for crack detection when using the DTSS. Ideally, the slip between cable and mantle should be well known before choosing a cable for a specific installation.

Fig. 6-20: Cables during the test at 2 m spacing

6.4 Slip of cables in concrete

To receive an estimation of the slip between cables with standard type round mantles and concrete, a simple test was carried out. The two dam cables that were tested in the previous setup were installed into three concrete blocks, 14 cm high, 21 cm wide and 20, 40 and 60 cm long. The concrete mix and the properties of the concrete at the time of testing (7 days after concreting) are summarized in Tab. 6-1.

Tab. 6-1: Concrete mix design and properties of specimens

cement CEM II 42.5 R [kg/m³]	aggregates [kg/m³]		water [kg/m³]	w/c-ratio [-]	unit weight [kg/m³]	compressive strength $\sigma_{cm,cyl,7d}$ [MPa]
	0/4	8/16				
270	915	1115	148.5	0.55	2410	30.0

Without actually measuring the strain in the fibers, they were pulled out of the concrete blocks while measuring the pulling force and the longitudinal deformation of the cable. The test setup is depicted in Figures 6-21 and 6-22. A sling that was tightly fixed with screw clamps was used to attach the cables to a load cell.

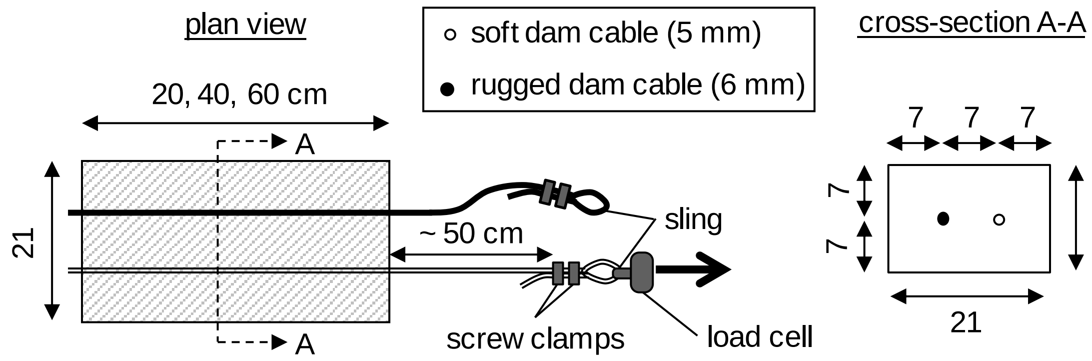

Fig. 6-21: Setup of the pullout test for slip evaluation of cables in concrete

The load was increased in steps of 100 N until the maximum value when the cables started to slip through the concrete specimen. Even though the sling fixation seemed to be very appropriate for the mechanical test of the cables, some slip of the fibers within the cable could be observed at high loads.

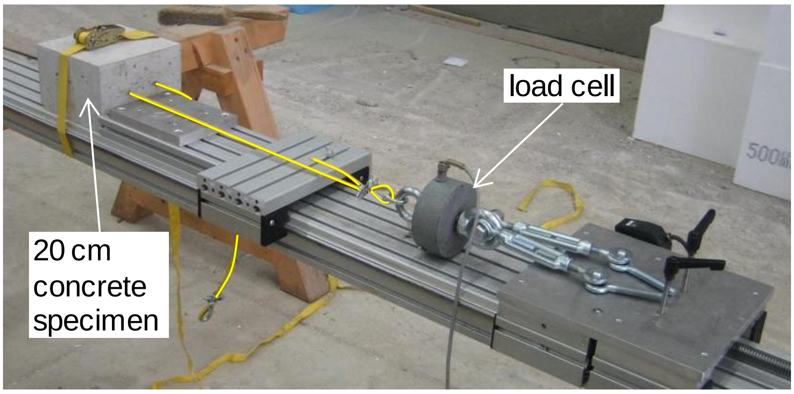

Fig. 6-22: The soft cable in the 20 cm concrete specimen during testing

As the friction between concrete and cable mantle is responsible for the load transfer, it could be expected that the 6 mm cable, which has a 20 % larger mantle surface can bear 1.2 times the load without being pulled out of the concrete. The results in Fig. 6-23 however show that the resistance of the soft cable is only around 50 % of the considerably stiffer 6 mm cable.

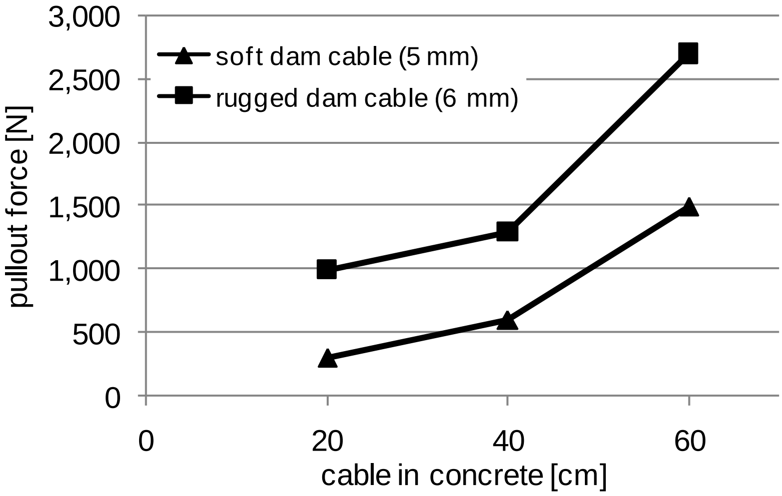

Fig. 6-23: Bond length of cable in concrete versus force until pullout

When roughly extrapolating the measuring points to the braking forces of the two dam cables of 4.2 and 3 kN respectively, the maximum embedded length, at which the cables could be pulled out of the concrete would be around 1 m for both. Taking the spatial resolution of the distributed strain measurements into account, this bond can be considered very well. Additional measures like carving the cable mantle should not be necessary when installing strain sensing cables into concrete structures.

7 Laboratory tests for strain and crack detection in concrete structures

7.1 Design an d physical properties of the concrete structures

The tests on strain and crack detection in concrete structures were carried out at the Oskar von Miller-laboratories of the Technische Universität München in Obernach, Germany in cooperation with the Brazilian research institute LACTEC, Curitiba. Basically two different concrete mixes were used for the tests. Two reinforced structures, a beam and a column were built of conventional concrete and the mixture of an RCC block that was also built was similar to mix designs as they are used for RCC dams.

The reinforced concrete beam is 10 m long, 0.4 m high and 0.3 m wide with a total weight of close to 3 tons (section 7.2). The reinforcement consists of bent steel meshes mainly for shear force reinforcement and seven 10 mm steel bars, one in each corner and additionally three in the bottom part. The concrete column is 8.6 m long, 0.3 m high and wide with a total weight of almost 2 tons (section 7.3). Four 10 mm reinforcement bars, one at each corner and bent reinforcement steel meshes were installed before concreting. Both reinforced structures were formed, constructed and equipped with strain sensors and cables while lying on the ground and transported to the testing site just before testing, at least 14 days after placing of the concrete. The concrete beam was placed onto two cushioned bearings and the concrete column was placed vertically into a precast foundation with an anchoring depth of 1.4 m. The purpose of the reinforcement steel in the skinny concrete structures on the one hand was to assure that they can bear their own weight before testing without breaking. On the other hand, the steel bars allowed a comfortable internal installation of the strain sensors and cables by clamping and/or gluing them onto the reinforcement before concreting.

The RCC block is 20 m long, 1 m wide and 1.2 m high. Since the RCC block was intended to crack due to its thermal volume change only, it was insulated with Styrofoam from all sides in order to trap the heat which is being generated during hydration. The goal was to cool the whole block down rapidly with ice water after the maximum heat had developed in order to provoke high temperature gradients and following temperature induced cracks. The concrete was placed and compacted in four layers of 30 cm each with the sensors placed on top of each layer (section 7.4). Similar to RCC as it is used in some dams, the concrete was dry and very suitable to be processed with heavy compactors. For optimum workability, the water content was regulated on site. Several concrete testing cylinders were filled and vibrated during concreting of each structure. The physical properties of the different concrete samples were evaluated in the laboratory of the department of concrete structures at the Technische Universität München and are summarized in Tab. 7-1.

Tab. 7-1: Physical properties of concrete and reinforcement steel used in the tests

component	beam and column	RCC block
character	conventional concrete	RCC
unit weight [kg/m³]	2,450	2,300**
compressive strength $\sigma_{cm,cyl,7d}$ [MPa]	-	16
compressive strength $\sigma_{cm,cyl,14d}$ [MPa]	27.0*	19.5
splitting tensile strength $\sigma_{msts,7d}$ [MPa]	-	1.5
splitting tensile strength $\sigma_{msts,14d}$ [MPa]	2.2	2.2
Young's modulus $E_{cm,7d}$ [MPa]	-	12,500
Young's modulus $E_{cm,14d}$ [MPa]	25,400	24,000
reinforcement steel:		
elastic limit f_{yk} [MPa]	500	-
Young's modulus E_s [MPa]	200,000	-
calculated strain until elastic limit:		
compressive strain $\varepsilon_{cs,14d}$ [µε]	1,060	810
tensile strain $\varepsilon_{ts,14d}$ [µε]	85	90
tensile strain steel ε_s [µε]	2,500	

* A small fraction of conventional concrete had a different compressive strength of $\sigma_{cm,cyl,14d}$ = 40 MPa but had not been taken into account.

** The low unit weight can be ascribed to the method of sampling as the probe was only slightly compacted by vibrating on a vibration table. This value represents an estimated 95 % of the minimal compaction

The ultimate elastic strain capacity for tension and compression is calculated according to Eq. 2-4. The results in micro strain are given in the lower part of Tab. 7-1. If the tensile strain in the RCC block for example exceeds 90 µε, the concrete undergoes inelastic deformation and cracks would be the result. By carrying out distributed strain measurements it should then be possible to locate regions with high tensile strain before this limit is exceeded and evaluate the position of cracks within the spatial resolution of the DTSS.

7.2 Reinforced concrete beam

7.2.1 Installation of strain sensing cables and other sensors

The focus of the installation was on the fiber optic strain sensing cable. An FBG sensor and electrical strain gauges were additionally installed to have single point reference measurements. Some considerations from other research teams that published their experiences on the installation of strain sensing cables before were taken into account. Kluth and Watley (2006) installed a very similar cable along a 35 m section of reinforcement steel cages for concrete foundation piles of a building. The cable was pre-strained by roughly 5,000 µε. Li, Parker et al. (2004) reported that the accuracy of strain measurements decreases at high strain levels above 2,500 µε tension and 1,700 µε compressional strain. However the maximum strain that could be measured was 28,300 µε for tension and 2,500 µε for compression. Both tests were made with the Sensornet DTSS using automatic internal temperature compensation. A pre-tension of 2,500 µε was applied by DeMerchant, Brown et al. (1999) in tests on a cantilever beam. The fact that actually no pre-tension is necessary as compression can directly be measured by distributed strain sensors was mentioned by Bao, DeMerchant et al. (2001) and Li, Parker et al. (2004).

The concrete beam was equipped with 40 m of strain sensing cable, which went through the beam in four loops. As depicted in Fig. 7-1, the cable sections in the upper part of the beam, which are supposed to experience longitudinal compression upon loading, were pre-strained by approximately 3,000 µε. In the lower part of the beam, the tension side, the strain sensing cable was loosely attached to the steel bars in several meter spacing with adhesive tape. To achieve uniform pre-tension in the compression side, the cable was deflected on pulley wheels at one end of the beam. After applying uniform strain, the ends of the cable were attached to the reinforcement steel with fast hardening polyester resin (Fig. 7-2). The intention of this setup was to measure strain and to locate the cracks in the tension side and see if compression (in this setup relaxation of the fiber) occurs in the compression side. The FBG sensor was installed in the middle of the beam on the bottom side, next to the strain sensing cable. Two electrical strain gauges (ESG) were attached to the reinforcement with fast hardening polyester resin in longitudinal direction. A third ESG was attached to the outside of the concrete beam just upon testing. After all sensors had been installed, the beam was concreted and left curing for 14 days.

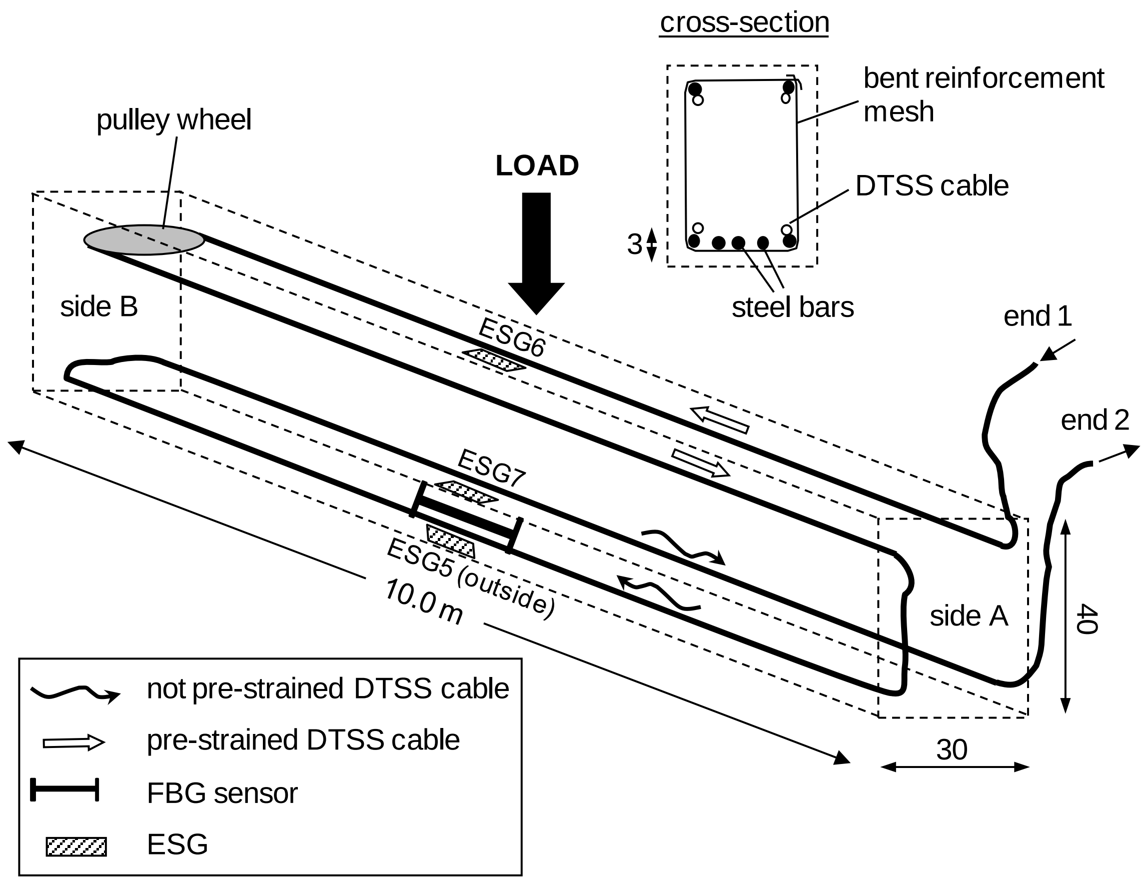

Fig. 7-1: Sensors inside of the reinforced concrete beam

A reference measurement was taken one day before the concrete was poured and the day after concreting. No significant losses could be found in the OTDR reading within the installed strain sensing cable.

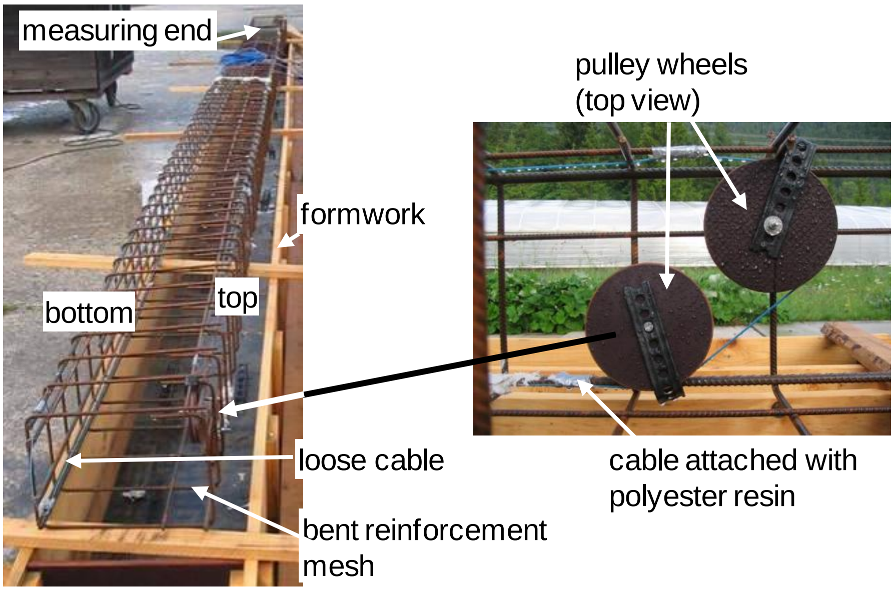

Fig. 7-2: Installation of the cables on the reinforcement steel

7.2.2 Execution of the test

The beam was placed at the test site 14 days after concreting (Fig. 7-3). It was placed on two rubber cushions on each end. A distance transducer was installed in the middle of the beam to measure the deformation under load. The DTSS was connected to “side A” where the measuring hut was located so that the two way pre-strained section of the cable is measured at first and the loose section in the tensile side of the beam as second (Fig. 7-1). An empty water tank with a filling capacity of 2.2 m³ (total maximum weight ~ 25 kN) was attached to the middle of the concrete beam. The water level and thus the weight was recorded.

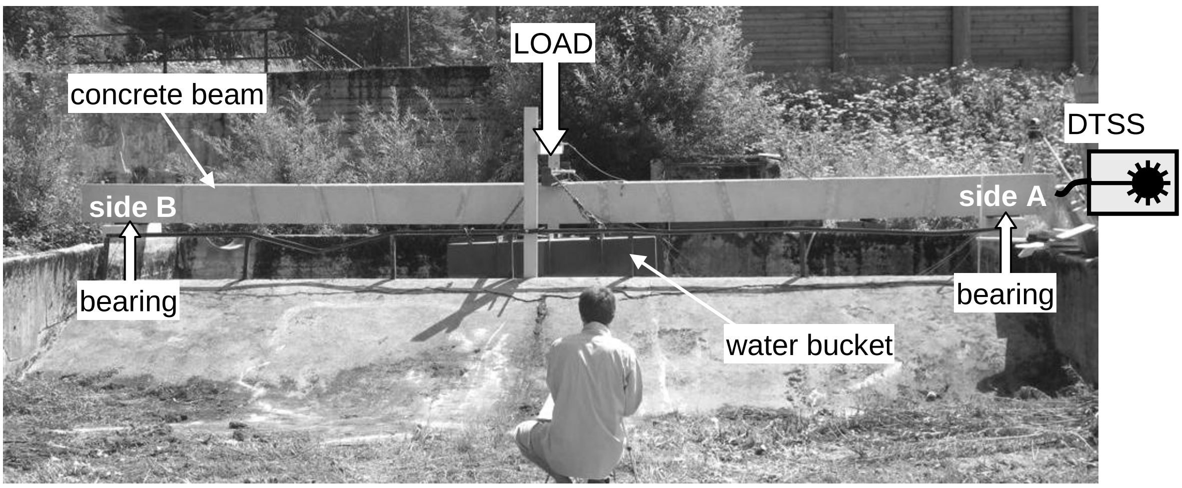

Fig. 7-3: The concrete beam during the test

Having this setup it was planned to prepare, check and start all sensing devices and then fill the water bucket slowly until failure of the beam. As the beam did not fail and some measuring instruments did not record the data, a second cycle of filling and emptying the bucked was carried out. The complete filling of the tank, thus loading of the beam took 50 minutes.

7.2.3 Strain measurements in the concrete beam

As expected, multiple small cracks could be observed throughout the middle half of the lower part of the beam. As depicted in Fig. 7-7, the spacing between the cracks was quite uniform with about 20 cm. No outstanding large cracks could be observed. The measuring period of the DTSS was set to 4 minutes, which means that the device averages multiple measurements over the selected time span of 4 minutes. As the entire test took only a few hours, the temperature compensation, which can automatically be made with the Sensornet DTSS, was not carried out for the sake of higher strain resolution. The presented data consequently reflects the Brillouin shift without distinguishing between temperature and strain. The entire shift of the Brillouin frequency is regarded as a change in strain (see chapter 3).

The strain that was measured in the strain sensing cable is shown in Fig. 7-4. As sketched in Fig. 7-1, the cable makes two loops. The situation of the cable in the sections of the beam is sketched below the graphs. The left part of Fig. 7-4 shows the pre-strained 20 m of cable in the upper part of the beam, the right side the loose, not pre-strained cable part in the lower side of the beam. Two of the displayed measurements that are represented by the dashed curves were taken as reference measurements while the beam was lying on the plain ground, before and after concreting. They show that the pre-tension in the upper part of the beam is not uniform. However the strain transfer at the pulley wheels at around 10 m shows no significant effect on the strain, proving their general functionality. After concreting, the strain distribution slightly increases except for the part around 15 m, thus in the center of the beam in the fiber that is running backward towards end “A”. Here the strain drops significantly and is not recovering. The reason can be found in the installation of the DTSS cable next to the single point sensing instruments in the center part of the beam. The fiber has probably been hindered in longitudinal movement as it might have been glued onto the reinforcement with the polyester resin that was used to attach the other instruments. Local losses due to bending can also be the reason for undefined strain patterns but in the present test those could be canceled out by an OTDR optical loss measurement, which did not show significant local losses anywhere within the beam.

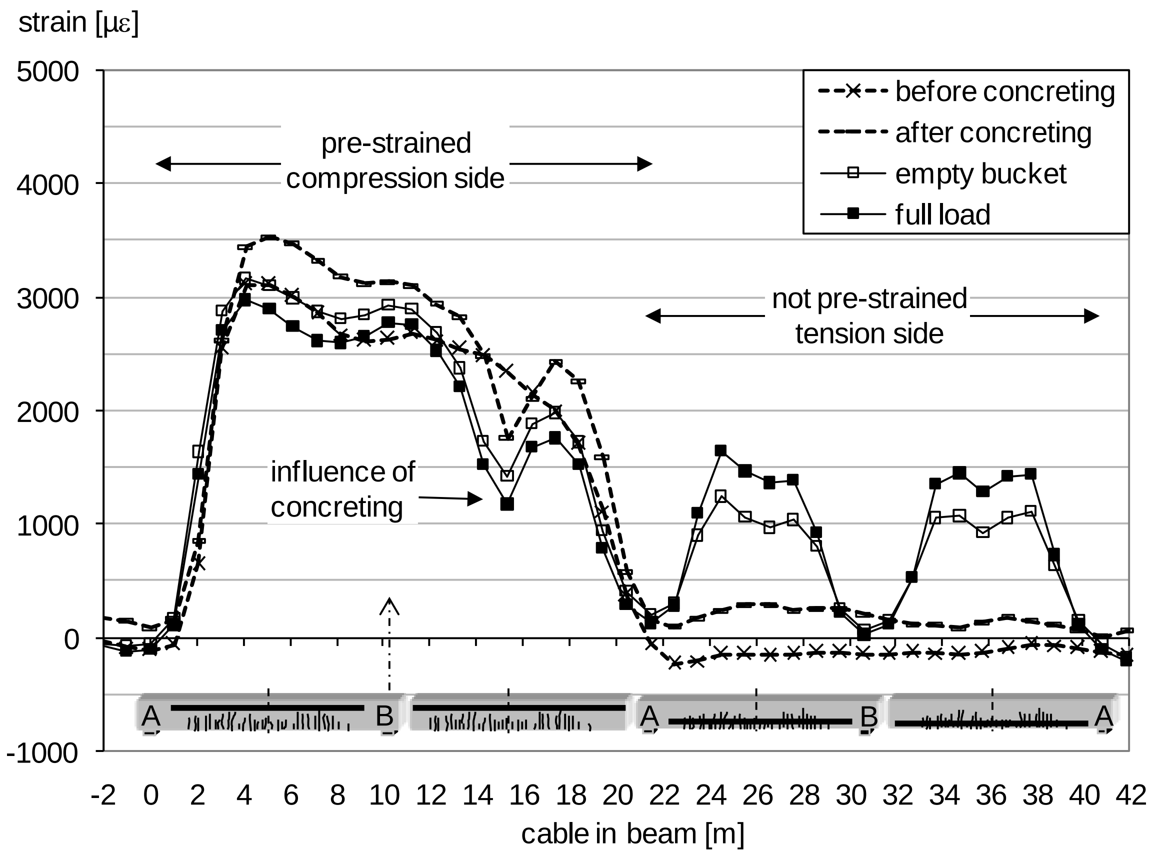

Fig. 7-4: Strain measurements before and after loading

Abrupt changes of strain at the turning points of the cable can be displayed very well despite the 1 m resolution of the DTSS and without additional measures. The second set of curves (solid lines) show the strain development before and during loading of the beam. The difference from the reference measurement results from the deformation due to self-weight of the beam. Differences before loading and at full load of 25 kN are very obvious especially in the tension side of the beam with values of around 500 µε. For a better evaluation, the pre-strain is subtracted from the measurements. Figure 7-5 shows the changes in strain since the beginning of the second loading cycle, which was entirely recorded. The self-weight of the beam is consequently not taken account for.

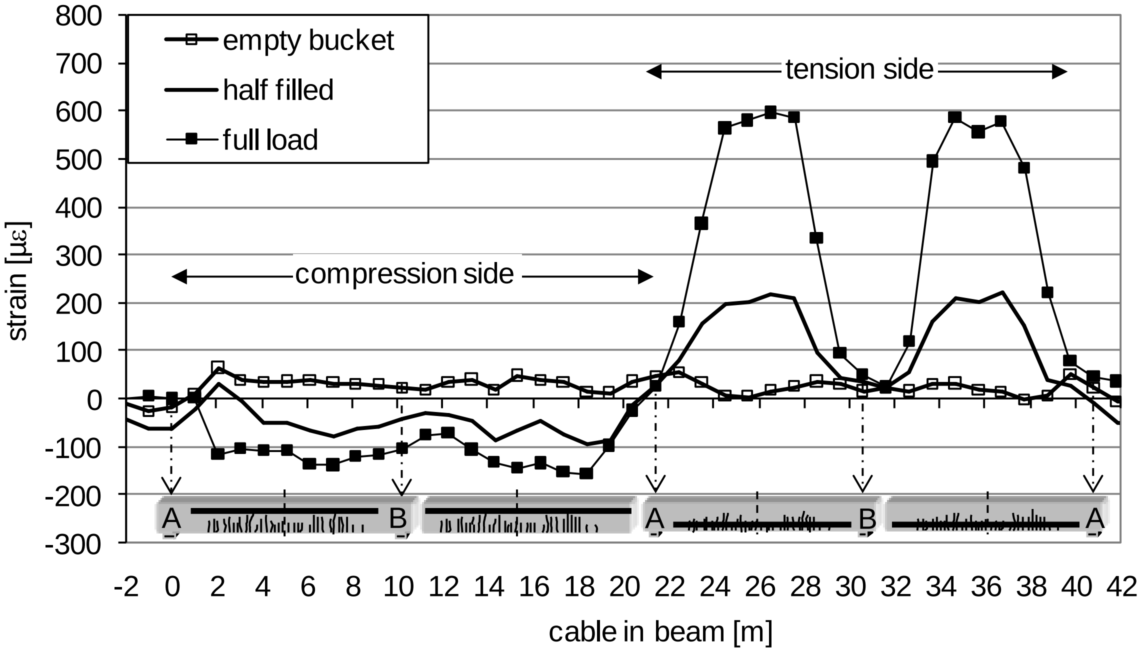

Fig. 7-5: Strain development during loading of the concrete beam

In the beginning, the tank is empty thus no significant changes can be observed. When filling the tank thus loading the beam with up to 25 kN weight, the different cable sections can be distinguished very clearly. The strain in the compression side thus the upper side of the beam decreases by almost 150 µε. In the lower part of the beam, the loading leads to an increase in strain of almost 600 µε. The timely development of the strain in the four measuring points in the center of the beam is shown in Fig. 7-6. The strain in all cable points shows very good coherence, especially in the 2^{nd} loading cycle. A reference point for all measurements was set in between the two cycles as the concrete beam was deformed above its elastic limits during the first loading cycle. Measurements from the compression side during the first loading cycle were not recorded.

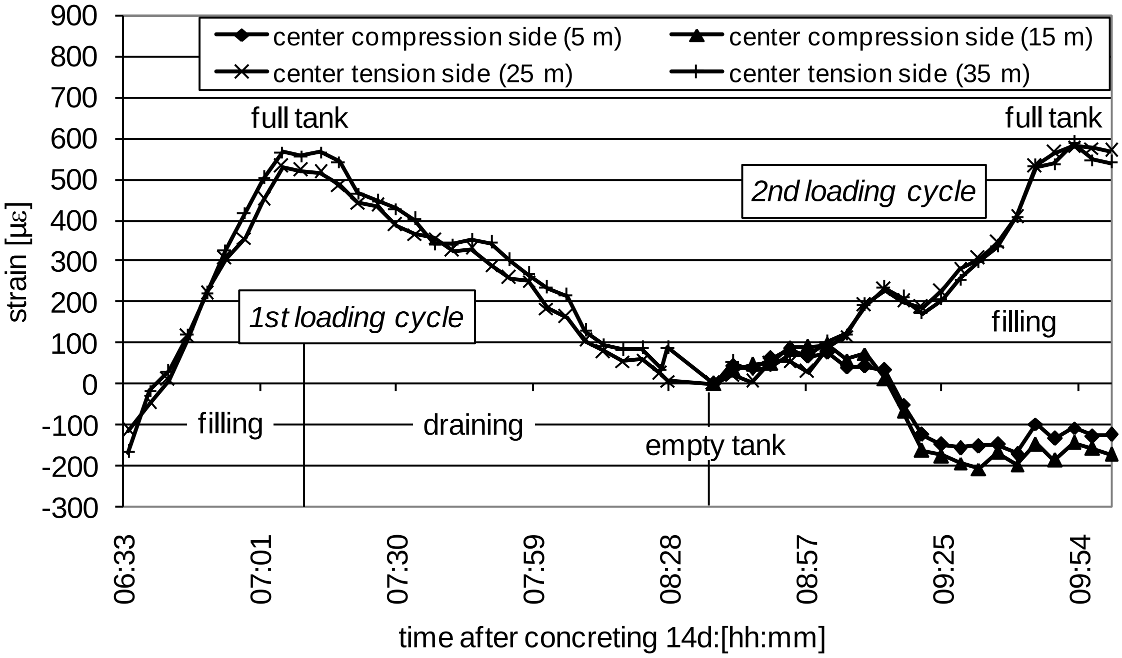

Fig. 7-6: Timely development of strain in the four center points of the beam

The crack pattern that was registered while fully loading the beam is plotted in the upper section of Fig. 7-7. The graph below shows the qualitative strain distribution along the cables in the lower part of the beam. Strain is depending on the distribution of the bending moment and the appearance of cracks. They appear where the tensile strength of the concrete is exceeded and the load is taken from the steel only. Like the moment, the strain has its maximum in the center of the beam. The lower graphs show the average strain of both loops in the center sections in the compression and the tension parts of the beam that were measured by the DTSS at full load. The measured curve follows the qualitative curve in the uncracked part of the beam. The strain then remains rather constant throughout the middle 5 m of the beam with even a little depression in the middle. However the DTSS measurement seems to follow the crack pattern with smaller cracks in the middle, which is a sign of actually lower strain. The maximum strain in the tension side of the beam is 1,400 με and thus below the technical elastic limit of structural steel of 0.2 % (2,000 με). The maximum measured compressive strain in the upper side of the beam is 600 με which is well below the elastic compressive strain limit of this concrete of 1,060 με (Tab. 7-1).

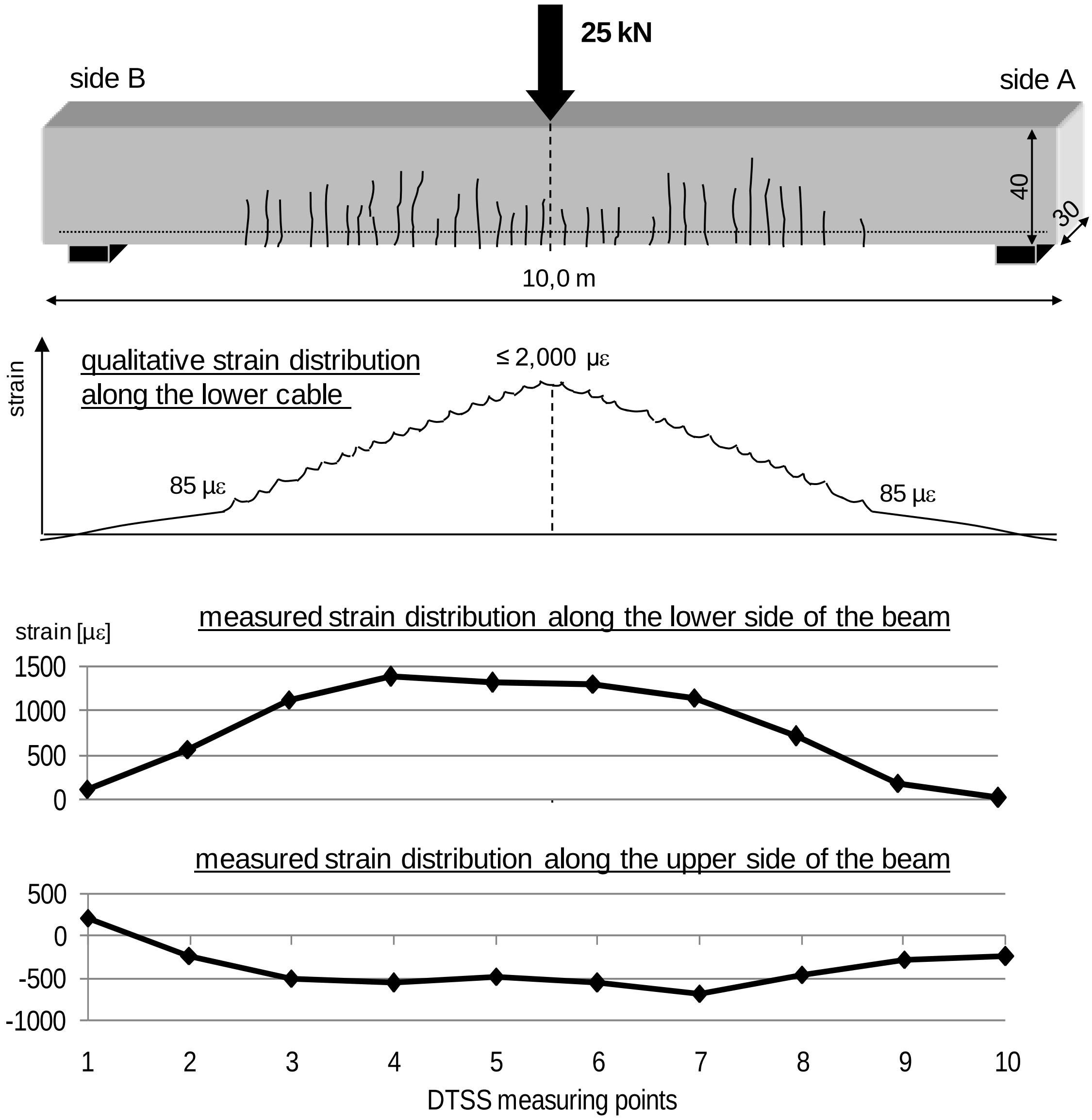

Fig. 7-7: Crack pattern after full loading and strain in the tension and compression side of the beam

As the calculation of strain in the cracked reinforced concrete is very complex, an easy estimation by means of geometry will give a useful approximation. An equivalent static system, involving the load of the beam per unit length and the point load from the water tank is used to calculate the deflection line, assuming linear conditions along the beam. The total length of the affected beam is 9.4 m. The 0.3 m cantilever on each end of the beam is neglected in the calculations for the deflection line. As the total deflection in the middle of the beam including self-weight was measured to 5.55 cm, the according deflection line can be calculated using Equations 7-1 to 7-3. Summing up the deflection due to load per unit length and maximal point load (25 kN), the deflection line appears as shown next to the equations. To calculate the actual extension of the strain sensing cable in the lower and upper side of the beam, the cubic parabolic shaped bending line is simplified to be a circular arc (grey line).

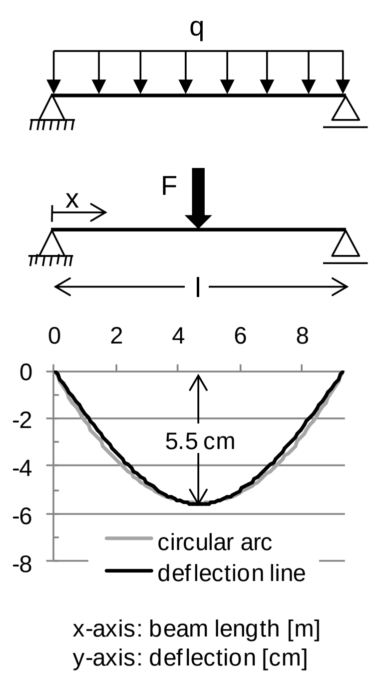

$$\xi = \frac{x}{l} \; ; \; \beta = \frac{l}{2}$$

$$EIw(x) = \frac{ql^4}{24} \cdot \left(\xi^4 - 2\xi^3 + \xi\right) \qquad \textit{Eq. 7-1}$$

<u>for x ≤ β</u>

$$EIw(x) = \frac{Fl^3}{6} \cdot \left[\beta\xi \cdot \left(-\xi^2 - \beta^2 + 1\right)\right] \qquad \textit{Eq. 7-2}$$

<u>for x ≥ β</u>

$$EIw(x) = \frac{Fl^3}{6} \cdot \left[\beta\xi \cdot \left(-\xi^2 - \beta^2 + 1\right) + \left(\xi - \beta\right)^3\right] \qquad \textit{Eq. 7-3}$$

$w(x)$	deflection [m]
F	point load [N]
q	load per unit length [N/m]

The alternation of length can be calculated from the circular segment using the following sketch and Equations 7-4 to 7-7. As the concrete was in cracked condition, the neutral axis in the beam is moving towards the pressure side. A constant shift of 5 cm from the center axis is assumed. The chord length can then be calculated by iteration from Eq. 7-4 as the 9.4 m length of the neutral arc is not changing and the deflection was measured to be 5.55 cm at full load including the deflection due to self-weight. From the chord length, which is 0.82 mm shorter than the initial 9.4 m, the radius R (199.0 m) and the angle α (2.71°) can be calculated. The strain sensing cable was placed next to the lower reinforcement, 3 cm from the edge of the beam (Fig. 7-1). The distance from the neutral axis r is assumed to be constant at 22 cm. Applying Eq. 7-7, the elongation of the arc at the location of the cable can be calculated to 9.77 mm. By integrating the measured strain from the lower graph in Fig. 7-7 over the length of the beam, the total deformation is calculated to $\sum \varepsilon = \int_1^{10} f(\varepsilon) \cdot dx =$ 7.75 mm. The calculated and the measured elongation are deviating by 20 %. However multiple simplifications and assumptions were made in the calculation of the strain This shows that the magnitude of measured strain is in the right range.

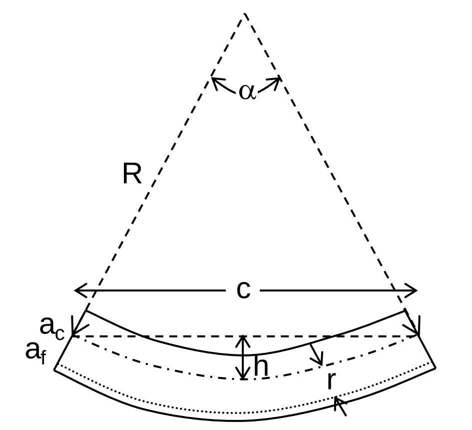

$$a_c = \arctan\left(\frac{2h}{c}\right) \cdot \frac{4h^2 + c^2}{2h}$$ *Eq. 7-4*

$$R = \frac{4h^2 + c^2}{8h}$$ *Eq. 7-5*

$$\alpha = 4 \cdot \arctan\left(\frac{2h}{c}\right)$$ *Eq. 7-6*

$$a_f = \alpha \cdot (R + r)$$ *Eq. 7-7*

R	radius [m]
c	chord [m]
h	segment height (deflection) [m]
a_c	arc of the circle in the neutral axis of the beam in cracked condition [m]
a_f	arc of the circle at the fiber location [m]
r	distance between neutral axis and fiber [m]

Calculating the strain in the compression part of the beam the same way, the total deformation comes out to 5.3 mm. Integrating the mean of the two center points of the strain sensing cable on the compression side (Fig. 7-7), the total deformation can be calculated to 3.83 mm, which is 27 % smaller than the estimated value.

7.2.4 Comparison with a FBG strain sensor and ESGs

Electronic strain gauges and a fiber Bragg grating sensor were installed into the middle part of the beam where the strain was expected to reach its maximum (Fig. 7-1). Figure 7-8 shows the complete data set of all measurements in the center of the beam. The FBG sensor was the only instrument that was recording data during the entire test, the ESGs - and some DTSS data are only available in fractions or in the second round of loading the beam. A first significant difference in the different measuring methods is the data density. Three FBG measurements are recorded every second, the ESG gives a value every 2 seconds and the DTSS is averaging over 4 minutes to improve the data quality. The single point measurement of the FBG sensor showed to be very sensitive. It shows the process of loading and unloading the beam very detailed. Even the additional strain that was put on the beam from people standing on it can be seen. The waved shape of the curve while unloading, thus releasing water from the bucket after the first loading, indicates the opening of three water releasing valves at different times. The residual strain of 200 με after the first loading cycle indicates that the deformations of the beam are already inelastic which happens when the tensile strength of the concrete is exceeded. ESG 5 was attached onto the outside of the tensile zone of the beam. The excessive rise of strain indicates that a crack went right through the sensor.

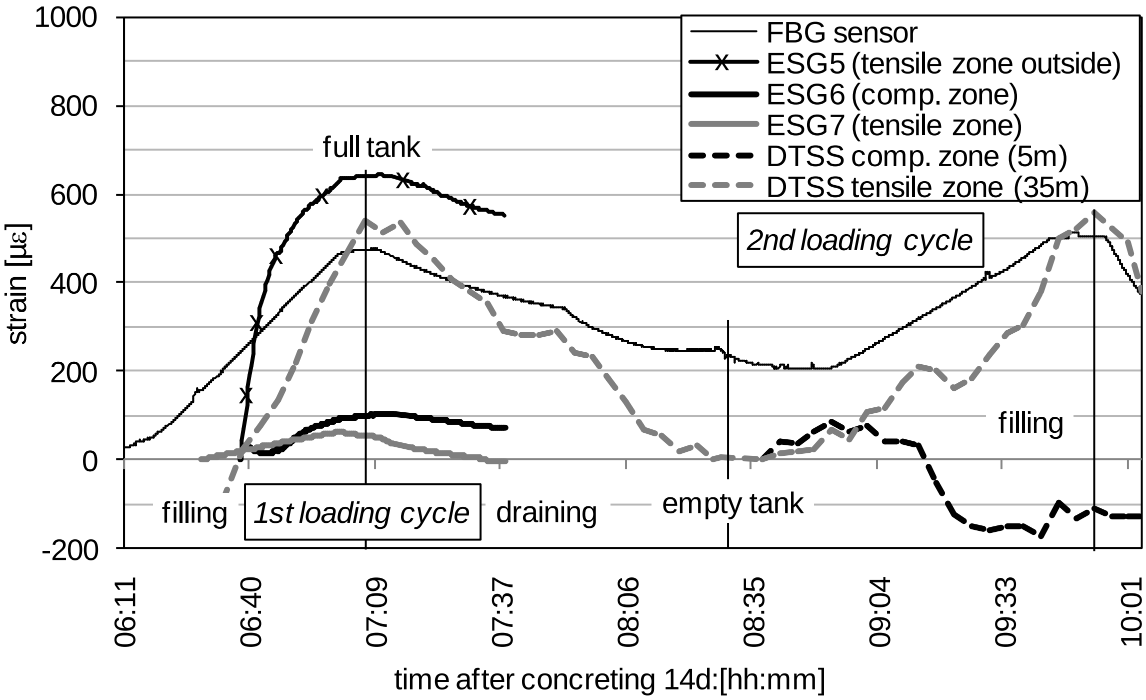

Fig. 7-8: Comparison of all sensors installed in the concrete beam

The DTSS measurement in the tension side of the beam at 35 m cable length also follows the FBG sensor with larger overall strain values. While the strain difference during the second loading cycle in the FBG sensor is 300 με, the DTSS measures an increase of 550 με.

7.3 Reinforced concrete column

7.3.1 Installation of strain sensing cables and other sensors

Basically a second concrete beam, 8.6 m long and 0.3 m high and wide was formed, reinforced with reinforcing steel bars and mesh and equipped with fiber optic strain sensing cable and electrical strain gauges. Just before the tests, the structure was taken out of the formwork and was placed vertically into a precast foundation, which had a depth of 1.4 m, creating a concrete column that sticks 7.2 m out of the ground. The electrical strain gauges were installed to have single point reference measurements. The basic sensor installation concept was the same as described for the concrete beam in section 7.2.1. Four reinforcement steel bars were placed on each edge inside a bent steel reinforcement mesh to give basic strength to the structure. While lying on the ground, the strain sensing cable on the pressure side was pre-strained by around 3,000 $\mu\varepsilon$ and redirected on pulley wheels. The cable sections on the tension side were left loosely attached to the reinforcement steel bars. Additionally, three ESGs were attached to the reinforcement steel in the lower part of the column before concreting, two on the tension and one on the compression side. The layout of the sensors in the structure is depicted in Fig. 7-9.

The DTSS device was connected to an optical fiber at end 1. From there, the cable goes loosely into the lower part of the column before passing the entire tension side three times. In the turning points, the cable is loosely attached to the reinforcement steel with fabric tape. After the third passage, which ends in the top part of the column, the cable is pre-strained on its way downwards. The pulley wheel in the bottom part guides the cable up to the top again, where it is attached with fast hardening resin. From there it is loosely guided downwards where it ends at end 2. The ESGs were attached to the reinforcement steel about 1.8 m above the ground surface thus above the main crack that appeared during the experiment. After all sensors had been installed, the beam was concreted and left curing for 18 days. No significant optical losses could be found within the installed optical strain sensing cable.

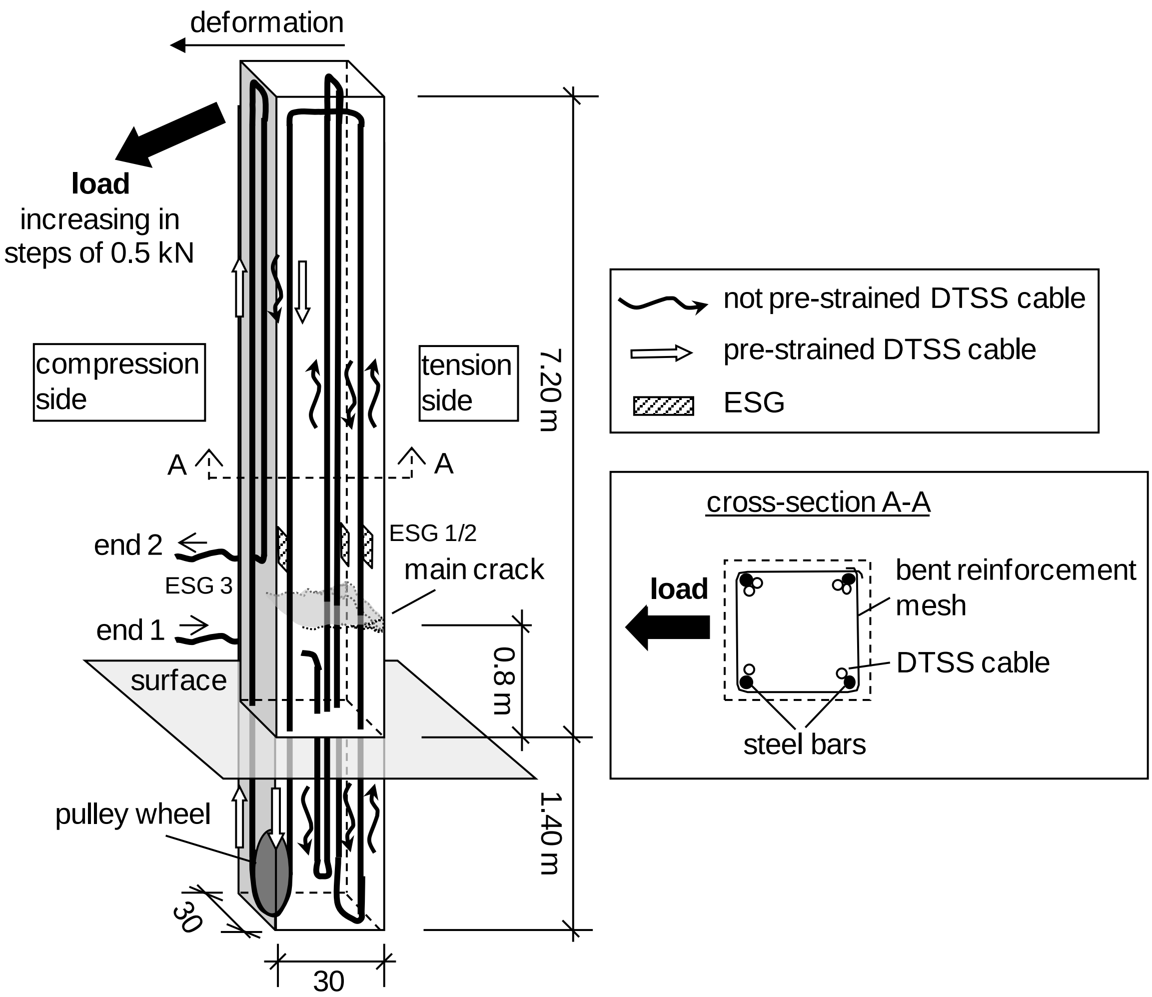

Fig. 7-9: Instrumentation layout and setup of the column

7.3.2 Execution of the test

The column was placed into the precast foundation 18 days after concreting. An electrical displacement transducer was attached to the tip of the column leading to the ground along a vertical steel beam that was located a few meters next to the column (Fig. 7-10). The measuring device itself was placed into a measuring hut next to the column. To apply load, a steel cable was also attached to the top of the column. It was connected to an electrical load transducer and a tensioning device in a distance of roughly 50 m, so the load that is applied to the column can be assumed to be horizontal.

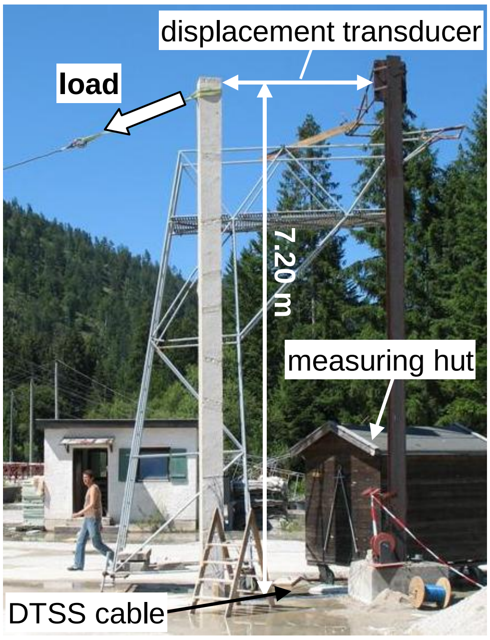

Fig. 7-10: The concrete column during testing

With all measurements running, the load on the column was increased in steps of close to 500 N. The loading came along with a deformation of the column. The relation between load and displacement of the tip is depicted in Fig. 7-11.

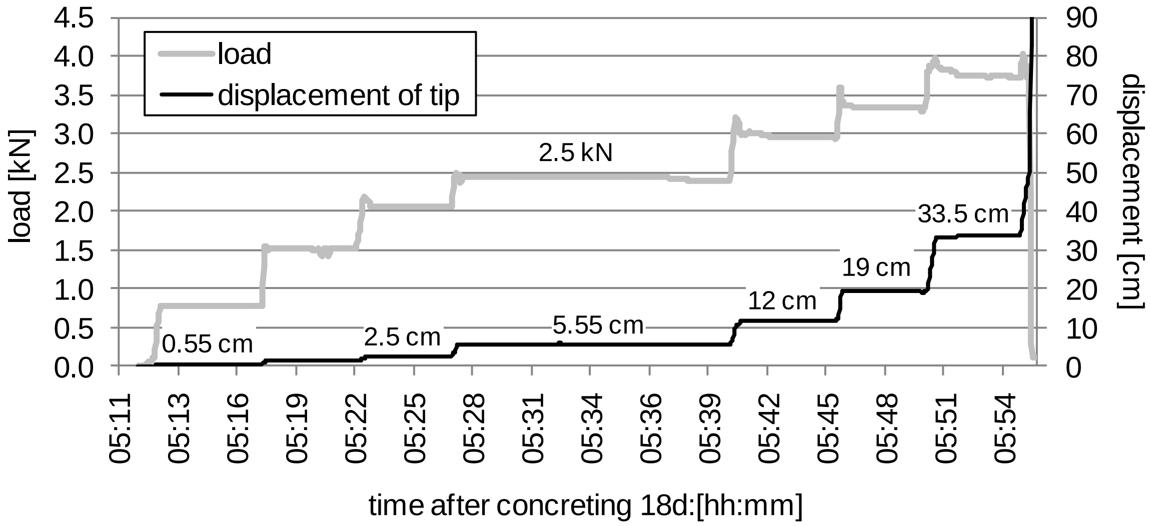

Fig. 7-11: Load versus displacement of the column tip

The horizontal axis shows the time after concreting of the column. The entire test took 45 minutes and ended with the total failure of the column when a load of 4.0 kN was reached.

7.3.3 Strain measurements in the concrete column

After the load was increased to 2.0 kN, several small cracks appeared on the lower tension side of the column. When increasing the load, apart from additional small cracks, one main crack appeared 0.8 m above the ground, at which the column finally broke. Photos of the main crack at 2.5, 19 and 33.5 cm displacement of the tip are shown in Fig. 7-12.

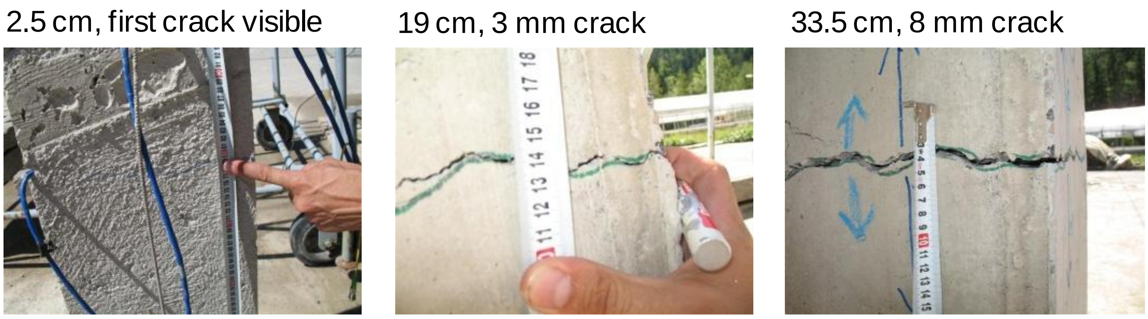

Fig. 7-12: Development of the main crack referring to the displacement of the tip

The measuring period of the DTSS was set to 4 minutes. Figure 7-13 shows an overview of the strain throughout the fiber inside the column at different displacements of the tip (Fig. 7-11) and a reference measurement that was taken before the loading started. The vertical situation in the column can be seen in the sketched columns on the bottom of the figure. The reference measurement, which mainly comprises the pre-strain, was subtracted from the subsequent measurements to display the changes in strain due to loading only. Referring to Fig. 7-9, the loose cable goes up and down the column three times on the tension side and then passes the compression side twice. On the tension side, the tension on the fiber is clearly marked by the three peaks.

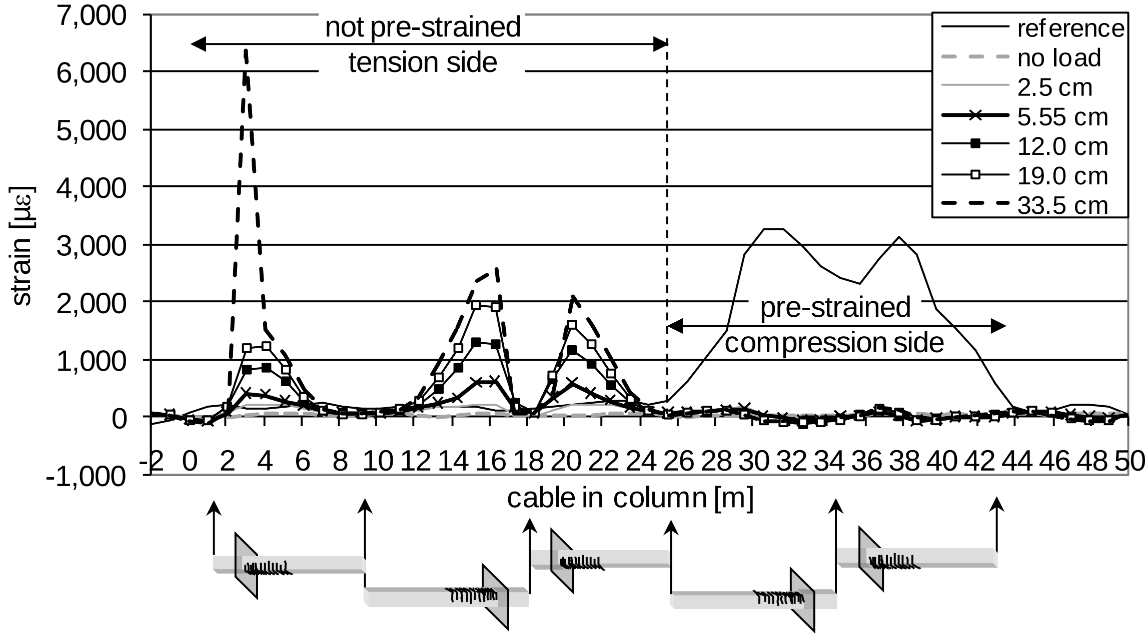

Fig. 7-13: Strain distribution in the concrete column during testing

Figure 7-14 allows a better assignment of the strain. The cable meters next to the graphs correspond to the cable in the tension side of the structure and the numbers next to the column refer to the distance z over ground.

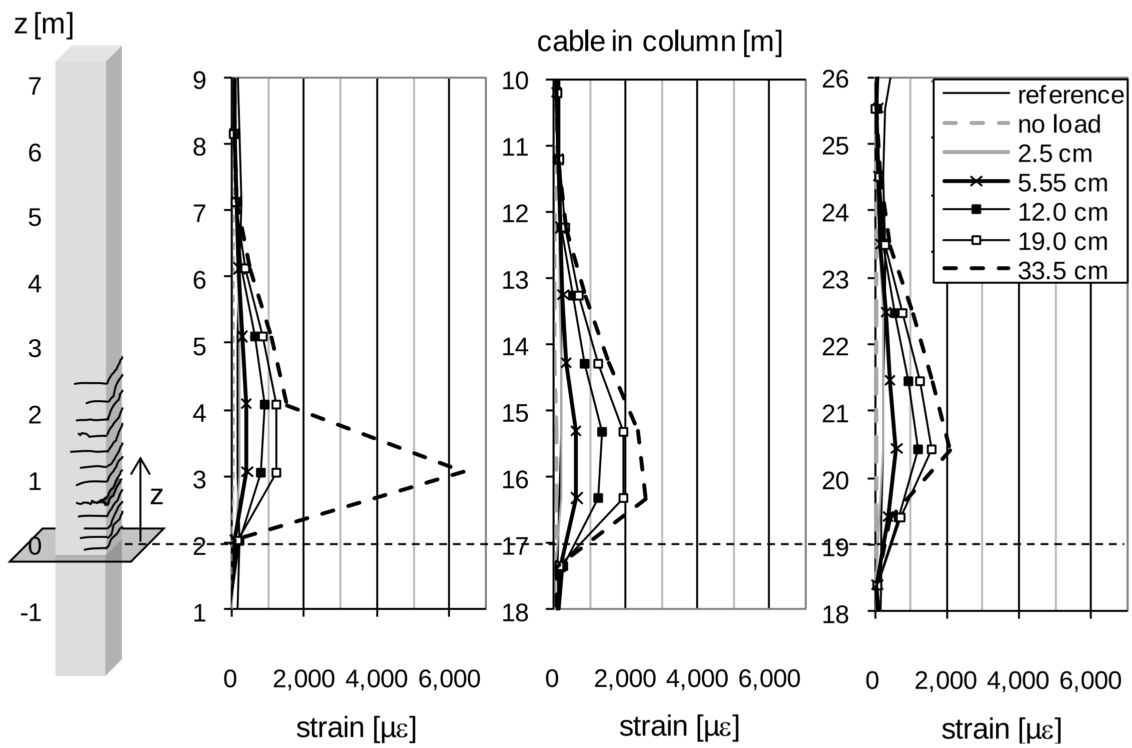

Fig. 7-14: Strain distribution along the tension side of the column at different displacements of the tip

For a more detailed evaluation of the early stages of loading, the strain development along the fiber is magnified in Fig. 7-15. Before loading, the strain distribution is not entirely constant, which is caused by small temperature changes between the measurement before loading the beam and the beginning of the test. At the initial load step of 750 N, the tip moves by only 0.55 cm, which results in an increase of the DTSS strain readings of up to 70 με in the tension side of the column. The situation of the points of fixation in the top and the bottom of the beam also become visible. When further increasing the displacement of the tip, the strain in the whole column rises. The cracked region with considerably higher strain values becomes visible at a displacement of 2.5 cm. When further bending the column, the shape of the strain curves in the tension side of the beam turn from rather uniform along the column towards distinct strain peaks where the main crack and consequently a strain peak is located.

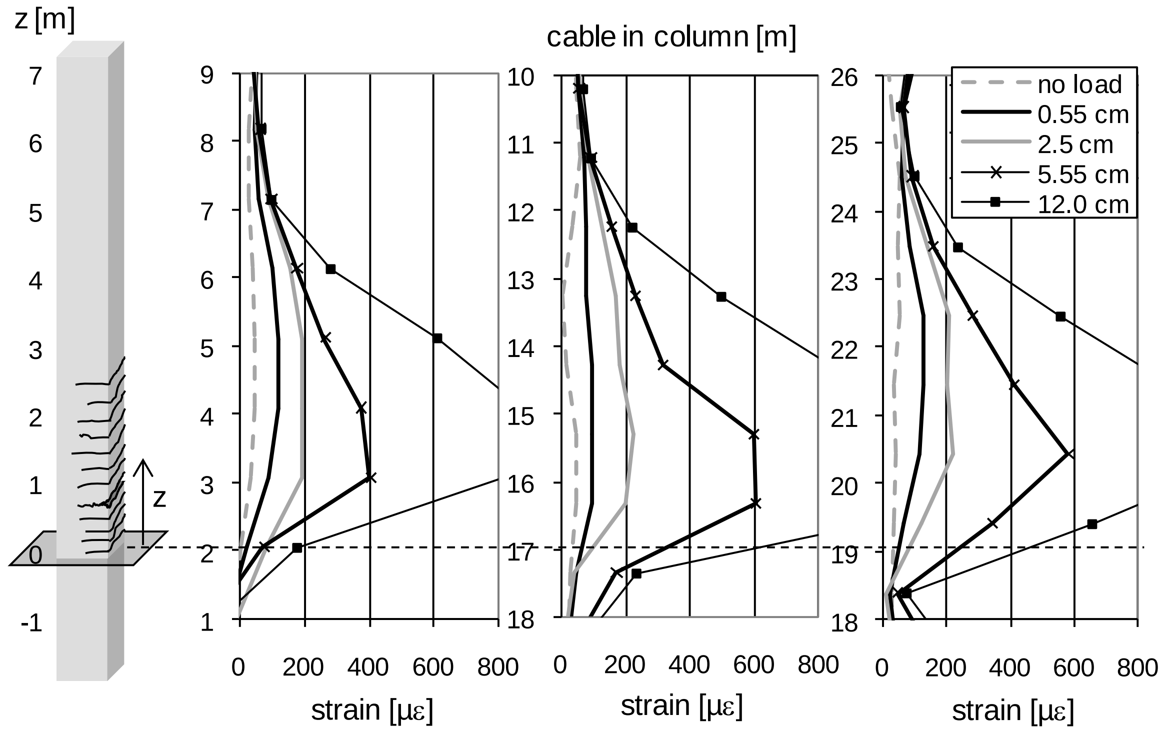

Fig. 7-15: Detailed strain distribution along the tension side of the column

A detailed view on the strain distribution along the compression side of the beam is depicted in Fig. 7-16. The compression side shows an undefined influence, which mainly refers to temperature changes. The reference measurement was taken while the compression side was directly irradiated by the sun and the 1.4 m of the column inside the foundation was rather cooled.

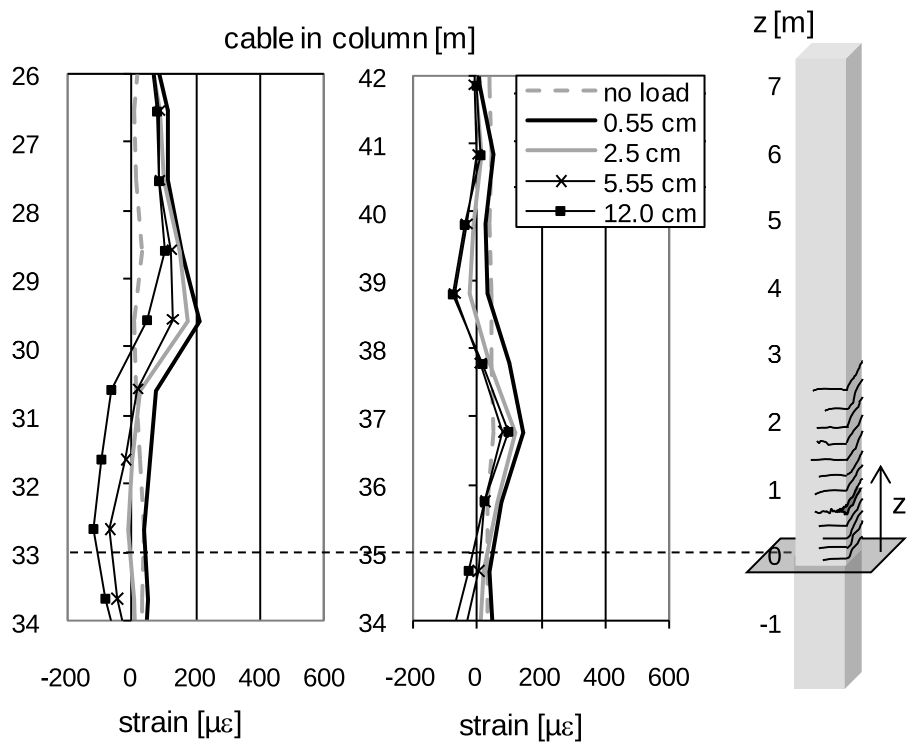

Fig. 7-16: Detailed strain distribution along the compression side of the column

Figure 7-17 shows the strain development at the main crack on the tension and the compression side and the displacement of the tip. Loading begins at 5:12. The strain measurements on the tension side rise very significantly when the displacement reaches 2.5 cm in the 3rd load step. A strong difference between the measurement at 3.1 m and the other two measurements in the tension side is remarkable during the constant displacement of 5.55 cm. This effect can be explained with the influence of the un-strained zone in the foundation which reduces the measured strain in that measuring point due to the spatial resolution of the measurements. The strain distribution in the pre-strained compression part of the column shows a little decrease of strain until a displacement of 12 cm, followed by a significant increase until the failure of the column. The cables were installed inside of the reinforcement steel cage in the concrete. The compression zone in the cross section of the column decreases when the cracks and the displacement grow. It seems like the pressure zone shifts towards the outside of the reinforcement cage, resulting in rising strain values in the cables, which at that point are located in the tension zone.

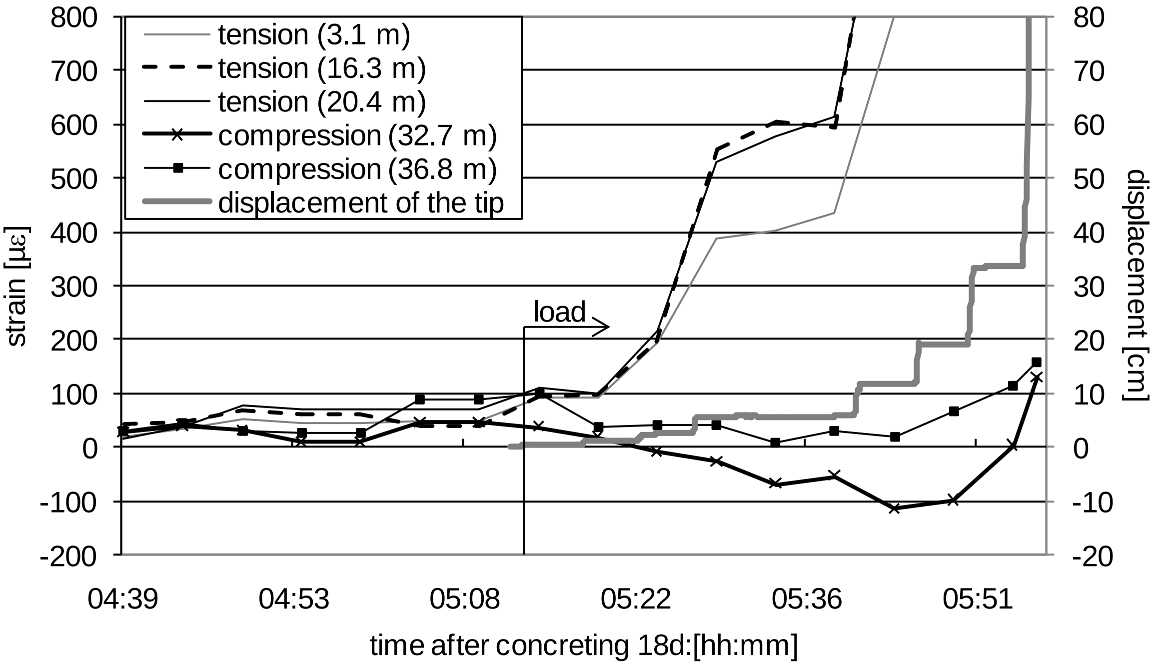

Fig. 7-17: Strain development during loading of the concrete column at z = 1 m

To illustrate the quality of the DTSS measurements in the column, the expected and the measured strain distributions are compared in Fig. 7-18. The cracks that are drawn in the column on the left reflect the actual cracks in the concrete at a displacement of 5.55 cm, just the main crack which is highlighted, did not stand out at that time.

The graph next to the beam shows the qualitative strain distribution along the tension side of the beam. Following the bending moment, the strain linearly rises towards the bottom of the column, leading to cracks when the maximum tensile strain the concrete can bear is exceeded ($\varepsilon_{ts,14d}$ = 85 με). The little peaks show the strain around the cracks, where the concrete does not contribute to the strain transfer any more with a larger peak at the main crack. The graph next to it shows the average strain distribution of the three cable parts in the tension side of the column, which follows the qualitative strain distribution quite good. Only in the bottom, the abrupt changes in strain cannot be displayed due to the spatial resolution of the DTSS measurements of 1 m. Also the location of the exceeding tensile strain of the concrete is not apparent at the location of the first crack where the DTSS strain values are around 200 με.

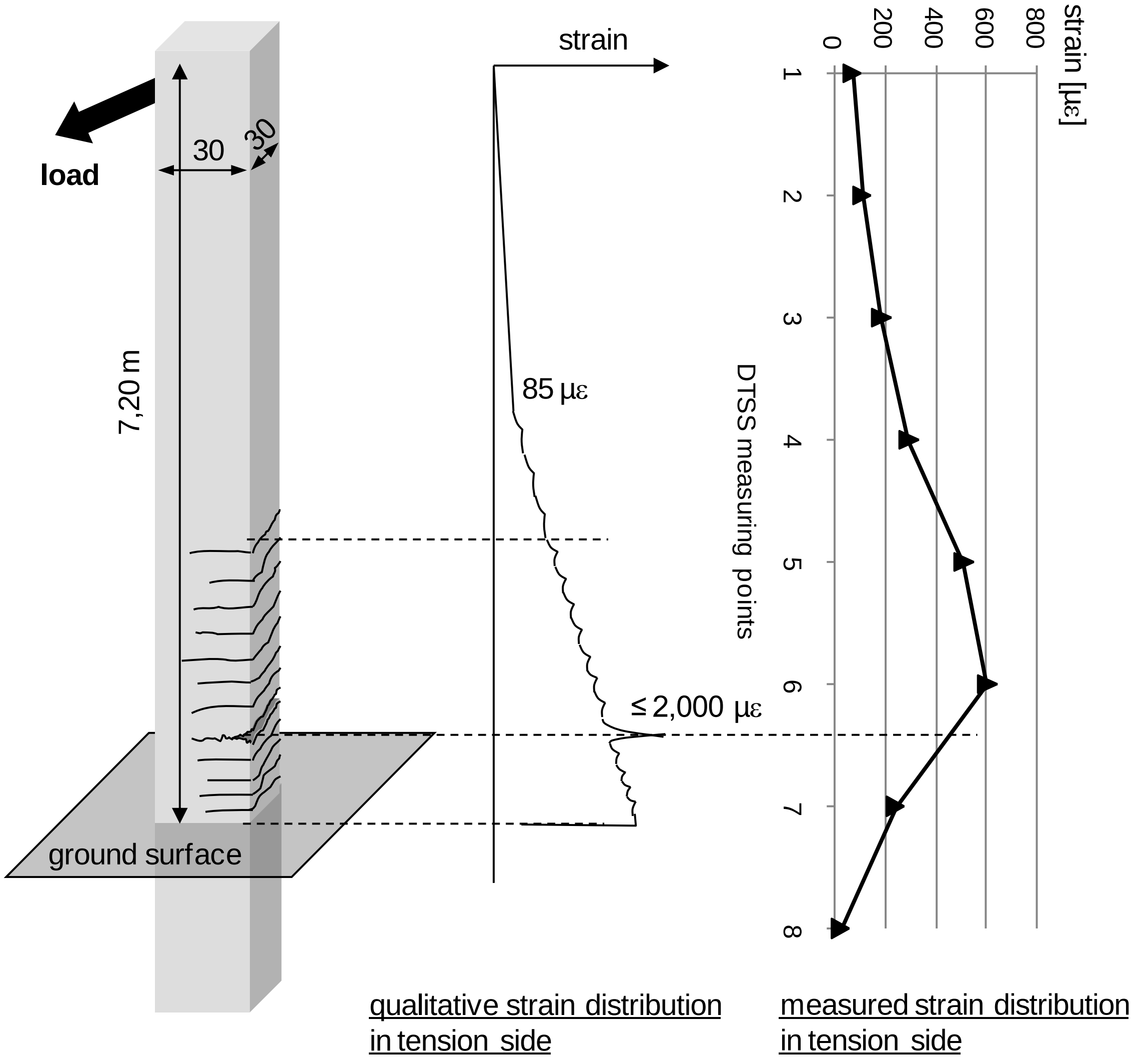

Fig. 7-18: Crack pattern during loading and strain in the tension part of the beam at 5.55 cm displacement of the tip (or 2.5 kN load)

For an estimation of total deformation of the cables, the deflection line at 5.55 cm was calculated by applying Eq. 7-8, and compared with a circular arc. As the shape of the two lines is quite comparable, the same geometrical calculations as for the concrete beam in section 7.3.3 were made, using Equations 7-4 to 7-7. The eccentricity of the neutral axis was assumed to be constant at 3 cm along the entire column. According to those calculations, the total elongation of the strain sensing cable on the tension side is 2.31 mm. By integrating the measured strain from Fig. 7-18, the total strain comes out to 2.12 mm.

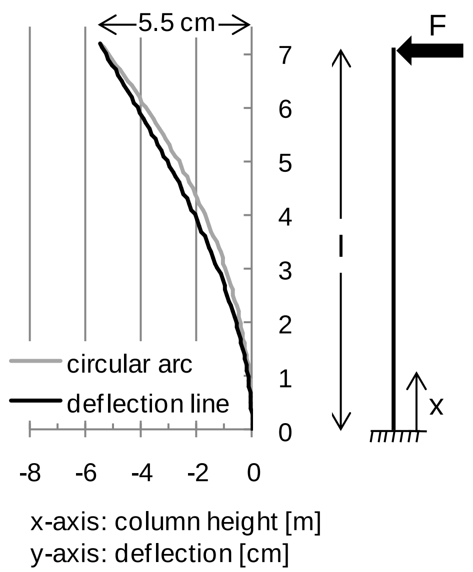

$$\xi = \frac{x}{l}$$

$$EIw(x) = \frac{Fl^3}{6} \cdot \left(-\xi^3 + 3\xi^2\right) \qquad \textit{Eq. 7-8}$$

w(x)	deflection [m]
F	point load [N]

The results from the approximated geometrical approach and the measured values are very close with the measured strain being only 9 % lower. Those numbers would even become closer when taking the reduction of tensile strain due to compaction from vertical stresses due to self-weight of the column into account.

7.3.4 Comparison with ESGs

The comparison with the ESGs is divided into the compression and the tension side. As pictured in Fig. 7-19, the distributed strain measurement follows the readings from the electronic strain gauges with great accuracy during most of the time. Strain gauge ESG 2 is being affected by a crack in the last load step as it increases excessively. Also in the step when the displacement stays constant at 5.55 cm, the DTSS and ESG 2 show very similar results while ESG 1 seems not to be considerably strained, yet.

The comparison between ESG and DTSS in the compression side also shows very similar results. In Fig. 7-20, the strain resolution on the vertical axis is 8 times higher as in the previous analysis for the tension side in Fig. 7-19. It shows that the measurements of both sensors only vary between 10 and 100 με. The strain development indicates the decrease in strain in both strain sensing devices and the following increase when the displacement of the tip exceeds 5.55 cm. When the load is increased to the final load step before failing, the strain gauge is getting damaged while the strain sensing cable is still intact, showing a further increase in strain until total failure of the concrete column.

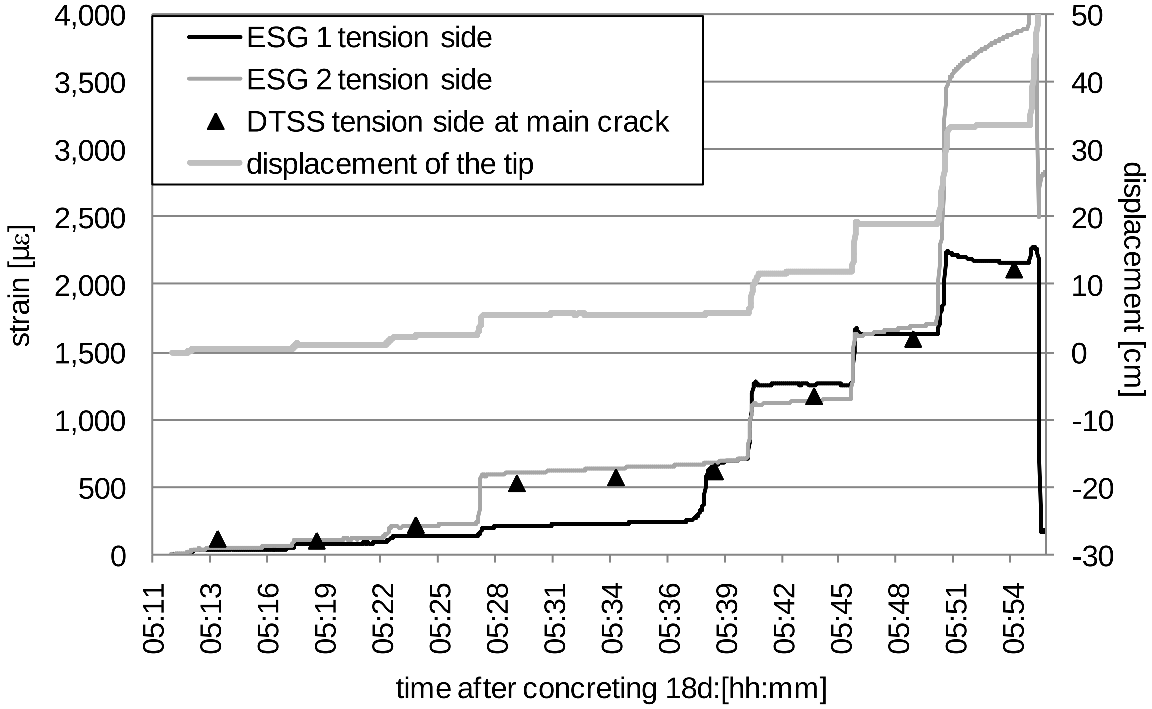

Fig. 7-19: Comparison between DTSS and ESGs on the tension side

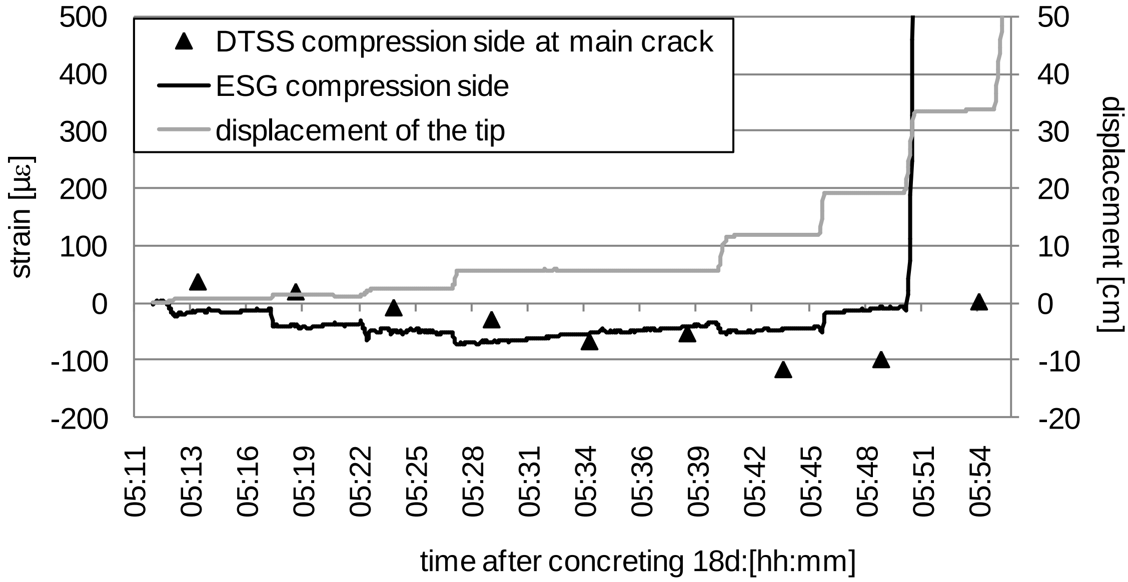

Fig. 7-20: Comparison between DTSS and ESG on the compression side of the column

Like in the tests on the concrete beam, the measurements on the concrete column show the applicability of the distributed method. The strain data is in good agreement with estimated strain distributions and in excellent agreement with the measurements from the ESGs that were located next to the strain sensing cable. However cracks could not directly be measured due to the spatial resolution of only 1 m. The measurements consequently show the average strain from elastic and plastic deformation within the spatial resolution.

7.4 Roller compacted concrete block

7.4.1 Installation of the strain sensing cables and other sensors

A roller compacted concrete (RCC) block, 20 m long and 1 m wide was constructed in four layers of 30 cm each. The concrete mix and its installation followed the procedures for regular RCC placing. The RCC block was equipped with the blue 2 mm strain sensing cable form Tab. 5-1, a separate temperature sensing cable and FBG strain sensors in the middle part, where the maximum strain and following cracks were expected. Similar to RCC as it is used in some dams, the concrete was very dry and very suitable to process with a vibrating plate compactor. For optimum workability, the water content was regulated on site. In the following, the layers of RCC are referred to as layers 1 to 4 and the instrumentation levels above layers 1 to 3 are referred to as levels 1 to 3.

The first 30 cm layer of concrete was brought onto the ground and compacted. Three lines of strain sensing cable were placed on top of the first concrete layer and pre-strained. Both ends were tightly secured to maintain the pre-tension. On the ends of the block, the cable was returned with pulley wheels as they were also used in the concrete column and beam. A well protected temperature sensing cable was laid next to the strain sensing cable, following all three rounds. The second layer was concreted, compacted and three rounds of DTSS and two rounds of DTS cable were installed in the same manner as in the previous level. On top of the third, thus the level at a height of 90 cm, only 11 m of temperature sensing cable was left to guide it next to the three rounds of strain sensing cable. The instrumentation of the RCC block is sketched in Fig. 7-21. The cables above the first layer are marked red, the DTSS cable solid, the DTS cable dashed. “End 1” marks the first end of the DTSS cable, thus the end where the DTSS was attached, “end A” the first end of the DTS cable. The cross section through the center of the block shows the mean situation of the cables in the RCC block.

The DTS cable is a protected standard telecommunications cable which can be used for temperature sensing without being affected by strain. For the present setup with a Brillouin based DTSS and the Raman based DTS, the installation of an additional temperature sensing cable would however not have been necessary. Strain in the fibers does not affect the Raman shift in the reflected light spectrum. The temperatures that were measured by the DTS to manually compensate the DTSS strain values could as well be measured in the multi mode or single mode fibers of the strain sensing cable, also using a DTS system.

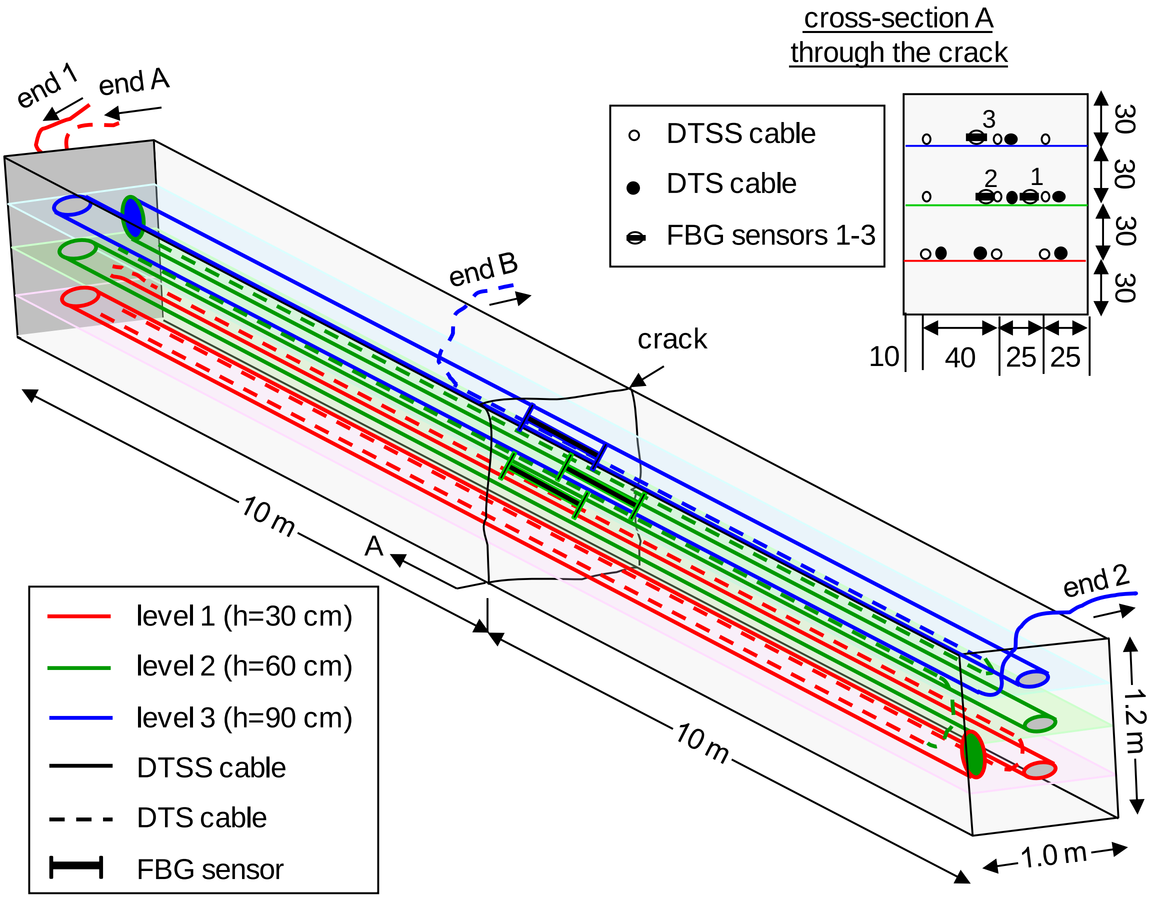

Fig. 7-21: Instrumentation inside of the RCC block

For reference measurements concerning strain, three FBG sensors were installed next to the DTSS cable in the center part of the RCC block. For a safe installation, the FBG sensors were placed onto a slab of conventional concrete as depicted in Fig. 3-20. Two FBG sensors were installed in instrumentation level 2 (green) and one at 90 cm elevation (blue). The sensing devices were placed into a measuring hut next to the RCC block (Fig. 7-22 right). The end of the RCC block before compacting the first RCC layer and the block after removing the formwork and the insulation, are also depicted in Fig. 7-22.

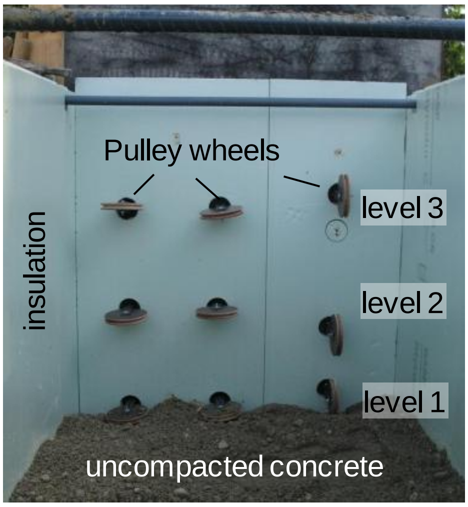

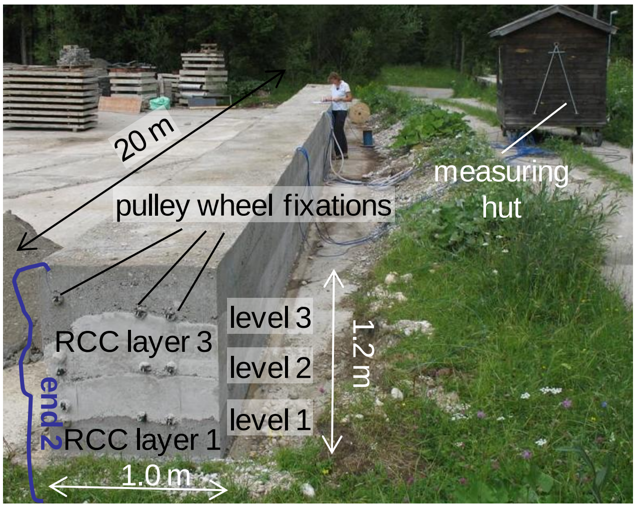

Fig. 7-22: End of the RCC block before compacting the first layer (left) and the block after removing the insulation (right)

The OTDR trace in Fig. 7-23, which shows the optical losses within the tested fiber, shows one significant loss at 120 m and two minor losses at 89 and 130 m. Except for the loss at 130 m, they all appear close to the turning points at the end of the RCC block. During concreting and compaction, the pulley wheels were protected by a vertical wooden board, which was placed right onto the cables causing those losses. In the rest of the block, even the compaction with a heavy vibrational compactor did not considerably harm the skinny 2 mm strain sensing cable. As the fiber is continuous, the whole block could be measured from either side of the cable.

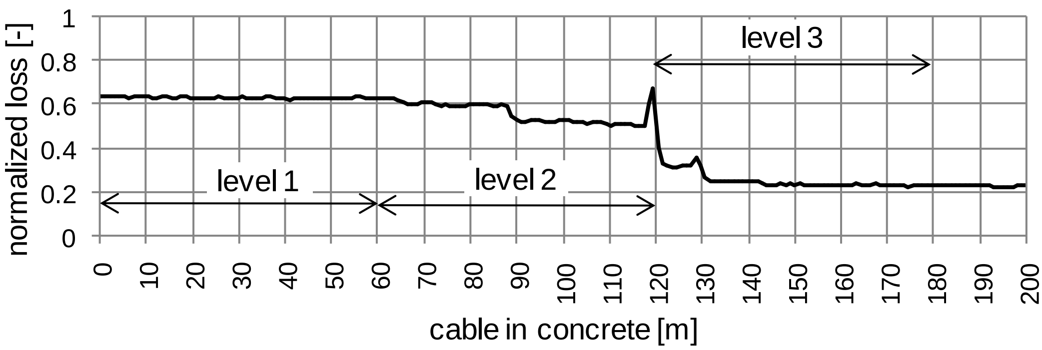

Fig. 7-23: OTDR trace of the strain sensing cable inside the RCC block

The measurements in the temperature and the strain sensing cables started shortly after the construction of the RCC block was finished. For the sake of strain resolution and manageable data volume, the measuring time for the DTSS was set to 20 minutes.

7.4.2 Temporal strain development and temperature interactions

The basic idea behind the construction and the measurement of the RCC block was the evaluation of strain and cracks in RCC under lifelike conditions. Excessive strain was expected to develop in the middle part of the block due to the contraction of the concrete that is cooling down after the hydration heat reached its maximum. In order to enforce the effect, the RCC block was insulated from all sides except the ground during the first week after construction (Fig. 7-22 left). The ground was pretreated to hinder the block from movement at its base. The heat was supposed to stay inside of the block while insulated. Cracks were expected to develop in the middle part of the block when the insulation was removed and the middle section was cooled with iced water from the outside and from the inside through a tube that was installed into the structure in the middle part. The hydration heat caused the temperatures to increase by about 20 K within the first day after concreting. However the insulation could not entirely hold the heat within the concrete block, which linearly cooled down to 35 °C within the first week as depicted in Fig. 7-24. The effect of the removed insulation 7 days after concreting can particularly be seen in the wavy temperature development in the thin red line, which reflects a DTS measuring point only 10 cm from the outside of the sun illuminated side of the block. The negative algebraic sign for strain which refers to the right vertical axis indicates longitudinal compression of the fibers.

In the center of the concrete, the influence of ambient temperature is damped and follows it with a time delay of several hours and an amplitude of less than 0.5 °C. The effect of the removed insulation and the cooling of the block can be seen in the small increase in the drawdown of temperature towards the end of the depicted time interval. The not-temperature compensated DTSS strain measurements are also shown in Fig. 7-24. Outside of the block (-2 m), the strain exactly follows the ambient temperature due to the Brillouin shift that is caused by temperature changes and recorded as a change in strain. In the center of the block in level 1 (red) and level 2 (green) the temperatures are steadily decreasing. The DTSS values also show this constant decrease. Considerably delayed from the ambient temperatures the strain measurements also show an up and down movement at a magnitude of up to 400 με. This comes quite unexpected as the maximum influence of the daily temperature cycle inside the concrete until the insulation is removed was only 0.5 °C. Calculating the corresponding Brillouin shift using the temperature coefficient from Tab. 5-3, the temperature change would lead to a Brillouin shift of 0.5315 MHz. Transferring this shift into strain, the maximum daily variation would only be 12.4 με, which is beyond the strain resolution of the DTSS. As the temperature was measured in the temperature sensing cable with the DTS at the same time, this abnormality can be solved by manually compensating the strain for temperature. Referring to section 8.5, the internal temperature compensation of the DTSS system by evaluating the temperature from Brillouin power is not appropriate for those measurements. Therefore the method of combining DTS and DTSS measurements for temperature compensation is used in the following.

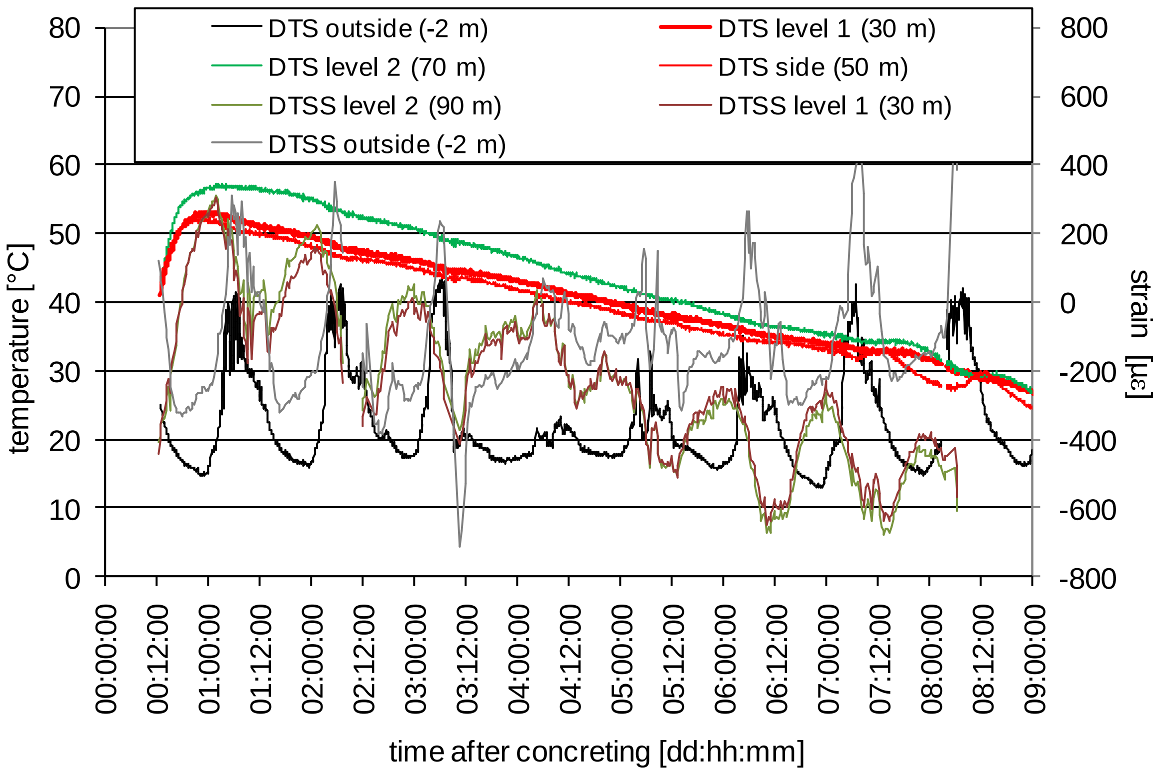

Fig. 7-24: Temperature development and temperature dependence of strain data

As strain and temperature were measured in the same points of the fiber at the same time, the Brillouin shift at any point in the fiber can be temperature compensated by solving Eq. 3-14 for the change in strain, which leads to Eq. 7-9.

$$\Delta\varepsilon_T = \frac{\Delta\nu_B - C_{\nu T} \cdot \Delta T}{C_{\nu\varepsilon}} \qquad \textit{Eq. 7-9}$$

ε_T	temperature compensated strain [με]
ν_B	Brillouin frequency shift [Hz]
T	temperature [K]
$C_{\nu T}$	absolute temperature coefficient [Hz/K]
$C_{\nu\varepsilon}$	absolute strain coefficient [Hz/με]

This calculation implies the exact temperature and strain coefficients for this cable, which are listed in Tab. 5-3. The temperature and strain development in the center of the block in instrumentation level 1 and 2 are plotted into the graph in Fig. 7-25, this time also showing the temperature compensated data, which is directly calculated from the Brillouin shift.

Surprisingly, the raw Brillouin shift does not show the up and down movement that was observed in the uncompensated strain values. Seven days after concreting, the strain values start to follow the temperature variations in the center of the block. The reason for that behavior lies in the choice of reference section for calibration. This was chosen to be the internal buffered fiber section (Fig. 5-3). As the internal buffered fiber is behaving differently to temperature changes, this is affecting the raw strain measurements in the whole fiber, even though the temperature in the RCC block is not changing in the daily cycle. Frequency changes are consequently induced by temperature changes outside the RCC, affecting the fiber inside the RCC. Those changes cannot be accounted for in Eq. 7-9, which depends on measured frequency shift and temperature values at the specific measuring points along the cable.

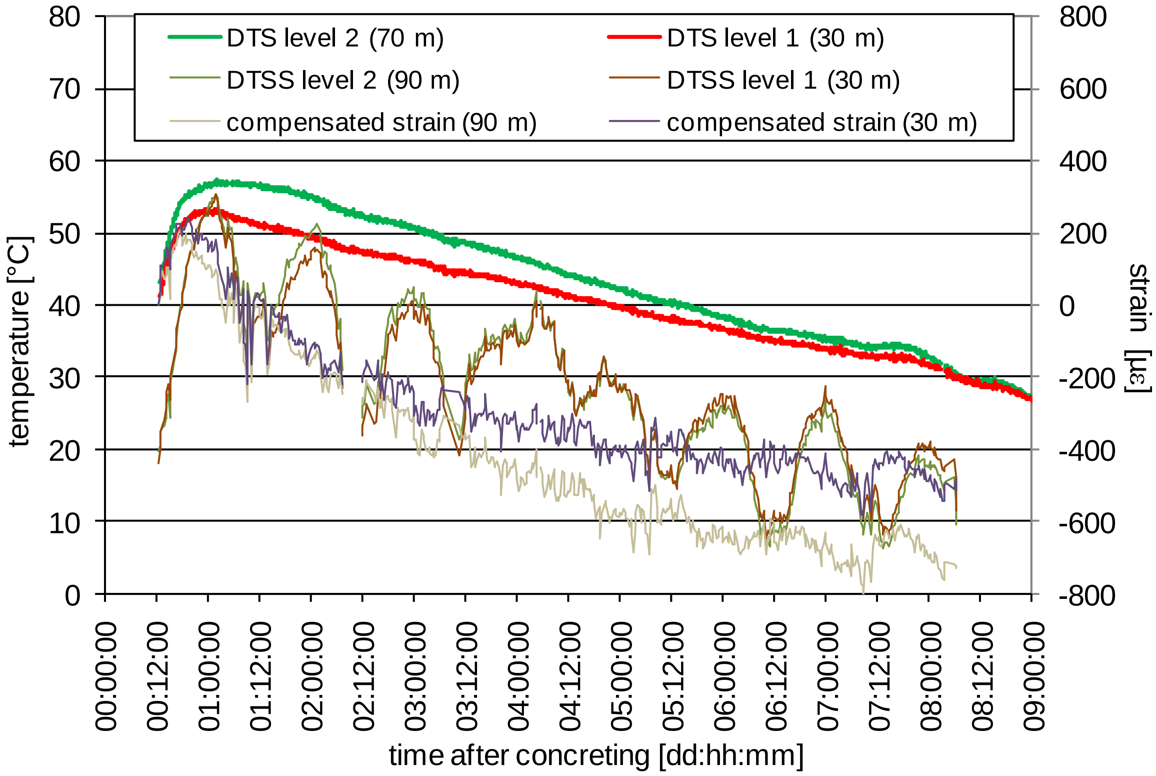

Fig. 7-25: Temperature compensation with parallel measured temperature data

Before the tests on the crack started, the reference section was set to a part of the strain sensing cable that was located in a water bucket and consequently the effect vanished. The daily influence of the temperature in the present tests can more or less be eliminated by comparing measurements that were taken at the same time in the morning, when the ambient temperatures were close to equal. Unfortunately however, the temperature and strain coefficients of that specific cable were not perfectly evaluated before the installation. This is the explanation for the decreasing strain values of almost 800 $\mu\varepsilon$ in the middle of the block during the first 8 days after concreting.

Assuming a constant longitudinal coefficient of thermal expansion α_T of $7 \cdot 10^{-6}$ K^{-1} for the RCC (Nolting 1989), a decrease of temperature in the block during the first 8 days of 25 K and no deformation impediment in the foundation, the maximum expectable strain in the middle of the beam can be calculated by using Eq. 2-7.

$$\varepsilon = \Delta T \cdot \alpha_T \qquad \textit{Eq. 2-7}$$

Referring to the equation, the dropping temperature would not exceed compressive strain of 170 $\mu\varepsilon$. As the precise coefficients for strain and temperature cannot be reliably re-calculated, the uncompensated strain values are used to evaluate the tests on the RCC block.

Referring to Figures 2-3 and 7-26, the RCC block was under external restraint from the foundation. It was observed before that multiple cracks form along a dam foundation under restraint conditions, merging to one large crack in some distance from the foundation (ACI 2001; ACI 2007).

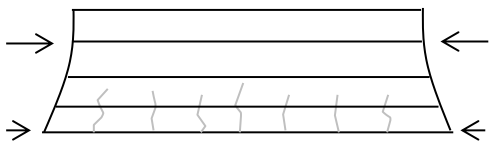

Fig. 7-26: Sketch of the longitudinal deformation of the RCC block

The geometry of the RCC block is very slim; hence a single crack just due to thermally induced contraction did not appear.

7.4.3 Distributed crack detection in the RCC block

As no crack appeared 15 days after concreting, a crack was forced into the center of the RCC block in two steps. A first small crack was barely visible from the outside. In a second step, that crack was widened to more than 1 mm one day later (Fig. 7-27).

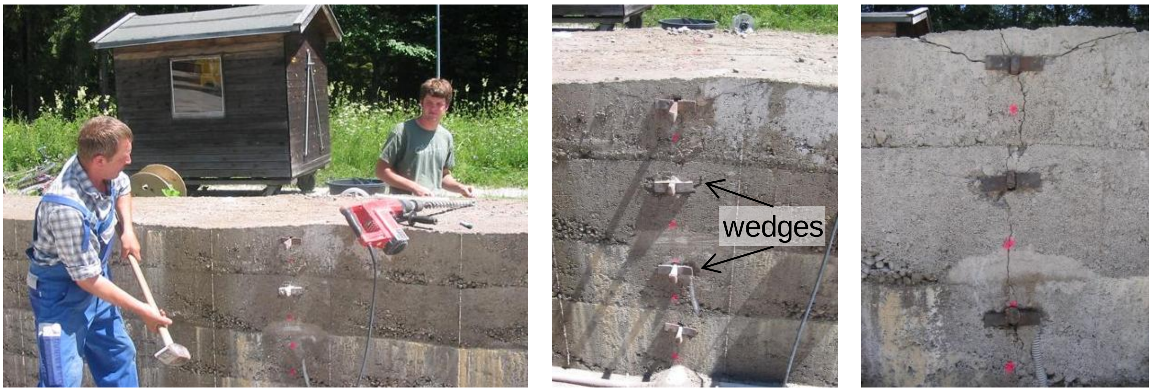

creating the crack | crack <1 mm | crack >1 mm

Fig. 7-27: Creating the crack in the RCC block

DTS temperature measurements were only made in the first 9 days after concreting, wherefore only uncompensated strain measurements can be evaluated in the following. To minimize the effect of temperature on strain measurements, strain data that was recorded at 8 am on different days, when temperatures on the test site in Obernach were quasi identical, are compared in the following. A reference measurement was taken in the morning, almost 11 days after concreting. The curve in the lower part of Fig. 7-28 shows this reference measurement, which is referring to the right vertical axis. The high amounts of strain of up to 5,500 με mainly refer to the influences from the concrete compaction and the pre-tension during installation of the cables. From the following measurements that were taken 15 ("no crack"), 16 ("crack < 1mm") and 17 days after concreting ("crack > 1 mm"), the reference measurement was subtracted.

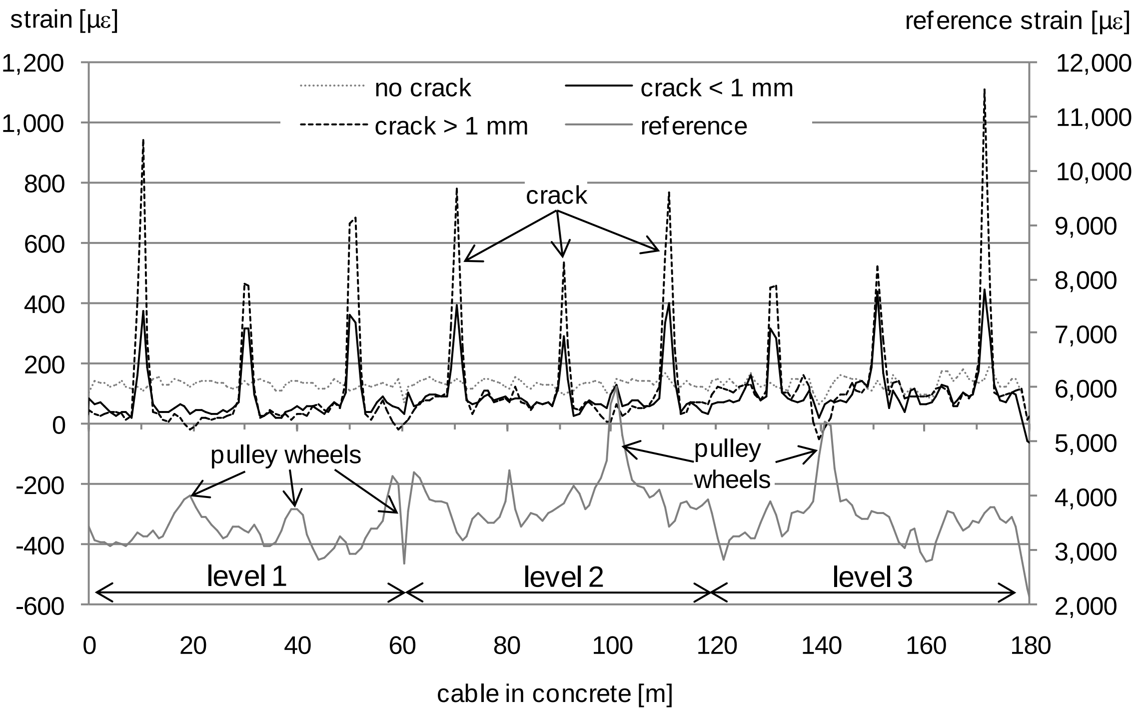

Fig. 7-28: Strain distribution along the cable in the RCC

Constantly higher strain in the "no crack"-measurement is a result of higher temperatures during that measurement in comparison to the reference measurement. The nine peaks that can be seen very clearly represent the strain sensing cable passing the crack nine times, increasing from the small (solid line) to the large crack (dashed line).

The large benefit of distributed strain sensing is its opportunity to develop an insight view of a large concrete body. With a well planned setup of the cables, distributed temperature sensing allows to produce interpolated temperature cross-sections through an entire dam to detect regions with high temperature gradients to gather information on potential regions that are susceptible to cracking. In the following, the same approach is pursued in terms of the direct detection of strain in the concrete structure. Figure 7-29 shows the strain development within the entire RCC block between 4 and 15 days after concreting. The strain is interpolated linearly within the measuring points. The measurements that were closest to the outside were extrapolated linearly to the outside edge of the block.

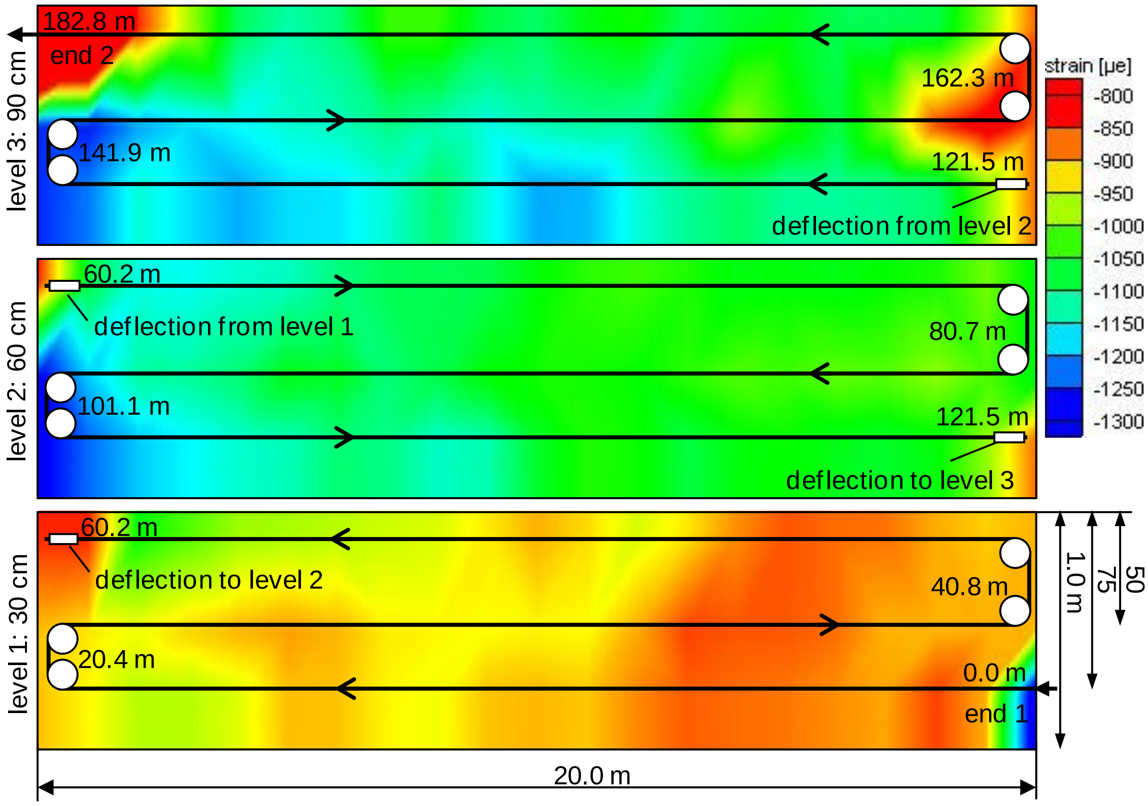

Fig. 7-29: Interpolated strain distribution in the instrumentation levels before a crack was visible (between 4 and 15 days after concreting)

The measurement traces that are shown in Fig. 7-28 start at “end 1” in the lowest instrumentation level (lower right in Fig. 7-29), lead through level 2 and leaving level 3 after 182.8 m in the concrete (upper left in Fig. 7-29). The cable meters inside of the RCC are marked in significant points. Uneven numbers result from the spatial resolution of the DTSS of 1.021 m. The displayed data show the strain development between 4 and 15 days after concreting without temperature compensation. Due to the decrease of the temperatures in the concrete that are affecting the Brillouin shift, strain values come out very low. Strain peaks can mainly be found in the ends of the block, where the cables come very close to the edge of the RCC, consequently being significantly influenced by the ambient temperature. The strain peaks at “end 1” and “end 2” are a result of the spatial resolution of the measurements as the cable is entering the concrete at those points where it is still affected by the ambient temperature. Strain peaks in the center of the beam that are considerably above the measuring accuracy cannot be recognized. The following figures show the strain development between a reference measurement, 15 days after concreting and the insertion of a small crack, 16, and a large crack 17 days after concreting.

After a small crack of less than 1 mm was forced into the RCC, the strain data shows a considerable change in its distribution (Fig. 7-30). The colored contour interval hereby ranges from -50 to 450 με. The increase in strain that is caused by the crack is visible throughout all three levels. Next to the crack, no considerable decrease of strain can be measured due to slip and spatial resolution. The compression thus negative strain, which is located at end 2, can be referred to the influence of the ambient temperature.

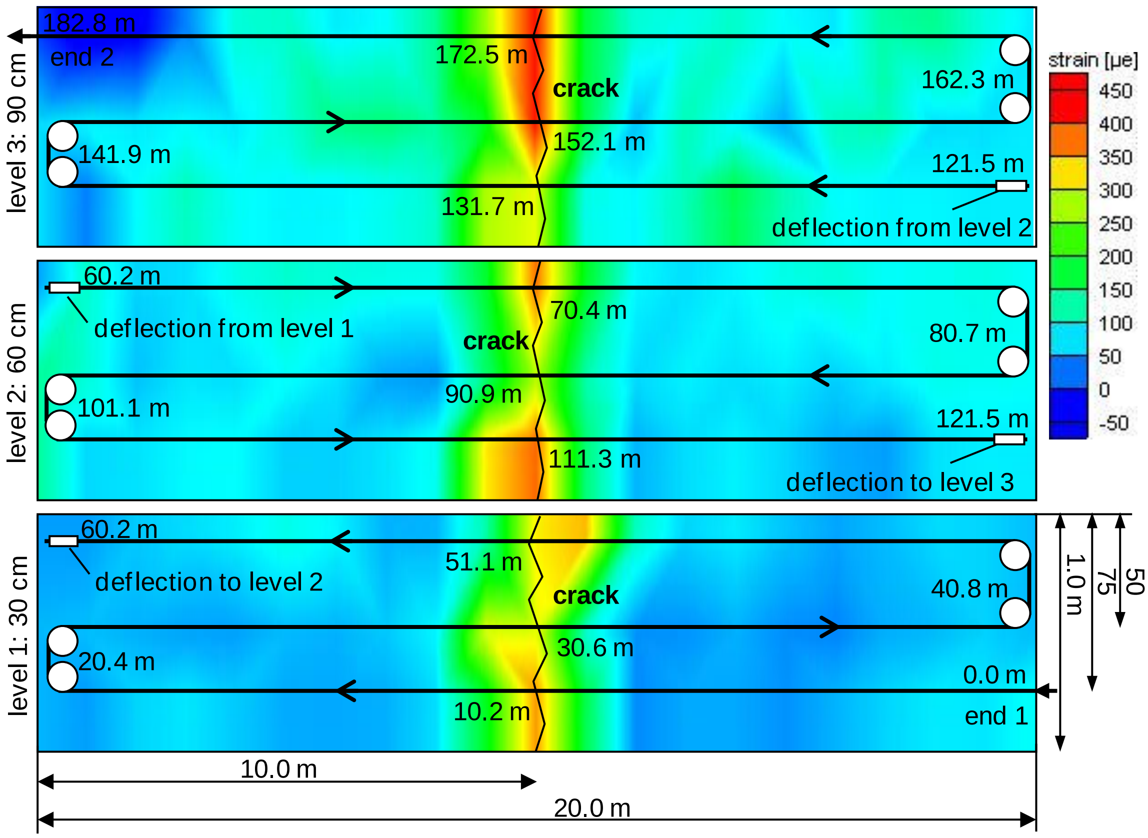

Fig. 7-30: Interpolated strain distribution in the instrumentation levels at a crack width of < 1mm

After the crack was widened, strain values within the cracked part raised up to more than 1,000 με (Figures 7-28 and 7-31). The strain distribution is very similar to the previous figure with higher strain values in the middle part of the block. The contour interval is the same as for the small crack. The rest is not affected.

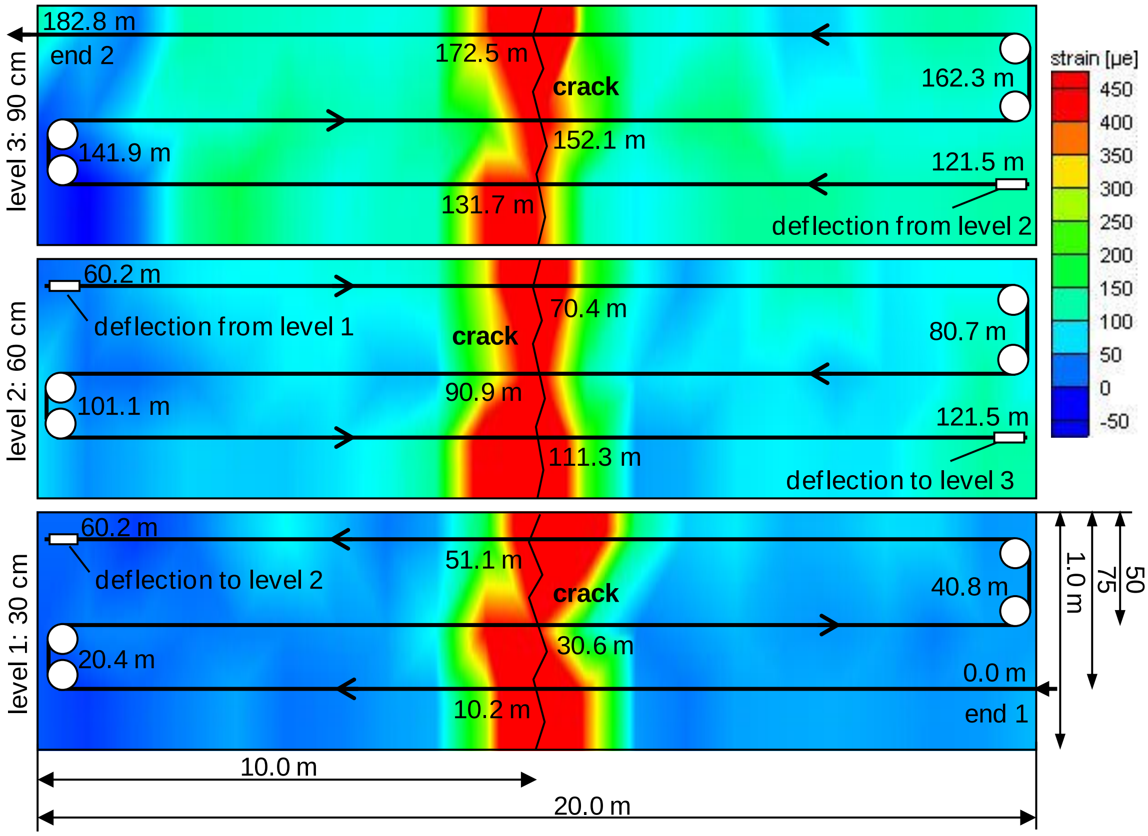

Fig. 7-31: Interpolated strain distribution in the instrumentation levels at a crack width of > 1mm

If the instrumentation layout is chosen very well, the strain occurrence in a structure can be evaluated not only in horizontal slices but could also show the strain within the longitudinal or cross section. Figure 7-32 shows the complete longitudinal strain distribution within the RCC block after the first crack was induced into the structure.

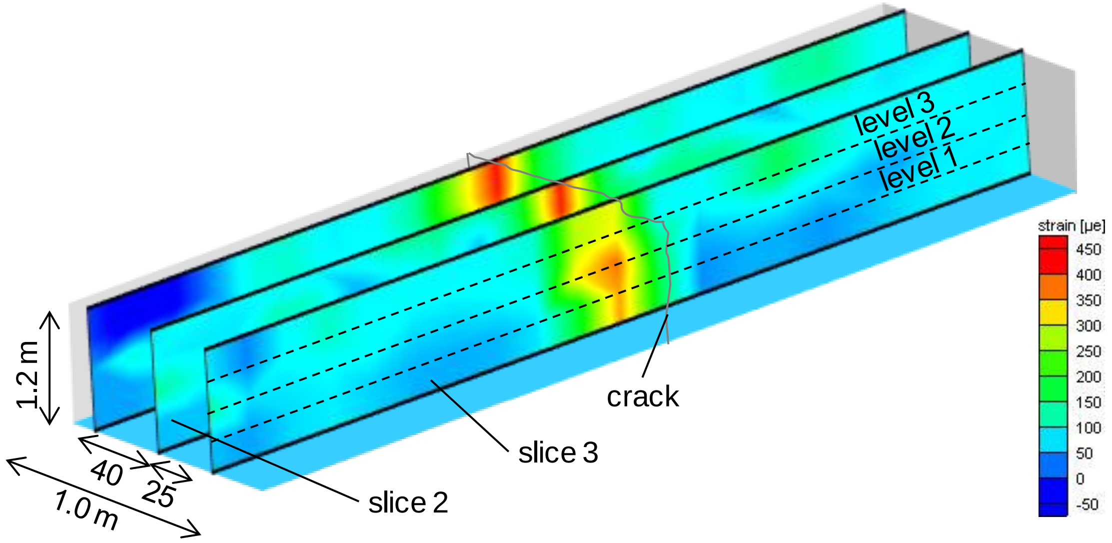

Fig. 7-32: Longitudinal-vertical strain-cross sections through the RCC block at a crack width of < 1mm

7.4.4 Evaluation of crack width in the RCC block

Laboratory test in chapter 6 show, that the evaluation of deformation of the fiber at spacings that are greater than the spatial resolution of the DTSS is possible and very accurate. As the total deformation equals to the crack width, this can be applied for the RCC block. According to the lab experiments, the strain of each peak from the measurements in Fig. 7-28 is integrated over the affected length. The result is the corresponding absolute deformation at each of the nine peaks, which is assumed to represent the crack width. This method is applicable as 3 to 4 DTSS measuring points in every cable section are affected by the crack. The crack width on the outside of the RCC block was very difficult to measure on the rough surface and varied in the heterogeneous concrete.

The numbers in Tables 7-2 and 7-3 show the crack width in all three layers in all three vertical slices of the RCC block towards the right, referring to Fig. 7-32. The mean crack width herby is 0.62 mm, which is in great accordance to the visually evaluated mean surface crack width of less than 1 mm.

Tab. 7-2: Crack widths of the small crack in the cross section

DTSS measurement [mm]	slice 1	slice 2	slice 3	visual inspection
level 3	0.70	0.55	0.46	
level 2	0.53	0.43	0.77	< 1 mm
level 1	0.74	0.67	0.68	

The crack width of the large crack in Tab. 7-3 varies between 0.72 and 1.56 mm at an average of 1.16 mm. This value is again agreeing with the observation of the surface crack width of more than 1 mm in average.

Tab. 7-3: Crack widths of the large crack in the cross section

DTSS measurement [mm]	slice 1	slice 2	slice 3	visual inspection
level 3	1.47	0.75	0.72	
level 2	1.10	0.78	1.50	> 1 mm
level 1	1.51	1.05	1.56	

Small variations from the actual strain widths can be expected as the fiber was not perfectly calibrated in the run-up of the experiments.

7.4.5 Crack detection with fiber Bragg grating strain sensors

Three FBG strain sensors were installed parallel to the strain sensing cable in the middle of the RCC block, where the crack was induced. Their locations in instrumentation level 2 and 3 are depicted in the view and the cross-section in Fig. 7-21. The measurements from the three FBG sensors during induction of the first, small crack are depicted in Fig. 7-33. The left graph mainly shows the large impact of the crack on FBG sensor 2, which is situated in the middle of level 2. The strain rises by more than 1,600 $\mu\varepsilon$ which is equal to 0.32 mm referring to the 20 cm measuring range of the FBG sensor. The equivalent DTSS value that is listed in Tab. 7-3 is 0.42 mm.

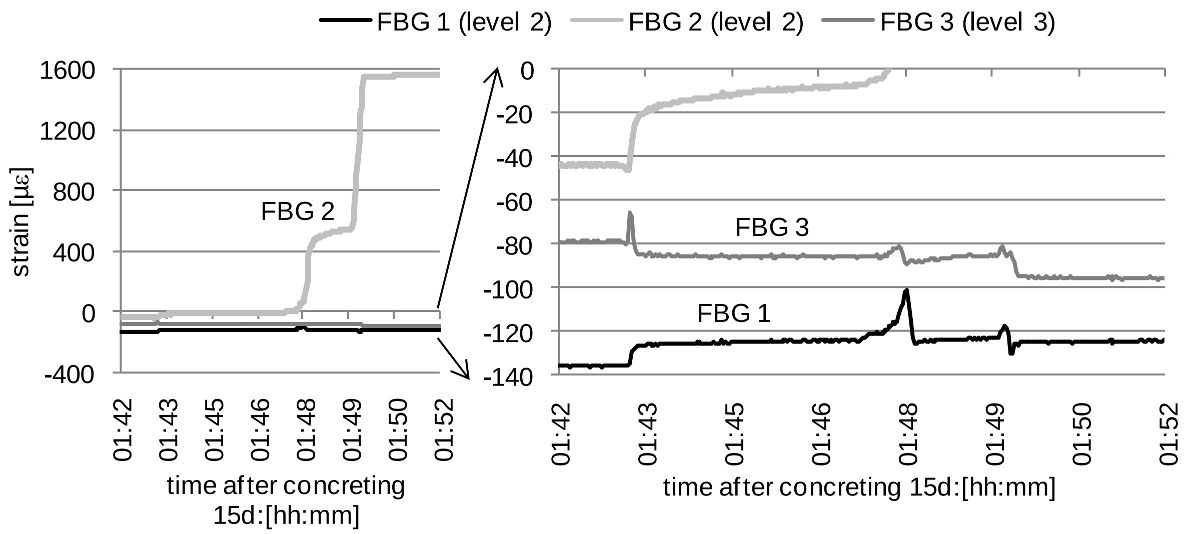

Fig. 7-33: Crack detection with FBG sensors in the RCC block

The right side of Fig. 7-33 presents an enlarged section of the left graph in order to show the changes of the other two FBG sensors in more detail. The FBG sensor 1 in level 2 shows an increase of strain of 15 µε and the FBG sensor in level 3 shows a decrease in strain of 20 µε. Obviously, the crack missed the two FBG sensors and consequently they only show very small changes in strain. The distributed strain sensing method is surely more suitable for the detection and evaluation of cracks in concrete, as their location is usually random. The calculations and the comparison with FBG 2 also show that the evaluation of crack widths in the range of 0.1 mm with the DTSS will be possible at lifelike conditions.

8 Strain measurements in the RCC dam Fundão in Brazil

8.1 Project “Hydropower plant Fundão”

The RCC dam Fundão in Brazil was equipped with vibrating wires, fiber Bragg grating temperature sensors and fiber optic cables for temperature sensing within the concrete. Strain sensing was carried out by 3 FBG strain sensors as they were also used in the tests in Obernach and for the first time ever, around 830 m special cable for distributed fiber optic strain sensing was installed into the RCC of the dam (Moser 2006; Hoepffner, Moser et al. 2007).

The RCC dam as part of the Hydropower plant (HPP) Fundão is 43 m high with a crest length of 446 m and impounds the water of Rio Jordão. It is located in the south of Brazil in the state of Paraná, 300 km west of the city of Curitiba, half way towards HPP Iguaçu. HPP Fundão is part of a chain of hydropower plants in Rio Jordão and has a total capacity of 122.5 MW. The dam was constructed of 163,000 m^3 RCC (Moser, Hoepffner et al. 2006) and 54,000 m^3 conventional vibratable concrete (CVC). The RCC and CVC concrete mixes are summarized in Tab. 8-1. With 50 kg/m^3 cementitious content, the RCC is considered low cementitious concrete (< 99 kg/m^3; ICOLD 2003). The base of the dam has an elevation of 667.0 m ASL in the center and the crest of the spillway is at 705.5 m ASL. The floor of the inspection gallery is at 672.25 m ASL.

Tab. 8-1: Concrete mixes (at 680 m elevation)

<table>
<tr><td colspan="2">component</td><td>RCC</td><td>upstream CVC</td></tr>
<tr><td colspan="2">cement [kg/m³]</td><td>50</td><td>209</td></tr>
<tr><td colspan="2">fly ash [kg/m³]</td><td>20</td><td>0</td></tr>
<tr><td colspan="2">free water [kg/m³]</td><td>130</td><td>174</td></tr>
<tr><td rowspan="4">[kg/m³]</td><td>retarder</td><td>1.3</td><td>0.84</td></tr>
<tr><td>0 - 0.63 mm</td><td>1191</td><td>963</td></tr>
<tr><td>0.63 - 25 mm</td><td>631</td><td>1103</td></tr>
<tr><td>25 - 50 mm</td><td>631</td><td>0</td></tr>
<tr><td colspan="2">unit weight [kg/m³]</td><td>2654*</td><td>2450</td></tr>
</table>

*theoretical air free density (TAFD)

The construction of the dam started in the Brazilian winter of 2005 and it was impounded for the first time in May 2006.

8.2 Installation of strain sensing cables

A unique measuring program was planned for the RCC dam Fundão. Some of the middle blocks of the dam were equipped with multiple fiber optic sensing devices and conventional vibrating wire temperature sensors for comparison (Moser, Soares et al. 2006). Two types of fiber optic cables were installed, 1.2 km of very rugged, steel sheathed cable for distributed temperature sensing in a cross section of the dam and roughly 830 m of special fiber optic cable for distributed strain sensing. The rather soft 5 mm dam cable which is shown in Tab. 5-1, was installed. It includes 2 single mode (SM) and 2 multi mode (MM) fibers, which are tightly packed within the cable for good strain transmission. The MM fibers allow redundant distributed temperature measurements with a Raman based distributed temperature sensor in the same cable. Redundancy for distributed strain sensing is given by the 2 SM fibers.

The installation of strain sensing cables in an RCC dam was never reported before and therefore it could not be referred to any experience of doing so. Several installations were made in reinforced concrete before, so some experience could be adapted from those (section 2.2.4). The installation was done by skilled local engineers. The complete fiber optic strain sensing installation with some pictures from crucial points is given in Fig. 8-1. The total length of the strain sensing cable is 830 m, which is installed in three of the 25 blocks. Five loops were separately installed in order to reduce the risk of losing measuring data in case of the damage of the cable, three in block 11 and one in block 9 and 15 respectively. The largest fraction of cable was installed close to the upstream edge of the dam. Loop 1 and 2 in block 11 were laid across the dam from the upstream (loop 1) to the downstream side (loop 2). The cable was pre-strained with 20 to 60 N by using weights and a tension spring balance. This equals strain between 1,000 and 5,000 με.

To receive a uniform pre-strain distribution, pulley wheels were used in some of the turning points as it is shown in pictures number 3, 7 and 8 in Fig. 8-1. This method was especially suitable for guiding the cable along the reinforcement steel of the waterstops where the pulley wheels could easily be attached. In other points, the cable was attached to metal wire with fabric tape, pre-strained and then locked into position by fixing the wire with a nail that was driven into the RCC. This option can be seen in picture number 1. The pre-straining of the vertically installed cable was achieved by hanging weights onto the cable that was guided around a pulley wheel that is attached to the reinforcement steel (picture 7). In places where the cable was guided along reinforcement steel it was additionally loosely attached with fabric tape at several meters spacing (picture 4). As the protection of the rather sensitive strain sensing cable is vital for the measurements, special efforts had been undertaken especially before each concreting step. In horizontal installations, a several centimeter deep trench was cut into the last layer of RCC before laying out the cables (picture 5 in Fig. 8-1). After all preparations on the cables were finished, the trench was filled up with CVC early enough so it could start to harden before the next layer of RCC was installed with heavy machinery. Other parts of the horizontal cable were installed into the CVC, up to only 20 cm from the upstream face. The CVC could be poured onto the cables without previous preparations. Vertical cable was attached to the vertical reinforcements that were concreted with CVC as well. No further protection measures were needed.

After all concrete works were finished, each fiber within the 5 cable loops was tested. The fibers of each loop with the lowest attenuation were connected to one entire fiber that could be measured without the need of changing connectors or the location of the DTSS. During installation, the cable completely broke in block 15 which was discovered but could not be fixed in time. Therefore the longer part of the cable in block 15 was connected as final part of the whole installation. One other break in loop 3 in block 11 could be repaired. The locations of the damages and other sources of loss are marked in Fig. 8-1. The connecting cables between the blocks are low price standard fiber optic cables with SM and MM fibers inside that were spliced to the fibers of the strain sensing cable. The measurements were carried out from block 11. Picture 6 in Fig. 8-1 shows the location and the instruments inside of the inspection gallery. In the final setup, the DTSS was connected to the end of the fiber that leads towards block 9 followed by block 11, loop 1, loop 2, loop 3 and block 15 in the end.

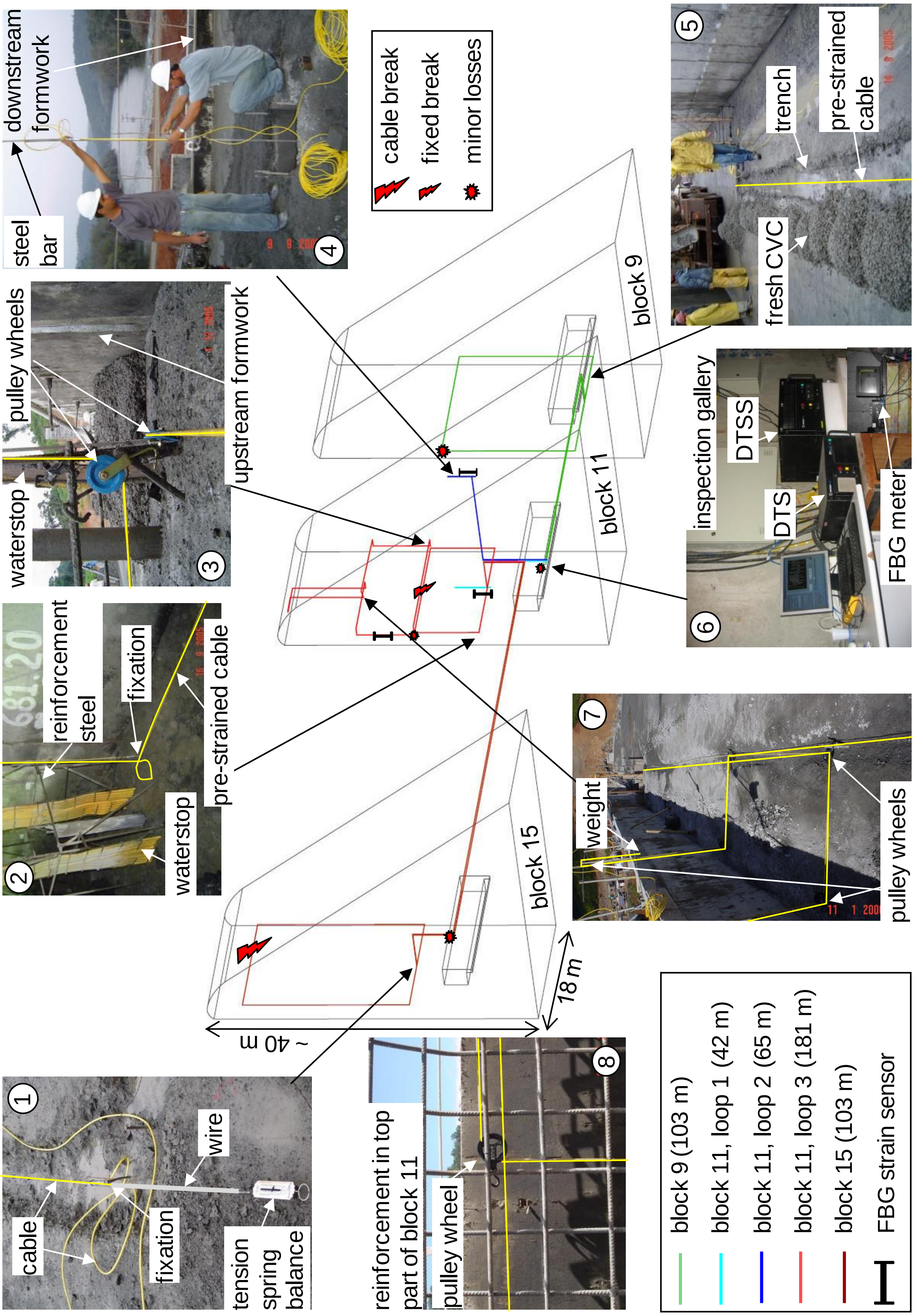

Fig. 8-1: Installation of the strain sensing cables in the RCC dam

The OTDR trace of all connected loops in Fig. 8-2 shows the amount of loss in the fiber and the situation of local sources of attenuation, regarding fiber length after the connector to the DTSS. The cable break in block 15 terminates the measuring section. The reflections and considerable loss in loop 3 originate from a break in the cable that was noticed and splice under rough conditions during concreting. After the fiber was spliced, it was placed into a splicing cassette and packed into a plastic bag to protect it against moisture.

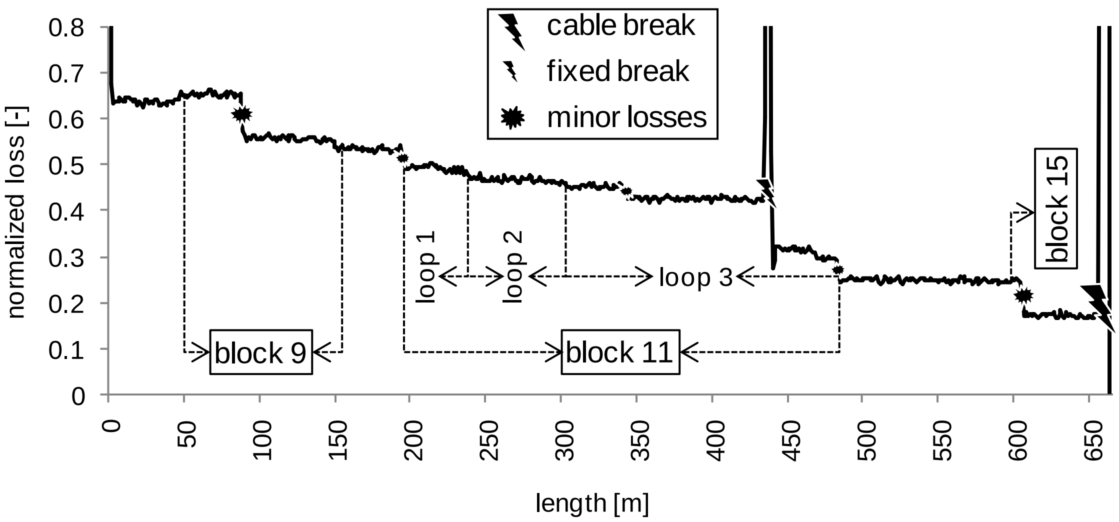

Fig. 8-2: OTDR reading of the entire DTSS cable until the cable break

The local loss in block 9 is located in a turning point where the cable is fixed with a nail as previously described. The small losses at the beginning and in the end of block 11 are losses from the splicing and the local attenuation at roughly 600 m is situated at the point where the cable enters the concrete after it was guided vertically through an instrumentation tube.

8.3 Strain measurements during impoundment

Strain measurements were carried out during the 5 days of first impoundment between May 15 and 20 in the year 2006. The measurement time of the DTSS was set to 15 minutes during the whole time. The data that is presented in the following is not temperature compensated for the sake of strain resolution. Therefore, only those measurements were used that have been taken in the morning hours of the according day at close to uniform ambient conditions. An analysis of the effect of automatic DTSS temperature compensation by using Brillouin power is given in section 8.5. As described in the previous section, the measurements were taken from one steady place in the inspection gallery for almost 5 days straight. The second cable part in block 15 was not measured during impoundment.

Figure 8-3 shows the reference strain reading at the first day of measurements in the entire fiber. The peaks in the measurements with considerable negative values mostly are the location of the splice connections. The first 50 m of cable lead from the DTSS device to block 9. In block 9, the cable was pre-strained in sections. At 150 m, the cable leads back to block 11 and into the concrete at loop 1, the section of cable, which leads across the dam towards the upstream side. This section was relatively weakly pre-strained. The next section is loop 2 that leads across the dam towards the downstream side and back, followed by loop 3. It stands out that the strain values in loop 3 stay at high values throughout the whole block as the cable was guided and entirely pre-strained using pulley wheels with no zero-strain nail-fixed points.

In the damaged part of the fiber, the strain values show randomly high or low values due to reflections of the light in the fiber. On the way to block 15, the cable was placed in a water bath, which was used for strain and temperature calibration as described in section 5.3. On the rest of the way, the cable was guided through a plastic tube along the ceiling of the gallery. The measurements end at the break of the fiber in block 15 after 657 m of measured fiber.

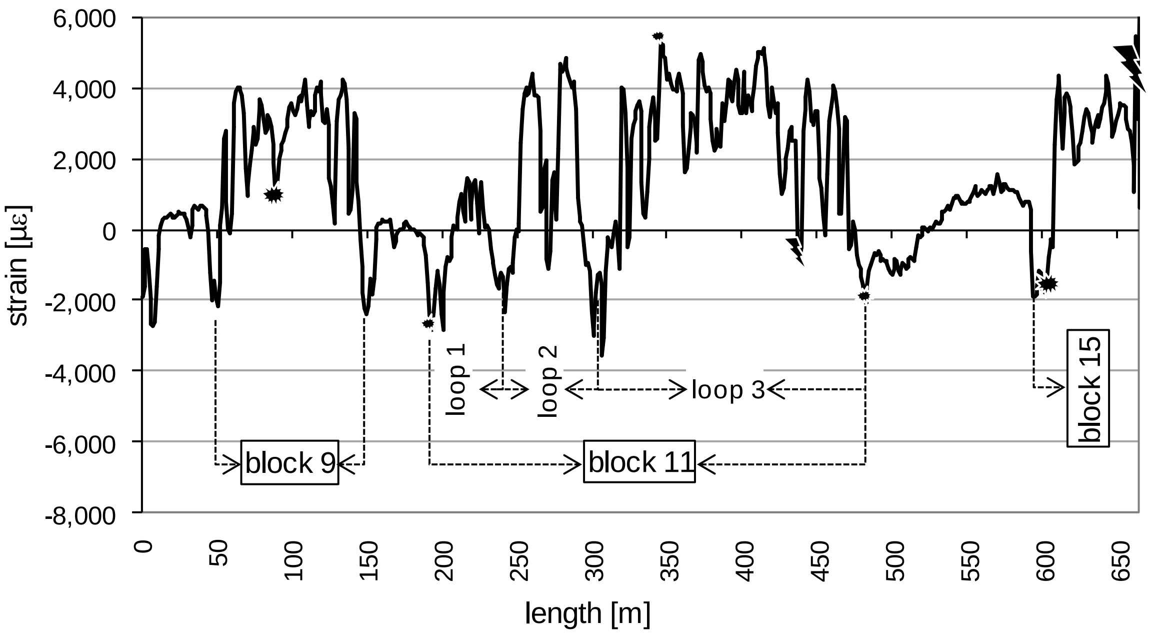

Fig. 8-3: Reference measurement before impoundment

The cable section in block 9 is enlarged in Fig. 8-4 to show the difference between fixed cable sections and cable that is guided through a pulley wheel. While the strain in the fix points is distinctively low, the pulley wheel is only affecting the pre-tension marginally, just enough to notice its location. Pulley wheels have the advantages of less installation work, safer cable guidance with a predetermined bending radius and a continuously pre-strained cable. Furthermore, sudden changes of strain that appear at fix points cannot optimally be determined at a spatial resolution of 1.021 m.

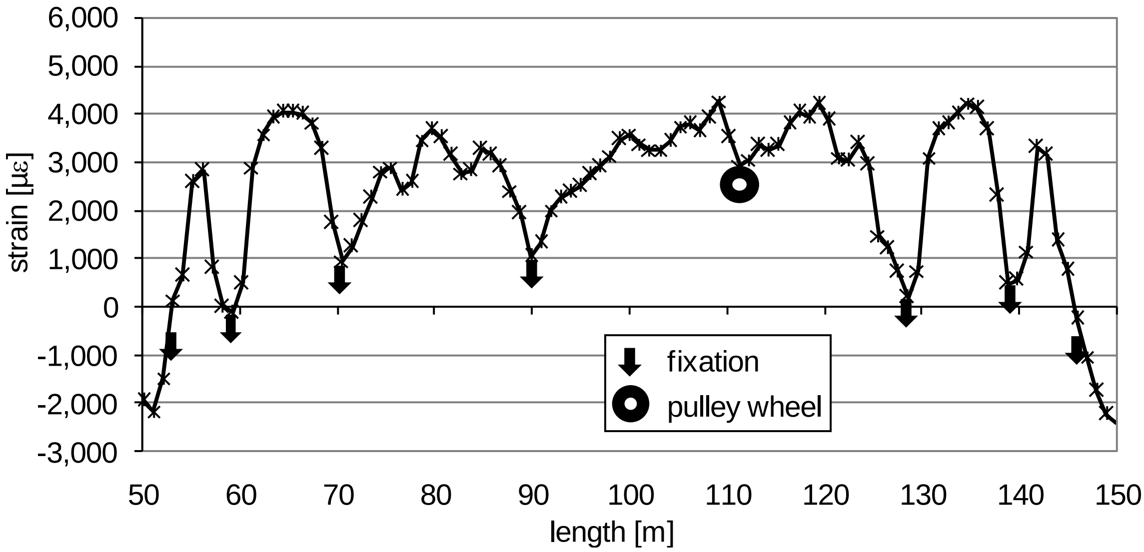

Fig. 8-4: Reference strain measurement in block 9 (green in Fig. 8-1)

The temporal developments of strain during the 5-day impoundment in three significant cable sections are displayed in Fig. 8-5. The measuring point that is represented by the solid black line is located in the horizontal part of loop 2 at 680.3 m ASL in the very center of the dam. The gray lines show the strain measurements in the upper parts of the cable in block 9 (689.1 m ASL, solid gray) and 11 (704.8 m ASL, crossed gray). The locations of the measuring points are also sketched into the 3D view of the blocks in the upper right part of Fig. 8-5. At an elevation of 704.8 m ASL, the horizontal top part of the cable in block 11 is located only 70 cm below the crest of the spillway and only a few decimeters away from the upstream edge of the concrete. The location is reflected in the variations in Fig. 8-5 that follow the development of the ambient temperature with a little delay. In block 9 and in the center of the dam, this development can also be observed but with a delay of 12 hours. The temperature in the center of the dam can be expected to develop very slowly, not due to ambient influences but rather due to the hydration heat that is present. Referring to the calibration coefficients for temperature and strain in Tab. 5-2, a Brillouin shift that represents a change of 100 με would be equal to a daily temperature change of 1.9 K in the concrete.

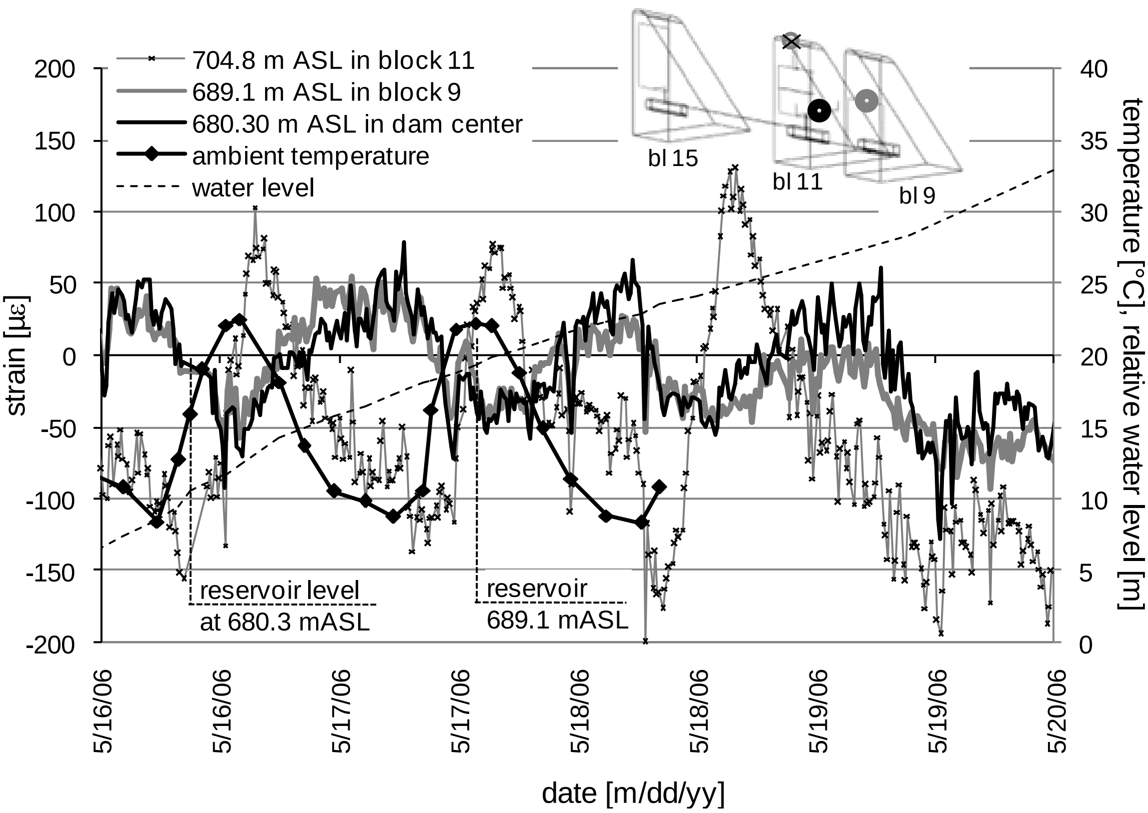

Fig. 8-5: Strain development in 3 significant locations in block 9 and block 11

To verify the assumption of no crack development in the dam during the first impoundment, the differences in the strain readings from the first measurement when the impoundment started to the last measurement just before the water overtopped the crest of the spillway are depicted in Figures 8-6 to 8-8. The strain scale is different in every figure in order to allow a clearer view on locally strained regions.

Figure 8-6 shows the strain development in the cable sections of block 9 and 15 that are facing the upstream side of the dam. Strain measurements were carried out without compensating for temperature. Consequently, the strain values, which are generally very low, are a result of decreasing concrete temperatures that are affecting the Brillouin shift and thus are interpreted as changes in strain. The only points that stand out are the blue sections on the left side of block 15 and the right side of block 9, which however indicate compression at a very low amount of around 50 με comparing to the rest of the fiber.

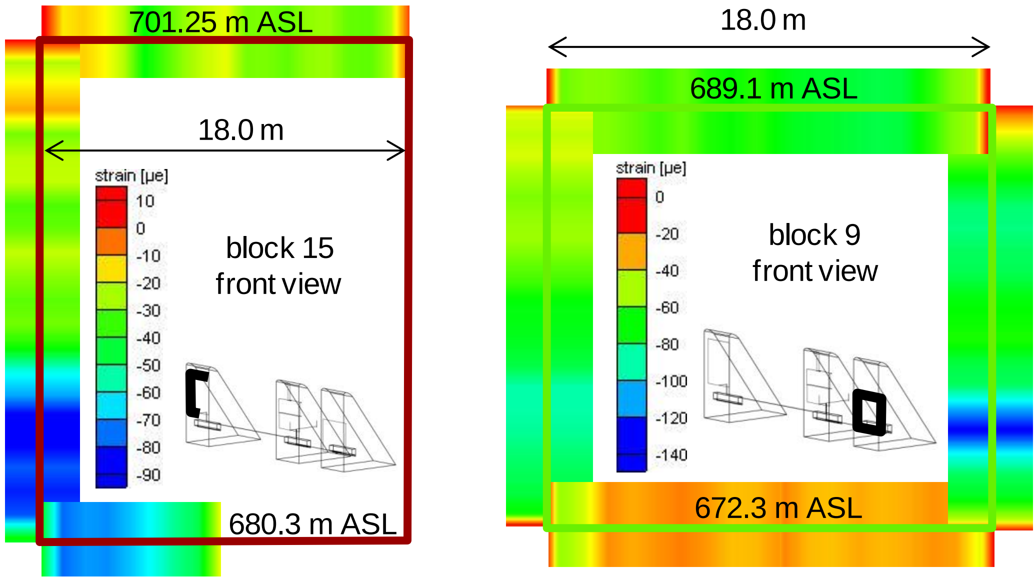

Fig. 8-6: Strain development during impoundment in blocks 15 (left) and 9 (right)

The colors in Fig. 8-7 indicate low strain values in the upper part of block 11 and up to 100 µε higher values in the middle and lower part. As the considered measurements were taken the morning hours, this again shows a thermal influence. The lower part is already affected by the water temperature of the reservoir (16.0 °C) which is higher than the ambient temperatures during nighttime. Additionally, cracks would appear as very distinct sections of considerably higher strain.

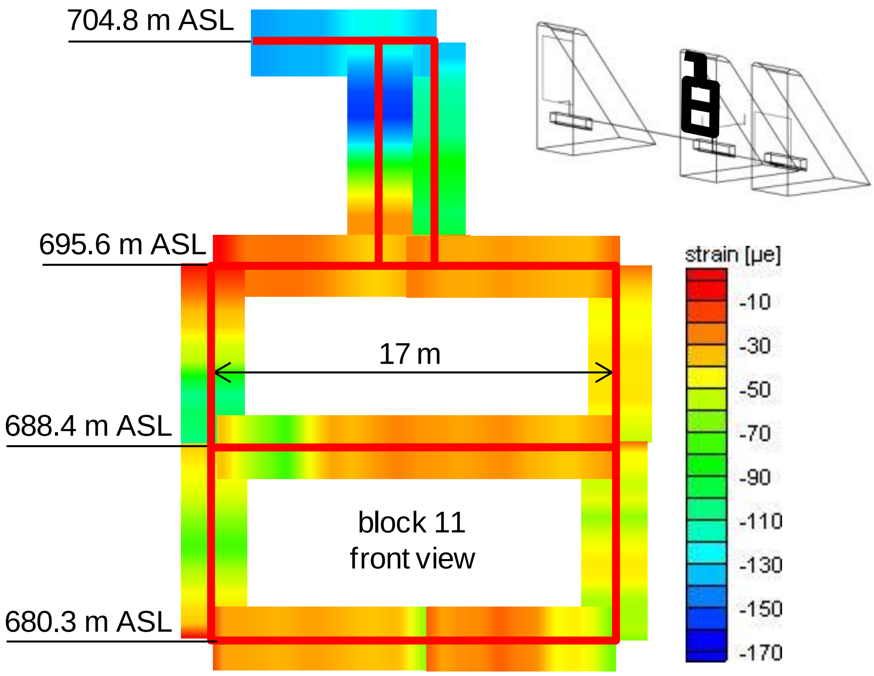

Fig. 8-7: Strain development during impoundment in block 11

Figure 8-8 shows the changes in strain during impoundment in the cable loops 1 and 2. The cable was laid across the dam and then vertically along a 5 m long steel bar on each side. Except for the compression in the downstream vertical part of the cable, the orange colored part of the cable slightly towards the upstream face from the center of the dam shows local strain. This value however differs from the greenish rest by 20 με only, which is equal to the resolution of the sensing device. However this section with very local strain should be further monitored in the future as it might indicate the formation of a longitudinal crack.

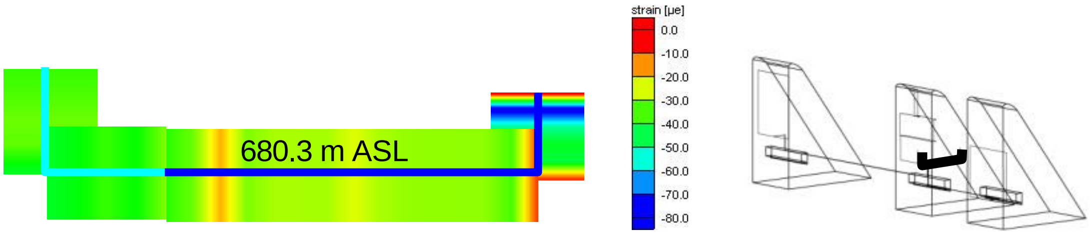

Fig. 8-8: Strain development during impoundment in the cross-section through block 11

Even though the measurements were made during first impoundment of Fundão dam, no significant changes of strain or the development of cracks could be observed. This is in accordance with Andriolo (1998) who states, that among others, ambient temperature changes are the main source of cracks, rather than the load from the water. Additional measurements several months or years after the presented ones could give more meaningful information on the appearance of cracks or openings of horizontal joints. The water temperature of the reservoir would then be quite steady and the heat from hydration will be mostly vanished. Temperature differences between the measurements should however be cancelled out by taking simultaneous DTS temperature measurements to compensate the strain measurements for temperature.

8.4 Comparison with Fiber Bragg Grating sensors

Three FBG strain sensors were vertically installed into the dam next to the strain sensing cable. As depicted in Fig. 8-1, two FBG sensors were installed next to the cable in loops 1 and 2 on the upstream and the downstream side at an elevation of 680.3 m ASL, 3-4 m away from the surface of the dam. The third FBG sensor was placed next to the strain sensing cable in loop 3 at an elevation of 690.4 m ASL. Figure 8-9 shows the whole recorded strain data set. The impoundment took place between May 15 and 20. The rising water level can be seen in the significant rise of the two FBG sensors at 680.3 m ASL. The sensor in loop 2, which is located close to the downstream side of the dam, shows a strain increase of 18 με during impoundment that is slowly decreasing afterwards. The rise of strain in the same level on the upstream side of the dam is lower with only 10 με, which decreases again right after the impoundment was complete.

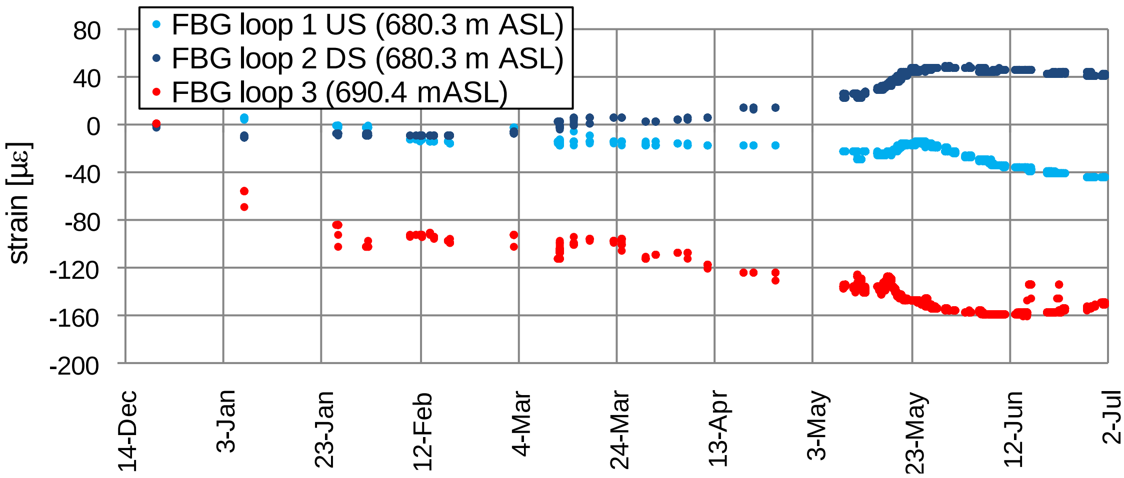

Fig. 8-9: FBG strain sensor readings during impoundment

All three FBG sensors indicate a rise in vertical strain during impoundment. The development before the impoundment can primarily be connected to the cooling of the concrete as the hydration heat is dissipating. The decrease after impoundment, which is considerably higher on the two upstream FBG sensors can be referred to the temperature effect in the FBG reading as it is also not temperature compensated. In loop 3, the FBG sensor is installed only about 50 cm from the upstream face of the dam. The sensor in loop 2 is located about 3 m from the upstream face and in loop 1 about 4 m from the downstream face.

In Fig. 8-10, the strain values from the FBG sensors are compared with the DTSS measurements. The measured strain values at the specific cable parts, where the FBG sensors are located, are compared with the FBG measurements of two sensors, the rise of the water level in the reservoir and the ambient temperature. The DTSS measurement varies by ± 60 με following a 12 h delay from the ambient temperature. The effect of the rising reservoir level becomes visible in the DTSS measurement in the end of the curve when the peaks of the strain data are damped. The following variations are only ± 30 με. This is obviously an effect of the reservoir water at 15.9 °C that is damping the temperature variations. This appears as strain in the not-temperature compensated mode. The rise in strain that was measured by the FBG sensors cannot be confirmed by the DTSS measurements as it is beyond the strain resolution of the DTSS device.

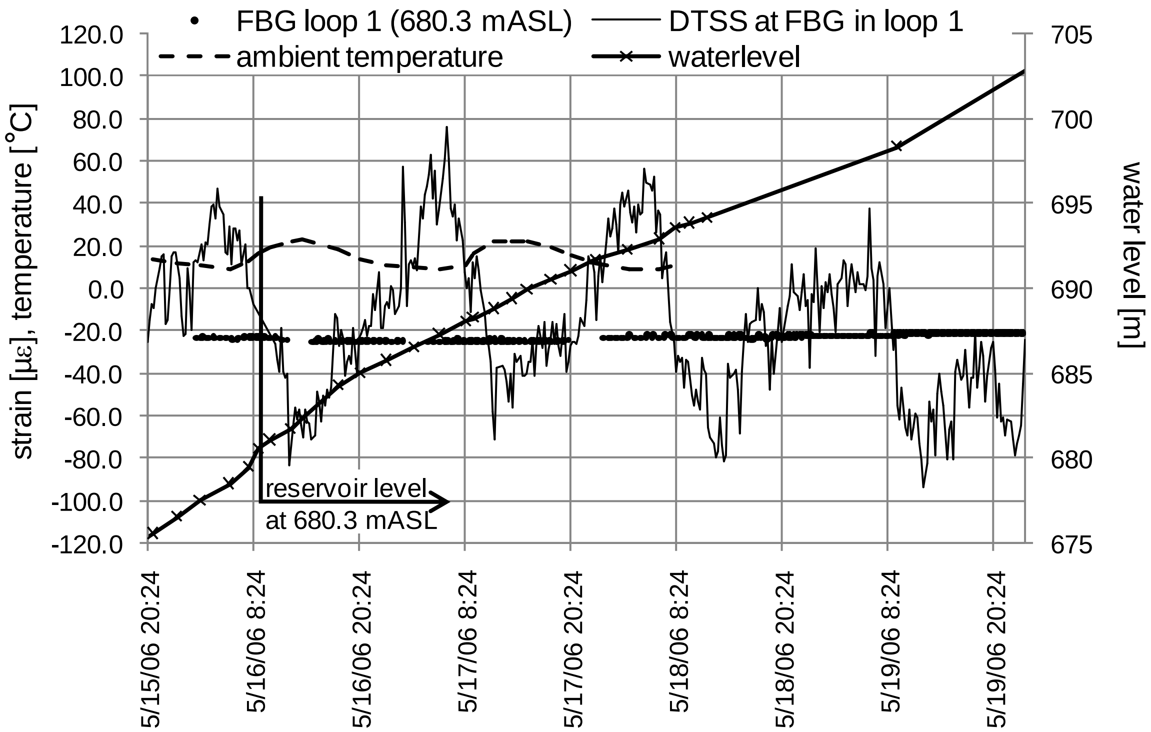

Fig. 8-10: Comparison with the FBG sensor in loop 1 at 680.3 m ASL

The measuring point that is compared in Fig. 8-11 is located in loop 3 only about 50 cm away from the upstream surface of the dam at an elevation of 690.4 m ASL. Referring to the FBG sensors and sensing sections further inside of the dam, the strain variations at the FBG sensor in loop 3 are higher. The DTSS measurements follow the ambient temperature again and vary by ± 80 με until the effect of the rising water level leads to a quite significant damping of the values again with a delay of about 12 hours. The up and down movement of the FBG sensor data could not be indicated by the DTSS strain readings due to insufficient strain resolution.

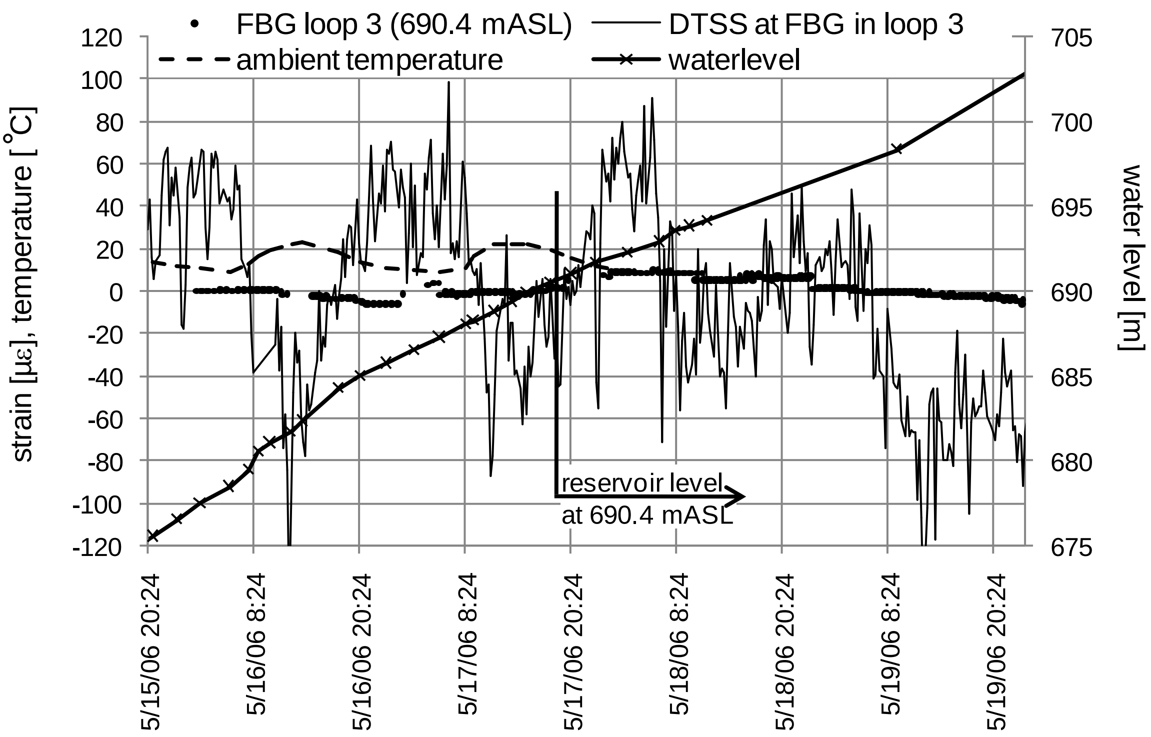

Fig. 8-11: Comparison with the FBG sensor in loop 3 at 690.4 m ASL

The duration of the measurements with the DTSS was limited to the days during impoundment, so a long time comparison of the two strain sensors was not possible. Assuming the entire amount of the Brillouin shift in the strain sensing fiber inside of the dam is referring to changes in temperature, it can be evaluated by using the calibration coefficients.

Figure 8-12 shows the temperature developments in the fiber sections at the FBG sensors that are directly calculated from the Brillouin shift using the temperature coefficient C_T. The uppermost line represents the raw Brillouin shift in the cable at the FBG sensor in loop 1. The temperature in loop 2 (dark blue), close to the downstream side of the dam varies within ± 1 K, which seems very reasonable as this side is facing towards south, thus representing the shadow side of the dam. The colors refer to the overview in Fig. 8-1.

The temperature influence in the cable part at the FBG sensor in loop 1 (light blue, thin) is more affected by the ambient temperature and the sun radiation than at the FBG sensor in loop 2 with variations of ± 1.5 K and a significant decrease towards the end of the measurements. The cable at FBG sensor 3 (red) is affected by the temperature changes the most with up to ± 2.5 K, as it is only installed several decimeters away from the upstream surface of the dam.

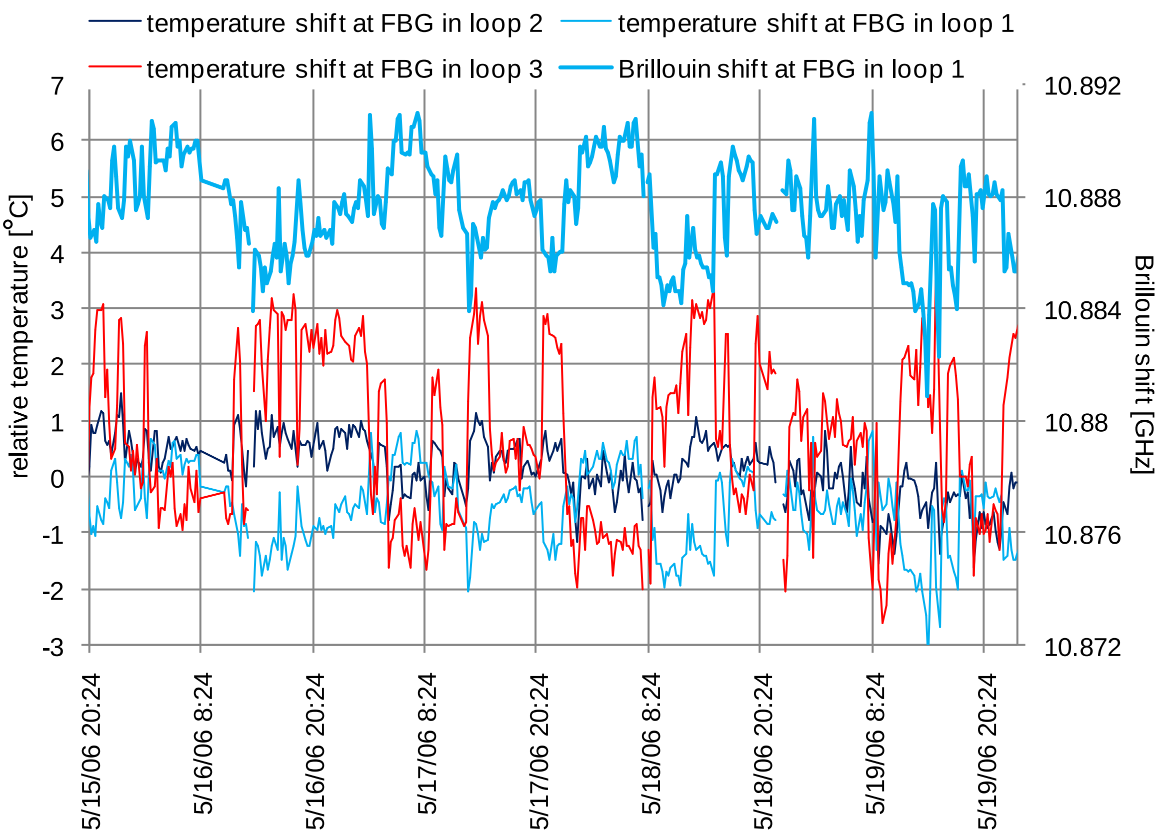

Fig. 8-12: Comparison with FBG sensor in loop 1 at 680.3 m ASL

8.5 Effects of temperature compensation using Brillouin power

Brillouin shift is depending on temperature and strain in the specific fiber section. Transferring Brillouin shift into strain without accounting for Brillouin shift due to changes in temperature, results in raw, not temperature compensated strain (section 3.3.4). The Sensornet DTSS system is capable of separately evaluating strain and temperature in the same fiber section at the same time. The temperature is calculated from changes in power of the backscattered Brillouin shift, which is mainly depending on changes in temperature at a specific point in the fiber. The referring equations are given in section 3.3.4. Having both, the total Brillouin shift and the change in temperature, the Brillouin shift due to temperature can be calculated and subtracted from the total Brillouin shift. The remaining shift can be calculated into strain using Eq. 3-7. This represents the temperature compensated strain. The Sensornet DTSS does the temperature compensation automatically, outputting raw and compensated strain data. The measurements that were presented in all previous tests were not compensated by automatic DTSS temperature calculations using Brillouin power. This section presents the effect of the automatic DTSS temperature compensation on the measuring data on the example of strain measurements in the RCC dam in Fundão. The quality of the temporal development of the measurements is evaluated by calculating the standard deviation of the strain data that was recorded during the 5 days of impoundment (Eq. 8-1).

$$\sigma_X = \sqrt{\frac{\sum_{i=1}^{n}(X_i - \overline{X})^2}{(n-1)}} \qquad \textit{Eq. 8-1}$$

σ_X	standard deviation
n	number of samples
$\overline{X}$	mean of measurements

Applying the standard deviation to the raw strain values that were not temperature compensated by any means, the curve in Fig. 8-13 can be plotted. Significant uncertainties appear at points of fixation, splice connections and at places with local losses. The standard deviation is very low with values of seldom more than 70 με even though the strain was not temperature compensated. In the water bath between block 11 and 15, the standard deviation is 10 με. This shows that the raw strain measurements are very robust and consistent despite some local sources of loss are present in the first 500 m of the fiber.

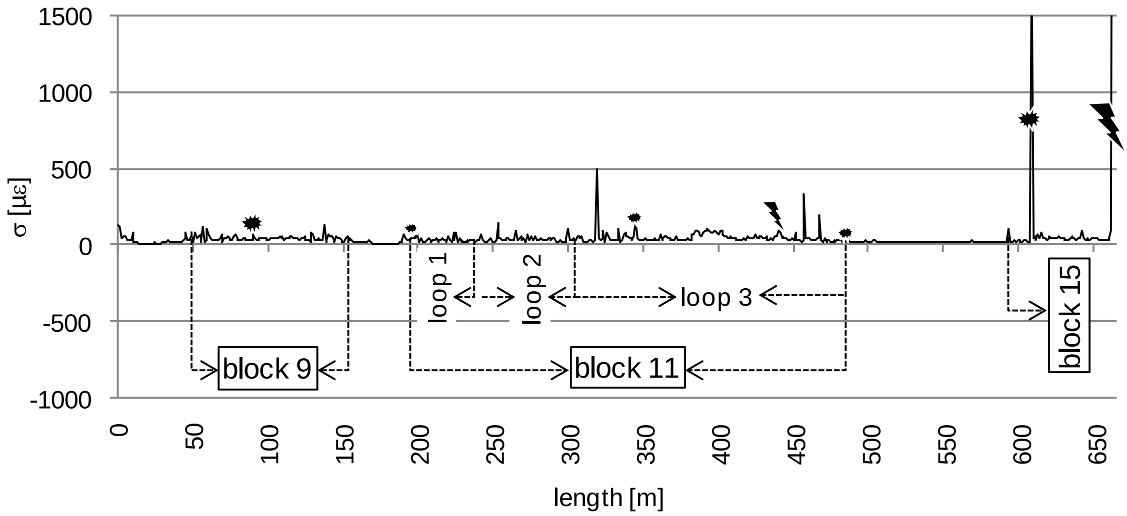

Fig. 8-13: Standard deviation of raw strain data along the fiber in the dam without temperature compensation

The DTSS temperature compensation is supposed to cancel out the influence of temperature. Figure 8-14 shows the standard deviation of the automatically temperature calibrated strain versus the length of the fiber. Comparing this curve with the strain measurements from Fig. 8-3, the qualitative shape of the curve is quite similar. The amount of strain in the fiber seems to be directly connected with the quality of the DTSS temperature compensated strain measurements. The dashed line shows the polynomial trend in the standard deviation and illustrates a significant rise with increasing fiber length. A sudden decrease of quality especially after the cable damage in loop 3 cannot be identified.

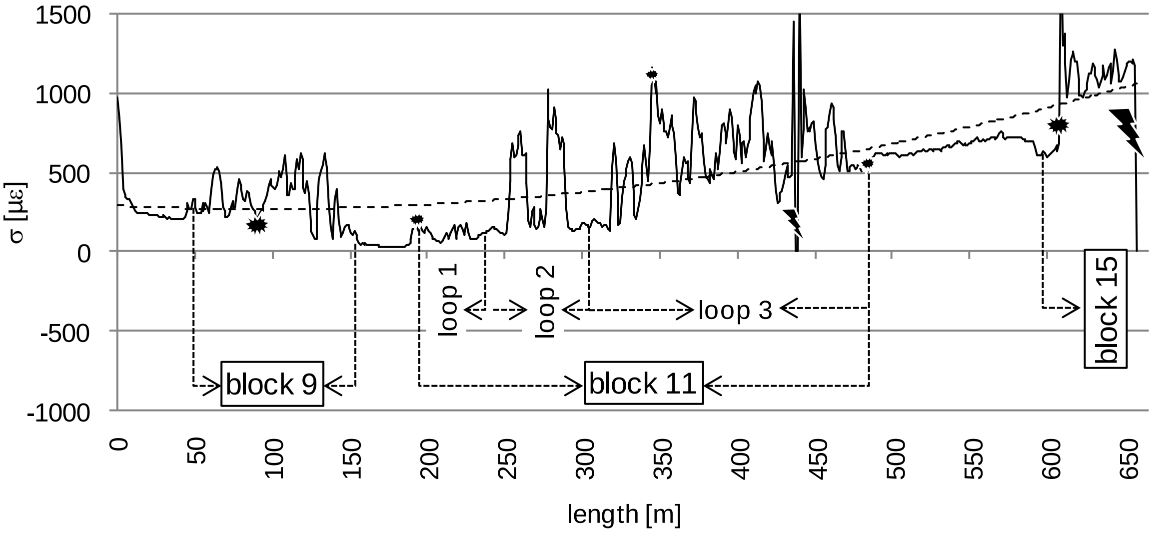

Fig. 8-14: Standard deviation of automatically DTSS temperature compensated strain data along the fiber in the dam

While the pre-strained cable allows good localization of the fixation points, the drawback when automatically compensating for temperature is a considerable rise in noise at rising strain levels, which was also reported by Li, Parker et al. (2004). This relation is also applying to the present tests, which can be seen in the graphs in Fig. 8-15. They show the dependence of the strain level to the standard deviation in two cable loops that were installed into the dam. At strain values between 1,000 and 3,000 με, the standard deviations significantly increase, which means, that the quality of the measurements decreases. At the maximum strain in loop 3 of 7,000 με, the standard deviation reaches values of up to 1,100 με.

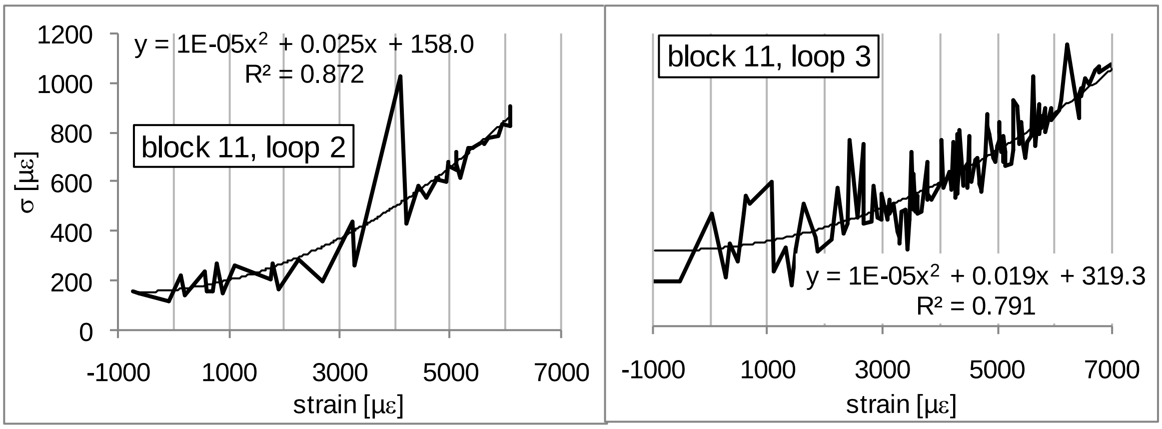

Fig. 8-15: Standard deviation versus strain in cable loops 2 and 3 in block 11

Distributed Brillouin sensors are able not only to detect strain but also longitudinal compression of the fiber as discussed before. Pre-straining is therefore not implicitly necessary and should be kept to a very minimum in order to guarantee more reliable measuring results when using temperature calibration by Brillouin power.

The present evaluations show that automatic DTSS temperature compensation by evaluating the Brillouin power should in most cases not be used for the sake of quality. Best results are achieved by using raw strain values where the influence of temperature can be neglected or cancelled out. Cables with multiple fibers inside allow temperature compensation by parallel distributed temperature measurements using a DTS system.

9 Laboratory tests on distributed strain sensing in embankment dams

9.1 Introduction

The boundary conditions for the installation of distributed strain sensing cables in earth structures like embankment dams are very different from the installation into concrete as the bond between earth and cable is depending on stress perpendicular to the cable, thus the depth where the cable is installed. Johansson and Watley (2004) reported on the installation of strain sensing cables into 5 embankment dams in Sweden. The following tests show the general possibility of installing strain sensing cables directly into soil materials as they are mainly used for filters in embankment dams. Using a heavy-duty press at the University of Innsbruck, the installation of the cables in different depths of a dam can be simulated.

9.2 Material properties

The two dam cables that are displayed in Tab. 5-1 were installed into material of two different grading curves (Fig. 9-1). The first one is a 4/8 mm gravel, the other one a widely stepped 0/16 mm gravel. More silty or clayey material could not be used in those tests as the time for the pore water pressure to disappear after loading would have exceeded the available time.

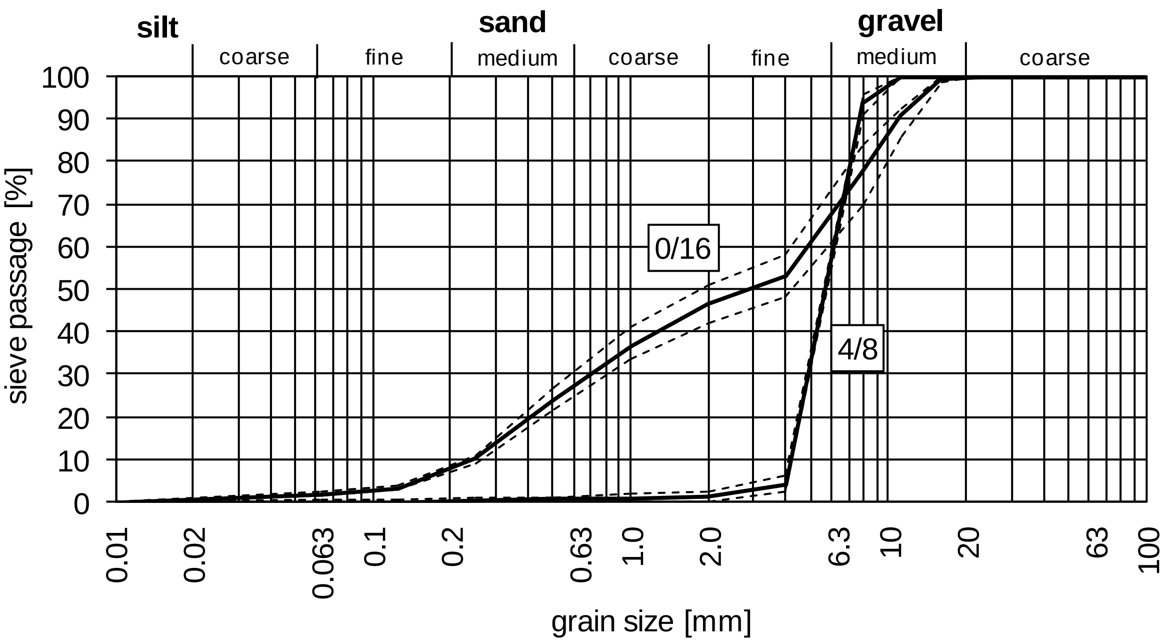

Fig. 9-1: Grading curves of the two soil materials

The water content and the bulk density of the materials were evaluated from the loose material before installing. The stiffness moduli of both materials were estimated from their deformation at the highest load steps, which was considered elastic, by using Eq. 9-1.

$$E_s = \frac{\Delta\sigma}{\varepsilon'}$$ *Eq. 9-1*

E_s	stiffness modulus [MPa]
$\Delta\sigma$	stress difference [MPa]
ε'	strain [-]

Table 9-1 shows the properties of both materials. The grains of the 4/8 gravel were considerably rounder than of the 0/16 material. It was therefore assumed that the cables would more likely be damaged from the 0/16 material. The 4/8 gravel was additionally used as filter for draining water for both tests in the bottom 10 cm of the test apparatus.

Tab. 9-1: Material properties

material	4/8 grit	0/16 grit
		
installation	filter, test 1	test 2
bulk density [kg/m³]	1,500	1,630
water content [%]	1.18	2.19
stiffness modulus E_s [MPa]	87.0	44.0

9.3 Test setup

The aim of the tests in soil material was to evaluate the influence of vertical stress on two types of cable in two types of material and the slip of both cables at different vertical stresses. It is expected to receive information on the advantages and disadvantages of softer or stiffer, more rugged cables and their behavior in different depths in soil material. The main parts of the test setup were a strongly reinforced steel box with internal dimensions of 3.78 m length, 68 cm width and a height of 60 cm, a high capacity press that can apply a maximum pressure of 1,600 kN and a 3 m long and 30 cm wide I-profile steel beam (Fig. 9-4, 507 kg) with shear force reinforcements in the middle section. The maximum vertical stress that can be applied on the 0.9 m² soil surface is consequently close to 1.8 MPa (1,800 kN/m²). In order to protect the steel box from plastic deformation, the maximum stress for this test was limited to 1.6 MPa. Vertical stress on the horizontally buried cable can roughly be estimated from the overburden stress of the soil material by using Eq. 9-2.

$$\sigma = \gamma \cdot z \qquad \textit{Eq. 9-2}$$

σ	overburden stress [Pa]
γ	bulk density [N/m³]
z	depth [m]

At a bulk density of compacted soil material of 20 kN/m³ and a maximum load of 1.6 MPa, the maximum simulatable depth of the cable in a dam can be estimated to 80 m.

For the evaluation of slip in soil material at different depths, a pulling mechanism was designed. Figure 9-2 shows the plan view of the installation, Fig. 9-3 on the left the cross section through A-A. The solid cable sections inside the soil material are loosely laid out and therefore are only affected by changes in vertical stress. The dashed cable sections are initially also loosely installed, thus are affected by vertical stress, but can additionally be pulled by the pulling mechanism which is depicted on the right in Fig. 9-3. The polystyrene and the formwork panels were used to fill the space between the sides of the steel tray and the soil material that was supposed to be compacted by the plunger. A 10 cm filter layer of 4/8 mm gravel was placed on the bottom of the steel box followed by 15 cm soil material (4/8 in the first test and 0/16 in the second), where the cables were placed on top. Another 15 cm of soil material was placed on top of the cables.

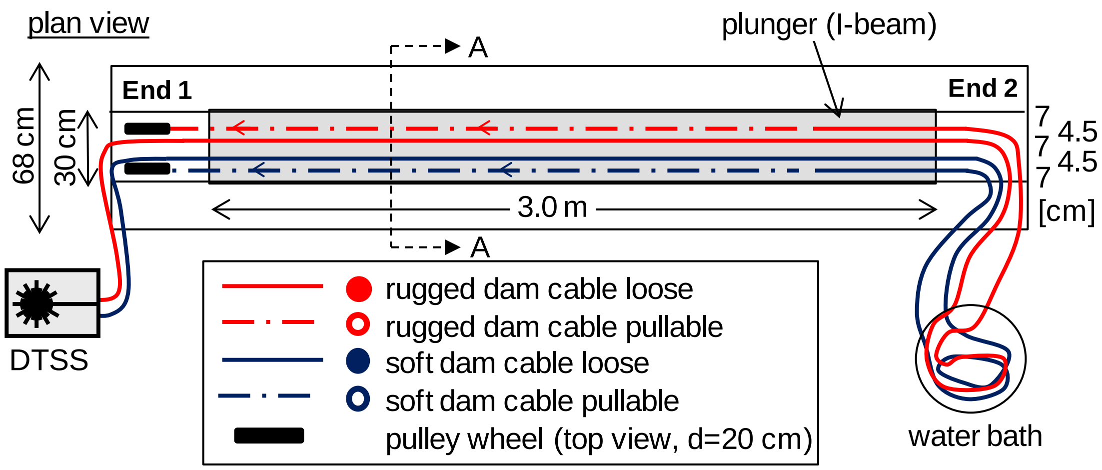

Fig. 9-2: Plan view of the test setup

To keep the initial humidity of the material constant and to assure a perfect horizontal plane for the plunger for uniform pressure, a 1 cm thick layer of sand was placed on top of the soil. After the first test, the material was removed (except for the filter layer) and the 0/16 material was installed.

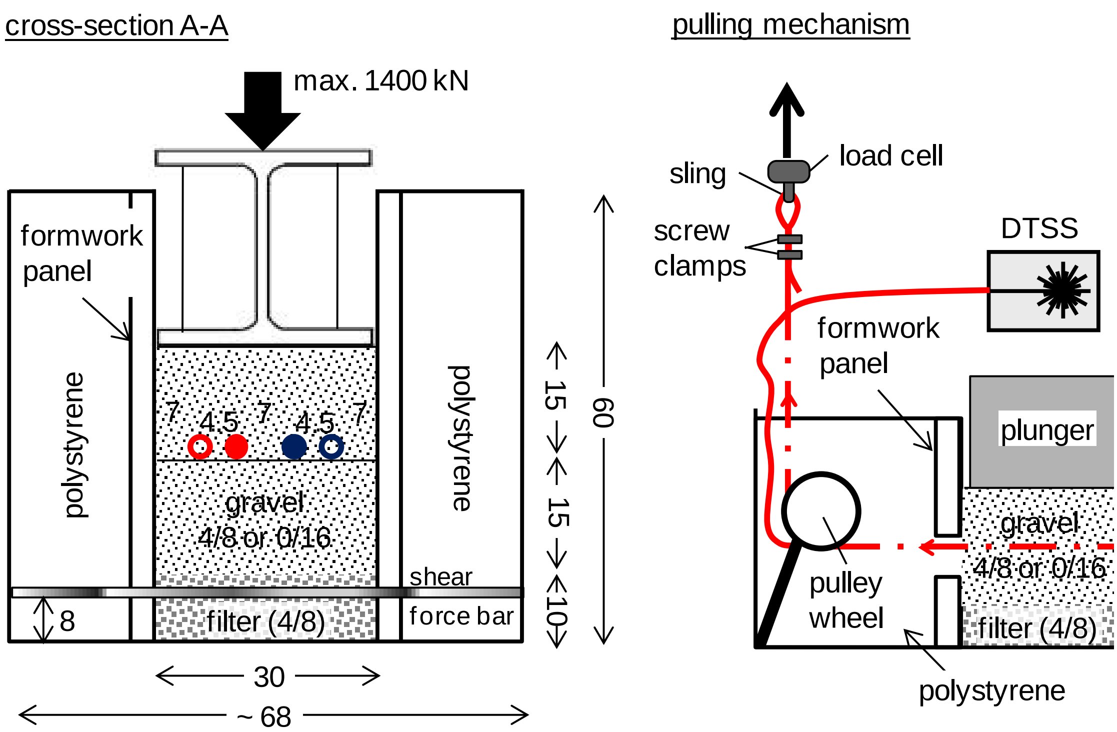

Fig. 9-3: Cross section of the test setup and pulling mechanism (units in cm)

At one end of the steel box the cables were loosely guided into a water bucket (reference section) and then back into the soil material (Fig. 9-4). On the other end of the box, one end of each cable was clamped into the pulling mechanism that was equipped with a distance laser and a load cell. The pulling mechanism was vertically installed over this end of the steel box. The other ends of the cables were connected to the DTSS.

Fig. 9-4: Photos of the test setup

A PT100 thermocouple was placed into the water bucket and connected to the DTSS. A few mm space was left between the plunger and the formwork panels to allow free sliding.

9.4 Execution of the tests

The two soil materials were tested one after another. As the 4/8 mm gravel was expected to be less harming for the cables, this was tested first. As vertical deformations of the soil material were expected during loading, the press was adjusted in a way that the pressure was kept constant during the pullout tests to ensure constant vertical stress. The pullout tests were carried out during two load steps, one at a vertical stress of 0.7 MPa, the second at full load of 1.6 MPa. Before and after the pullout tests, the load of the press was increased in steps of 100 or 200 kN and the strain was measured after each load step. The OTDR trace was monitored to identify potential fiber damage and to stop further loading before breaking a fiber. The same procedure was carried out for both soil materials. The cable sections inside the steel box and thus the soil material are summarized in Fig. 9-5. An equivalent system is introduced for better visualization of the data in the upcoming graphs. The soft cable in 0/16 gravel material was not tested.

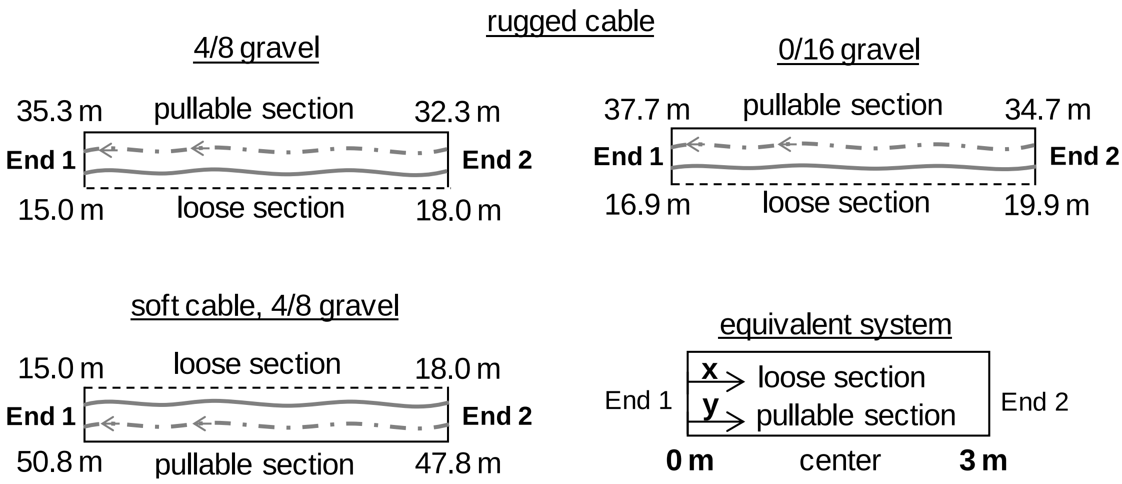

Fig. 9-5: Cable meters at the entrance and exit of the tested soil material

9.5 Influence of soil material and vertical stress on cables and fibers

The most important issue is to insure the integrity of a cable that is installed into a structure. Optical fibers will crack as a result of excessive strain or bending. Excessive strain can be reduced by controlling the slip within the cable. The first parts of the cables that run through the soil material cannot be pulled and thus are only affected by vertical stress from the press. Losses in the rugged cable in 4/8 material at no stress and maximum stress are shown in the OTDR trace in Fig. 9-6. The normalized power indicates losses at the connector and at the splice between the pigtail and the dam cable. Following the setup, the cable is first passing the soil material where it is only affected by vertical stress. In the end section, it is additionally pulled at constant load steps.

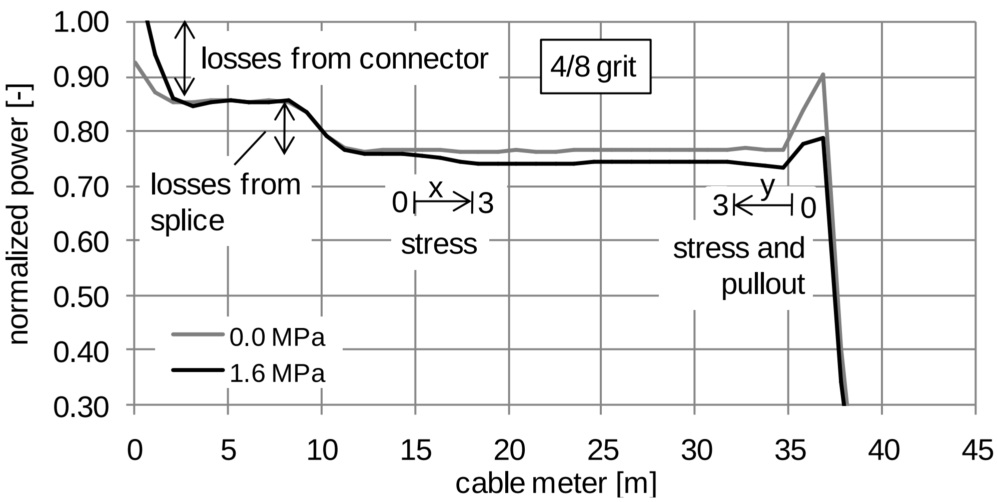

Fig. 9-6: Losses in the rugged cable at minimum and maximum stress

The OTDR trace only shows very small losses even at maximum load in both sections. A different picture shows Fig. 9-7 where the losses in the rugged cable in 0/16 material are shown at 3 vertical stress steps. While no losses can be noted in the stress-only part of the cable at 0.9 MPa vertical stress, losses increase in the second section of the cable. At the end of the pullout tests at 0.7 MPa, those losses were not visible, yet. When increasing the stress to the maximum, the losses in the second part of the cable increase drastically while they are considerably lower in the first, the stress-only-part. The explanation could be the impact of a single stone in the heterogeneous 0/16 gravel leading to microbending of the measured fiber.

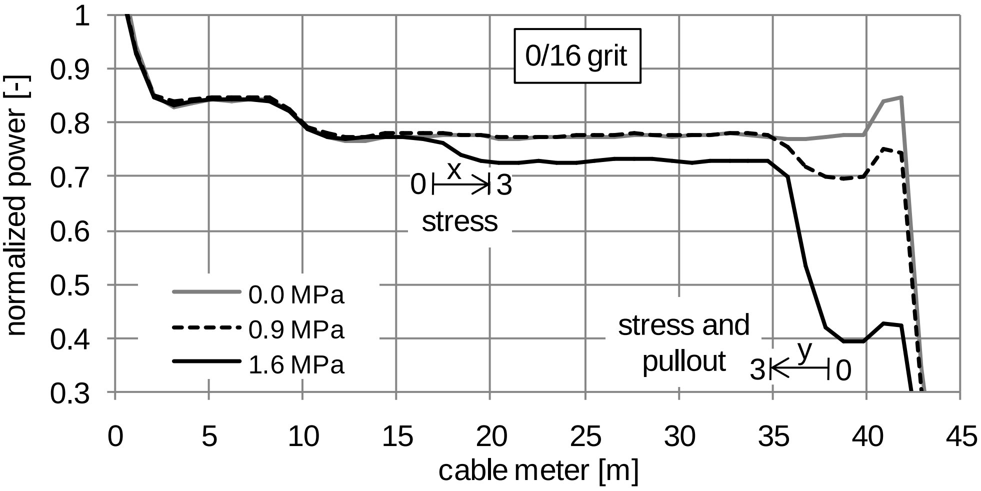

Fig. 9-7: Losses in the rugged cable at minimum and maximum stress

The two photos in Fig. 9-8 show the rugged cable after testing in 4/8 material on top and in 0/16 material in the bottom picture. Many small marks in the cable mantle can be seen in the upper picture while the lower one shows a single strong mark. This pattern could be observed along the entire embedded cable. The vertical deformations of the 0/16 material were considerably higher than of the 4/8 material during loading. As the 0/16 material has a higher heterogeneity, vertical deformations are in addition more differential with larger stones being able to puncture the cable. Vertical deformations of the narrowly stepped 4/8 material were smaller and more uniform. Additionally, the stones were very round with quasi no spikes.

Fig. 9-8: Rugged cable after testing in 4/8 (top) and 0/16 material (bottom)

The hysteresis in Fig. 9-9 shows the behavior of the losses when loading and then reducing the vertical stresses on the rugged cable in 0/16 material. All losses disappear after a while after completely unloading the soil. The losses are also depending on the compactness of the packing as they decrease slower than they initially increased.

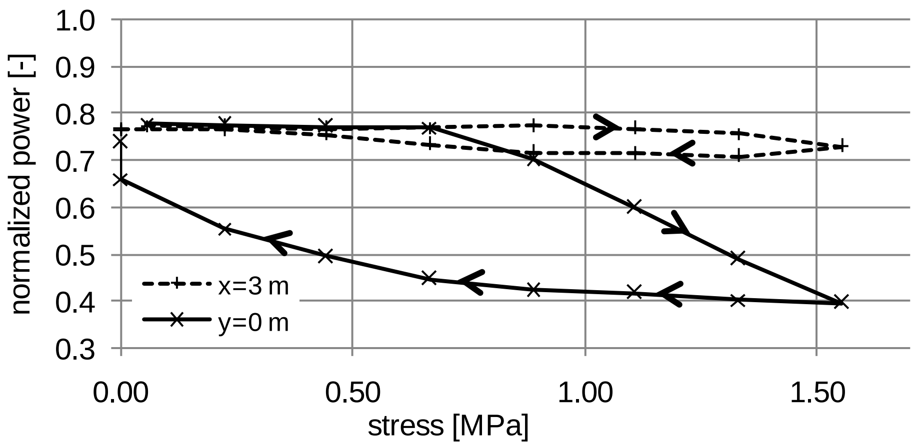

Fig. 9-9: OTDR behind the embedded rugged cable part in 0/16 gravel

The soft dam cable was installed next to the rugged cable. It showed considerably higher losses when applying stress. Figure 9-10 shows the losses in the 4/8 material at half and full load.

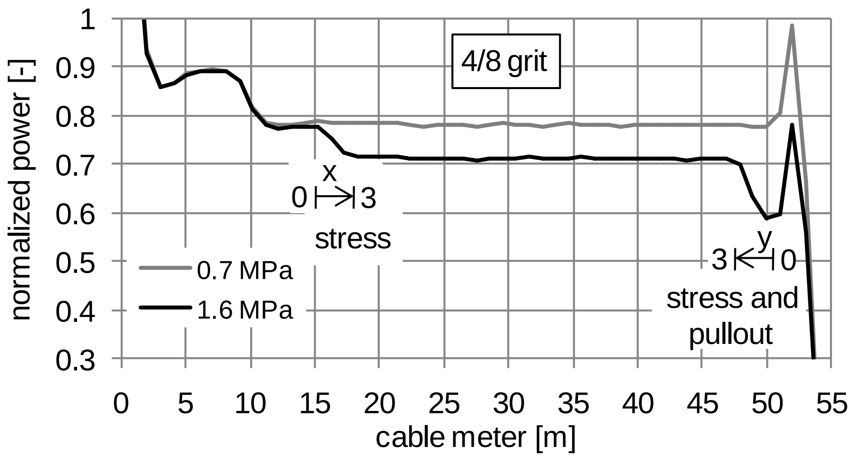

Fig. 9-10: Loss in the soft cable at half and maximum load

While the losses in the same material in the rugged cable were 0.02 power units or less per passage in the same load step (Fig. 9-6), the losses in the soft cable are around 0.1 power units per passage.

All cables in both soil materials could be loaded to the maximum without breaking. Microbending due to differential vertical and some horizontal deformations of the soil, can be considered the main source of the losses. When the power of light that is propagated along the fiber becomes weaker, the quality of strain measurements decreases as the signal-to-noise-ratio (SNR) decreases. High loads in soil material should therefore not be applied to those cables over a very long section as the losses sum up. The losses that occurred in the present tests were small enough not to affect the quality of strain measurements.

9.6 Influence of soil material and vertical stress on strain measurements

Bending and strain along the cable, which are initiated from differential vertical and horizontal deformations of the soil material, lead to elongation of the cable. To cancel out residual strain from the pulling tests, the strain values in the following were evaluated for the stress-only-sections. An influence of pressure on the fibers, discussed in section 3.3.2 for hydrostatic pressure, can be neglected. The strain in the rugged cable in Fig. 9-11 shows that the maximum strain value in both materials is very similar with close to 2,000 με at full load. The reason for the differing strain distributions can again be connected to the heterogeneity of the soil material which causes elongation and bending of the cables.

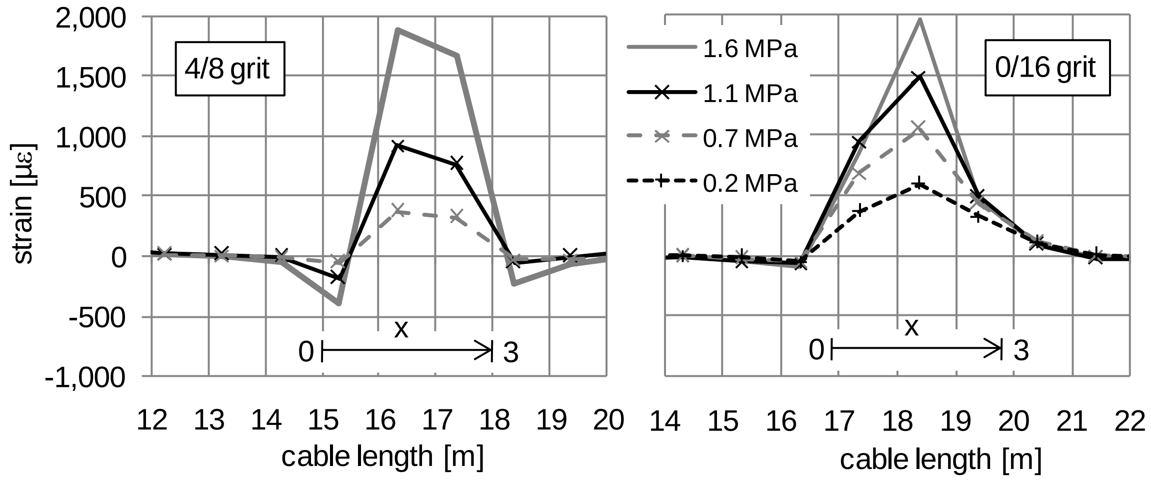

Fig. 9-11: Strain due to vertical stresses in the rugged cable

Strain measurements in Fig. 9-12 show the affected DTSS measuring points of the rugged cable in both soil materials. The rise of strain at maximum load indicates ongoing non-elastic vertical, lateral and longitudinal deformation of the soil material, leading to deformations and consequently strain in the fibers.

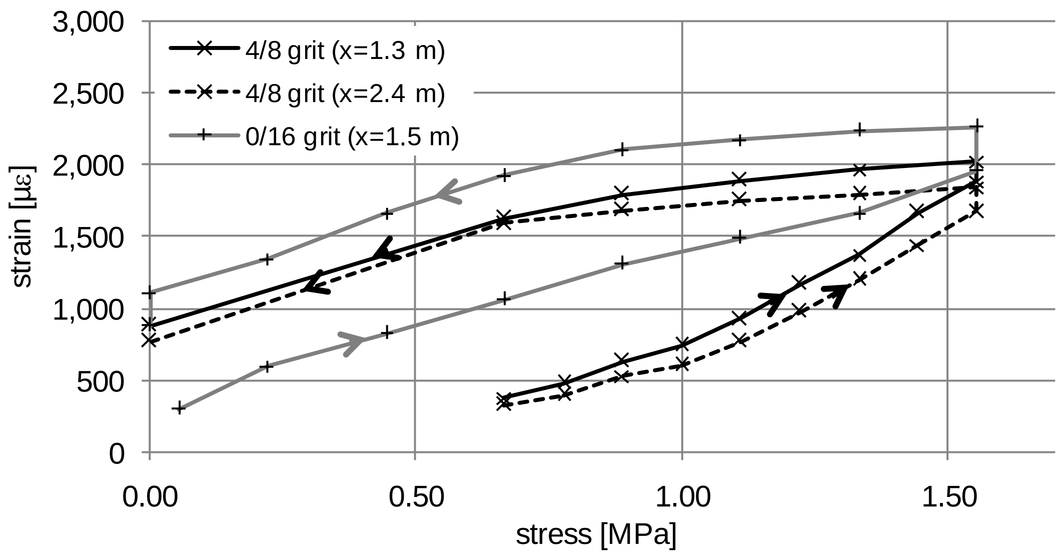

Fig. 9-12: Strain hysteresis of the rugged cable under load

At this stage of testing it seems very keen to generalize the strain development in specific cables due to stress for different soil materials. The soil material was not entirely compacted so non-elastic deformation took place. However an estimation for the dependence between stress and strain could be made by introducing a relation like Eq. 9-3.

$$C_{\sigma_\perp} = \frac{\partial\varepsilon}{\partial\sigma_\perp} \qquad \textit{Eq. 9-3}$$

$C_{\sigma\perp}$	stress coefficient [με/MPa]
$\sigma_\perp$	vertical stress [MPa]
ε	strain [με]

Referring to the strain development in the affected cable parts in Fig. 9-12, the stress coefficient $C_{\sigma\perp}$ could be calculated from the strain-stress development in the releasing part of the curve above 1.0 MPa stress, which is assumed to behave elastic. For the 4/8 material, the factor can be calculated to 290 and 350 με/MPa for the 0/16 grit. More tests would be necessary to validate a linear and repeatable relationship between grit size, stress and measured strain.

9.7 Load transfer between soil material and cable

Pullout tests were carried out at 0.7 and 1.6 MPa vertical stress for each soil material. A test in 4/8 material without applying stress except from the 15 cm overlying material showed that the cables started to move after applying only a few Newton pullout force for both cable types. Some slip could be noticed during the tests, which could be mainly referred to slip in the pulling rig. Strain development versus pullout force for the rugged cable in 4/8 material is depicted in Fig. 9-13. The increase of measured strain along the cable between the two vertical stress steps can be referred to strain due to the increase of vertical load as discussed in the previous section. The dashed line refers to strain just outside the steel box on the pulling side (y = -0.4 m). The solid black line represents the first measuring point inside of the gravel (y = 0.6 m), the grey line a measuring point in the center of the soil material (y = 1.6 m). The strain in the first measuring point of the 4/8 material rises with rising pullout force but even decreases after around 700 N for both vertical stress levels. This can partly be referred to a toothing effect, which appears when the grains of the soil material hook into the cable mantle and thus hinder the movement at greater loads. As no slip of the cable through the soil material could be observed, the following decrease is the result of slip and strain distribution within the cable at high loads. The measuring point in the center of the 4/8 material is not affected even at loads of more than 1 kN, which indicates a very good force transfer between cable and soil.

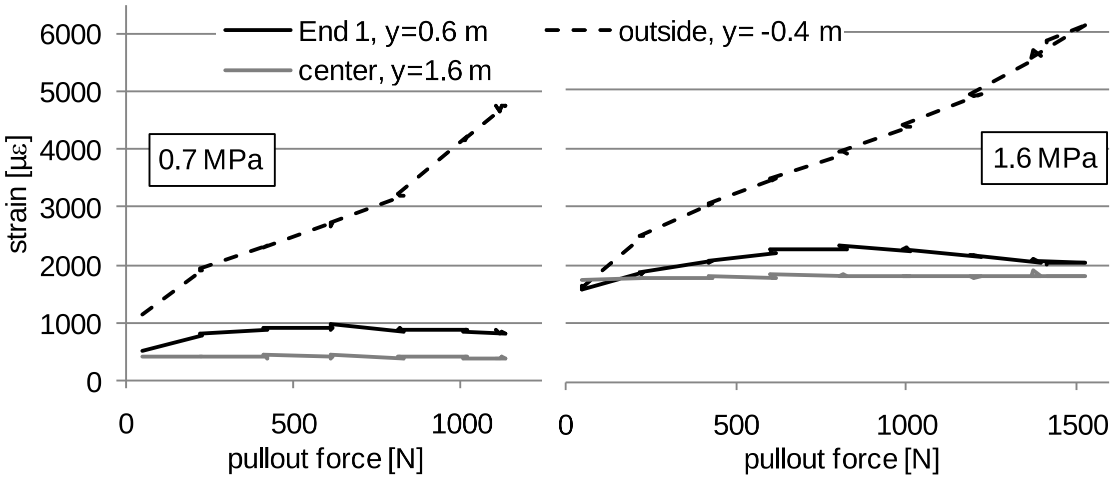

Fig. 9-13: Pullout tests on the rugged cable in 4/8 material

The same tendencies can be seen in the strain – pullout force graphs for the 0/16 material in Fig. 9-14. Here, the strain due to the pullout force is considerably smaller, which has to be related to some external restraint. The strain in the first measuring point at the start of the soil material (y = 0.1 m) shows an increase in the first load step and a damping in the further strain development. Again, the middle section is not affected by the pulling, indicating a good force transfer between 0/16 gravel and cable.

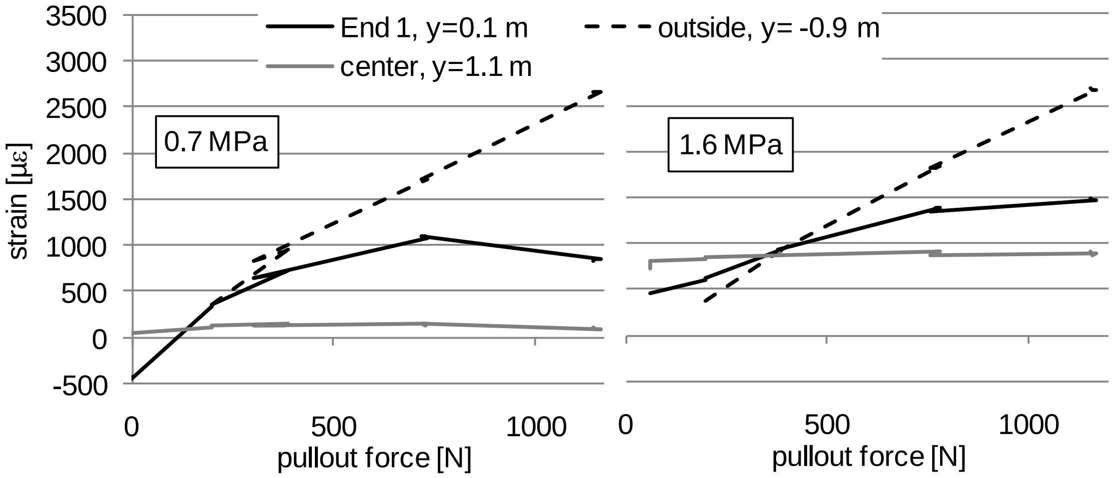

Fig. 9-14: Pullout tests on the rugged cable in 0/16 material

The pullout tests in the soft cable embedded into the narrowly stepped 4/8 material show that the influence of pulling on the cable is stronger than for the rugged cable. Strain measurements in Fig. 9-15 indicate that the cable at 0.7 MPa vertical stress is influenced by the pulling until the measuring point in the center of the soil material (y = 1.8 m). When the pullout force is increased to around 700 N, the strain in the center part starts to decrease. At 1.6 MPa, the effect on the center measuring section is still visible but weaker. The load transfer is consequently better at high loads.

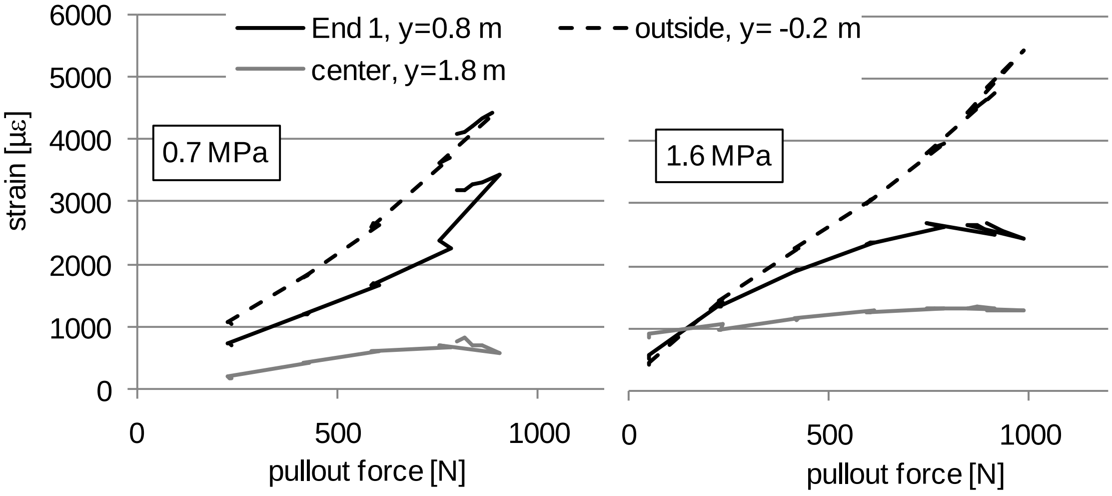

Fig. 9-15: Pullout tests in the soft cable in 4/8 material

Comparing the rugged and the soft cable in 4/8 material, the pulling effects the soft cable much more. This can be explained with the softer sheath material where the toothing effect can only develop less. The tests also showed that there is no particular need for anchors or other measures in case the cable is buried in enough depth so the vertical strain is high enough to slightly deform the cable mantle, leading to a toothing effect (Fig. 9-8). It is favorable to embed the cables into narrowly graded material to reduce the risk of cable damage. Due to the limited time for the tests, no statements can be made on the long-term creeping behavior of the cables in soil.

10 Field test for the detection of surface movements and shear zones in landslides

10.1 Introduction

The previously discussed tests on strain sensing in concrete structures and soil material showed the great benefits of using robust optical strain sensing cables in harsh environments. Landslides and reservoir landslides are often found in remote mountainous regions that are difficult to access and where measuring instruments are exposed to harsh environmental conditions. Strain sensing cables in reservoir landslides could also be part of an integral (maybe dormant) measuring system that is also capable of measuring strain in a dam (Hoepffner, Singer et al. 2008).

10.2 The "Aggenalm landslide" test site

The Aggenalm landslide is situated in the Bavarian Alps about 80 kilometers southeast of Munich and 3 kilometers southeast of the town of Bayrischzell. In the north it borders to the "Sudelfeld", Germany's largest contiguous skiing resort. One of the main access routes to the skiing resort crosses the landslide. In 1935, after being triggered by heavy rainfall, the Aggenalm landslide destroyed three bridges and the road to the Sudelfeld area. Again after extreme precipitation in 1997 a debris flow originated from the landslide area and blocked the road. Since 2001 the landslide has been surveyed periodically twice a year by the Bavarian state office for the environment (Bayerisches Landesamt für Umwelt), showing average movement rates of about 2 cm/a. The displacement vectors that are shown in the orthophoto in Fig. 10-1 show the total amounts and directions of movements between 2001 and 2005. The maximum displacement occurred in the southernmost point close to the road at 8.0 cm in 5 years (Thuro, Wunderlich et al. 2007).

Due to the growing economic relevance of the Sudelfeld access road for the tourism of the region, a detailed engineering geological investigation of the Aggenalm landslide was carried out in order to assess the underlying processes. Additionally, in the course of the research funding program "Geotechnologies" of the Deutsche Forschungsgemeinschaft (DFG), the Aggenalm landslide was selected as the test site for the installation of an innovative early warning system for alpine instable slopes (Thuro, Wunderlich et al. 2007). The entire instrumentation as it was planned and partly already installed to this date is also shown in Fig. 10-1. It includes a terrestric positioning system (TPS – e.g. a reflectorless tacheometer), a global navigation satellite system (GNSS – here a global positioning system (GPS)), coaxial cables for time domain reflectometry (TDR) measurements and fiber optic (FO) cables.

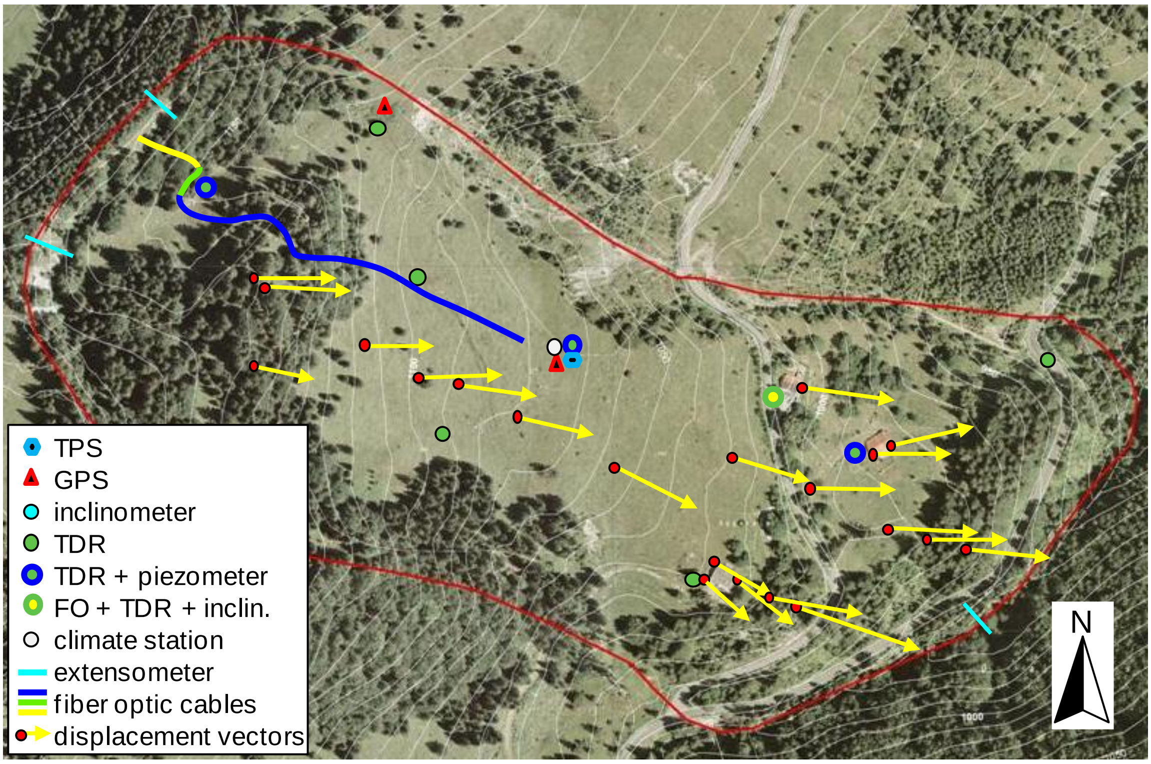

Fig. 10-1: Orthophoto (scale circa 1:5,000) with displacement vectors (max. displacement: 8 cm) and planned instrumentation

10.3 Geology

Tectonically the area of the Aggenalm landslide is part of the Lechtal nappe of the Northern Calcareous Alps, which is built up by various sedimentary rocks of mainly Triassic to Cretaceous age. Due to the alpine orogeny, the rock mass is folded into several large synclines and heavily faulted. In the last ice age the area was covered by glaciers, which resulted in typical glacial morphology and the abundance of various glacier deposits (Hoepffner, Singer et al. 2008).

The Aggenalm slope is mainly built up by the “Kössen formation”, an alternating sequence of limestone and marl, and the overlying “Oberrhät limestone” – massive limestones and dolomites (Fig. 10-2). The whole sequence dips parallel to the slope with an average angle of 22°. The marls, which underlie most of the slope are sensitive to weathering and with time are decomposed to a clay-rich residual rock. This process coincides with a distinctive reduction of the rock mass strength

(Nickmann, Spaun et al. 2006) and is mainly responsible for the instability of the slope.

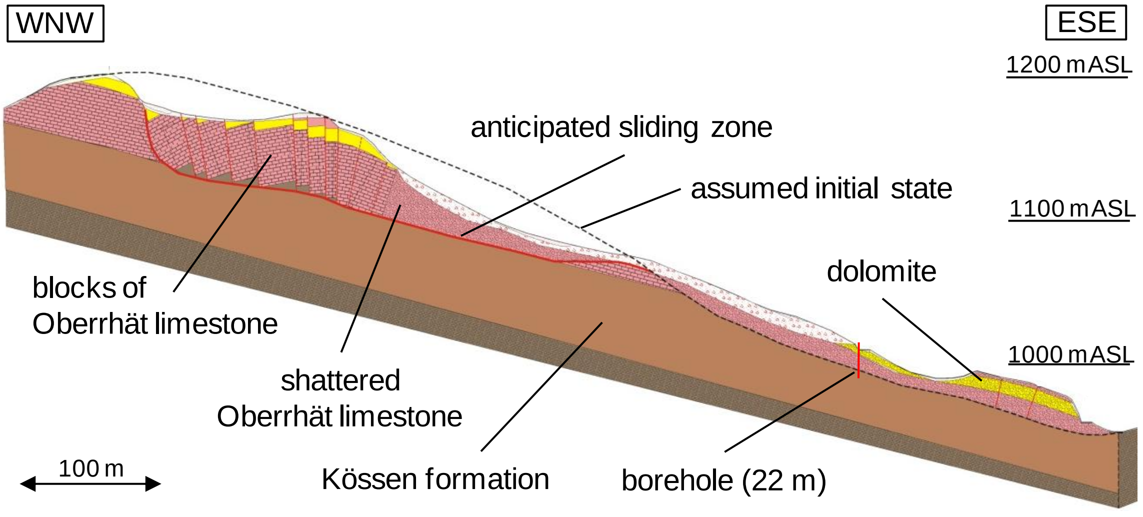

Fig. 10-2: Interpreted geological cross section direction WNW – ESE (Jung 2007)

In the upper part, the Aggenalm landslide can be classified as a rock spread according to Cruden and Varnes (1996). Further downhill, with increasing deformation, the rock mass continuously disintegrates and the mechanism of the landslide changes into a very slow debris flow. As the events of 1935 and 1997 have shown, the Aggenalm landslide is sensitive to heavy precipitation and the accompanying rise in ground water levels.

10.4 Monitoring layout

For the hazard assessment of a landslide it is essential to have detailed information about the distribution, orientation and amount of deformation in four dimensions (on the surface and in the depth alongside boreholes and with high temporal resolution). Additionally the effect of triggering mechanisms (as e.g. precipitation) to the movement and their temporal relation is of great importance. Distributed fiber optic strain sensing could be an appropriate system to gather some of the required information. In the following tests, the strain sensing cables were installed close to the surface to monitor surface movements and the formation of cracks and vertically to evaluate the location of the shear zone in the lower part of the landslide. The whole measuring setup of different conventional and new monitoring systems is plotted into Fig. 10-1.

10.4.1 Near-surface installation of strain sensing cables for the monitoring of surface movements

Strain sensing cables for the monitoring of surface movements were installed into the upper part of the landslide, starting just below the main scarp. Several secondary and tertiary movements were spotted in this part of the landslide, which is abundantly covered with trees and bushes. The saber-like growth habit of the trees also gives evidence of ongoing surface movements. The soft dam cable, which was introduced in section 5.2, was installed at a length of 44 m, marked yellow in Fig. 10-3. The subsequent 23 m of the same cable were loosely placed onto the forest soil. As no electricity or road access is given to that part of the landslide, the strain sensing cable was extended towards the better accessible lower part of the slope. The 300 m long extension cable, which is depicted in Tab. 5-1 is a standard fiber optic cable with single mode and multi mode fibers inside. As the fibers are embedded into a gel, no strain can be transferred from the cable mantle into the fibers. To protect the cable from mechanical forces, it was placed into an armored plastic tube.

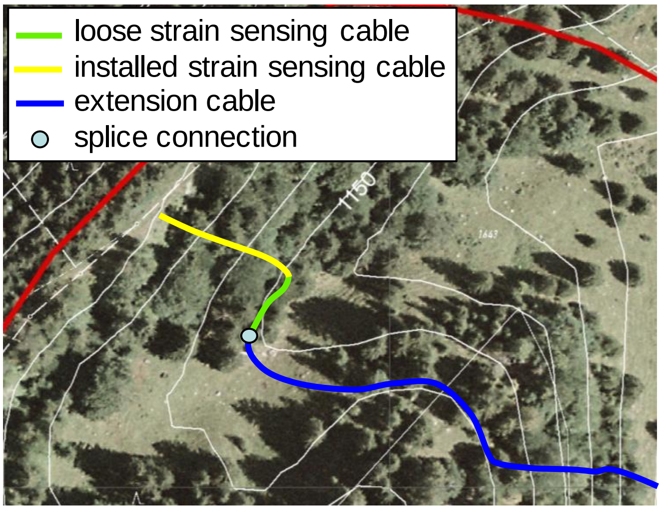

Fig. 10-3: Location of the strain sensing cable

For calibration of the strain sensing cable, a cable piece of at least 5 to 10 m is spliced to the lower end of the extension cable and placed into a water bath next to the DTSS. The temperature can then be monitored via the external PT100 thermocouple (section 5.3).

The strain sensing cable was aligned in a way that a large secondary and a minor surface movement are within the measurable section. After the ideal alignment was evaluated, a 15 to 20 cm deep trench was dug out of the forest soil where possible. At places where roots or rocks were in the way, the cable was either guided underneath or over the obstacle. The trench was filled up with the excavated material after installation and compacted by hand where possible. As the load even of the compacted forest soil material for force transfer is negligible (chapter 9), additional anchors were used to hinder the cable from tearing out of the soil or freely slipping inside the trench. The anchors were designed in a way so they will not harm the cable, also in case of ground movements. They were driven into the soil at 1-3 m spacing, depending on the ground. In case of ground motion, creeping slip between cable and anchor as well as movements of the anchors are expected. Consequently strain is distributed locally along the cable and the fiber, making it possible to locate and evaluate cracks or local movements. The layout of the installation is depicted in Fig. 10-4. An anchor is depicted at a preliminary testing stage and from above after installation. On the upper end, the strain sensing cable was securely tied to a tree that is supposed not to be affected by the secondary movement.

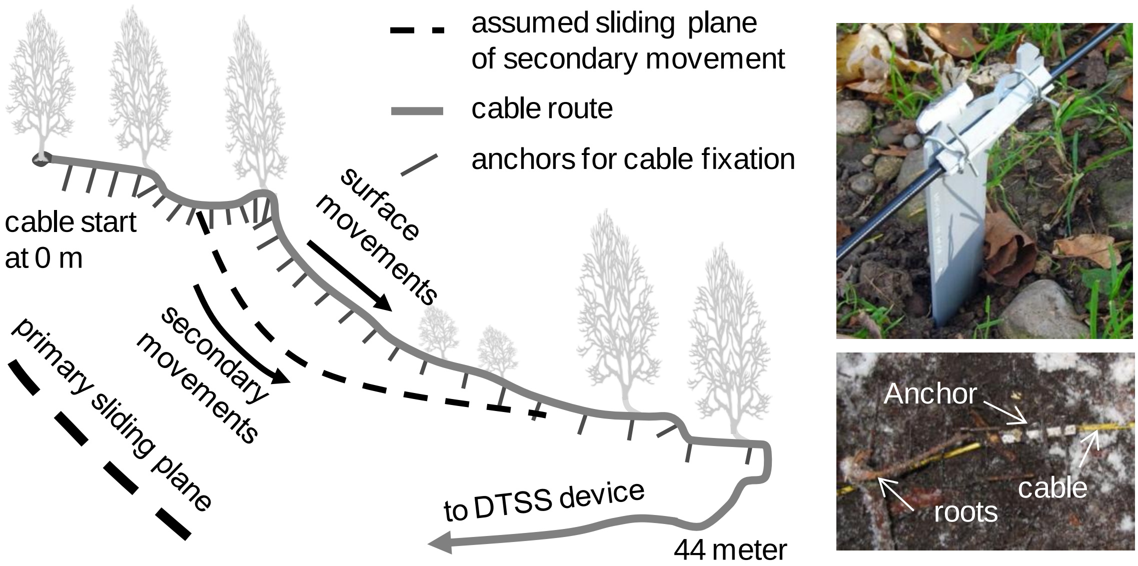

Fig. 10-4: Installation scheme with anchors

In the photos in Fig. 10-5 the alignment of the cable is highlighted. On the left photo, the connection to the final tree and the passage through the secondary crack are shown. A saber-like growth habit of the trees at the crack indicates ongoing ground motion. The right photo shows the installation works on the cable in the lower part of the measurable section. The installation was made in fall 2007 during first snowfall. The reference measurements were taken in May 2008. No damages or visible movements could be noticed after the cable was installed for the 6 months of winter.

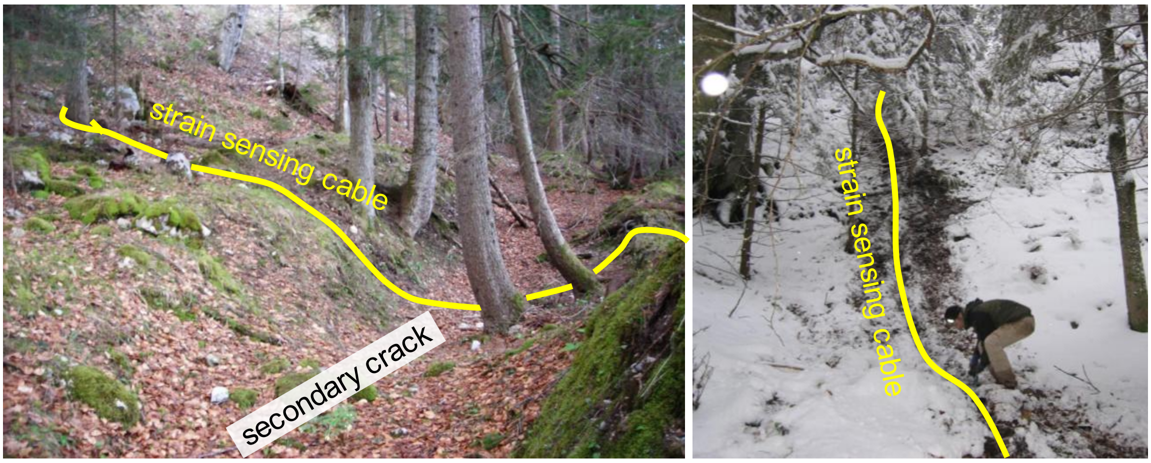

Fig. 10-5: Photos of the installation. Left: upper section, right: lower section

10.4.2 Vertical installation of strain sensing cables for the monitoring of shear zones

Shear zones are vital parameters in order to obtain information on the thickness of a landslide and thus its volume. It is generally not possible to evaluate the depth of a shear zone from boring profiles only (Cornforth 2007). For more than a decade, the time domain reflectometry (TDR) measuring technique proved to be a very appropriate method for the detection of localized shear planes (see section 10.6). However deformation detection reaches its limit, when the coaxial cable is gradually bent with no significant change of the cable cross section geometry. In that case, inclinometers can be used to evaluate the detailed information and direction of the subsoil movements. Fiber optic strain sensing in combination with TDR could represent an alternative to evaluate distinct shear planes as well as large shear zones (Fig. 10-7 right).

In the present installation, a fiber optic strain sensing cable and a coaxial cable (Ø 12 mm) for TDR measurements were attached onto the outside of an inclinometer casing, which can later be used to validate the measurements. The rugged 6 mm dam cable, depicted in Tab. 5-1, was used for the vertical installation. The borehole has a total depth of 22 m. A geological profile was evaluated from the drilling core (Fig. 10-11). The installation in the borehole is depicted in Fig. 10-6. A loop configuration of the strain sensing cable has several advantages. In case the fibers are damaged, measurements can still be undertaken from the other end of the cable. As the cable passes the entire borehole twice, redundancy in the measurements is given. By arranging the cables at 90° around the inclinometer casing it might be possible to evaluate the direction of the subsoil movement (180° in the bottom 1 m).

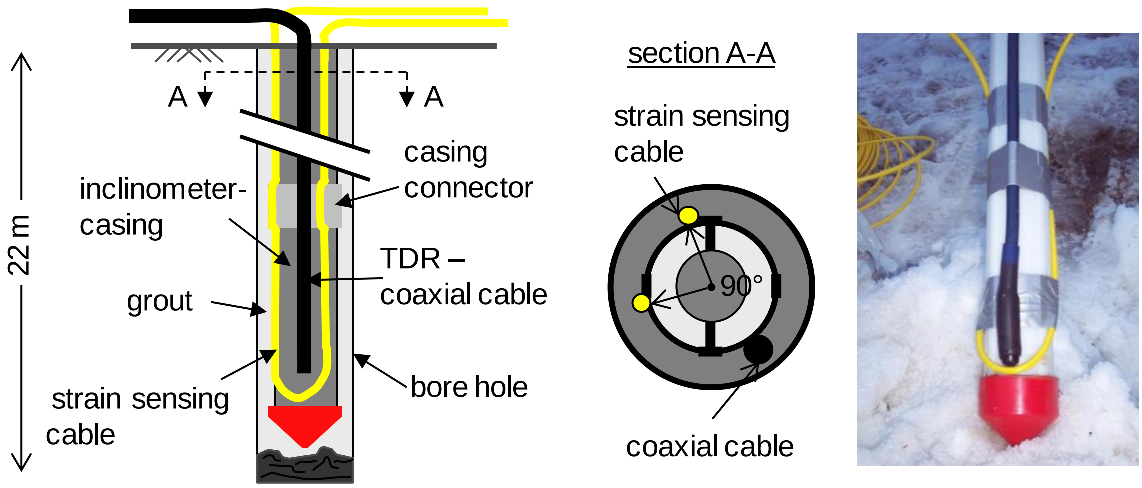

Fig. 10-6: Vertical installation in the borehole

After the equipped inclinometer casing was placed into the borehole, the interface between cables, casing and rock mass was filled with grout. It is very important to match the physical properties of the grout to the particular geology to avoid interactions between the two materials that could affect the measurements (Thuro, Wunderlich et al. 2007). This is particularly important when working in soil. On the other hand the grout should not be too stiff to avoid the fiber optic cable from breaking due to very localized shear deformations of the grout (Fig. 10-7 left).

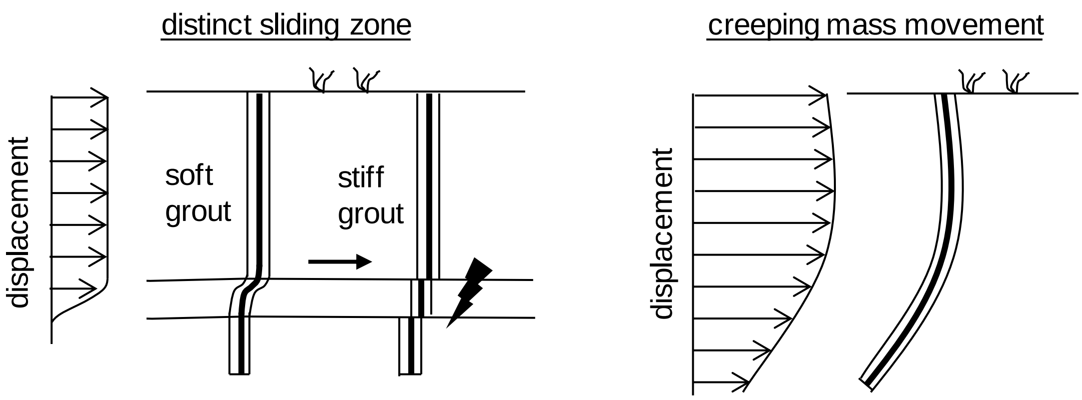

Fig. 10-7: Interaction of grout, strain sensing cable and surrounding rock mass

As TDR sensing needs shear deformations and optical fibers are very sensitive to shear forces, an appropriate balance of the physical grout properties has to be chosen to meet the requirements for both sensing systems and the particular geology. The properties of the grout that was used in the test are listed in Tab. 10-1. The grout material at installation had an initial marsh-time of 55 s.

Tab. 10-1: Grout properties

w/B-ratio [-]	grout-density [kg/dm³]	compressive strength σ_{28d} [MPa]	permeability [m/s]
0.6	1.64	2.5	10^{-10}

10.5 First reference measurements

10.5.1 Near-surface installed cable

The Aggenalm landslide is moving at an average rate of about 2 cm/a, recorded with a wire extensometer, which is installed at the main scarp and surface bound geodetic measurements. As the DTSS was just available for several days, it was only possible to take a reference measurement as no movements within a few days could be expected.

The functionality of extending the strain sensing cable with a standard fiber optic cable could, as expected, be confirmed. In Fig. 10-8, the total fiber length is divided into a first section with constant residual strain between fiber and coating in the extension cable and a second section with the strain sensing cable.

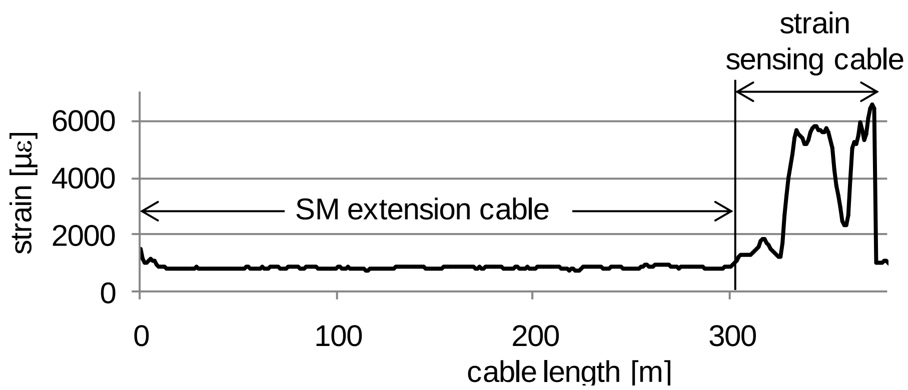

Fig. 10-8: Strain measurement along the entire surface cable

This setup allows monitoring a landslide many kilometers away from the sensing device, making it possible to use a fiber from an existing communication cable or a specially armored cable as extension, depending on the situation and the expected mechanical impacts.

The reference measurement in the installed cable section, which is depicted in Fig. 10-9, reflects the pre-strain that was applied on the cable during installation and some deformations that happened since installation. However this does not give information on movements since its installation as it is not possible to distinguish between pre-tension and movements as no geodetic reference measurements were made. The length of the cable and the anchor positions refer to the horizontal axis. The elevation of the cable is schematically plotted for better orientation. In future measurements, the reference measurement has to be subtracted to evaluate the location and amount of deformation of the ground.

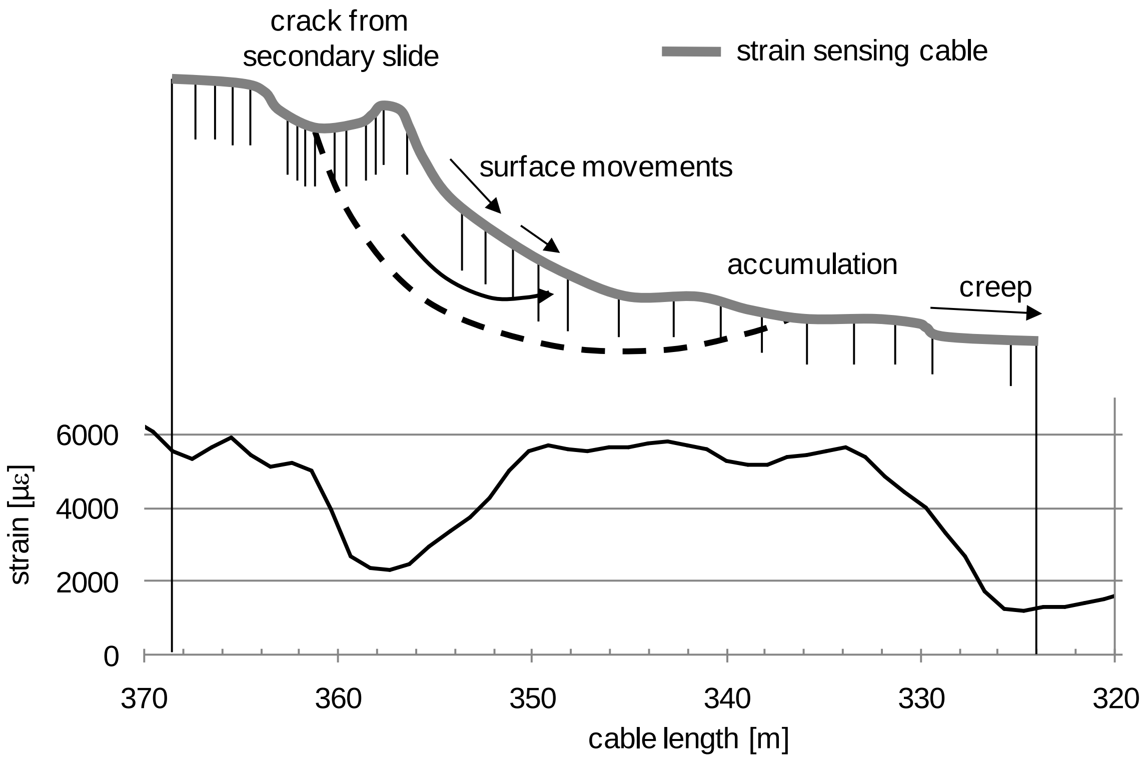

Fig. 10-9: Reference measurement for surface movements in the strain sensing section (anchor positions and measurement refer to cable length)

10.5.2 Vertically installed cable

Analogous to the measurements of surface movements, only a reference measurement could be carried out at the vertical installation. Figure 10-10 shows the total cable, which is installed inside the borehole. At the bottom, the cable was attached to the inclinometer casing with adhesive tape thus no strain was measured.

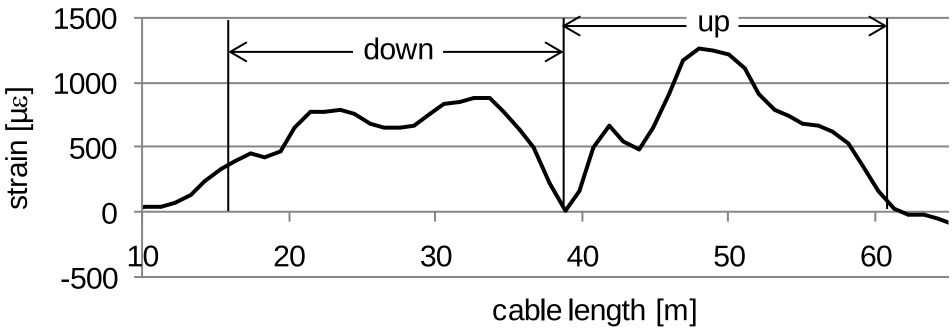

Fig. 10-10: Section of strain sensing cable inside the borehole

To make strain distribution along the borehole more visual, the upward and downward leading parts of the cable are divided and placed next to the geological profile in Fig. 10-11. If significant localized subsoil movements would have taken place between installation and the reference measurement, this might be visible as distinct strain peaks.

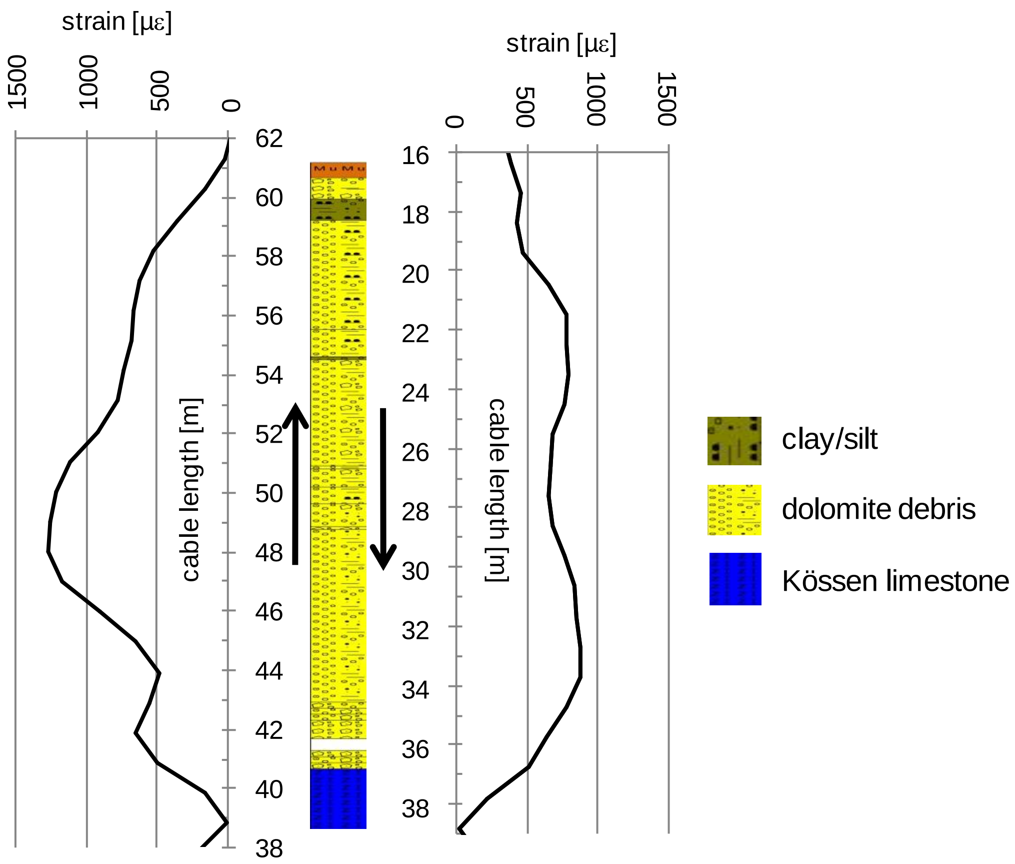

Fig. 10-11: Reference measurement for subsoil movements and shear zones

Also deformation measurements that were carried out with the TDR after installation and shortly before the reference measurements on the strain sensing cable did not show any movements, yet. This is not surprising since the installation of a coaxial cable parallel to an inclinometer casing prohibits an effective transmission of the rock mass deformation to the cable and results in a rather gradual deformation of the coaxial cable, which cannot be measured. Only after a considerable amount of deformation (several centimetres) the measurement will start to change the cable geometry and therefore produce results. At this time the inclinometer will almost certainly be near the end of its lifetime, so that the TDR measurements can considerably prolong the lifetime of a subsurface deformation measurement site. Future measurements on both the fiber optic cable and the TDR cable and validation by inclinometer measurements will show the accuracy and applicability of that setup.

10.6 Time domain reflectometry (TDR) versus distributed fiber optic strain sensing for shear zone monitoring

As the principle of both systems, fiber optic strain sensing and time domain reflectometry, which is to get information from a cable placed into the ground is quite similar at first sight, the merits and the combination of both systems are briefly discussed in the following.

Time domain reflectometry can be described as “cable-based radar”: The TDR cable tester emits electric pulses, which are sent through a coaxial cable. When these pulses approach a deformed portion of the coaxial cable, a signal is reflected to the cable tester. As with radar, due to the known propagation velocity of the electromagnetic wave, by measuring the time span between emission and reception of the electric pulse, the distance to the deformation can be determined (similar to the time-of-flight in OTDR measurements). Furthermore the analysis of the reflected signal (amplitude, width, form etc.) can reveal information about the type and amount of deformation. When the rock mass starts to move, the coaxial cable is deformed (e.g. altering the distance between inner and outer conductor of the cable). This results in a change of the electric properties (impedance) of the cable, which can be measured with TDR. A detailed description of the underlying physics and the setup for landslide monitoring is given in O’Connor and Dowding (1999). Depending on the TDR device, the spatial resolution of the measurements can be in the centimeter range, comparable to OTDR measurements. The diameter of the copper wire inside the coaxial cable limits the measurable shear deformation to several decimeters. Research is currently carried out to improve the evaluation of the reflected signals in terms of type and amount of deformation (Singer, Thuro et al. 2006).

As discussed in section 10.4.2, optical fibers are very sensitive to shear deformations as the fibers could easily break. Using an OTDR, rising losses before the break can be located but no reliable information on the amount of movements or potential secondary sliding zones can be gathered. Local deformations of the strain sensing cable also constitute a problem regarding the spatial resolution of the DTSS of 1.021 m. A combination of both systems could help to improve the monitoring of mass movements. In the bottom pictures in Fig. 10-12, the direct comparison between TDR and DTSS measurements is illustrated. In this setup, strain measurements can be used to locate and evaluate large shear zones while TDR measurements can evaluate localized shearing that cannot be evaluated by the optical fiber.

When taking special measures, strain sensing with fiber optic cable could also be possible at shallow localized shear planes. If the direction of movement is known, the installation of a strain sensing cable into an inclined borehole could be an option as the deformation of the ground is not transferred into shear but mostly into strain along the cable in the shear plane. Enough bond between cable and grout material is mandatory in that case.

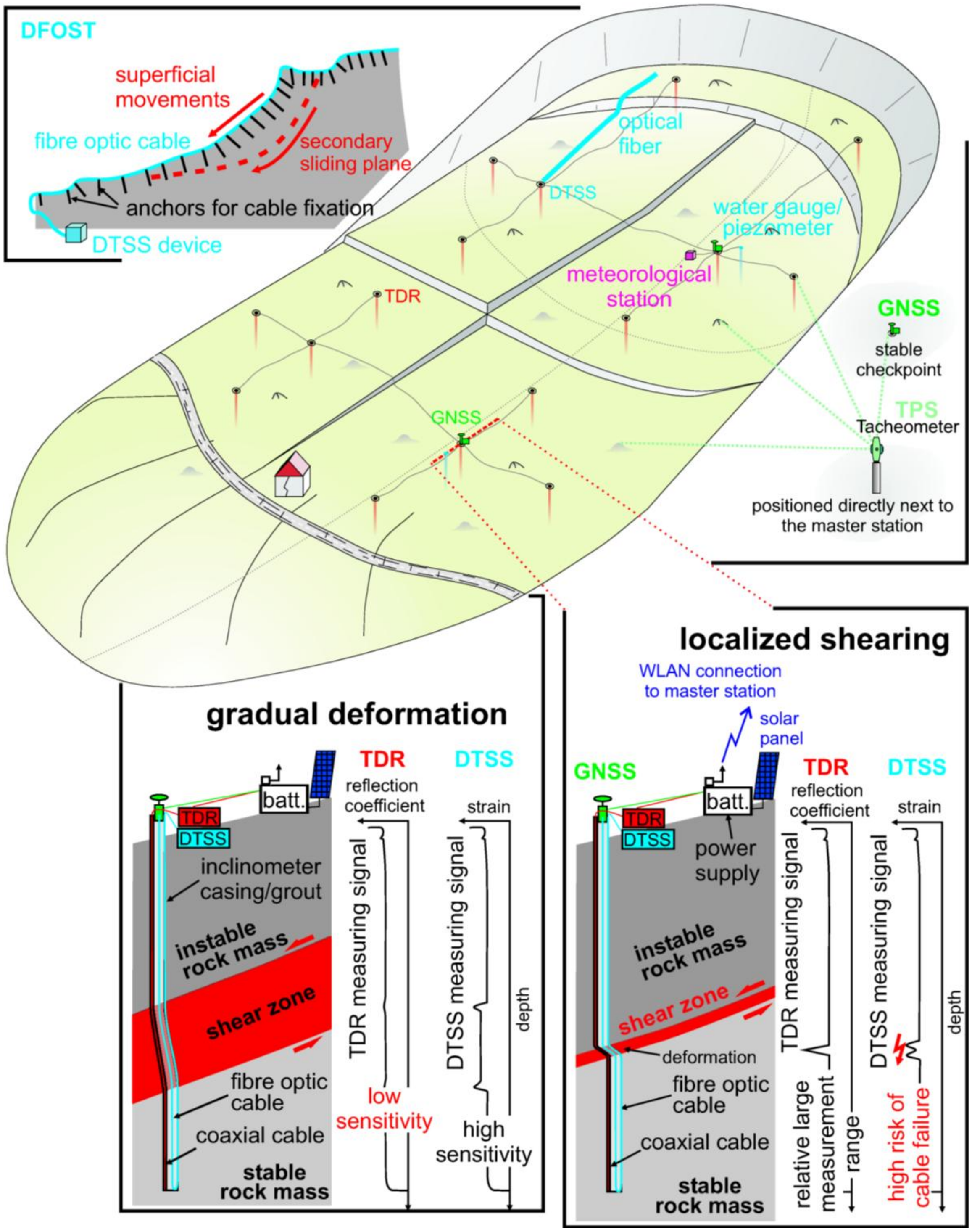

Fig. 10-12: Proposed landslide monitoring setup involving distributed fiber optic strain sensing (Hoepffner, Singer et al. 2008)

11 Summary and future prospects for distributed fiber optic strain sensing in hydraulic engineering

11.1 Cables and strain sensing systems

Having investigated the applicability of fiber optic strain sensing in concrete and soil, several installation- and sensing concepts showed to work very well in terms of crack- and strain detection. However it was also found out that more research for validation and optimization of the present tests is needed.

Research on the improvement of Brillouin based strain sensing systems is still going on. New methods for reducing the spatial resolution, increasing the sensing length or handling the temperature compensation are being developed and tested. Low-priced strain sensors allow decent quality strain measurements at reduced spatial resolution. The executed tests showed that particular attention should be given to the design and the installation of the strain sensing cables, which constitute the actual sensor. A minimum amount of slip inside the cable is necessary to receive strain data from local a deformation below the spatial resolution of the strain sensing system. It could be shown that strain, which is applied in a 0.5 m section of a fiber cannot be measured at all (section 6.2). The accuracy of a measurement rises with rising strained fiber lengths. Further tests are needed to define the minimum section of cable that needs to be affected for accurate strain measurements. When a large amount of strain was applied on the cable mantle only, considerable local slip could be observed, compensating the strain (section 6.3). The maximum applicable strain is consequently not limited to the extension limit of the optical fiber of around 3 % as the strain is getting redistributed in the cable due to slip. The cable design has to be well chosen before installation to avoid damage and allow the necessary amount of slip. Once a cable is installed, the possible sensing method could be chosen afterwards. Single ended methods based on spontaneous Brillouin scattering are preferred for most applications in rugged environments. In any case, the perfect pre-calibration of the cables concerning Brillouin shift versus strain and temperature is very important. The tests showed that the automatic temperature compensation of the DTSS device by evaluating the temperature from the Brillouin power is not adequate at that stage of development. It is therefore suggested to either use the raw strain data in case temperature changes are negligibly small or if the focus is on local deformations and relative changes. In any other case the simultaneous combination of a Brillouin and a Raman based sensor will give the best resolution. In that combination, the measuring period of both instruments should be set as high as temperature changes allow in order to minimize the noise in the compensated measurement.

To increase the range of applications for distributed fiber optic strain sensing, further research is necessary in the development of special cables. Installing a copper wire into a tube within the cable, which is uncoupled from the rest of the cable could allow the measurements of water movements using the heat-up method and strain in the same cable using both a Raman and a Brillouin based sensing system. A copper wire that would be in connection with the optical fibers would affect the strain measurements due to its different Young's modulus and the considerably larger coefficient of thermal expansion.

11.2 Concrete

Cables for distributed strain sensing were installed into three different concrete specimens, a reinforced concrete beam, a reinforced concrete column and an RCC block (chapter 7). The goal was to evaluate the applicability and accuracy of the distributed strain sensing technology in concrete for crack detection. In case many cracks occur within the spatial resolution of 1.02 m, the average strain is measured which reflects the amount of total deformation. Distributed strain measurements were compared with single point measurements from fiber Bragg grating (FBG) strain sensors and electrical strain gauges (ESG) which showed excellent agreement in the concrete column (section 7.3.4).

A single crack that was forced into the RCC block could be localized with high precision within the spatial resolution (section 7.4.4). The crack width could be evaluated by integrating the strain in the strained fiber section over cable length (with respect to spatial resolution). Laboratory tests proved the applicability of that method (chapter 6). It was shown that crack widths of 0.1 mm could be evaluated with high precision. The bond between concrete and cables was proved to be very good (section 6.4). Slip at their interface of around 1 m can only be expected at tensile forces on the cables that are close to their braking limit.

More than 800 m of strain sensing cable were installed into an RCC dam in Brazil (chapter 8). The cables were pre-strained and guided trough pulley wheels at the turning points. This procedure allows to measure strain even at small amounts as the straightness of the cable can be guaranteed. It also allows a secure localization of points of fixation and thus the location of measuring sections within the dam.

Compressional strain however could also be measured without pre-straining the cables. The amount of pre-tension should in sake of measuring range and data quality not exceed 2,000 με in case internal temperature compensation suing Brillouin power is used (section 8.5). Non-temperature compensated strain measurements during impoundment showed the influence of temperature in cable sections that were installed close to the dam's faces (section 8.3). When installing strain sensing cables into a concrete structure it is inevitable to have skilled personnel taking care of the cable's integrity during the whole construction period. By installing the cable in multiple loops, measurements from both sides of the fiber still allow a total coverage of the structure also in case of a damaged cable. Merging many loops to one, leaving the damaged loop at the end, allows covering the whole structure from one end with one single strain sensing system. However for every project, the benefit and the work for installing fiber optic strain sensing cables have to be well evaluated.

11.3 Soil material

Two different cables, one 5 mm in diameter with a soft polyurethane (PU) sheath, the second one with a diameter of 6 mm and a stiffer, more rugged mantle, also made of PU (Tab. 5-1), which were especially designed for the installation into embankment dams, were tested in two different soil materials, a 4/8 and a 0/16 mm gravel (chapter 9). To simulate different installation depths in a dam and the impact of soil pressure on the cables, on the strain measurements and on the attenuation in the fibers, stress was applied on the soil materials where the cables were installed into. The maximum applied stress was 1.6 MPa. Both cables showed marks in the mantle after the tests but the losses in the soft cable were considerable higher (section 9.5). The narrowly graded 4/8 material had a smaller effect on both cables. Local deformations of the sheath of the cables cause a toothing effect, which leads to a very good transfer of deformations from the soil material to the cable without the need of anchors (section 9.7).

The strain due to deformation of the cables within the soil material was rising with rising stress at a rate of roughly 290 με/MPa for the 4/8 and 350 με/MPa for the 0/16 mm soil material. For a statement on the linear rise of strain depending on the soil material, compaction and stress, additional tests are necessary (section 9.5). Specific cable mantle designs that protect the fibers from lateral loads while allowing longitudinal strain could be part of the solution. The present tests were carried out in a short period of time so the effect of creep between cable and soil material as well as within the cable could not be considered. Many possibilities for the installation of strain sensing cables into embankment dams can be thought of. Figure 11-1 shows some installation possibilities in the longitudinal section of a dam where distributed strain sensing can be expected to deliver useful data to identify areas of decreasing stresses and deformations. Combining strain sensing with temperature sensing, the same cable could at the same time be used to monitor the water levels and potential regions of increasing seepage using the gradient method.

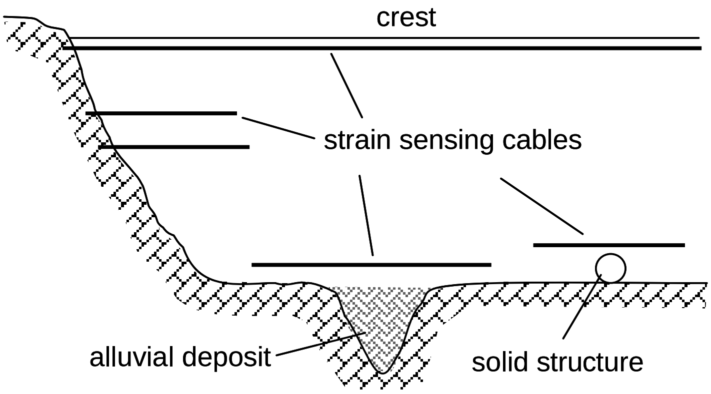

Fig. 11-1: Some possibilities for fiber optic strain sensing in an embankment dam

11.4 Landslides

Fiber optic strain sensing cables were installed into a landslide, which is moving at an average rate of 2 cm/a, to monitor surface and subsurface movements. For the evaluation of surface cracks, 44 m of strain sensing cable were installed across secondary and tertiary movements and cracks on the main mass movement (section 10.4.1). As the load transfer between cable and ground was not adequate in the installed depth of 0-20 cm, additional anchors were driven into the ground with the cable attached. As the measured section is located in the difficult to access upper part of the landslide, the strain sensing cable was extended by a standard fiber optic cable with single mode fibers inside. The reference measurement showed that the setup was perfectly measurable. The accuracy for deformation measurements will have to be proved in upcoming measuring campaigns.

To detect and evaluate a large shear zone, one cable was vertically installed into a borehole (section 10.4.2). It was attached to an inclinometer casing next to a coaxial cable for TDR measurements. The space between installations and subsoil was filled with grout material, which should on the one hand match the physical properties of the surrounding soil material but on the other hand be soft enough not to damage the fiber optic cable due to local shearing of the grout. The reference measurement on the cable that was placed into the 22 m deep hole in a loop showed that the cable was not damaged and perfectly measurable (section 10.5.2).

The unproblematic extension of the measured fiber shows the applicability for landslide monitoring in remote regions where the sensing system could be located several 10 kilometers away from the mass movement. For the monitoring of slopes around a reservoir, it will be possible to guide the cable along the reservoir, crossing the regions to be monitored. Landslide monitoring at a reservoir could also be part of an integral measuring system by installing strain sensing cables into the dam and the landslide, measuring strain, temperatures, water levels and velocities in and around the structure without depending on weather conditions. Research on using distributed fiber optic temperature sensing for landslide monitoring is recently being carried out at the University of Innsbruck, Austria: "Distributed saturation- and flow velocity measurements in alpine areas".

11.5 Long-range strain sensing

The accuracy and the measurable distance of several 10 km make distributed strain sensing an appropriate system for long range sensing applications at sensitive and maybe inaccessible structures or sections of a structure.

Dikes / levees

Along dikes and levees, strain sensing cables could act as a sleeping system, which is measured upon requirement during or after flood events. Fiber optic cables that are woven into geosynthetics can give information on the behavior of a structure and at the same time remediate and support it (section 4.3.3). With a Raman based distributed temperature sensor (DTS), the temperature and thus the seepage along the same cable can be measured. Protection measures may however be required to protect the cable against rodent animals without reducing the strain transfer to the fibers.

Canals and pipelines

Attaching fiber optic strain sensing cables to pipelines or installing them into the sealing system of a canal can give valuable information on critical deformations or cracks (Hoepffner, Schäfer et al. 2007). They could either be installed as a sleeping system or can be used as a permanent alarm system in case the canal or pipeline is located in a region, which is susceptible to earthquakes, landslides or ground settlements due to the collapse of subsoil cavities.

Index of used symbols and abbreviations

Symbols and abbreviations are explained in the text or following the equations. Some symbols or indices might have different definitions throughout the text. Temperatures and temperature differences are given equally in °C and K.

References

ACI (2001): *Control of Cracking in Concrete Structures*. ACI 224R-01, Report by ACI Committee 224, American Concrete Institute (ACI).

ACI (2007): *Report on Thermal and Volume Change Effects on Cracking of Mass Concrete*. ACI 207.2R-07, Report by ACI Committee 207, American Concrete Institute (ACI).

Adler, S.; Stützel, F.; Wichter, L.; Wienberg, N. (2006): *Untersuchungen zur Rissausbildung in Verpresskörpern um die Zugglieder von Gewinde-Einstabankern*. Geotechnik, Vol. 29, No. 4, pp. 670-680.

Agrawal, G. P. (2001): *Nonlinear fiber optics*. 3rd edition, Academic Press, ISBN 0 1204 5143 3, 466 p.

Alahbabi, M. N.; Cho, Y. T.; Newson, T. P. (2006): *Long-range distributed temperature and strain optical fibre sensor based on the coherent detection of spontaneous Brillouin scattering with in-line Raman amplification*. Measurement Science Technology, Vol. 12, pp. 1082-1090.

Andriolo, F. R. (1998): *The use of Roller Compacted Concrete*. Officina de Textos, Sao Paolo, Brazil, ISBN 85 86238 10 4, 554 p.

Ansari, F.; Libo, Y. (1998):. *Mechanics of Bond and Interface Shear Transfer in Optical Fiber Sensors*. Journal of Engineering Mechanics, Vol. 124, No. 4.

Aufleger, M. (1996): *Ein Beitrag zur Auswertung von Erddruckmessungen in Staudämmen*. Dissertation. Berichte des Lehrstuhls für Wasserbau und Wasserwirtschaft, Report No. 78, Technische Universität München, ISSN 0947-7187.

Aufleger, M. (2000): *Verteilte faseroptische Temperaturmessungen im Wasserbau*. Habilitation, Berichte des Lehrstuhls für Wasserbau und Wasserwirtschaft. Report No. 89, Technisch Universität München, ISSN 1437-3513.

Aufleger, M.; Conrad, M.; Strobl, T.; Malkawi, A. I. H.; Duan, Y. (2003): *Distributed fibre optic temperature measurements in RCC dams in Jordan and China*. Proceedings of the 4th International Symposium on Roller Compacted Concrete (RCC) Dams, 17-19 November 2003, Madrid, Spain, pp. 401-407.

Banerjee, P. P. (2004): *Nonlinear optics: theory, numerical modeling and applications.* ISBN 978 0 8247 0965 5, 314 p.

Bao, X.; DeMerchant, M.; Brown, A.; Bremner, T. (2001): *Tensile and Compressive Strain Measurement in the Lab and Field with the Distributed Brillouin Scattering Sensor*. Journal of Lightwave Technology, Vol. 19, No. 11.

Bastianini, F.; Matta, F.; Galati, N.; Nanni, A. (2006): *Distributed strain measurement in steel slab-on-girder bridge via Brillouin Optical Time Domain Reflectometry*. Proceedings of the 3rd International Conference on Bridge Maintenance, Safety and Management (IABMAS'06), 16-19 July 2006, Porto, Portugal.

Bastianini, F.; Matta, F.; Galato, N.; Nanni, A. (2005): *A Brillouin smart FRP material and a strain data post processing software for structural health monitoring through laboratory testing and field application on a highway bridge*. Proceedings of the congress on Sensors and smart structures technologies for civil, mechanical, and aerospace systems, 7-10 March 2005, San Diego, California, pp. 600-611, Vol. 5765, ISBN 0 8194 5764 9.

Bastianini, F.; Rizzo, A.; Galati, N.; Deza, U.; Nanni, A.; Masayoshi, T. (2005): *Discontinuous Brillouin strain monitoring of small concrete bridges: comparison between near-to-surface and "smart" FPR fiber installation techniques*. Proceedings of the congress on Sensors and smart structures technologies for civil, mechanical, and aerospace systems, 7-10 March 2005, San Diego, USA, pp. 612-623, Vol. 5765, ISBN 0 8194 5764 9.

Bernini, R.; Fraldi, M.; Minardo, A.; Minutolo, V.; Carannante, F.; Nunziante, L.; Zeni, L. (2006): *Identification of defects and strain error estimation for bending steel beams using time domain Brillouin distributed optical fiber sensors*. Smart Materials and Structures, No. 15, pp. 612-622.

Bongolfi, B.; Pascale, G. (2003): *Internal Strain Measurements in Concrete Elements by Fiber Optic Sensors*. Journal of Materials in Civil Engineering (ASCE), Vol. 15, No. 2, pp. 125-133, ISSN 0899-1561.

Bosnjak, D. (2000): *Self-induced cracking problems in hardening concrete structures*. Dissertation, Department of Structural Engineering, Norwegian University of Science and Technology, Trondheim.

Botsis, J.; Humbert, L.; Colpo, F.; Giaccari, P. (2005): *Embedded fiber Bragg grating sensor for internal strain measurements in polymeric materials*. Optics and Lasers in Engineering, Vol. 43, No. 3-5, pp. 491-510, ISSN 0143-8166.

Briancon, L.; Nancey, A.; Villard, P. (2005): *Development of Geodetect: A new Warning System for the Survey of Reinforced Earth Constructions*. Studia Geotechnica et Mechanica, Vol. XXVII, No. 1-2, pp. 23-32.

Brown, A. W.; DeMerchant, M. D.; Bao, X.; Bremner, T. W. (1999): *Analysis of the precision of a Brillouin scattering based distributed strain sensor*. Proceedings of the conference on Sensory Phenomena and Measurement Instrumentation for Smart Structures and Materials, 1-4 March 1999, Newport Beach, California, Vol. 3670, pp. 359-365, ISBN 0 8194 3144 3.

Brunner, F.; Macheiner, K.; Woschitz, H. (2007): *Monitoring of deep-seated mass movements*. Proceedings of the 3rd International Conference on Structural Health Monitoring of Intelligent Infrastructure, 13-16 November 2007, Vancouver, Canada.

Bureau of Reclamation (1987): *Design of Small Dams*. 3rd edition, United States Department of the Interior, ISBN 978 0 1600 3373 5, 902 p.

Brunner, F. K. (2004): *Fibre Optic Sensors: An Overview*. Proceedings of the 1st FIG International Symposium on Engineering Surveys for Construction Works and Structural Engineering, 28 June - 1 July 2004, Nottingham, United Kingdom.

Chiao, R. Y.; Townes, C. H.; Stoicheff, B. P. (1964): *Stimulated Brillouin Scattering and Coherent Generation of Intense Hypersonic Waves*. Physical Review Letters, Vol. 12, No. 21, pp. 592-595.

ClimChAlp (2008): *Slope Monitoring Methods - A State of the Art Report*. Work Package 6: Monitoring, Prevention & Management of specific effects of climate change on nature, Interreg III B Alpine Space, Climate Change, Impacts and Adaptation Strategies in the Alpine Space.

Conrad, M. (2006): *A contribution to the thermal stress behaviour of Roller-Compacted-Concrete (RCC) gravity dams*. Dissertation. Berichte des Lehrstuhls für Wasserbau und Wasserwirtschaft, Report No. 105, Technische Universität München, ISSN 1437-3513.

Conrad, M.; Aufleger, M.; Malkawi, H. A. I. (2003): *Investigations on the Modulus of Elasticity of young RCC*. In: Roller Compacted Concrete Dams, proceedings of the 4th International Symposium on Roller Compacted Concrete (RCC) Dams, 17- 19 November 2003, Madrid, Spain, pp. 729 – 733, ISBN 90 5809 564 9.

Conrad, M.; Hoepffner, R.; Aufleger, M. (2007): *Innovative monitoring devices for an integral observation of thermal stress behaviour in large RCC dams*. Proceedings of the 5th International Symposium on Roller Compacted Concrete (RCC) Dams, 3-4 November 2007, Guiyang, China.

Cornforth, D. H. (2007): *Seven deadly sins of landslide investigation, analysis and design*. Proceedings of the 1st North American Landslide Conference, 3.-8. June 2007, Vail, Colorado.

Cruden, D. M.; Varnes, D. J. (1996): *Landslide Types and Processes*. In: K. A. Turner and R. L. Schuster, Landslides - Investigation and Mitigation, Special Report 247. ISBN 0 309 06151 2.

Davis, C. C. (undated): *Fiber Optic Technology and its role in the Information Revolution*. http://www.ece.umd.edu/~davis/optfib.html.

DeMerchant, M.; Brown, A.; Bao, X.; Bremner, T. (1999): *Structural monitoring by use of a Brillouin distributed sensor*. Applied Optics, Vol. 38, No. 13, pp. 2755-2759.

DIN 1045-1 (2001): *Tragwerke aus Beton, Stahlbeton und Spannbeton*. Deutsches Institut für Normung e. V. (DIN).

Donlagic, D.; Culshaw, B. (1999): *Microbend Sensor Structure for Use in Distributed and Quasi-Distributed Sensor Systems Based on Selective Launching and Filtering of the Modes in Graded Index Multimode Fiber*. Journal of Lightwave Technology, Vol. 17, No. 10, pp. 1856-1868.

Doremus, R. H. (2002): *Viscosity of silica*. Journal of Applied Physics, Vol. 92, No. 12, pp. 7619-7629.

Döring, H. (2006): *Hochauflösende faseroptische Längen- und Ausdehnungsmessung*. Tagungsband des V. Mittweidaer Talsperrentags, 10-11 May 2006, ISSN 1437-7624 and Wasserwirtschaft, Issue 1-2/2007, pp. 12-14, ISSN 0043-0978.

Dunnicliff, J. (1993): *Geotechnical Instrumentation for Monitoring Field Performance*. ISBN 0 471 00546 0, 575 p.

Dunstan, M. R. H. (2004): *The state-of-the-art of RCC dams in 2003 - an update of ICOLD Bulletin No. 125.* Proceedings of the International Symposium on Roller Compacted Concrete Dams, 17-19 November 2003, Madrid, Spain, pp. 39-48, ISBN 90 5809 564 9.

Dunstan, M. R. H.; Ibánez-de-Aldecoa, R. (2003): *Quality control in RCC dams using the direct tensile test on jointed cores*. Proceedings of the International Symposium on Roller Compacted Concrete Dams, 17-19 November 2003, Madrid, Spain, pp. 943-950, ISBN 90 5809 564 9.

Facchini, M. (2001): *Distributed optical fiber sensors based on Brillouin scattering*. Dissertation, Institut de transmissions, ondes et photonique, department d´électricité, École Polytechnique Fédérale de Lausanne (EPFL), No. 2521.

Farhadiroushan, M.; Parker, R. T. (1998): *Distributed strain and temperature sensing system*. US Patent 6380534, WO 98/27406.

Fell, R.; MacGregor, P.; Stapledon, D.; Bell, G. (2005): *Geotechnical Engineering of Dams*. ISBN 04 1536 440 9, 932 p.

Fellay, A. (2003): *Extreme temperature sensing using Brillouin scattering in optical fibers*. Dissertation, Institut de transmissions, ondes et photonique, department d´électricité, École Polytechnique Fédérale de Lausanne (EPFL), No. 2728.

FEMA (2005): *Federal Guidelines for Dam Safety - Earthquake Analyses and Design of Dams*. Federal Emergency Management Agency, USA, FEMA 65.

Geinitz, E. (1998): *Verteilte Temperatur- und Dehnungssensorik in Glasfasern durch stimulierte Brillouin-Streuung mit hoher Ortsauflösung und bei großen Sensorlängen*. Dissertation, Physikalisch-Astronomische Fakultät der Friedrich-Schiller-Universität Jena.

Goff, D. R. (2002): *Fiber Optic Reference Guide - A Practical Guide to Communications Technology*. 3rd edition, ISBN 0 240 80486 4, 260 p.

Gong, Y. D. (2006): *Guideline for the design of a fiber optic distributed temperature and strain sensor*. Optics Communications, Vol. 272, pp. 227-237, ISSN 0030-4018.

Habel, W. R. (2006): *Neue Möglichkeiten der Zustandsüberwachung durch strukturintegrierte faseroptische Sensoren*. VDI Jahrbuch 2006/2007 – Bautechnik, ISBN 3 18 401656 0.

Habel, W. R.; Hofmann, D. (2007): *Faseroptische Messverfahren zur Überwachung von Stahl- und Betonbauten*. Bauen in Deutschland, Vol. 4, No. 1, p. 37-40.

Hecht, E. (2001): *Optics*. 4th edition, ISBN 0 80 538566 5, 680 p.

Heller, V. (2008): *Landslide generated impulse waves: Prediction of near field characteristics*. Dissertation, Mitteilungen der Versuchsanstalt für Wasserbau, Hydrologie und Glaziologie der ETH Zürich, Report No. 204.

Higuchi, K.; Fujisawa, K.; Asai, K.; Pasuto, A.; Marcato, G. (2007): *Application of new landslide monitoring technique using optical fiber sensor at Takisaka Landslide, Japan*. Proceedings of the 1st North American Landslide Conference, 3-8 June 2007, Vail, Colorado.

Hiroyuki, S. (2001): *Landslide Monitoring by Optical Fiber Sensor*, Presentation, PWRI - Public Works Research Institute, Japan.

Hoepffner, R.; Moser, D. E.; Aufleger, M.; Neisch, V. (2007): *Performance of distributed and single point systems for crack detection in concrete dams*. Proceedings of the Symposium during the 75th annual meeting of ICOLD, 27 June 2007, St. Petersburg: "Dam Safety Management. Role of State, Private Companies and Public in Designing, Constructing and Operating of Large Dams".

Hoepffner, R.; Schäfer, P.; Aufleger, M. (2007): *Identification and reduction of water losses from open water channels and pipelines*. Proceedings of the International Workshop on Availability and Quality Management of Water in the MENA Region, 18-20 November 2007, Irbid, Jordan.

Hoepffner, R.; Singer, J.; Thuro, K.; Aufleger, M. (2008): *Development of an integral system for dam and landslide monitoring based on distributed fibre optic technology*. Proceedings of the 15th Biennial Conference of the British Dam Society in Warwick - Ensuring reservoir safety into the future, 10-13 September 2008, Warwick, Great Britain.

Holst, A.; Habel, W. R.; Lessing, R. (1992): *Fiber-optic intensity-modulated sensors for continuous observation of concrete and rock-fill dams*. 1st European Conference on Smart Structures and Materials, 12-14 May 1992, Glasgow, Great Britain, SPIE Vol. 1777, pp. 223-226.

Holzmann, M. (2008): *Studie zur Anwendbarkeit verschiedener Materialmodelle in der FE-Berechnung von Staudämmen*. Diploma thesis, Institut für Infrastruktur, Arbeitsbereich für Geotechnik und Tunnelbau and Arbeitsbereich für Wasserbau, Universität Innsbruck, Austria.

Horiguchi, T.; Kurashima, T.; Tateda, M. (1989): *Tensile Strain Dependence of Brillouin Frequency Shift in Silica Optical Fibers*. IEEE Photonics Technology Letters, VOL. 1, No. 5.

Horikawa, M.; Komiyama, M.; Hirata, K.; Uchiyama, H. (2004): *Measuring instruments for optical fiber sensing*. In: Sensing Issues in Civil Structural Health Monitoring, F. Ansari, ISBN 1 4020 3660 4, pp. 393-402.

Hotate, K. (2004): *Fiber Optic nerve System with optical correlation domain technique for smart structures and smart materials*. In: Sensing Issues in Civil Structural Health Monitoring, F. Ansari, ISBN 1 4020 3660 4, pp. 219-228.

Hotate, K.; Tanaka, M. (2002): *Distributed fiber Brillouin strain sensing with 1-cm spatial resolution by correlation-based Continuous-Wave Technique*. IEEE Photonics Technology Letters, Vol. 14, No. 2, pp. 179-181.

ICOLD (2002): *Reservoir Landslides: Investigation and Management - Guidelines and case histories*. International Commission on Large Dams (ICOLD), Bulletin No. 124.

ICOLD (2003): *State-of-the-art of Roller Compacted Concrete dams*. International Commission on Large Dams (ICOLD), Bulletin No. 125.

Inaudi, D. (2005): *Overview of fibre optic sensing to structural health monitoring applications*. Proceedings of the International Symposium on Innovation & Sustainability of Structures in Civil Engineering, 20-22 November 2005, Nanjing, China.

Inaudi, D.; Glisic, B. (2005): *Application of distributed Fiber Optic Sensory for SHM*. 2nd International Conference on Structural Health Monitoring of Intelligent Infrastructure, 16-18 November 2005, Shenzhen, China.

Inaudi, D.; Glisic, B. (2005): *Development of distributed strain and temperature sensing cables*. Proceedings of the 17th International Conference on Optical Fibre Sensors, 23-27 May 2005, Bruges, Belgium, SPIE Vol. 5855.

Inaudi, D.; Vurpillot, S.; Casanova, N.; Osa-Wyser, A. (1996): *Development and field test of deformation sensors for concrete embedding*. Proceedings of the Conference on Smart Structures and Materials: Industrial and Commercial Applications of Smart Structures Technologies, 25 February 1996, San Diego, California, SPIE Vol. 2751.

Jasenek, J. (2007): *The theory and application of fiber optic sensors with spread parameters*. Online article, Project THEIERE - Thematic Harmonisation in Electrical and Information Engineering in Europe, http://www.eaeeie.org/theiere_bratislava/index.html.

Johansson, S.; Dahlin, T.; Farhadiroushan, M.; Friborg, J. (2000): *New and improved monitoring systems for embankment dams*. Elforsk rapport 00:14, Sweden.

Johansson, S.; Parker, T.; Watley, D. (2004): *Distributed strain measurements for embankment dams - Laboratory tests, Installation, and initial monitoring Experiences*. Elforsk rapport 03:19, Sweden.

Johansson, S.; Watley, D. (2004): *Dam Safety - Experience from Distributed Strain Measurements in five Embankment Dams*. Elforsk rapport 07:52, Sweden.

Johansson, S.; Watley, D. (2005): *Distributed sensing of seepage and movements using optical fibres - Results from some embankment dams in Sweden*. International Water Power & Dam Construction.

Johansson, S.; Watley, D. (2005): *Distributed strain measurements for embankment dams - Field tests at Ajaure Dam 2004-05*. Elforsk rapport 05:32, Sweden.

Jones, J. D. C.; McBride, R. (1998): *Multiplexing optical fiber sensors*. In: Optical Fiber Sensor Technology, K. T. V. Grattan and B. T. Meggitt, ISBN 0 412 78290 1.

Jung, S.-C. (2007): *Untersuchung der Hangbewegung an der Aggenalm östlich des Sudelfelds zwischen Bayrischzell und Oberaudorf*. Diploma thesis. Lehrstuhl für Ingenieurgeologie, Technische Universität München.

Kalosha, V. P.; Ponomarev, E. A.; Chen, L.; Bao, X. (2006): *How to obtain high spectral resolution of SBS-based distributed sensing by using nanosecond pulses*. Optics Express, Vol. 14, No. 6., pp. 2071-2078.

Kluth, R.; Farhadiroushan, M.; Park, D. S.; Lee, S. U.; Kim, J., Y.; Kim, Y. S. (undated): *Case Studies on Distributed Temperature and Strain Sensing (DTSS) by using optic fibre*. Online article, http://www.sensornet.co.uk/module/page-303/zone-1/article_id-8/articles_action-view_article.

Kluth, R.; Watley, D. (2006): *Utilising dam monitoring Technology for Monitoring Structural Behaviour of Foundations*. Proceedings of the International conference on Re-use of Foundations for Urban Sites (RuFUS), 19-20 October 2006, Watford, United Kingdom.

Komatsu, K.; Fujihashi, K.; Okutsu, M. (2002): *Application of the optical sensing technology to the civil engineering field with fiber strain measurement device (BOTDR)*. Proceedings of SPIE: Advanced Sensor Systems and Applications, Vol. 4920, pp. 352-361.

Kurashima, T.; Horiguchi, T.; Ohno, H.; Izumita, H. (1998): *Strain and Temperature characteristics of Brillouin spectra in optical fibers for distributed sending techniques*. Proceedings of the 24th European Conference on Optical Communication (ECOC '98), 20-24 September 1998, Madrid, Spain.

Kurashima, T.; Horiguchi, T.; Izumita, H.; Furukawa, S.; Koyamada, Y. (1993): *Brillouin Optical-Fiber Time Domain Reflectometry*. IEICE Transactions on Communications, Vol. E76-B, No. 4, pp. 382-389.

Kurashima, T.; Horiguchi, T.; Tateda, M. (1990): *Thermal effects on the Brillouin frequency shift in jacketed optical silica fibers*. Applied Optics, Vol. 29, No. 15, pp. 2219-2222.

Kurashima, T.; Usu, T.; Tanaka, K.; Nobiki, A. (1997): *Application of fiber optic distributed sensor for strain measurement in civil engineering*. Proceedings of SPIE - The International Society for Optical Engineering: Smart Materials, Structures, and Integrated Systems. Adelaide, Australia, Vol. 3241, pp. 247-258.

Kurokawa, S.; Shimano, K.; Sumitro, S.; Suzuki, M. (2004): *Global Concrete Structure Monitoring by utilizing Fiber Optic*. Proceedings of the 2nd International Conference on Bridge Maintenance, Safety and Management (IABMAS'04), 18-22 October 2004, Kyoto, Japan, ISBN 9 0580 9680 7.

Kutzner, C. (1996): *Erd- und Steinschüttdämme für Stauanlagen*. ISBN 3 432 26811 4, 256 p.

Lambe, T. W.; Whitman, R.V. (1969): *Soil mechanics.* 1st edition, ISBN 0 4715 1192 7, 553 p.

Lange, J.; Benning , W. (2006): *Verfahren zur Rissanalyse bei Betonbauteilen*. Fachtagung Bauwerksdiagnose (NDT in Civil Engineering), 23-24 February 2006, Berlin, Germany.

Le Floch, S. (2001): *Etude de la diffusion Brillouin stimulée dans les fibres optiques monomodes standard. Application aux capteurs de température et de pression.* Dissertation, Université de Bretagne occidentale, Brest, France.

Lenke, P.; Nöther, N. (2007): *Stimulated Brillouin scattering in graded index multimode optical fiber by excitation of the fundamental mode only*. Proceedings of SPIE - Nonlinear Optics and Applications II, 16-18 April 2007, Prague, Czech Republic, Vol. 6582.

Li, X.; Parker, T.; Farhadiroushan, M.; Blacklaw, D. (2004): *Evaluating a Concept of Using Distributed Optical Fiber Temperature and Strain Sensor for Continuous Monitoring of Casing and Completion Mechanical Deformation in Intelligent Wells*. Proceedings of the Offshore Technology Conference, 3-6 May 2004, Houston, Texas.

Lienhart, W.; Brunner, K. (2003): *Monitoring of bridge deformations using embedded fiber optical sensors*. Proceedings of the 11th International Symposium on Deformation Measurements, 25-28 May, Santorini, Greece, pp. 555-561.

Mahlke, G.; Gössing, P. (2001): *Fiber Optic Cables - Fundamentals, Cable Design, System Planning*. 4th edition, ISBN 3 89578 162 2, 304 p.

Measures, R. (2001): *Structural Monitoring with fiber optic technology*. 1st edition, ISBN ISBN 0 12 48743 4, 716 p.

Mendez, A.; Morse, T. F.; Reinhart, L. J. (1993): *Experimental results on embedded optical fiber sensors in concrete*. Proceedings of SPIE, Smart Structures and Materials: Smart Sensing Processing and Instrumentation, Vol. 1918: pp. 420-427.

Merzbacher, C.; Kersey, A.; Friebele, E. (1996): *Fiber optic sensors in concrete structures: a review*. Smart Materials Structures, Vol. 5, pp. 196-208.

Mills, D. L. (1998): *Nonlinear Optics - Basic Concepts.* 2nd edition, ISBN 3 540 64182 3, 263 p.

Moser, D. E. (2006): *Medidas múltiplas de características de barragens de concreto compactado com rolo utilizando instrumentação por fibra ótica*. Master thesis, Setor de Tecnologia, Universidade federal do Paraná, Curitiba, Brazil.

Moser, D. E.; Aufleger, M.; Hoepffner, R.; Neisch, V.; Soares, M.; Filho, J. (2007): *Temperature and strain measurements in RCC dams using fibre optic instrumentation*. Proceedings of the 5th International Conference on Dam Engineering, 14-16 February 2007, Lisbon, Portugal, ISBN 978 981 05 7585 4, pp. 367-374.

Moser, D. E.; Hoepffner, R.; Aufleger, M.; Soares, M. A. (2006): *The application of new instrumentation methods towards optimal joints spacing criteria and fast construction of RCC Dams*. Proceedings of the 22nd ICOLD Congress: Dams in the societies of the XXI. Century, 18–23 June 2006, Barcelona, Spain.

Moser, D. E.; Soares, M. A.; Marques, F. J.; Aufleger, M. (2006): *Instrumentação por fibra ótica em barragens no Brazil - Estudio de caso pioneiro UHE Fundão*. Proceedings of the Brazilian Symposium on Dams Instrumentation, São Paulo, Brazil.

Muckenthaler, P. (1989): *Hydraulische Sicherheit von Staudämmen*. Dissertation, Berichte des Lehrstuhls für Wasserbau und Wasserwirtschaft, Report No. 61, Technische Universität München, ISSN 0935-6002.

Murata, H. (1996): *Handbook of optical fibers and cables*. 2nd edition. ISBN 0 8247 9719 1, 552 p.

Nanni, A.; Yang, C. C.; Pan, K.; Wang, J.-S.; Michael, R. R. J. (1991): *Fiber-Optic Sensors for Concrete Strain/Stress Measurement*. ACI Materials Journal, Vol. 88, No. 3, pp. 257-264.

Nickmann, M.; Spaun, G.; Thuro, K. (2006): *Engineering geological classification of weak rocks*. Proceedings of the 10th IAEG International Congress - Engineering geology for tomorrow's cities, 6-10 September 2006, Nottingham, United Kingdom, paper No. 454.

Nöther, N.; Wosniok, A.; Krebber, K.; Thiele, E. (2007): *Dike monitoring using fiber sensor-based Geosynthetics*. Proceedings of the III ECCOMAS Thematic Conference on Smart Structures and Materials, 9-11 July 2007, Gdansk, Poland.

Nöther, N.; Wosniok, A.; Krebber, K.; Thiele, E. (2008): *A distributed fiber optic sensor system for dike monitoring using Brillouin optical frequency domain analysis*. Proceedings of SPIE - Smart Structures and Materials & Nondestructive Evaluation and Health Monitoring, 9-13 March 2008, San Diego, California.

Nöther, N.; Wosniok, A.; Thiele, E.; Krebber, K. (2006): *Sensorbasierte Geotextilien zur Deichertüchtigung*. Presentation at RIMAX-Workshop für Nachwuchs-wissenschaftler, Risikomanagement extremer Hochwasserereignisse (RIMAX), 16-17 October 2006, Koblenz, Germany.

Nolting, E.H. (1989): *Zur Frage der Entwicklung lastunabhängiger Verformungen und Wärmedehnzahlen junger Betone.* Institut für Baustoffe der Leibniz Universität Hannover, Report No. 56.

O'Connor, K. M.; Dowding, C. H. (1999): *GeoMeasurements by Pulsing TDR Cables and Probes*. ISBN 0 8493 0586 1, 424 p.

Osuji, S. O.; Anyata, B. U. (2007): *Susceptibility of Clay Core to Cracks in Rockfill Dams by Finite Element Modeling*. Advanced Materials Research, Vol. 18-19, pp. 35-41.

Padevet, P. (2002): *Influence of Temperature on Concrete and its Modulus of Elasticity*. Proceedings of the 40th EAN International Conference on experimental stress analysis, 3-6 June 2002, Prague, Czech Republic.

Park, Y. (2003): *Investigation of the Ability of Filters to Stop Erosion through Cracks in Dams*. Dissertation, Department of Civil Engineering, Blacksburg, Virginia Polytechnic Institute and State University.

Parker, T. R.; Farhadiroushan, M.; Feced, R.; Handerek, V., A.; Rogers, A., J. (1998): *Simultaneous Distributed Measurement of Strain and Temperature from Noise-Initated Brillouin Scattering in Optical Fibers*. IEEE Journal of Quantum Electronics, Vol. 34, No. 4, pp. 645-659.

Parker, T. R.; Farhadiroushan, M.; Handerek, V. A.; Rogers, A. J. (1997): *A fully distributed simultaneous strain and temperature Sensor using Spontaneous Brillouin Backscatter*. IEEE Photonics Technology Letters, Vol. 9, No. 7, pp. 979-981.

Parker, T. R.; Farhadiroushan, M.; Handerek, V. A.; Rogers, A. J. (1997): *Temperature and strain dependence of the power level and frequency of spontaneous Brillouin scattering in optical fibers*. Optics Letters, Vol. 22, No. 11, pp. 787-789.

Pircher, W.; Schwab, H. (1982): *Monitoring and Alarm equipment at the Finstertal and Gepatsch Rockfill dams*. In: Die Talsperren Österreichs, Heft 26, 13. Talsperrenkongress in Rio de Janeiro 1982, ISBN 3 211 81693 3 (GB), ISBN 0 387 81693 3 (D).

Riemer, W. (1992): *Landslides and Reservoirs*. Proceedings of the 6th International Symposium on Landslides, 10-14 February 1992, Christchurch, New Zealand, Vol. 3.

Schmid, R. (1992): *Das Tragverhalten von Erd- und Steinschüttdämmen mit Asphaltbeton-Kerndichtung*. Dissertation. Berichte des Lehrstuhls für Wasserbau und Wasserwirtschaft, Report No. 70, Technische Universität München, ISSN 0939-0308.

Schrader, E. K. (1995): *RCC: current practices, controversies and options*. International Journal on Hydropower & Dams, September 1995, pp. 80-88.

Schrader, E. K.; López, J.; Aridah, M. F. (2003): *Mix design and properties of RCC at Mujib Dam - high and low cementitious content*. International Symposium on Roller Compacted Concrete Dams, 17-19 November, Madrid, Spain, ISBN 90 5809 564 9, pp. 859-864.

Schuster, R. L. (2006): *Interaction of Dams and Landslides—Case Studies and Mitigation*. U.S. Department of the Interior. Reston, U.S. Geological Survey, Professional Paper 1723, 107 p.

Schwab, H. (1984): *Verformungsmechanismen von Asphaltbeton-Kerndichtungen in Staudämmen*. In: Mitteilungen des Instituts für Bodenmechanik, Felsmechanik und Grundbau an der Fakultät für Bauingenieurwesen und Architektur der Universität Innsbruck, Festschrift zum 60. Geburtstag von Prof. Walter Schober, Report No. 5.

Schwab, H.; Pircher, W. (1985): *Structural behaviour of a high Rockfill Dam - Comprehensive interpretation of measurements and conclusions on stress-strain relationships*. In: Die Talsperren Österreichs, Heft 30, 15. Talsperrenkongress in Lausanne 1985, ISBN 3 201 01315 3.

Semenza, E. (2005): *La storia del Vajont raccontata dal geologo che ha scoperto la frana.* ISBN 8 8892 8801 9, 280 p.

Siew, P. F.; Puapansawat, T.; Wu, Y. H. (2003): *Temperature and heat stress in a concrete column at early ages*. ANZIAM Journal, Vol. 44(E), pp. C705-C722.

Singer, J.; Thuro, K.; Sambeth, U. (2006): *Development of a Continuous 3D-Monitoring System for Unstable Slopes using TDR*. Felsbau, Vol. 24, No. 3, pp. 16-23.

Striegler, W. (1998): *Dammbau in Theorie und Praxis*. 2nd edition, ISBN 3 345 00561 1, 400 p.

Sutherland, R. L. (2003): *Handbook of nonlinear optics*. 2nd edition, ISBN 0 8247 4243 5, 976 p.

Tateda, M.; Horiguchi, T.; Kurashima, T.; Ishihara, K. (1990): *First measurement of strain distribution along field-installed optical fibers using Brillouin Spectroscopy*. Journal of Lightwave Technology, Vol.8, No. 9, September 1990, pp. 1269-1272.

Thévenaz, L. (2006): *Fibre Distributed sensing for a more secure society*. Proceedings of the Symposium on Photonics Technologies for 7th Framework Program, 12-14 October 2006, Wroclaw, Poland, pp. 43-51.

Thévenaz, L.; Facchini, M.; Fellay, A.; Niklès, M.; Robert, P. (2001): *Field tests of distributed temperature and strain measurement for smart structures*. Proceedings of the 4th Pacific Rim Conference on Lasers and Electro-Optics (CLEO/Pacific Rim 2001), 15-19 July 2001, pp. I-490-I-491.

Thévenaz, L.; Niklès, M.; Fellay, A.; Facchini, M.; Robert, P. (1998): *Truly distributed strain and temperature sensing using embedded optical fibers*. Proceedings of SPIE: 5th Annual Symposium on Smart Structures and Materials - Sensory Phenomena and Measurement Instrumentation for Smart Structures and Materials, 1-5 March 1998, San Diego, California, Vol. 3330, pp. 301-314.

Thuro, K.; Wunderlich, T.; Heunecke, O. (2007): *Development and testing of an integrative 3D early warning system for alpine instable slopes (alpEWAS)*. In: Geotechnologien. Science Report No. 10, Kick-Off-Meeting 10 October 2007, Technische Universität Karlsruhe, Programme und Abstracts, 10: 101-112.

USACE (2000): *Engineering and Design: Roller Compacted Concrete*. Engineer Manual EM 1110-2-2006 (January 2000), U.S. Army Corps of Engineers (USACE), Washington D.C.

Watley, D.; Johansson, S. (2004): *Optical allusions*. Waterpower magazine, 10 December 2004.

Wieczorek, G. F. (1996): *Landslide Triggering Mechanisms*. In: Landslides - Investigation and Mitigation, Special Report 247. K. A. Turner and R. L. Schuster. ISBN 0 309 06151 2.

Wiegrink, K.-H. (2002): *Stress measurements in RCC with stressmeter*. Roller Compacted Concrete Dam Construction in the Middle East, 4-10 April 2002, Irbid, Jordan, pp. 494-501.

Wu, Z.; Xu, B.; Takahashi, T.; Harada, T. (2006): *Performance of a BOTDR optical fibre sensing technique for crack detection in concrete structures*. Structure and Infrastructure Engineering, Vol. 4, No. 4, August 2008, pp. 311-323.

Zhang, P. (2003): *High-resolution Photon Counting-OTDR Based Interrogation of Multiplexing Broadband FBG Sensors*. Dissertation. Faculty of the Virginia Polytechnic Institute and State University, Blacksburg, Virginia.

Zhou, Z.; Ou, J. (2004): *Development of FBG Sensors for structural health monitoring in civil infrastructures*. In: Sensing Issues in Civil Structural Health Monitoring, F. Ansari, ISBN 1 4020 3660 4, pp. 197-208.

Zhu, Y.; Semprich, S.; Ma, Y.; Cao, W.; Wang, H. (2007): *Berechnungen von Temperatur- und Spannungszuständen in RCC-Staumauern*. Wasserwirtschaft, issue 5/2007, pp. 28-35.

Appendix

A1. Conventional landslide monitoring methods for small surface extensions (<1 km^2) from ClimChAlp (2008)

A2. Conventional landslide monitoring methods for medium surface extensions (1-25 km^2) from ClimChAlp (2008)

A3. Commercially available distributed strain sensing devices

A1. Conventional landslide monitoring methods for small surface extensions (<1 km^2) from ClimChAlp (2008)

Morphology	Coverage	Monitoring Method	Quantity measured	Accuracy	Comments
predominantly flat	single point(s)	**RTK-GPS**	3D relative or absolute single point movements	P[40]: 2 - 4 cm H[41]: 4 - 8 cm	Real time monitoring requires a GSM/UMTS connection or a radio link.
		R/DGPS	3D relative or absolute single point movements	P: 0.5 - 2 cm H: 1.0 - 4 cm	For high precision survey fixed points are needed with centring forced and vertex in a stable position. Continuous monitoring requires the institution of an elaboration centre connected in real time to the sensor.
		Tacheometry	3D relative or absolute single point movements	0.5 - 2 cm	For high precision survey fixed points are needed with centring forced and vertex in a stable position. Continuous monitoring requires the installation of automatic total stations connected in real time to the elaboration centre.
		Precise Levelling	single points altitude movement	0.15 - 3 mm/km[42]	For high precision survey fixed levelling points are needed in a stable position
		Geotechnology	various		In general relative measurements
	area-wide	**Terrestrial Laserscanning**	changes in volume & topography	2.5 - 7 cm	It is possible to install an automatic scanner. The real time monitoring is affected by the elaboration time.
		Geoelectric	changes in electric resistivity of subsurface		Distribution of resistivity changes indicates changes in landslide water regime and can be seen as evidence for changes inside a landslide
		Microseismic	magnitude of acoustic signals		Correlation of slope acoustic events and landslide velocity/degree of slope instability. This is more applicable to developing rotational or toppling failures than translational slides.
predominantly vertical	single point(s)	**Tacheometry**	3D relative or absolute single point movements	1 - 4 cm	For high precision survey fixed points are needed with centring forced and vertex in a stable position. Continuous monitoring requires the installation of automatic total stations connected in real time to the elaboration centre.
	area-wide	**Terrestrial Photogrammetry**	difference along a prefixed direction between surfaces	~ (1.5 - 4) × camera distance	This method allows the construction of 3D movement vectors.
		Terrestrial Laserscanning	changes in volume & topography	2.5 - 7 cm	It is possible to install an automatic scanner. The real time monitoring is affected by the elaboration time.
		Ground-based InSAR	change in line-of-sight distances	0.3 – 0.7 mm	

A2. Conventional landslide monitoring methods for medium surface extensions (1-25 km²) from ClimChAlp (2008)

Morphology	Coverage	Monitoring Method	Quantity measured	Accuracy	Comments
predominantly flat	single point(s)	**RTK-GPS**	3D relative or absolute single point movements	P: 3 - 4 cm H: 6 - 8 cm	For high precision survey fixed points are needed with centring forced and vertex in a stable position. Real time monitoring require a GSM connection or a radio link
		R/DGPS	3D relative or absolute single point movements	P: 1 - 2 cm H: 2 - 4 cm	For high precision survey fixed points are needed with centring forced and vertex in a stable position. Continuous monitoring requires the institution of an elaboration centre connected in real time to the sensor
		Tacheometry	3D relative or absolute single point movements	1 - 4 cm	For high precision survey fixed points are needed with centring forced and vertex in a stable position. Continuous monitoring requires the installation of automatic total stations connected in real time to the elaboration centre.
		Precise Levelling	single points altitude movement	0.15-3 mm/km	For high precision survey fixed levelling points are needed in a stable position
		Geotechnology	various		In general relative measurements
	area-wide	**Geoelectric**	changes in electric resistivity of subsurface		Distribution of resistivity changes indicates changes in landslide water regime and can be seen as evidence for changes inside a landslide
		Microseismic	magnitude of acoustic signals		Correlation of slope acoustic events and landslide velocity/degree of slope instability. This is more applicable to developing rotational or toppling failures than translational slides.
		Aerial photogrammetry(helicopter)	difference in altitude between surfaces	~ (1.5 - 4) × camera distance	This method allows the construction of 3D movement vectors.
		Direct aerial photogrammetry (helicopter)	difference in altitude between surfaces	~ (1.5 - 4) × camera distance, min. 15 - 25 cm	This method allows the construction of 3D movement vectors.
		Airborne Laserscanning (from helicopter)	difference in altitude between surfaces	15 - 25 cm	-
predominantly vertical	single point(s)	**Tacheometry**	3D relative or absolute single point movements	1.5 - 7 cm	For high precision survey fixed points are needed with centring forced and vertex in a stable position. Continuous monitoring requires the installation of automatic total stations connected in real time to the elaboration centre.
	area-wide	**Aerial photogrammetry(helicopter)**	difference along a prefixed direction between surfaces	~ (1.5 - 4) × camera distance	This method allows the construction of 3D movement vectors.

A3. Commercially available distributed strain sensing devices

company	Neubrex	Omnisens	OZ Optics	Sensornet	Yokogawa
instrument	Neubrescope NBX-6000	DiTeSt series (several models)	Foresight™ series (several models)	DTSS	AQ8603
measuring principle	BOTDA	BOTDA	BOTDA	BOTDR	BOTDR
sensor configuration	loop	loop or mirror end	loop	single end	single end
measuring range (max.)	20 km	30 km	40 km	24 km	24 km
spatial resolution (best)	0.1 m	0.5 m	0.1 m	1 m	1 m
sampling interval	0.05 m	0.1 m	0.05 m	1 m	0.05 m
temperature resolution (best)	N/A	± 0.1 K	± 0.003 K	± 1 K	N/A
temperature accuracy (best)	± 1 K	N/A	± 0.1 K	N/A	± 1 K
strain resolution (best)	N/A	± 2 $\mu\varepsilon$	± 0.05 $\mu\varepsilon$	± 20 $\mu\varepsilon$	± 1 $\mu\varepsilon$
strain accuracy (best)	± 25 $\mu\varepsilon$	± 20 $\mu\varepsilon$	± 2 $\mu\varepsilon$	N/A	± 100 $\mu\varepsilon$
headquarter	Japan	Switzerland	Canada	Great Britain	Japan

Bisher erschienene Berichte des Lehrstuhls und der Versuchsanstalt für Wasserbau und Wasserwirtschaft, Technische Universität München

Nr. 1 **Häusler Erich:** Energieumwandlung bei einem frei fallenden, kreisrunden Strahl in einem Wasserpolster, 1962, *vergriffen*

Nr. 2 **Spiekermann, Günter:** Instabile Formen des Schußstrahles beim Abfluß unter Schützen und seine Kraftwirkungen auf die Schützenkonstruktion, 1962, *vergriffen*

Nr. 3 **Linder Gaspar:** Über die Gestaltung von Durchlaßausläufen, 1963, *vergriffen*

Nr. 4 **Knauss Jost:** Modellversuche über die Hochwasserentlastungsanlagen an kleinen Rückhaltespeichern in Südbayern, 1963, *vergriffen*

Nr. 5 **Mahida Vijaysinh:** Mechanismus der Schnellsandfiltration, 1964, *vergriffen*

Nr. 6 **Rothmund, Hermann:** Energieumwandlung durch Strahlumlenkung in einer Toskammer, 1966, *vergriffen*

Nr. 7 **Häusler Erich:** Luftsiphons für den pneumatischen Verschluß von Wassereinlauföffnungen, 1966, *vergriffen*

Nr. 8 **Seus Günther J.:** Die Anfangskavitation, 1966, *vergriffen*

Nr. 9 **Knauss Jost:** Schießender Abfluß in offenen Gerinnen mit fächerförmiger Verengung, 1967, *vergriffen*

Nr. 10 **Häusler Erich; Bormann Klaus:** Schießender bzw.strömender Abfluß in Bächen
Schultz Gert A.: Die Anwendung von Computer-Programmen für das Unit-Hydrograph-Verfahren am Beispiel der Iller
Bauch Wolfram: Untersuchungen über Wasserstandsvorhersagen an einem 600 m langen Modell der Donaustrecke Regensburg-Straubing, 1967, *vergriffen*

Nr. 11 **Schultz Gert A.:** Bestimmung theoretischer Abflußganglinien durch elektronische Berechnung von Niederschlagskonzentration und Retention (Hyreun-Verfahren), 1968, *vergriffen*

Nr. 12 **Raumer Friedrich von:** Verteilung von Bewässerungswasser in Kanälen - Eine Systematik großer Kanalsysteme zur Verteilung von Bewässerungswasser unter besonderer Berücksichtigung von Regulier- und Meßvorgängen, 1968, *vergriffen*

Nr. 13 **Bormann Klaus:** Der Abfluß in Schußrinnen unter Berücksichtigung der Luftaufnahme, 1968

Nr. 14 **Scheuerlein Helmut:** Der Rauhgerinneabfluß, 1968, *vergriffen*

Nr. 15 **Koch Kurt:** Die gegenseitige Strahlablenkung auf horizontaler Sohle, 1968

Nr. 16 **Bauch Wolfram:** Die Hochwasserwelle im ungestauten und gestauten Fluß, 1968

Nr. 17 **Marr Gerhard:** Vergleich zweier Differenzenverfahren in einem mathematischen Modell zur Berechung von instationären Abflußvorgängen in Flüssen, 1970, *vergriffen*

Nr. 18 **Herbrand Karl:** Der räumliche Wechselsprung, 1970, *vergriffen*

Nr. 19 **Seus Günther J.:** Betrachtungen zur Kontinuitätsbedingung der Hydromechanik;
Zielke Werner: Zur linearen Theorie langer Wellen in Freispiegelgerinnen, 1971

Nr. 20 **Häusler Erich:** Entnahmetürme mit Luftsiphons, 1971, *vergriffen*

Nr. 21 **Herbrand Karl:** Das Tosbecken mit seitlicher Aufweitung, 1971

Nr. 22 **Knauss Jost:** Hydraulische Probleme beim Entwurf von Hochwasserentlastungsanlagen an großen und kleinen Staudämmen, 1971, *vergriffen*

Nr. 23 **Zielke Werner:** Brechnung der Frequenzganglinien und Eigenschwingungen von Rohrleitungssystemen
Zielke Werner; Wylie E. Benjamin: Zwei Verfahren zur Berechnung instationärer Strömungen in Gasfernleitungen und Gasrohrnetzen, 1971

Nr. 24 **Knauss Jost:** Wirbel an Einläufen zu Wasserkraftanlagen, 1972, *vergriffen*

Nr. 25 **Kotoulas Dimitrios:** Die Wildbäche Süddeutschlands und Griechenlands, Teil 1, 1972, *vergriffen*

Nr. 26 **Keller Andreas:** Experimentelle und theoretische Untersuchungen zum Problem der modellmäßigen Behandlung von Strömungskavitation, 1973, *vergriffen*

Nr. 27 **Horn Heinrich:** Hochwasserabfluß in automatisch geregelten Staustufen, 1973

Nr. 28 **Bonasoundas Markos:** Strömungsvorgang und Kolkproblem am runden Brückenpfeiler, 1973

Nr. 29 **Horn Heinrich; Zielke Werner:** Das dynamische Verhalten von Flußstauhaltungen, 1973

Nr. 30 **Uslu Orhan:** Dynamische Optimierung der Fließbeiwerte in mathematischen Flußmodellen und Berücksichtigung der Vorlandüberströmung - Eine Anwendung des Operations Research im theoretischen Flußbau, 1974

Nr. 31 **Kotoulas Dimitrios:** Die Wildbäche Süddeutschlands und Griechenlands, Teil 2, 1975, *vergriffen*

Nr. 32 **50 Jahre Versuchsanstalt Obernach**
Hartung Fritz: Einführung: Was treiben eigentlich die Obernacher?
Knauss Jost: Strategien und Entscheidungshilfen beim Hochwasserschutz in Städten, dargestellt am Beispiel der Hochwasserfreilegung der Stadt Harburg an der Wörnitz
Häusler Erich: Abstürze und Stützschwellen in hydraulischer und konstruktiver Betrachtung (Mindestfallhöhen zur Erzielung einer genügenden hydraulischen Wirksamkeit)
Seus Günther J.; Hack Hans-Peter: Erster Vergleich der Ergebnisse des physikalischen Modells in Obernach mit denen des neuen mathematischen Modells
Uslu Orhan; Schmitz Gerd: Parameteridentifikation und Sensitivitätsanalyse bei mathematischen Modellen in der Hydrologie
Keller Andreas; Zielke Werner: Veränderung des freien Gasgehaltes in turbulenten Rohrströmungen bei plötzlichen Druckabsenkungen
Herbrand Karl: Zusammenführung von Schußstrahlen. Zwei praktische Beispiele konstruktiver Lösungen aus Modellversuchen
Zielke Werner: Grenzen der deterministischen Betrachtungsweise in der Strömungsmechanik, 1976

Nr. 33 **Probleme der Arbeit des beratenden Ingenieurs in der Wasserwirtschaft der Entwicklungsländer.** Symposium am 13.10.1976 in Wallgau
Bauch Wolfram: Besondere Probleme bei der Planung und Ausführung der Gesamtentwässerung Busan/Korea
Bormann Klaus: Wasserkraftstudie West Kamerun und Bau der Wasserkraftanlage Batang Agam, Indonesien, zwei Entwicklungshilfe-Projekte unter extremen Bedingungen
Raumer Friedrich von: Zielvorstellungen und Verwirklichung eines wasserwirtschaftlichen Mehrzweckprojektes in Ecuador
Krombach Jürgen: Der beratende Ingenieur in Entwicklungsländern gestern und heute: Berater, Kontrolleur, Entwicklungshelfer oder Geschäftsmann? (am Beispiel wasserwirtschaftlicher Projekte), 1977

Nr. 34 **50 Jahre Versuchsanstalt Obernach,** Feierstunde am 14.10.1976 in Wallgau
Hartung Fritz: Die Wasserbauversuchsanstalt Obernach im Strom der Zeit
Bischofsberger Wolfgang: Laudatio für Professor Dr.-Ing. E. Mosonyi
Mosonyi Emil: Wasserbau, Technik oder Kunst? 1977

Nr. 35 **50 Jahre Versuchsanstalt Obernach,**
Ausleitungen aus geschiebeführenden Flüssen, Seminar am 15.10.1976 in Obernach
Cecen Kazim: Die Verhinderung des Geschiebeeinlaufes zu Wasserfassungsanlagen
Midgley D.C.: Abstraction of water from sediment-laden rivers in Southern Africa
Jacobsen J.C.: Geschiebefreie Triebwasserfassungen - Modellversuche am Beispiel des sogenannten Geschiebeabzuges
Scheuerlein Helmut: Die Bedeutung des wasserbaulichen Modellversuchs für die Gestaltung von Ausleitungen aus geschiebeführenden Flüssen, 1977

Nr. 36 **Hack Hans-Peter:** Lufteinzug in Fallschächten mit ringförmiger Strömung durch turbulente Diffusion, 1977

Nr. 37 **Csallner Klausotto:** Strömungstechnische und konstruktive Kriterien für die Wahl zwischen Druck- und Zugsegment als Wehrverschluß, 1978

Nr. 38 **Kanzow Dietz:** Ein Finites Element Modell zur Berechnung instationärer Abflüsse in Gerinnen und seine numerischen Eigenschaften, 1978

Nr. 39 **Keller Andreas; Prasad Rama:** Der Einfluß der Vorgeschichte des Testwassers auf den Kavitationsbeginn an umströmten Körpern - Ein Beitrag zur Frage der Rolle der Kavitationskeime bei Strömungskavitation, 1978

Nr. 40 **Hartung Fritz:** 75 Jahre Nilstau bei Assuan - Entwicklung und Fehlentwicklung, 1979, *vergriffen*

Nr. 41 **Knauss Jost:** Flachgeneigte Abstürze, glatte und rauhe Sohlrampen
Scheuerlein Helmut: Wasserentnahme aus geschiebeführenden Flüssen
Häusler Erich: Unkonventionelle neuere Stauhaltungswehre an bayerischen Flüssen als gleichzeitige Sohlsicherungsbauwerke, 1979, *vergriffen*

Nr. 42 **Seus Günther J.; Joeres Erhard P.; Engelmann Herbert M.:** Lineare Entscheidungsregeln und stochastische Restriktionen bei Bemessung und Betrieb von Speichern, 1979, *vergriffen*

Nr. 43 **Meier Rupert C.:** Analyse und Vorhersage von Trockenwetterabflüssen - Eine Anwendung der Systemhydrologie, 1980, *vergriffen*

Nr. 44 **Treske Arnold:** Experimentelle Überprüfung numerischer Berechnungsverfahren von Hochwasserwellen, 1980, *vergriffen*

Nr. 45 **Csallner Klausotto; Häusler Erich**: Abflußinduzierte Schwingungen an Zugsegmenten - Ursachen, Sanierung und allgemeine Folgerungen
Herbrand Karl; Renner Dietrich: Aufnahme und Wiedergabe der Bewegung von Schwimmkörpern mit einem Video-Meßsystem
Keller Andreas: Messungen des Kavitationskeimspektrums im Nachstrom eines Schiffes - die ersten Großausführungsmessungen mit der Laser-Streulichtmethode
Knauss Jost: Neuere Beispiele für Blocksteinrampen an Flachlandflüssen
Scheuerlein Helmut: Der gelbe Fluß - nach wie vor Chinas Sorge oder die Unerbittlichkeit der Natur gegenüber 4000 Jahren menschlicher Bemühungen
Seus Günther J.: Nochmals: Das Muskingum-Verfahren. Fingerübungen zu einem bekannten Thema als "gradus ad parnassum" sowie neue Gedanken zur Interpretation des Anwendungsbereiches und eine Lösung des Problems der Nebenflüsse
Treske Arnold: Hochwasserentlastung an Dämmen. Zwei konstruktiv ähnliche Lösungen im Modellversuch, 1981, *vergriffen*

Nr. 46 **Schmitz Gerd:** Instationäre Eichung mathematischer Hochwasserablauf-Modelle auf der Grundlage eines neuen Lösungsprinzips für hyperbolische Differentialgleichungs-Systeme, 1981, *vergriffen*

Nr. 47 **Scheuerlein Helmut:** Der wasserbauliche Modellversuch als Hilfsmittel bei der Bewältigung von Verlandungsproblemen in Flüssen
Knauss Jost: Rundkronige und breitkronige Wehre, hydraulischer Entwurf und bauliche Gestaltung
Keller Andreas: Maßstabseffekte bei der Anfangskavitation, 1983, *vergriffen*

Nr. 48 **Renner Dietrich:** Schiffahrtstechnische Modellversuche für Binnenwasserstraßen - Ein neues System und neue Auswertungsmöglichkeiten, 1984, *vergriffen*

Nr. 49 **Sonderheft: Erhaltung und Umbau alter Wehre** (Wasserbau im historischen Ensemble, drei Beispiele aus dem Hochwasserschutz bayerischer Städte), 1984, *vergriffen*

Nr. 50 **Knauss Jost; Heinrich B.; Kalcyk H.:** Die Wasserbauten der Minyer in der Kopais - die älteste Flußregulierung Europas, 1984, *vergriffen*

Nr. 51 **Hartung Fritz; Ertl Walter; Herbrand Karl:** Das Donaumodell Straubing als Hilfe für die Planung und Bauausführung der Staustufe Straubing, 1984

Nr. 52 **Hahn Ulrich:** Lufteintrag, Lufttransport und Entmischungsvorgang nach einem Wechselsprung in flachgeneigten, geschlossenen Rechteckgerinnen, 1985

Nr. 53 **Bergmann Norbert:** Entwicklung eines Verfahrens zur Messung und Auswertung von Strömungsfeldern am wasserbaulichen Modell, 1985

Nr. 54 **Schwarz Jürgen:** Druckstollen und Druckschächte - Bemessung und Konstruktion, 1985, *vergriffen*

Nr. 55 **Schwarz Jürgen:** Berechnung von Druckstollen - Entwicklung und Anwendung eines mathematischen Modells und Ermittlung der felsmechanischen Parameter, 1987

Nr. 56 **Seus Günther J.; Edenhofer Johann; Czirwitzky Hans-Joachim; Kiefer Ernst-Martin; Schmitz Gerd; Zunic Franz:** Ein HN-Modellsystem für zweidimensionale, stationäre und instationäre Strömungen beim Hochwasserschutz von Städten und Siedlungen, 1987

Nr. 57 **Knauss Jost:** Die Melioration des Kopaisbeckens durch die Minyer im 2. Jt.v.Chr. – Kopais 2 - Wasserbau und Siedlungsbedingungen im Altertum, 1987

Nr. 58 **Mtalo Felix:** Geschiebeabzug aus Kanälen mit Hilfe von Wirbelröhren, 1988

Nr. 59 **Yalin M. Selim; Scheuerlein Helmut**: Friction factors in alluvial rivers
Yalin M. Selim: On the formation mechanism of dunes and ripples
Keller Andreas: Cavitation investigations at one family of NACA-hydrofoils at different angles of attack, as a contribution to the clarification of scale effects at cavitation inception, 1988

Nr. 60 **Schmitz Gerd H.:** Strömungsvorgänge auf der Oberfläche und im Bodeninneren beim Bewässerungslandbau. Grundlagen, Kritik der herkömmlichen Praxis und neue hydrodynamisch-analytische Modelle zur Oberflächenbewässerung, 1989

Nr. 61 **Muckenthaler Peter:** Hydraulische Sicherheit von Staudämmen, 1989, *vergriffen*

Nr. 62 **Kalenda Reinhard:** Zur Quantifizierung der hydraulischen Versagenswahrscheinlichkeit beweglicher Wehre, 1990

Nr. 63 **Knauss Jost:** Kopais 3, Wasserbau und Geschichte, Minysche Epoche - Bayerische Zeit (vier Jahrhunderte - ein Jahrzehnt), 1990

Nr. 64 **Kiefer Ernst-Martin, Liedl Rudolf, Schmitz Gerd H. und Seus Günther J.:** Konservative Strömungsmodelle auf der Basis krummliniger Koordinaten unter besonderer Berücksichtigung von Wasserbewegungen im ungesättigt-gesättigten Boden, 1990

Nr. 65 **Hartung Fritz:** Der ägyptische Nil 190 Jahre im Spiel der Politik (1798-1988)
Hartung Fritz: Gedanken zur Problematik der Nilwehre
Döscher Hans-Dieter und Hartung Fritz: Kritische Betrachtungen zum Stützwehr im Toschka-Entlastungsgerinne des Assuan-Hochdammes, 1991

Nr. 66 **Schmitz Gerd H., Seus Günther J. und Liedl Rudolf:** Ein semi-analytisches Infiltrations-modell für Füllung und Entleerung von Erdkanälen
Keller Andreas P.: Chinese-German comparative cavitation tests in different test facilities on models of interest for hydraulic civil engineering, 1991

Nr. 67 **Liedl Rudolf:** Funktionaldifferentialgleichungen zur Beschreibung von Wasserbewegungen in Böden natürlicher Variabilität - Beiträge zur Theorie und Entwicklung eines numerischen Lösungsverfahrens, 1991

Nr. 68 **Zunic Franz:** Gezielte Vermaschung bestehender Kanalisationssysteme - Methodische Studien zur Aktivierung freier Rückhalteräume unter besonderer Berücksichtigung der Abflusssteuerung, 1991

Nr. 69 **Eickmann Gerhard:** Maßstabseffekte bei der beginnenden Kavitation - Ihre gesetzmäßige Erfassung unter Berücksichtigung der wesentlichen Einflußgrößen, 1991

Nr. 70 **Schmid Reinhard:** Das Tragverhalten von Erd- und Steinschüttdämmen mit Asphaltbeton-Kerndichtungen, 1991

Nr. 71 **Kiefer Ernst-Martin:** Hydrodynamisch-numerische Simulation der Wasserbewegung im ungesättigten und gesättigten Boden unter besonderer Berücksichtigung seiner natürlichen Variabilität, 1991

Nr. 72 **Strobl Th., Steffen H., Haug W. und Geiseler W.-D.:** Kerndichtungen aus Asphaltbeton für Erd- und Steinschüttdämme, 1992

Nr. 73 **Symposium: Betrieb, Unterhalt und Modernisierung von Wasserbauten.**
Garmisch-Partenkirchen, 29. - 31. Oktober 1992

Nr. 74 **Heilmair Thomas und Strobl Theodor:** Erfassung der sohlnahen Strömungen in Ausleitungs-strecken mit FST-Halbkugeln und Mikro-Flowmeter - ein Vergleich der Methoden, 1994

Nr. 75 **Godde Dominik:** Experimentelle Untersuchungen zur Anströmung von Rohrturbinen - Ein Beitrag zur Optimierung des Turbineneinlaufs, 1994

Nr. 76 **Knauss Jost:** Von der Oberen zur Unteren Isar
Alte und neue Wasserbauten rund um die Benediktenwand. Bachumleitungen - Treibholzfänge - durchschwallte Rohre - eine besondere Entlastungsanlage
Sohlensicherung an der Unteren Isar. Sohlstufenkonzept - Belegung der Sohle mit größeren Steinen in offener Anordnung, 1995

Nr. 77 **Knauss Jost:** Argolische Studien: Alte Straßen - alte Wasserbauten. Talsperre von Mykene; Flußumleitung von Tiryns; Hydra von Lerna; Küstenpass Anigraia, 1996

Nr. 78 **Aufleger Markus:** Ein Beitrag zur Auswertung von Erddruckmessungen in Staudämmen, 1996

Nr. 79 **Heilmair Thomas:** Hydraulische und morphologische Kriterien bei der Beurteilung von Mindestabflüssen unter besonderer Berücksichtigung der sohlnahen Strömungsverhältnisse, 1997

Nr. 80 **Maile Willibald:** Bewertung von Fließgewässer-Biozönosen im Bereich von Ausleitungskraftwerken (Schwerpunkt Makrozoobenthos), 1997

Nr. 81 **Knauss Jost:** Olympische Studien: Herakles und der Stall des Augias. Kladeosmauer und Alpheiosdamm, die Hochwasserfreilegung von Alt-Olympia, 1998

Nr. 82 **Symposium: Planung und Realisierung im Wasserbau - Vergleich von Zielvorstellungen mit den Ergebnissen,** Garmisch-Partenkirchen 15. – 17. Oktober 1998

Nr. 83 **Hauger Stefan:** Verkehrssteuerung auf Binnenwasserstraßen – Ein Beitrag zur Optimierung der Schleusungsreihenfolge in Stillwasserkanälen und staugeregelten Flüssen, 1998

Nr. 84 **Herbrand Karl:** Schiffahrtstechnische Untersuchungen der Versuchsanstalt Obernach; Ein Rückblick auf ein traditionelles Untersuchungsgebiet der VAO, 1998

Nr. 85 **Hartlieb Arnd:** Offene Deckwerke – Eine naturnahe Methode zur Sohlstabilisierung eintiefungsgefährdeter Flußabschnitte, 1999

Nr. 86 **Spannring Michael:** Die Wirkung von Buhnen auf Strömung und Sohle eines Fließgewässers – Parameterstudie an einem numerischen Modell, 1999

Nr. 87 **Kleist Frank:** Die Systemdurchlässigkeit von Schmalwänden. Ein Beitrag zur Herstellung von Schmalwänden und zur Prognose der Systemdurchlässigkeit, 1999

Nr. 88 **Lang Tobias:** Geometrische Kriterien zur Gestaltung von Kraftwerkseinläufen. Experimentelle Untersuchungen an Rohr-S-Turbine und Durchströmturbine, 1999

Nr. 89 **Aufleger Markus:** Verteilte faseroptische Temperaturmessungen im Wasserbau, 2000

Nr. 90 **Knauss Jost:** Späthelladische Wasserbauten. Erkundungen zu wasserwirtschaftlichen Infrastrukturen der mykenischen Welt, 2001

Nr. 91 **Festschrift** aus Anlass des 75-jährigen Bestehens der Versuchsanstalt für Wasserbau und Wasserwirtschaft der Technischen Universität München in Obernach – Oskar v. Miller-Institut, 2001

Nr. 92 **Wildner Harald:** Injektion von porösem Massenbeton mit hydraulischen Bindemitteln, 2002

Nr. 93 **Wildbach Naturversuche**
Loipersberger Anton und Sadgorski Constantin: Schwemmholz in Wildbächen – Problematik und Abhilfemaßnahmen; Geschiebeuntersuchungen; 1D und 2D Abflussmodelle in einem Wildbach
Rimböck Andreas: Naturversuch Seilnetzsperren zum Schwemmholzrückhalt in Wildbächen – Planung, Aufbau, Versuchsdurchführung und Ergebnisse
Hübl Johannes und Pichler Andreas: Zur berührungslosen Erfassung der Fließtiefe und Fließgeschwindigkeit in einem Wildbachgerinne zum Zeitpunkt des Durchganges der Hochwasserwelle, 2002

Nr. 94 **Rimböck Andreas:** Schwemmholzrückhalt in Wildbächen – Grundlagen zu Planung und Berechnung von Seilnetzsperren, 2003

Nr. 95 **Nothhaft Sabine:** Die hydrodynamische Belastung von Störkörpern, 2003

Nr. 96 **Schmautz Markus:** Eigendynamische Aufweitung in einer geraden Gewässerstrecke – Entwicklung und Untersuchungen an einem numerischen Modell, 2003

Nr. 97 **Neuner Johann:** Ein Beitrag zur Bestimmung der horizontalen Sicherheitsabstände und Fahrrinnenbreiten für Wasserstraßen, 2004

Nr. 98 **Göhl Christian:** Bypasseinrichtungen zum Abstieg von Aalen an Wasserkraftanlagen, 2004

Nr. 99 **Haimerl Gerhard:** Groundwater Recharge in Wadi Channels Downstream of Dams - Efficiency and Management Strategies, 2004

Nr. 100 **Symposium: Lebensraum Fluss – Hochwasserschutz, Wasserkraft, Ökologie. Band 1;** Wallgau, Oberbayern, 16. bis 19. Juni 2004

Nr. 101 **Symposium: Lebensraum Fluss – Hochwasserschutz, Wasserkraft, Ökologie. Band 2;** Wallgau, Oberbayern, 16. bis 19. Juni 2004

Nr. 102 **Huber Richard:** Geschwindigkeitsmaßstabseffekte bei der Kavitationserosion in der Scherschicht nach prismatischen Kavitatoren, 2004

Nr. 103 **Exposed Thermoplastic Geomembranes for Sealing of Water Conveyance Canals**, Guidelines for Design, Supply, Installation, 2005

Nr. 104 **Workshop „Anwendung und Grenzen physikalischer und numerischer Modelle im Wasserbau“.** Wallgau, Oberbayern, 29. und 30. September 2005

Nr. 105 **Conrad Marco:** A contribution to the thermal stress behaviour of Roller-Compacted-Concrete (RCC) gravity dams – Field and numerical investigations, 2006

Nr. 106 **Schäfer Patrick:** Basic Research on Rehabilitation of Aged Free Flow Canals with Geomembranes, 2006

Nr. 107 **Deichertüchtigung und Deichverteidigung in Bayern.** Beiträge zur Fachtagung am 13. und 14. Juli 2006 in Wallgau, Oberbayern, 2006

Nr. 108 **Porras Pablo:** Fiber optic temperature measurements – Further Development of the Gradient Method for Leakage Detection and Localization in Earthen Structures, 2007

Nr. 109 **Perzlmaier Sebastian:** Verteilte Filtergeschwindigkeitsmessung in Staudämmen, 2007

Nr. 110 **Wasserbau an der TU München** – Symposium zu Ehren von Prof. Theodor Strobl am 16. März 2007 in Wallgau, Oberbayern, 2007

Nr. 111 **Haselsteiner Ronald:** Hochwasserschutzdeiche an Fließgewässern und ihre Durchsickerung, 2007

Nr. 112 **Schwarz Peter und Strobl Theodor:** Wasserbaukunst - Oskar von Miller und die bewegte Geschichte des Forschungsinstituts für Wasserbau und Wasserwirtschaft in Obernach am Walchensee (1926-1951). 120 Seiten, Preis: 9,80 €, 2007

Nr. 113 **Flutpolder: Hochwasserrückhaltebecken im Nebenschluss**. Beiträge zur Fachtagung am 19. und 20. Juli 2007 in Wallgau, Oberbayern. ISBN 978-3-940476-03-6, 240 Seiten, durchgehend farbige Abbildungen, Preis: 34,80 €, 2007

Nr. 114 **Assessment of the Risk of Internal Erosion of Water Retaining Structures: Dams, Dykes and Levees.** Intermediate Report of the European Working Group of ICOLD. ISBN 978-3-940476-04-3, 220 Seiten, Preis: 29,80 €, 2007

Nr. 115 **14. Deutsches Talsperrensymposium** (14th German Dam Symposium) and **7th ICOLD European Club Dam Symposium**. Beiträge zur Tagung am 17. bis 19. September 2007 in Freising (Contributions to the Symposium on 17 - 19 September 2007 in Freising, Germany). ISBN 978-3-940476-05-0, 570 Seiten, Preis: 49,80 €, 2007

Nr. 116 **Niedermayr Andreas:** V-Rampen – Ökologisch weitgehend durchgängige Querbauwerke. ISBN 978-3-940476-06-7, 240 Seiten, Preis: 29,80 €, 2008

Nr. 117 **Hafner Tobias:** Uferrückbau und eigendynamische Gewässerentwicklung – Aspekte der Modellierung und Abschätzungsmöglichkeiten in der Praxis. ISBN 978-3-940476-07-4, 206 Seiten, Preis: 29,80 €, 2008

Nr. 118 **Wang Ruey-wen:** Aspects of Design and Monitoring of Nature-Like Fish Passes and Bottom Ramps. ISBN 978-3-940476-10-4, 280 Seiten, Preis: 29,80 €, 2008

Nr. 119 **Fischer Markus:** Ungesteuerte und gesteuerte Retention entlang von Fließgewässern – Beurteilung der Wirksamkeit möglicher Maßnahmen unter Verwendung hydrodynamisch-numerischer Modellierung. ISBN 978-3-940476-11-1, 220 Seiten, Preis: 29,80 €, 2008

Nr. 120 **Fiedler Katharina:** Erfassung hydromorphologischer Vorgänge bei Hochwasser mit Hilfe von ADCP-Messungen. ISBN 978-3-940476-12-8, Preis: 29,80 €, 2008

Nr. 121 **Hoepffner Roland:** Distributed Fiber Optic Strain Sensing in Hydraulic Concrete and Earth Structures. Measuring Theory and Field Investigations on Dams and Landslides. ISBN 978-3-940476-13-5, Preis: 29,80 €, 2008

Nr. 122 **Gewässermorphologie und EU-WRRL:** Beiträge zur Fachtagung am 24. und 25. Juli 2008 in Wallgau, Oberbayern. ISBN 978-3-940476-15-9, 230 Seiten, durchgehend farbige Abbildungen, Preis: 34,80 €, 2008